



**HAL**  
open science

# Numerical simulation of non-reactive aerodynamics in Internal Combustion Engines using a hybrid RANS/LES approach

Al Hassan Afailal

► **To cite this version:**

Al Hassan Afailal. Numerical simulation of non-reactive aerodynamics in Internal Combustion Engines using a hybrid RANS/LES approach. General Mathematics [math.GM]. Université de Pau et des Pays de l'Adour, 2020. English. NNT : 2020PAUU3028 . tel-03140392

**HAL Id: tel-03140392**

**<https://theses.hal.science/tel-03140392>**

Submitted on 12 Feb 2021

**HAL** is a multi-disciplinary open access archive for the deposit and dissemination of scientific research documents, whether they are published or not. The documents may come from teaching and research institutions in France or abroad, or from public or private research centers.

L'archive ouverte pluridisciplinaire **HAL**, est destinée au dépôt et à la diffusion de documents scientifiques de niveau recherche, publiés ou non, émanant des établissements d'enseignement et de recherche français ou étrangers, des laboratoires publics ou privés.

Université de Pau et des pays de l'Adour  
Ecole Doctorale des Sciences Exactes et de leurs Applications



## PHD THESIS

Subject: Fluid dynamics and applied mathematics

# Numerical simulation of non-reactive aerodynamics in Internal Combustion Engines using a hybrid RANS / LES approach

Al Hassan AFAILAL

Wednesday, December 16, 2020

Prof. Shia-Hui PENG	Swedish Defence Research Agency, FOI, Stockholm	Rapporteur
Prof. Yannick HOARAU	Université de Strasbourg	Rapporteur
Dr. Jacques BORÉE	ISAE-ENSMA, Poitiers	Examineur
Dr. Jérémy GALPIN	Framatome, Lyon	Examineur
Dr. Rémi MANCEAU	Université de Pau, CNRS	Directeur de thèse
Dr. Christian ANGELBERGER	IFP Énergies Nouvelles, Rueil-Malmaison	Promoteur de thèse
Dr. Anthony VELGHE	IFP Énergies Nouvelles, Solaize	Promoteur de thèse



## Remerciements

Et voilà la fin de trois magnifiques années au sein de l'IFPEN avec plein d'aventures, de challenges et d'apprentissages ! Mes premiers remerciements vont à ma mère Iman à qui je dédie ce travail. Ensuite, je tiens à remercier mes encadrants. Christian Angelberger, pour son précieux encadrement durant la deuxième moitié de la thèse. Son écoute, sa disponibilité et sa rigueur m'ont été d'une très grande aide pour accomplir ce travail. Jérémy Galpin, qui a encadré la première partie de cette thèse. Je suis très reconnaissant envers son expertise, sa présence et son professionnalisme. Je tiens aussi à remercier chaleureusement Anthony Velghe, deuxième encadrant de cette thèse, qui a toujours été présent pour apporter son aide informatique et technique, et sa bonne humeur. Je souhaite également remercier Rémi Manceau, directeur de thèse à l'université de Pau, pour ses précieux conseils et son expertise qui m'ont été très utiles. Ces trois années ont été aussi l'opportunité de faire de magnifiques rencontres avec les doctorants de l'IFPEN. Andreas mon collègue de bureau qui est devenu un grand ami. Son humour, ses boulettes et ses discussions interminables me manquent déjà. Edouard et ses nombreuses défaites au Tennis. Lefteris pour ses parenthèses artistiques. Louise pour sa zen attitude. Paul pour les séances à la salle de sport que nous trouvions toujours une excuse pour reporter. El gran Luis. La liste des rencontres est très longue, je suis sûr de ne pas tout citer : Outman, Maxime, Fabien, Matthieu, Alexandra, Stéphane, Alexis, Julien, Edouard, Zhihao, Abhijit... Je tiens aussi à remercier tendrement ma 'Aurlie' pour sa présence, sa gentillesse et son grand soutien pendant la phase de rédaction qui n'était pas toujours évidente.



# Table of contents

<b>List of figures</b>	<b>11</b>
<b>List of tables</b>	<b>21</b>
<b>1 Introduction</b>	<b>1</b>
1.1 Environmental context . . . . .	1
1.2 Spark-Ignition (SI) engines . . . . .	2
1.3 Roles of CFD in the SI engine development process . . . . .	4
1.4 Objectives of the present thesis . . . . .	5
1.5 Outline of the manuscript . . . . .	6
<b>I Modeling of ICE aerodynamics</b>	<b>9</b>
<b>2 Theoretical aspects of turbulent flows</b>	<b>11</b>
2.1 Governing equations . . . . .	11
2.2 Main characteristics of turbulence . . . . .	12
<b>3 Modeling approaches of turbulence</b>	<b>15</b>
3.1 Scale separation operator . . . . .	15

3.2	Reynolds Average Navier-Stokes (RANS) . . . . .	17
3.2.1	Reynolds decomposition . . . . .	17
3.2.2	Overview of RANS models . . . . .	18
3.2.3	Near-wall flow modeling . . . . .	20
3.3	Large-Eddy Simulation (LES) . . . . .	21
3.3.1	Filtered Navier-Stokes equations . . . . .	22
3.3.2	Temporal LES (TLES) . . . . .	24
3.3.3	Limitations of LES in industrial applications . . . . .	25
3.4	Hybrid RANS/LES turbulence models . . . . .	26
3.4.1	Concept . . . . .	26
3.4.2	Classification . . . . .	27
3.5	Literature review of CFD applied to ICE flows . . . . .	28
3.5.1	Characteristics of in-cylinder flows . . . . .	28
3.5.2	Cycle-to-Cycle Variations (CCV) . . . . .	30
3.5.3	Overview of RANS and LES simulations of ICE . . . . .	31
3.5.4	Hybrid RANS/LES models applied to ICE . . . . .	33
<b>II</b>	<b>Development of a hybrid RANS/LES model for ICE flows</b>	<b>39</b>
<b>4</b>	<b>Improvement of the HTLES model for wall-bounded flows</b>	<b>41</b>
4.1	Introduction . . . . .	41
4.2	Hybrid RANS/Temporal-LES approach . . . . .	42
4.2.1	Introduction . . . . .	42
4.2.2	Turbulence spectrum in the time domain . . . . .	42

---

4.2.3	Temporal-PITM . . . . .	43
4.2.4	The Hybrid Temporal-LES approach (HTLES) . . . . .	45
4.3	The HTLES approach based on the $k-\omega$ SST model . . . . .	47
4.3.1	Governing equations . . . . .	47
4.3.2	Implementation in the CONVERGE CFD code . . . . .	49
4.4	Development and validation of a shielding to enforce RANS at walls . . . . .	52
4.4.1	The elliptic shielding . . . . .	52
4.4.2	Validation in a Channel Flow . . . . .	55
<b>5</b>	<b>Development of EWA-HTLES for non-stationary flows</b>	<b>63</b>
5.1	Introduction . . . . .	63
5.2	Main features of four-stroke ICE flows . . . . .	64
5.3	Difficulties to use HTLES in cyclic engine flows . . . . .	64
5.4	Possible solutions . . . . .	65
5.4.1	Mapping a RANS solution . . . . .	66
5.4.2	Test of HTLES without averaged inputs . . . . .	66
5.4.3	Recursive method . . . . .	67
5.5	EWA-HTLES . . . . .	70
5.5.1	Exponentially Weighted Average (EWA) . . . . .	70
5.5.2	Definition of the temporal filter width . . . . .	72
5.5.3	Expression of the temporal filter width in EWA-HTLES . . . . .	80
5.5.4	Set of equations of EWA-HTLES . . . . .	81
5.6	Validation of EWA-HTLES on stationary configurations . . . . .	83

---

5.6.1	Simulation set-up . . . . .	83
5.6.2	Channel Flow . . . . .	84
5.6.3	Steady Flow Rig . . . . .	93
5.7	Conclusions . . . . .	105
<b>III Validation of HTLES on engine flows</b>		<b>107</b>
<b>6</b>	<b>Compressed tumble</b>	<b>111</b>
6.1	Presentation . . . . .	111
6.1.1	Configuration and computational domain . . . . .	111
6.1.2	Simulated operating conditions . . . . .	113
6.2	Numerical set-up . . . . .	113
6.2.1	Mesh configurations . . . . .	113
6.2.2	Numerical parameters . . . . .	115
6.2.3	Turbulence modeling . . . . .	115
6.2.4	Boundary conditions and initialization . . . . .	116
6.3	Post-processing of simulation results and experimental data . . . . .	117
6.4	Exploring the influence of the piston law . . . . .	119
6.5	Results for the uncompressed configuration . . . . .	125
6.5.1	Comparison with PIV, RANS and LES . . . . .	125
6.5.2	Analysis of EWA . . . . .	133
6.5.3	Modeled turbulence in HTLES . . . . .	135
6.5.4	Grid dependency . . . . .	142
6.6	Results for the compressed configuration . . . . .	149

---

6.6.1	In-cylinder pressure . . . . .	149
6.6.2	Mean velocity . . . . .	151
6.6.3	Turbulence modeling during compression . . . . .	153
6.7	Statistical convergence . . . . .	155
6.8	Conclusions . . . . .	158
<b>7</b>	<b>The Darmstadt engine</b>	<b>161</b>
7.1	Configuration and computational domain . . . . .	162
7.2	Numerical set-up . . . . .	165
7.2.1	Mesh configuration . . . . .	165
7.2.2	Numerical parameters . . . . .	166
7.2.3	Turbulence modeling . . . . .	167
7.2.4	Boundary conditions and initialization . . . . .	167
7.3	Results of the intake and compression . . . . .	169
7.3.1	Post-processing of simulation results and experimental data . . . . .	169
7.3.2	Results of the integral flow quantities . . . . .	171
7.3.3	Qualitative assessment of modeled turbulence in HTLES . . . . .	175
7.3.4	Results of mean and RMS velocities . . . . .	179
7.3.5	Grid dependency . . . . .	187
7.3.6	Convergence of the phase average . . . . .	194
7.4	Conclusions . . . . .	196

<b>IV</b>	<b>Conclusions and perspectives</b>	<b>199</b>
<b>8</b>	<b>Conclusions and perspectives</b>	<b>201</b>
8.1	Conclusions . . . . .	201
8.2	Perspectives . . . . .	205
	<b>Appendix Shear-stress transport model (SST)</b>	<b>225</b>
	<b>Appendix Development and validation of a hybrid temporal LES model in the perspective of applications to internal combustion engines</b>	<b>227</b>

# List of figures

1.1	Evolution of $CO_2$ emissions for passenger cars by fuel types (source: European Environment Agency). . . . .	2
1.2	The four-stroke cycle [36]. . . . .	3
2.1	Energy cascade of homogeneous isotropic turbulence [91]. . . . .	13
3.1	Typical ICE flow motions . . . . .	29
3.2	Illustration of some aerodynamic characteristics of a tumble type flow [15].	30
3.3	Cycle variability of the tumble ratio in the non-reacting Darmstadt engine obtained from a LES performed in Section 7.3.2.3. . . . .	31
4.1	Decomposition of the turbulence spectrum according to the T-PITM approach [28] . . . . .	44
4.2	Illustration of the cut-cell technique (encircled by the red line) and cell paring in CONVERGE [112]. . . . .	49
4.3	<b>Channel Flow:</b> Profile of the energy ratio $r$ along the wall-normal direction.	53
4.4	<b>Channel Flow:</b> Profiles of $\alpha^2$ over the altitude for three different values of $C_\eta$ .	54
4.5	<b>Channel Flow:</b> Illustration of the configuration. . . . .	55
4.6	<b>Channel Flow:</b> Contours and iso contours (white lines) of the mean axial velocity yielded by HTLES at a streamwise plane cut of the domain. . . . .	56

4.7	<b>Channel Flow:</b> Profile of the mean axial velocity over the spanwise direction at centerline yielded by HTLES. . . . .	57
4.8	<b>Channel Flow:</b> Profiles of the energy ratio $r$ along the wall-normal direction. . . . .	58
4.9	<b>Channel Flow:</b> Impact of the elliptic shielding on the dimensionless velocity profiles for the channel flow $Re_\tau = 1,000$ . . . . .	59
4.10	<b>Channel Flow:</b> Profile of the streamwise component of the Reynolds stress tensor: resolved $\overline{u'_x u'_x}^+$ ( <b>RES</b> ), modeled $\overline{\tau_{xx}}^+$ ( <b>SFS</b> ) and total $TOT = RES + SFS$ . . . . .	60
4.11	<b>Channel Flow:</b> Comparison of the targeted and the observed energy ratio $r$ . . . . .	61
4.12	<b>Channel Flow:</b> Comparison of the mean axial velocity along the wall-normal direction between RANS, LES and HTLES. . . . .	62
5.1	<b>Channel Flow:</b> Profiles predicted by the recursive HTLES with three different values for the lower bound - <b>Left:</b> $k = \frac{k_{sfs}}{r}$ - <b>Right:</b> energy ratio $r$ . . . . .	68
5.2	Transfer function of EWA. . . . .	71
5.3	<b>Synthetic signal:</b> Kraichnan turbulence spectrum in the frequency domain. . . . .	75
5.4	<b>Synthetic signal:</b> Time evolution of the synthetic signal and the filtered signal for different temporal filter-widths. . . . .	76
5.5	<b>Synthetic signal:</b> Evolution of $\tilde{k}$ for different values of the temporal filter widths. . . . .	77
5.6	<b>Sinusoidal synthetic signal:</b> Time evolution of the sinusoidal synthetic signal and the filtered signal for different temporal filter widths. . . . .	78
5.7	<b>Sinusoidal synthetic signal:</b> Phase averaged $\tilde{k}$ over 100 sine period for different $T_w$ values. . . . .	79
5.8	<b>Channel Flow:</b> Profiles of the imposed turbulent kinetic energy over the wall-distance. . . . .	85
5.9	<b>Channel Flow:</b> Profiles of the energy ratio $r$ along the wall-distance predicted by HTLES for the four different imposed profiles of $k$ . . . . .	86

5.10 <b>Channel Flow:</b> Profiles of the mean axial velocity $U^+ = \frac{\overline{U}_x}{u_\tau}$ along the wall-distance predicted by HTLES for the four different imposed profiles of $k$ . .....	87
5.11 <b>Channel Flow:</b> Profiles of the mean viscosity ratio along the wall-distance predicted by HTLES for the four different imposed profiles of $k$ . . . . .	88
5.12 <b>Channel Flow:</b> Comparison of the profile of an instantaneous temporal filter-width $T_w$ with the turbulence integral time scales. . . . .	89
5.13 <b>Channel Flow:</b> Comparison of the profiles of the instantaneous, the time-filtered and the statistical average axial velocities over the wall-distance . .	90
5.14 <b>Channel Flow:</b> Time evolution at a monitoring point located at half height of the channel of the instantaneous, the time-filtered and the statistically averaged axial velocities. . . . .	90
5.15 <b>Channel Flow:</b> Comparison of the profiles of the energy ratio $r$ over the wall-distance yielded by EWA-HTLES and HTLES AVG. . . . .	91
5.16 <b>Channel Flow:</b> Comparison of the profiles the dimensionless axial velocity $\frac{\overline{U}_x}{u_\tau}$ over the wall-distance yielded by DNS, EWA-HTLES and HTLES AVG. . .	92
5.17 <b>Steady Flow Rig:</b> Computational domain. . . . .	93
5.18 <b>Steady Flow Rig:</b> Schematic and geometrical parameters. . . . .	93
5.19 <b>Steady Flow Rig:</b> Cut-plane of the hexahedral mesh. . . . .	94
5.20 <b>Steady Flow Rig:</b> Comparison of the dimensionless mean velocity yielded by LDA measurements, EWA-HTLES and HTLES AVG along <i>line 1</i> . <b>-Left:</b> Axial component. <b>-Right:</b> Radial component. . . . .	96
5.21 <b>Steady Flow Rig:</b> Comparison of dimensionless RMS velocity yielded by LDA measurements and EWA-HTLES and HTLES AVG along <i>line 1</i> . <b>-Left:</b> Axial component. <b>-Right:</b> Radial component. . . . .	96
5.22 <b>Steady Flow Rig:</b> Comparison of the static pressure over the axial distance $x$ yielded by the experiment and EWA-HTLES and HTLES AVG. . . . .	97

5.23 <b>Steady Flow Rig:</b> Contours of the mean subfilter to the total turbulent kinetic energy $\frac{\overline{k_{sfs}}}{k}$ in the central plane yielded by EWA-HTLES. . . . .	98
5.24 <b>Steady Flow Rig:</b> Instantaneous contours of the velocity magnitude computed in EWA-HTLES at $t = 2 s$ . . . . .	99
5.25 <b>Steady Flow Rig:</b> Decomposition of the dimensionless RMS velocity along <i>line 1</i> into two components, <i>RES</i> the resolved part and <i>SFS</i> the modeled part. - <b>Left:</b> axial RMS velocity. - <b>Right:</b> radial RMS velocity. . . . .	99
5.26 <b>Steady Flow Rig:</b> Decomposition of the dimensionless RMS velocity along <i>line 2</i> into two components, <i>RES</i> the resolved part and <i>SFS</i> the modeled part. - <b>Left:</b> axial RMS velocity. - <b>Right:</b> radial RMS velocity. . . . .	100
5.27 <b>Steady Flow Rig:</b> Cut plane of the mean streamlines obtained with RANS, LES and HTLES. . . . .	101
5.28 <b>Steady Flow Rig:</b> Comparison of dimensionless mean velocity along <i>line 1</i> yielded by LDA measurements and RANS, HTLES and LES. - <b>Left:</b> axial component. - <b>Right:</b> radial component. . . . .	101
5.29 <b>Steady Flow Rig:</b> Comparison of dimensionless mean velocity along <i>line 2</i> yielded by LDA measurements and RANS, HTLES and LES. - <b>Left:</b> axial component. - <b>Right:</b> radial component. . . . .	102
5.30 <b>Steady Flow Rig:</b> Comparison of dimensionless RMS velocity along <i>line 1</i> yielded by LDA measurements and RANS, HTLES and LES. - <b>Left:</b> axial component. - <b>Right:</b> radial component. . . . .	103
5.31 <b>Steady Flow Rig:</b> Comparison of dimensionless RMS axial velocity along <i>line 2</i> yielded by LDA measurements and RANS, HTLES and LES. - <b>Left:</b> axial component. - <b>Right:</b> radial component. . . . .	104
5.32 <b>Steady Flow Rig:</b> Comparison of the axial profile of static pressure yielded by the experiment and RANS, HTLES and LES. . . . .	104
6.1 <b>Compressed Tumble:</b> (a) Sketch of the computational domain. (b) Zoom in on the compression chamber [10]. . . . .	112
(a) . . . . .	112

(b)	112
6.2 <b>Compressed Tumble:</b> Cut-plane in the symmetry plane of the domain at BDC. - <b>Left:</b> The whole computational domain. - <b>Right:</b> Zoom in on the compression chamber.	114
6.3 <b>Compressed Tumble flow:</b> Cut-plane in the symmetry plane of three meshes.	114
6.4 <b>Compressed Tumble:</b> Time evolution of the guillotine lift and the piston law.	116
6.5 <b>Compressed Tumble:</b> Sketch of the compression chamber and PIV laser sheet, Figure extracted from [10].	117
6.6 <b>Compressed Tumble:</b> Coordinate system, schematic of the optically accessible area (grey), and the vertical lines over which are extracted the 1D profiles.	118
6.7 <b>Compressed Tumble:</b> Time evolution of three piston laws for the uncompressed configuration.	120
6.8 <b>Compressed Tumble:</b> - <b>Left:</b> Time evolution of the piston velocity of three laws for the uncompressed configuration. - <b>Right:</b> Zoom in where the velocity is maximum during the intake.	121
6.9 <b>Compressed Tumble:</b> Time evolution of the acceleration of the piston along the cycle calculated from the smoothed law.	122
6.10 <b>Compressed Tumble:</b> Comparison of the time evolution of horizontal velocity at a monitoring point at half height of the channel obtained with three piston laws in RANS.	123
6.11 <b>Compressed Tumble:</b> Comparison of the time evolution of the pressure $\Delta P = (P - P_{plenum})/P_{plenum}$ at a monitoring point at half height of the channel obtained with three piston laws in RANS.	124
6.12 <b>Compressed Tumble:</b> Contours of the velocity magnitude extracted from PIV and RANS using three different piston laws.	124
6.13 <b>Compressed Tumble:</b> Contours and streamlines of the phase-averaged in-plane velocity in the symmetry plane of the compression chamber at 5 instants during the intake.	127

6.14 <b>Compressed Tumble:</b> Vertical 1D profiles of the phase-averaged velocity at 5 instants of the intake. . . . .	128
6.15 <b>Compressed Tumble:</b> Contours of the mean velocity fluctuations $\overline{u'_x u'_x}$ in the symmetry plane at 4 instants of the intake. . . . .	130
6.16 <b>Compressed Tumble:</b> Contours of the mean velocity fluctuations $\overline{u'_y u'_y}$ in the symmetry plane at 4 instants of the intake. . . . .	131
6.17 <b>Compressed Tumble:</b> Vertical 1D profiles of the mean velocity fluctuations at 4 instants of the intake. . . . .	132
6.18 <b>Compressed Tumble:</b> Contours of the integral time scale over $T_0$ during intake. . . . .	134
6.19 <b>Compressed Tumble:</b> contours of the temporal filter-width $T_w$ during intake.	134
6.20 <b>Compressed Tumble:</b> $Q^+$ –criterion iso surfaces at 3 in the symmetry plane colored by the instantaneous velocity magnitude at $-270$ CAD. . . . .	135
6.21 <b>Compressed Tumble:</b> Contours of the target energy ratio in the symmetry plane at $-270$ CAD ( $5^{th}$ cycle). . . . .	137
6.22 <b>Compressed Tumble:</b> A zoom in on the compression chamber at $-270$ CAD. - <b>Left:</b> Target energy ratio $r$ . - <b>Right:</b> $\alpha^2$ . . . . .	138
6.23 <b>Compressed Tumble:</b> Contours of $r$ in the symmetry plane at four instants during the intake. . . . .	139
6.24 <b>Compressed Tumble:</b> Contours of $\overline{k_{sfs}}/k$ in the symmetry plane at $-270$ CAD. . . . .	140
6.25 <b>Compressed Tumble:</b> Decomposition of the velocity fluctuations into two components, the resolved part RES and the modeled part SFS. . . . .	141
6.26 <b>Compressed Tumble:</b> Comparison of the in-plane phase-averaged velocity during the intake predicted by HTLES using three meshes. . . . .	143
6.27 <b>Compressed Tumble:</b> Vertical 1D profiles of the phase-averaged velocity during the intake predicted by HTLES using three meshes: M1 ( <b>finer</b> ), M2 ( <b>reference</b> ) and M3 ( <b>coarser</b> ). . . . .	144

6.28 <b>Compressed Tumble:</b> contours of the mean velocity fluctuations $\overline{u'_x u'_x}$ during the intake predicted by HTLES using three meshes. . . . .	146
6.29 <b>Compressed Tumble:</b> Contours of the mean velocity fluctuations $\overline{u'_y u'_y}$ during the intake predicted by HTLES using three meshes. . . . .	147
6.30 <b>Compressed Tumble:</b> 1D vertical profiles of the mean velocity fluctuations during intake predicted by HTLES using three meshes: M1 ( <b>finer</b> ), M2 ( <b>reference</b> ) and M3 ( <b>coarser</b> ). . . . .	148
6.31 <b>Compressed Tumble:</b> Time evolution of the in-cylinder pressure predicted by RANS, HTLES, and LES versus the experimental data. . . . .	150
6.32 <b>Compressed Tumble:</b> Contours and streamlines of the phase-averaged velocity during compression. . . . .	151
6.33 <b>Compressed Tumble:</b> Vertical 1D profiles of the phase-averaged velocity and the velocity fluctuations during compression. . . . .	152
6.34 <b>Compressed Tumble:</b> Contours of the phase-averaged viscosity ratio during compression in the symmetry plane. . . . .	153
6.35 <b>Compressed Tumble:</b> Time evolution of the number of the upwinded cell faces in RANS, HTLES and LES simulations. . . . .	154
6.36 <b>Compressed Tumble:</b> Evolution of the kinetic energy in the symmetry plane with numbers of averaging cycles at 3 instants of the intake stroke. . . . .	156
6.37 <b>compressed tumble:</b> Vertical 1D profiles of the first two statistical moments at $-270 CAD$ . . . . .	157
6.38 <b>Compressed Tumble:</b> Vertical 1D profiles of the first two statistical moments at $-240 CAD$ . . . . .	157
6.39 <b>Compressed Tumble:</b> Vertical 1D profiles of the first two statistical moments at $-180 CAD$ . . . . .	158
7.1 <b>Darmstadt Engine:</b> Experimental setup [5]. . . . .	162
7.2 <b>Darmstadt Engine:</b> Illustration of the two available configurations of the engine, Figure adapted from [15]. . . . .	163

7.3	<b>Darmstadt Engine:</b> Computational domain. . . . .	164
7.4	<b>Darmstadt Engine:</b> A cut of M2 in the intake valve symmetry plane at the intake with a zoom in on the intake valve region. . . . .	165
7.5	<b>Darmstadt Engine:</b> Illustration of each mesh in the symmetry plane of the intake valve at $-260$ CAD. . . . .	166
7.6	<b>Darmstadt Engine:</b> Intake and exhaust valve lifts. . . . .	167
7.7	<b>Darmstadt Engine:</b> Time evolution of the static pressure at the inlet of the intake port and at the outlet of the exhaust port. . . . .	168
7.8	<b>Darmstadt Engine: -Left:</b> Schematic of the cylinder symmetry plane (the red line). <b>-Right:</b> Contour of the optically accessible cross-section area. . . . .	169
7.9	<b>Darmstadt Engine:</b> Schematic of the vertical centerline in the cylinder symmetry plane over which are extracted 1D profiles. . . . .	170
7.10	<b>Darmstadt Engine:</b> Illustration of the coordinate system, and the origin position, Figure adapted from [15]. . . . .	170
7.11	<b>Darmstadt Engine:</b> Time evolution of the in-cylinder pressure. . . . .	171
7.12	<b>Darmstadt Engine:</b> Time evolution of the trapped mass predicted by 3D simulations and compared to a 1D CFD simulation using GT-Power. . . . .	173
7.13	<b>Darmstadt Engine:</b> Time evolution of TR predicted by the simulations. . . . .	174
7.14	<b>Darmstadt Engine:</b> Time evolution of the standard deviation of TR predicted by HTLES and LES. . . . .	175
7.15	<b>Darmstadt Engine:</b> Contours of the energy ratio $r$ at $-260$ CAD at an arbitrary cycle in the symmetry plane of the intake valve. . . . .	176
7.16	<b>Darmstadt Engine:</b> Q-criterion iso surfaces at $10^5$ $1/s^2$ in the symmetry plane of the intake valve colored by the instantaneous velocity magnitude at an arbitrary cycle. . . . .	177
7.17	<b>Darmstadt Engine:</b> Contours of the phase-averaged viscosity ratio on the tumble plane during intake and compression. . . . .	178

---

7.18 <b>Darmstadt Engine:</b> Time evolution of the number of upwinded cell faces in CONVERGE. . . . .	179
7.19 <b>Darmstadt Engine:</b> Illustration of the flow evolution during intake and compression, Figure adapted from [55]. . . . .	180
7.20 <b>Darmstadt Engine:</b> Contours and streamlines of the phase-averaged 2D velocity magnitude in the cylinder symmetry plane at five instants during intake and compression. . . . .	181
7.21 <b>Darmstadt Engine:</b> 1D profiles of the phase-averaged velocity along the vertical centerline in cylinder symmetry line at four different instants. . . . .	182
7.22 <b>Darmstadt Engine:</b> Contours of $u_{y,RMS}$ in the cylinder symmetry plane during intake and compression. . . . .	184
7.23 <b>Darmstadt Engine:</b> Contours of $u_{z,RMS}$ in the cylinder symmetry plane during intake and compression. . . . .	185
7.24 <b>Darmstadt Engine:</b> 1D profiles of the RMS velocities over the vertical centerline in the cylinder symmetry plane at four different instants. . . . .	186
7.25 <b>Darmstadt Engine:</b> Time evolution of the tumble ratio over the crank angle using M1 ( <b>opaque</b> ) and M2 ( <b>transparent</b> ). . . . .	188
7.26 <b>Darmstadt Engine:</b> Standard deviation of the tumble ratio predicted by LES and HTLES using M1 ( <b>opaque</b> ) and M2 ( <b>transparent</b> ) . . . . .	189
7.27 <b>Darmstadt Engine:</b> Comparison of the contours and streamlines of the in-plane phase-averaged velocity in the symmetry plane of the cylinder predicted using two meshes: M1 ( <b>coarse</b> ) and M2 ( <b>reference</b> ). . . . .	190
7.28 <b>Darmstadt Engine:</b> 1D profiles of the phase-averaged velocity along the vertical centerline in cylinder symmetry line using M1 ( <b>opaque</b> ) and M2 ( <b>transparent</b> ) at four different instants. . . . .	191
7.29 <b>Darmstadt Engine:</b> Comparison of $u_{z,RMS}$ on the tumble plane predicted in: M1 ( <b>coarse</b> ) and M2 ( <b>reference</b> ). . . . .	193

- 
- 7.30 **Darmstadt Engine:** Evolution of the kinetic energy along the number of averaged cycles at: - **Left:**  $-260\text{ CAD}$ .- **Center:**  $-180\text{ CAD}$ .- **Right:**  $-90\text{ CAD}$ . . . . . 194
- 7.31 **Darmstadt Engine:** Convergence of the 1D Profiles of the phase averaged velocity and RMS velocity along the vertical centerline at  $-260\text{ CAD}$ . . . . . 195
- 7.32 **Darmstadt Engine:** Convergence of the 1D Profiles of the phase averaged velocity and RMS velocity along the vertical centerline at  $-180\text{ CAD}$ . . . . . 195
- 7.33 **Darmstadt Engine:** Convergence of the 1D Profiles of the phase averaged velocity and RMS velocity along the vertical centerline at  $-90\text{ CAD}$ . . . . . 196

# List of tables

4.1	<b>Channel Flow:</b> Main specifications. . . . .	55
4.2	<b>Channel Flow:</b> Flow rates given by the HTLES with and without the ES. . . .	59
4.3	<b>Channel Flow:</b> Comparison of the flow rates given by RANS, HTLES and LES to DNS data . . . . .	62
5.1	<b>Sinusoidal synthetic signal:</b> Main dimensionless specifications. . . . .	78
5.2	Coefficients of the HTLES approach. . . . .	82
5.3	<b>Stationary configurations:</b> Set of the numerical parameters used for RANS, HTLES and LES. . . . .	84
5.4	<b>Stationary configurations:</b> Turbulence models used for RANS, HTLES and LES. . . . .	84
5.5	<b>Channel Flow:</b> Flow rates yielded by DNS and HTLES. . . . .	92
5.6	<b>Steady Flow Rig:</b> Main specifications. . . . .	94
5.7	<b>Steady Flow Rig:</b> Comparison of the pressure drop given by the experiment and RANS, HTLES and LES. . . . .	105
6.1	<b>Compressed Tumble:</b> Dimensions of the compressed tumble. . . . .	112
6.2	<b>Compressed Tumble:</b> Grid resolutions of $M1$ , $M2$ , and $M3$ in each region. .	114
6.3	<b>Compressed Tumble:</b> Numerical parameters. . . . .	115

---

6.4	<b>Compressed Tumble:</b> Turbulence models used for RANS, HTLES and LES. . .	115
6.5	<b>Compressed Tumble:</b> $x$ -coordinate of the 1D vertical profiles. . . . .	118
6.6	<b>Compressed Tumble:</b> Specifications of the sinusoidal and the experimental piston motion laws. . . . .	120
7.1	<b>Darmstadt Engine:</b> Main specifications. . . . .	163
7.2	<b>Darmstadt Engine:</b> Grid resolution for each region and each phase of the four-stroke cycle for Mesh 2. . . . .	165
7.3	<b>Darmstadt Engine:</b> Numerical parameters. . . . .	166
7.4	<b>Darmstadt Engine:</b> Temperatures at the wall boundaries. . . . .	168
7.5	<b>Darmstadt Engine:</b> Experimental and predicted peak pressure at TDC. . . .	171
1	Constants of the shear-stress model . . . . .	225

# Chapter 1

## Introduction

### 1.1 Environmental context

The fight against global warming and the reduction of the atmospheric pollution are meaningful environmental concerns in our industrial societies. Greenhouse gas emissions from the transportation sector increased by 8% between 1990 and 2015, representing 23% of overall greenhouse gas emissions [27]. Following civil society and environmental organization pressures,  $CO_2$  emission targets for vehicle fleets set by the European commission are more and more stringent. These restrictions force the automobile industry to develop less polluting vehicles.

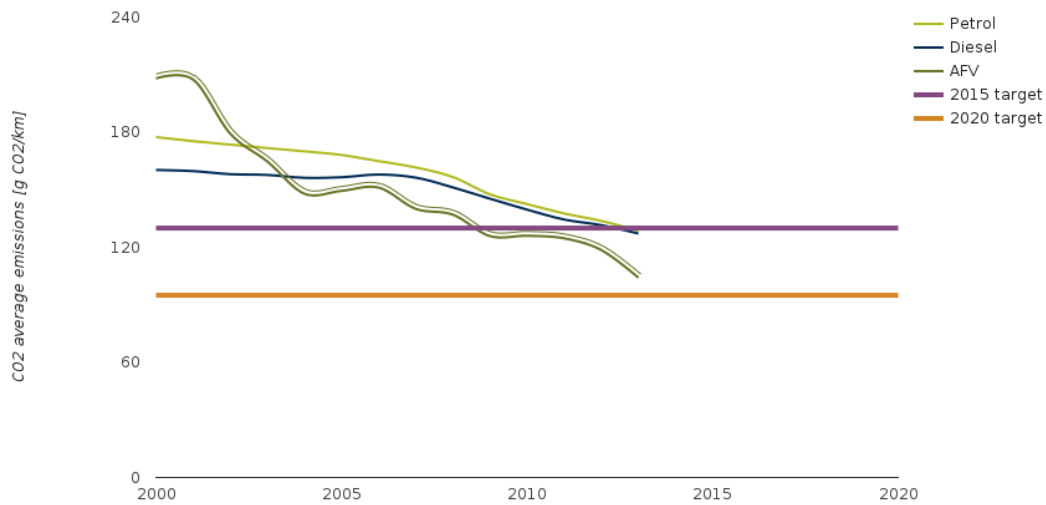


**Fig. 1.1** Evolution of CO<sub>2</sub> emissions for passenger cars by fuel types (source: European Environment Agency).

As shown in Figure 1.1, CO<sub>2</sub> emissions for Petrol (Gasoline), Diesel, and Alternative Fuel Vehicles (AFV) have been continuously decreasing since 2000 and the target for 2020 is very challenging, with a target CO<sub>2</sub> emission of 95 g per km [27].

In this context, electric vehicles appear as a promising alternative to thermal engine vehicles. However, despite its growing trend, the market share of electric vehicles only amounted to 2.6% of global car sales in 2019. Therefore, Internal Combustion Engines (ICE) will still be leading the market shares in the next years [98]. This is particularly true for hybrid electric vehicles that combine ICE with an electric propulsion system, and freight transport, for which ICE remains the more suitable propulsion solution.

## 1.2 Spark-Ignition (SI) engines

A growing number of vehicles worldwide are equipped with SI engines. These engines operate according to the four-stroke Otto cycle as illustrated in Figure 1.2:

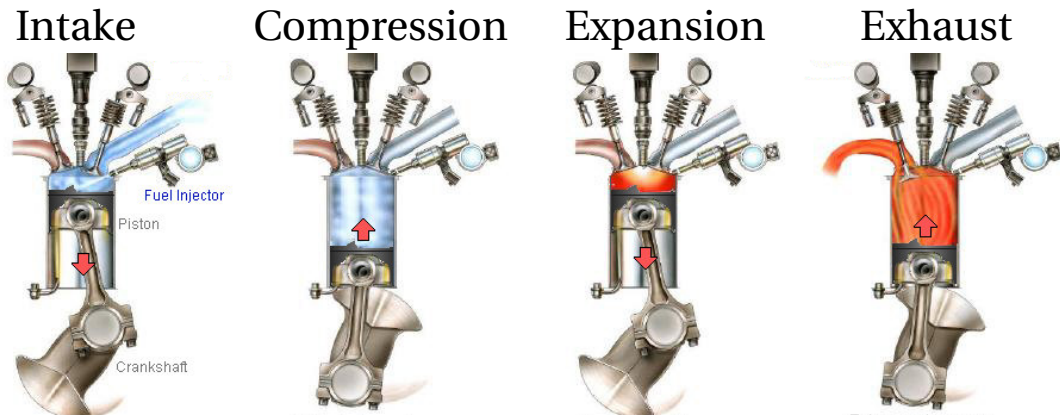


**Fig. 1.2** The four-stroke cycle [36].

1. The intake stroke: during this phase, the piston moves down and the intake valves open. Air is then drawn into the cylinder through the intake valves and the fuel is sprayed through a fuel injector.
2. The compression stroke: the piston moves towards TDC and all the valves close, resulting in the compression of the air-fuel mixture in the cylinder.
3. The expansion stroke: a spark discharge ignites the air-fuel mixture. The chemical energy of the fuel is released and converted into heat. The burnt gasses expand, pushing down the piston during the expansion stroke.
4. The exhaust stroke: the exhaust valves open, and as the piston moves toward TDC, the exhaust gas moves out from the cylinder as the piston moves up.

Car manufacturers dedicated important efforts to reduce  $CO_2$  emissions by increasing engine efficiency in different ways, such as:

- The reduction of the heat losses at the outer walls of the combustion chamber [64].
- The reduction of the combustion duration by acting on the in-cylinder aerodynamics.
- An optimized spark timing in order to release energy at the proper time in the cycle. This also depends on the in-cylinder flow, as the latter plays a major role to prepare the air-fuel mixture.

Modern SI engines include technologies that implement such strategies. In this context, special attention is dedicated to the in-cylinder flow as it was shown that it can promote

rapid and stable combustion in SI engines [51]. Indeed, most modern SI engines are designed in such a way that the air sucked into the combustion chamber forms a large-scale rotational motion around the axis perpendicular to the cylinder axis. This motion is called the tumble motion. As a consequence of its compression, it breaks down into small turbulent scales shortly before the combustion. The increased turbulence allows to obtain a better air-fuel mixture and higher combustion speed which enhances the engine efficiency.

Nonetheless, modern SI engines suffer from a limiting issue called Cycle-to-Cycle Variability (CCV), which manifests by substantial variations in in-cylinder conditions of the engine at a fixed operating point. The difficulty is that several engine parameters (e.g. spark timing and injected fuel mass) are set based on averaged data. Using these parameters in an engine with high CCV levels can lead to combustion efficiencies and pollutant levels that are far from the nominal values if in-cylinder conditions were perfectly repeatable.

### **1.3 Roles of CFD in the SI engine development process**

Industrials dedicate continuous effort to understand the occurrence of CCV, and to implement solutions to avoid them. Computational Fluid Dynamics (CFD) tools have become fundamental tools used today in the ICE development process. They can support the design of engine parts as well as provide a better understanding of the occurrence of CCV. Turbulent flows encountered in ICE are wall-bounded, characterized by Reynolds numbers between 10,000 and 30,000 [115], and comprise multi-physics processes such as combustion, multiphase flow, spray formation, and heat transfer.

Simulating all the scales of motion using Direct Numerical Simulation (DNS) remains far beyond computers' capabilities, both at present and in the near future. Therefore, turbulence modeling approaches are used to reduce the computational simulation cost.

Reynolds-Averaged Navier Stokes (RANS) is the most widely used approach in the industry, mainly because of its low computational cost. Nonetheless, this approach uses statistical averaging, which only provides phase averages of the flow quantities making CCV assessment difficult [115, 117]. Furthermore, several studies highlighted its limited accuracy in complex flows involving shear flows and flow separation that are encountered in ICE flows [24]. Alternatively, Large-Eddy Simulation (LES), is another

well-known approach, has an improved ability to predict unsteady phenomena such as CCV occurrences [114, 115]. LES uses spatial filtering to identify large turbulent scales and resolve them, while the unresolved small scales are modeled. LES requires that the grid size be sufficiently fine to solve a large enough part of the turbulent energy, inducing a high computational cost, especially near the wall where turbulent structures are small [7]. Wall modeling strategies reduce the computational cost of LES at the walls by modeling the boundary layers using wall-functions. Apart from the gain in computational cost, applications of wall-modeled LES (WMLES) in ICE flows have shown limited accuracy for the wall friction assessment [79, 96, 115].

An alternative to WMLES consists in combining RANS and LES models in the same computational domain in a so-called hybrid RANS/LES approach. Such approaches aim at reducing the computational cost of the simulations by using RANS at the walls and where a statistical description of the flow is sufficient. Furthermore, it was shown that some of these models could further decrease the simulation cost by using relatively coarser meshes than for LES [24, 26, 115, 124].

## 1.4 Objectives of the present thesis

Despite the development of different hybrid methods, few of them were applied to ICE flows. In this context, the present work aims to develop a hybrid RANS/LES model for ICE flows based on a theoretical framework capable of meeting the following requirements:

- The developed model must be compatible with ICE cyclic flows with moving wall boundaries and time-varying boundary conditions.
- It should be able to switch automatically between RANS and LES in order to be easily used in non-stationary flows.
- It should be able to operate in RANS at the walls and where the mesh is too coarse for LES.
- The model should be able to reduce the computational cost compared to LES by resolving turbulent scales in relatively coarse meshes.

Among the existing hybrid models, the Hybrid Temporal RANS/LES (HTLES) [80, 81, 129] approach was selected as the starting model for its theoretical framework and

its compliance with some of the requirements mentioned above. The model uses the multiscale approach [28, 29, 34, 118, 119] in the time domain to define the modeled scales, which offers a well-defined framework for the RANS-LES transition in stationary flows [19, 38]. Nevertheless, this model is recent, it is only compatible with stationary flows, and it has not been extensively used in complex configurations.

The present work aims at extending HTLES to ICE engine flows. First, HTLES was implemented in the Converge CFD code [112], and validated in stationary configurations. Particular attention was paid to the ability of HTLES to switch to RANS at the walls. It was found that the model has a grid-dependent behavior near the wall and did not ensure RANS at the walls. A shielding function that ensures RANS at the walls was developed for this purpose. HTLES was then extended to cyclic ICE flows by adapting the method for evaluating the mean quantities used in the model. The developed model was validated in stationary configurations. The results of the simulations were compared with the reference data and with RANS and LES. Finally, it was applied to two optical engines: the compressed tumble engine and the Darmstadt engine. The predictions of mean and rms velocities, as well as the ability of the model to resolve CCV were assessed and the results were compared with experimental findings, and with RANS and LES.

## 1.5 Outline of the manuscript

*Part I* introduces the governing flow equations and the main approaches of turbulence modeling

- *Chapter 2* provides the Navier Stokes equations and the main characteristics of turbulent flows.
- *Chapter 3* introduces the different modeling approaches of turbulence. It also comprises a literature review on the studies that applied RANS, LES and hybrid RANS/LES to ICE flows.

*Part II* is dedicated to the theoretical developments of the Hybrid Temporal RANS/LES (HTLES) model for cyclic ICE flows and its validation in stationary configurations:

- *Chapter 4* presents the theoretical framework of the original HTLES model, and details its implementation in the Converge CFD code. An elliptic shielding was developed to ensure that HTLES operates in RANS at the walls. Then a validation in

a channel flow is provided. The main findings of this Chapter were published (see Appendix 8.2):

Development and validation of a hybrid temporal LES model in the perspective of applications to internal combustion engines.

*Afailal A. H., Galpin J., Velghe A. and Manceau R.*

*Oil Gas Sci. Technol. – Rev. IFP Energies nouvelles, 74 (2019) 56 .*

- *Chapter 5* is dedicated to the extension of HTLES to cyclic ICE flows. It first discusses different approaches that have been explored in this work , before detailing the approach that was retained and developed. Finally, the developed model is validated in two stationary configurations: a channel flow at  $Re_\tau = 1,000$  [77] and a steady flow rig [127], which represents an engine-like configuration. For each configuration, the simulation results are analyzed and compared with the reference data and with RANS and LES.

*Part III* provides the results of the developed model in two non-reacting engine flows. For each engine, the simulation results were examined on different meshes, and compared with PIV findings, and with RANS and LES.

- *Chapter 6* presents the results of HTLES in the compressed tumble engine. This configuration consists of a simplified square engine that reproduces the generation and the tumble motion breakdown.
- *Chapter 7* exposes the results of HTLES in the Darmstadt engine. This configuration is similar to a SI engine.



# **Part I**

## **Modeling of ICE aerodynamics**



# Chapter 2

## Theoretical aspects of turbulent flows

This Chapter gives the governing equations and the main characteristics of compressible turbulent gas flows, which constitute the context of this work. It starts by providing the Navier-Stokes equations, before giving the main characteristics of turbulent flows.

### 2.1 Governing equations

The mathematical formulation of any Newtonian compressible flow expresses using Navier-Stokes equations – the continuity, momentum and energy equations :

$$\begin{cases} \frac{\partial}{\partial t}\rho + \frac{\partial}{\partial x_j}(\rho U_j) & = 0 \\ \frac{\partial}{\partial t}(\rho U_i) + \frac{\partial}{\partial x_j}(\rho U_i U_j) & = -\frac{\partial}{\partial x_i}p + \frac{\partial}{\partial x_j}\sigma_{ij} \\ \frac{\partial}{\partial t}(\rho E) + \frac{\partial}{\partial x_j}(\rho U_j E) & = -\frac{\partial}{\partial x_j}(U_i(p\delta_{ij} - \sigma_{ij}) + q_j) \end{cases} \quad (2.1)$$

where  $\rho$  denotes the density, and  $U_i$  is the  $i^{th}$  component of the velocity.  $p$  is the static pressure.  $\sigma_{ij} = 2\mu(S_{ij} - \frac{1}{3}S_{kk}\delta_{ij})$  is the stress tensor, with  $S_{ij} = \frac{1}{2}(\frac{\partial U_i}{\partial x_j} + \frac{\partial U_j}{\partial x_i})$  is the strain rate tensor.  $E$  is the total energy, and  $q$  is the heat flux.

The Redlich-Kwong equation of state [109] is used for gases to couple the density, pressure and temperature:

$$p = \frac{RT}{V_m - b} - \frac{a}{\sqrt{T}V_m(V_m + b)} \quad (2.2)$$

where  $R = 8.314 \text{ J.mol}^{-1}.\text{K}^{-1}$  is the gas constant.  $T$  is the temperature.  $V_m$  is the molar volume.  $a = 0.42748 \times \frac{R^2 T_c^{5/2}}{P_c}$  and  $b = 0.08664 \times \frac{RT_c}{P_c}$ , with  $T_c$  and  $P_c$  are the temperature and the pressure at the critical point.

One of the non-dimensional numbers used to characterize the flows is the Reynolds number [110]:

$$Re = \frac{UL}{\nu} \quad (2.3)$$

The Reynolds number expresses the ratio of the inertial forces to the viscous forces.  $U$  and  $L$  denote the characteristic velocity and length scale of the flow, respectively. A high Reynolds number means that the inertial forces overweight the viscous forces, possibly giving rise to chaotic flow motions, i.e, turbulence.

## 2.2 Main characteristics of turbulence

In order to understand turbulence processes, Richardson [113] introduced the energy cascade concept. According to this theory, turbulence is a composition of eddies of different sizes. The kinetic energy enters the turbulence at the largest eddies. This energy is then transferred from the large eddies to the small ones by inviscid processes. It goes on until reaching the smallest scales, where the turbulent energy is dissipated into heat by viscous forces. Kolmogorov completed this theory by quantifying the length, time and velocity scales to describe the smallest eddies:

- Kolmogorov length scale  $\eta = (\frac{\nu^3}{\varepsilon})^{1/4}$
- Kolmogorov time scale  $\tau_\eta = (\frac{\nu}{\varepsilon})^{1/2}$
- Kolmogorov velocity  $u_\eta = (\nu\varepsilon)^{1/4}$

where  $\nu$  is the kinematic viscosity of the fluid and  $\varepsilon = \overline{\nu \frac{\partial u'_i}{\partial x_k} \frac{\partial u'_i}{\partial x_k}}$  is the turbulent dissipation rate. The Reynolds averaging operator  $\overline{\quad}$  and the fluctuating velocities  $u'_i$  are introduced in Section 3.2.1.

In-depth analysis of the turbulence process can be achieved through the Fourier transformation of the turbulent energy, which expresses as:

$$E(\kappa, t) = \int \int \int_{-\infty}^{+\infty} \frac{1}{2} \phi_{ii}(x, t) \delta(|x| - \kappa) dx, \quad (2.4)$$

where  $\delta$  is the Dirac distribution,  $\kappa$  is the wave number related to the length scale of the eddies  $l$  as:  $\kappa = 2\pi/l$  and  $\phi_{ij}$  is,

$$\phi_{ij}(\kappa, t) = \frac{1}{(2\pi)^3} \int \int \int_{-\infty}^{+\infty} e^{-i\kappa r} R_{ij}(x, r, t) dr, \quad (2.5)$$

where  $R_{ij}$  is the two-point correlation,

$$R_{ij}(x, r, t) = \overline{u'_i(x, t) u'_j(x + dr, t)}. \quad (2.6)$$

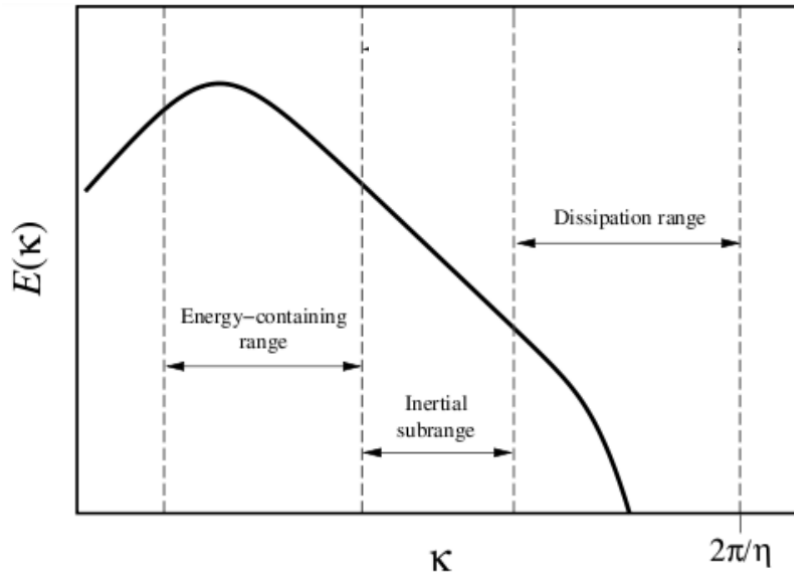


**Fig. 2.1** Energy cascade of homogeneous isotropic turbulence [91].

Figure 2.1 shows the energy cascade profile in the framework of Homogeneous Isotropic Turbulence (HIT). The energy spectrum can be divided in three regions [63]:

- Energy-containing range: consists of the largest eddies where the turbulence energy is generated by the mean flow.
- Inertial sub range: it this range the turbulent energy is transferred from large to small eddies. The turbulence is generally assumed to be isotropic in the inertial sub range. The energy in this range follows the Kolmogorov law:

$$E(\kappa) = C_{\kappa} \varepsilon^{2/3} \kappa^{-5/3} \quad (2.7)$$

where the Kolmogorov constant  $C_{\kappa}$  is around 1.5

- Dissipation range: the dissipation takes place within the smallest scales where viscous effects become preponderant leading to the dissipation of the turbulent kinetic energy into heat.

These analyses give an overview of turbulence mechanisms and have played an important role on turbulence modeling.

# Chapter 3

## Modeling approaches of turbulence

Direct Numerical Simulation (DNS) is the simplest approach to simulate turbulent flows since the Navier-Stokes equations are directly discretized and solved numerically [116]. However, such an approach is not possible for ICE flows that are turbulent and contain a wide range of length and time scales, which requires an unaffordable computational cost for their resolution [104, 115, 116, 122]. Instead of resolving all scales of motion, the computational cost associated with the simulation of turbulent flows can be reduced by resolving only some specific scales of the flow and model the unresolved scales using a physical model.

### 3.1 Scale separation operator

The scale separation operator  $\mathcal{F}$  aims to distinct the resolved and the unresolved turbulent scales. By applying this operator to any variable of the problem  $f$  the following decomposition is obtained:

$$f = \overline{f} + f' , \quad (3.1)$$

where  $\overline{f} = \mathcal{F}(f)$  and  $f'$  are the resolved and unresolved turbulent scales, respectively.

The scale separation operator admits two different natures, depending of the approach of describing the flow:

- Statistical approach (RANS) which consists of a statistical description of the flow where only averaged flow quantities are resolved. In this approach,  $\mathcal{F}$  relies on

statistical averaging:

$$\bar{f} = \frac{1}{N} \sum_{i=1}^N f_i, \quad (3.2)$$

where  $f_i$  is the  $i^{th}$  realization of the flow and  $N$  is the number of the included realizations.  $N$  must be sufficiently large enough to remove all the turbulent fluctuations from  $\bar{f}$ .

- Filtering approach (LES) which consists in separating the large energy-containing eddies from the small scales responsible for the energy dissipation. The general form of  $\mathcal{F}$  consists of the Kampe de Fériet and Betchov spatio-temporal low-pass filter [30]:

$$F(f)(x, t) = \int_{\mathcal{D}} \int_{-\infty}^t G(x, x', t, t') f(x', t') dx' dt' \quad (3.3)$$

where  $G$  is the filter's kernel

The set of equations obtained after applying the scale separation operator to the Navier-Stokes expresses as [116]:

$$\begin{cases} \frac{\partial}{\partial t} \bar{\rho} + \frac{\partial}{\partial x_j} (\bar{\rho} \bar{U}_j) & = -A_{1,j} \\ \frac{\partial}{\partial t} (\bar{\rho} \bar{U}_i) + \frac{\partial}{\partial x_j} (\bar{U}_j \bar{\rho} \bar{U}_i) & = -\frac{\partial}{\partial x_i} \bar{p} + \frac{\partial}{\partial x_j} \bar{\sigma}_{ij} - (A_{2,i} + A_{3,i} + A_{4,i}) \end{cases} \quad (3.4)$$

$A_i$  are the residual terms:  $A_1$ ,  $A_3$  and  $A_4$  are relative to the commutation errors of the scale separation operator and the spatial and temporal partial derivatives, while  $A_2$  is associated with the non-linearity of the convective term. It corresponds to the spatial derivative of the unresolved stress tensor. The residual terms express as [116]:

$$\begin{cases} A_{1,i} & = (\rho [F, \nabla \cdot] \mathbf{U}; \mathbf{e}_i) \\ A_{2,i} & = (\rho \nabla \cdot [F, \mathcal{B}] (\mathbf{U}, \mathbf{U}); \mathbf{e}_i) \\ A_{3,i} & = (\rho ([F, \nabla \cdot] \mathcal{B} (\mathbf{U}, \mathbf{U}) + [\mathcal{F}, \nabla] p + \nu [\mathcal{F}, \nabla^2] \mathbf{U}); \mathbf{e}_i) \\ A_{4,i} & = (\rho [F, \frac{\partial}{\partial t}] \mathbf{U}; \mathbf{e}_i) \end{cases} \quad (3.5)$$

with  $[f, g]h = f \circ g(h) - g \circ f(h)$  is the commutator operator,  $\mathcal{B}$  is the cross product,  $(f; g)$  is the scalar product,  $(\mathbf{e}_i)_{i=1,3}$  is the unit vector in the  $i^{th}$  coordinate direction and  $\mathbf{U}$  is the velocity vector.

## 3.2 Reynolds Average Navier-Stokes (RANS)

### 3.2.1 Reynolds decomposition

According to the Reynolds decomposition, any variable of the flow  $f$  writes as:

$$f = \bar{f} + f' \quad (3.6)$$

where  $\bar{f}$  is the statistical average of  $f$ , and  $f'$  are the turbulent fluctuations. In stationary flows, Monin and Yaglom [92] demonstrated that the statistical average can be replaced by a time average:

$$\bar{f} = \lim_{\Delta T \rightarrow +\infty} \frac{1}{\Delta T} \int_0^{\Delta T} f(\tau) d\tau \quad (3.7)$$

Contrary to stationary flows, the statistical average in cyclic flows (as ICE flows) is time varying and corresponds to a phase average [52]:

$$\bar{f}(t) = \frac{1}{N} \sum_{i=1}^N f(t + iT_0) \quad (3.8)$$

where  $t$  is the instant,  $N$  is the number of the included cycles to compute the phase average and  $T_0$  is the cycle period.

The averaging operator has the following properties:

Constant conservation	$\bar{a}$	=	$a$	
Linearity	$\overline{af}$	=	$a\bar{f}$	
	$\overline{f+g}$	=	$\bar{f} + \bar{g}$	
Commutativity	$[\frac{\partial}{\partial \xi}, \bar{(\cdot)}]$	=	0,	$\xi = t, x_i$
Projectivity	$\overline{f\bar{g}}$	=	$\bar{f}\bar{g}$	
Idempotence	$\overline{\bar{f}}$	=	$\bar{f}$	
	$\overline{f'}$	=	0	

where  $a$  is a constant, and  $f$  and  $g$  are functions depending on time and space. The Reynolds operator is idempotent and commutes with space and time operators. Therefore the residual terms  $A_i$  reduce to:

$$\begin{cases} A_{1,i} = A_{3,i} = A_{4,i} = 0 \\ A_{2,i} = (\nabla \cdot \tau, e_i) \end{cases} \quad (3.9)$$

$\tau_{ij}$  is the Reynolds stress tensor:

$$\tau_{ij} = \overline{u'_i u'_j} \quad (3.10)$$

In compressible flows, turbulent fluctuations can result in significant fluctuations in density, i.e.,  $\rho' \neq 0$ . Using the Reynolds operator in this situation leads to complex averaged equations. In this situation, we use the Favre average [39]:

$$\tilde{f} = \frac{\overline{\rho f}}{\bar{\rho}}. \quad (3.11)$$

The decomposition expresses as:

$$f = \tilde{f} + f'', \quad (3.12)$$

where  $f''$  is the unresolved part of  $f$ .

Despite the density average being not idempotent,  $\overline{f''} \neq 0$ , we use to derive averaged Navier-Stokes equations as it leads to much simpler equation than the ones obtained with the Reynolds average.

The set of equations given by the averaging operator is called Reynolds-Averaged Navier-Stokes (RANS) equations [39]:

$$\begin{cases} \frac{\partial}{\partial t} \bar{\rho} + \frac{\partial}{\partial x_j} (\bar{\rho} \tilde{U}_j) & = 0 \\ \frac{\partial}{\partial t} (\bar{\rho} \tilde{U}_i) + \frac{\partial}{\partial x_j} (\bar{\rho} \tilde{U}_j \tilde{U}_i) & = -\frac{\partial}{\partial x_i} \bar{p} + \frac{\partial}{\partial x_j} \bar{\sigma}_{ij} - \frac{\partial}{\partial x_j} \bar{\rho} \bar{\tau}_{ij} \\ \frac{\partial}{\partial t} (\bar{\rho} \tilde{E}) + \frac{\partial}{\partial x_j} (\bar{\rho} \tilde{U}_j \tilde{E}) & = -\frac{\partial}{\partial x_j} (\tilde{U}_j + \overline{U''} p + \rho \overline{U''_j E} - \overline{U''_i \sigma_{ij}}) + \tilde{q}_j \end{cases} \quad (3.13)$$

where  $\bar{\sigma}_{ij} = 2\mu(\tilde{S}_{ij} - \frac{1}{3}\tilde{S}_{kk}\delta_{ij})$  is the viscous stress strain tensor with  $\tilde{S}_{ij} = \frac{1}{2}(\frac{\partial \tilde{U}_i}{\partial x_j} + \frac{\partial \tilde{U}_j}{\partial x_i})$  the strain rate tensor, and  $\bar{\tau}_{ij} = \overline{u''_i u''_j}$  the turbulent stress tensor.

### 3.2.2 Overview of RANS models

The Reynolds stress tensor represents all the turbulent fluctuations. These fluctuations are not resolved in RANS and need to be modeled.

The first modeling method is called Reynolds Stress Model (RSM). It consists in solving a transport equation for each Reynolds stress component. This approach is rarely employed in the automotive industry because of its complexity and its computational cost, since at least the six transport equations related to the six components of  $\tau_{ij}$  needs to be solved. The second modeling method uses the turbulent-viscosity concept introduced by Boussinesq, in which the Reynolds stress tensor writes according to the Boussinesq relation (Boussinesq, 1877):

$$-\bar{\tau}_{ij} + \frac{2}{3}k\delta_{ij} = 2\nu_t\tilde{S}_{ij} \quad (3.14)$$

where  $k$  is turbulent kinetic energy and  $\nu_t$  is the turbulent viscosity. This approach is called the linear Eddy-Viscosity modeling (EVM) strategy. It reduces the resolution of the six-components of the Reynolds stress tensor to the assessment of a single scalar called turbulent viscosity  $\nu_t$ . This approximation is inspired from the Newton law for the molecular agitation stress [110] and is a retranscription of this law at a macroscopic scale. This remains a simple approximation of the physics of turbulence and the Boussinesq hypothesis is still the subject of many questions in terms of validation for simple-shear flows, swirling flows or flows with strong anisotropy [104]. Despite the limits of this approach, eddy-viscosity modeling is widely used in engineering applications. The eddy-viscosity approximation was studied by Prandtl who was one of the first to introduce an algebraic model of the turbulent viscosity based on the mixing length concept [105]. From a dimensional analysis, the turbulent viscosity can be interpreted as the product of a fluctuating velocity and a characteristic scale:

$$\nu_t = u'' l, \quad (3.15)$$

In RANS, these quantities are based on integral scales of the turbulence. For example, in the two-equation models, one transport equation solves the turbulent kinetic energy  $k$  which is related to the fluctuating velocity  $u'' \approx \sqrt{k}$  and another equation is dedicated to an additional turbulent quantity that allows to define the length or time scales of turbulence. In the  $k - \varepsilon$  model, the turbulent dissipation rate  $\varepsilon$  allows to compute the turbulent length scale  $l \approx \frac{k^{3/2}}{\varepsilon}$ . This model was generalized by Jones & Launder [74] for wall-bounded flows by introducing a damping function that provides an appropriate turbulent viscosity in the near wall regions. Wilcox proposed to resolve the turbulence frequency  $\omega$  in the two-equation  $k - \omega$  model [132]. The model enhances the near-wall modeling without any modification of the equations unlike the  $k - \varepsilon$  model. These two-equation models have been applied successfully in various applications. However both models suffer from a lack of versatility in certain configurations. For instance, the  $k - \varepsilon$  model showed a

lack of sensitivity to adverse pressure-gradients, which delays or prevents separation [62]. Furthermore, this model has some numerical issues in full-wall integration due to the non-linear damping functions introduced near-wall [74], as well as stiff boundary conditions for  $\varepsilon$  at no-slip surfaces. In contrast, the  $k - \omega$  model performs better than the  $k - \varepsilon$  model in situations with adverse-pressure gradients [89], and alleviates the numerical stability issues encountered in the  $k - \varepsilon$  model thanks to the simple formulation of  $\omega$  in the viscous sub layer [132]. Therefore, the main drawback of the  $k - \omega$  model is the strong dependency of the results on the free stream value of  $\omega$  as pointed in [89]. It has been shown that the magnitude of the eddy-viscosity can change by more than 100% by changing the free stream values of  $\omega$ . The shear-stress transport (SST) model [88] reduces this problem by using a zonal approach that switches between  $k - \omega$  and  $k - \varepsilon$  where they perform the best. This model is identical to the original  $k - \omega$  model in the inner 50% of the boundary layer and switches to the  $k - \varepsilon$  model in the free stream. The model uses the change of variable  $\varepsilon = C_\mu k \omega$  to transform the  $\varepsilon$ -equation into a  $\omega$ -equation so that one homogeneous set of equations based on  $k$  and  $\omega$  is obtained. The switch between the  $k - \omega$  model and the  $k - \varepsilon$  is operated using a blending function  $F_1$  that depends on the distance from walls. The set of equations of the  $k - \omega$  SST model is given in Appendix 8.2

### 3.2.3 Near-wall flow modeling

Wall boundaries give rise to boundary layers where the velocity varies from no-slip condition at wall to its free stream value. In these regions, the viscous effects play important role and the wall-distance is expressed in dimensionless wall-distance  $y^+ = \frac{u_\tau y}{\nu}$ . The dimensionless wall-distance can be seen as the ratio of the distance from the wall  $y$  to the viscous length scale  $\delta_\nu$ .

From a computational point of view, the resolution of the turbulence in the near-wall region requires high computational resources and is seldom affordable for industrial purposes. Instead of resolving the boundary layers, it is possible to use a wall modeling approach in which the effects close to the walls are taken into account through a model. The next Sections introduce the characteristics of turbulent flows near the wall, then propose a wall-function model. The resolution of the boundary layer in RANS requires a fine grid such as  $y^+ < 2$  in the whole computational domain [86]. Wall modeling allows to reduce significantly the computational cost. The mesh in the boundary layer can be coarsen in such a way that the condition  $y^+ < 2$  is no more necessary. The effects of the unresolved near wall physics is modeled by a wall-function. Wall-functions are derived

from the law-of-the-wall which has been established in the framework of a channel-flow in which strong assumptions have been considered. These assumptions are not verified in general flows. However, in practice the resolution of the boundary layer is challenging and the use wall functions is often preferable.

Wall-functions are in practice applied to compute the shear stress for the momentum equations at the walls as:

$$\tau_w = \rho u_\tau^{*2} \frac{\overline{U}_{t,p}}{\overline{U}_p^*} \quad (3.16)$$

where  $p$  indicates the cell adjacent to the wall,  $\overline{U}_{t,p}$  is the tangential mean velocity and  $u_\tau^*$  is the nominal shear velocity defined as:

$$u_\tau^* = C_\mu^{3/4} \sqrt{k_p} \quad (3.17)$$

$\overline{U}_p^*$  is given by the law-of-the wall [104]:

$$\overline{U}_p^* = u_\tau^* \left( \frac{1}{\kappa} \ln(y_p^*) + B \right) \quad (3.18)$$

where  $\kappa = 0.41$  and  $B = 5.2$ .  $y_p^*$  corresponds to:

$$y_p^* = \frac{y_p u_\tau^*}{\nu} \quad (3.19)$$

This formulation is applied for  $y_p^* \geq 11.3$ , which corresponds to the intersection of the log law and the linear law  $U^+ = y^+$ . For  $y_p^* < 11.3$ , the nominal mean velocity is calculated from the viscous sublayer profile:

$$\overline{U}_p^* = y_p^* u_\tau^* \quad (3.20)$$

This simple switch from Equation 3.18 to 3.20 at  $y_p^* = 11.3$  is motivated by the lack of theoretical results in the buffer layer.

### 3.3 Large-Eddy Simulation (LES)

In Section 2.2, the energy cascade theory showed that the turbulent process can be considered as a composition of eddies of different sizes. LES uses a low-pass filter that separates the large eddies from the small ones. The large eddies are resolved by the simulation while

the effects of the small eddies which are below the filter cutoff are taken into account by a mathematical model.

### 3.3.1 Filtered Navier-Stokes equations

In LES, the scale separation operator  $\mathcal{F}$  corresponds to a convolution filter [104]:

$$\mathcal{F}(f)(x, t) = \int f(x - \theta, t) G_{\Delta}(\theta, x) d\theta, \quad (3.21)$$

where  $\mathcal{F}(f) = \bar{f}$  are the filtered variables, which contains only the contribution of the large eddies. The integration is performed over the entire flow domain, and  $G_{\Delta}$  is the filter function which satisfies the normalization condition:

$$\int G_{\Delta}(\theta, x) d\theta = 1. \quad (3.22)$$

In simulations, the filter is not explicitly applied to the variables, but results from the combined influence of the subgrid viscosity and the numerical viscosity.

Spatial convolution filters are not idempotent, such that:

$$\begin{cases} \overline{\bar{f}} \neq \bar{f} \\ \overline{f'} \neq 0 \end{cases}. \quad (3.23)$$

To obtain the governing equations of the filtered scales, a convolution filter is applied to Navier-Stokes equations (see Equation (3.4)). The convolution filter commutes with time and space operators only if the filter-width is homogeneous in the entire flow domain. In practice, the filter-width is not strictly homogeneous in the entire computational domain. Therefore, when moving the derivative out of the integral, the commutation error is proportional to  $O(\Delta x^2)$  [42]. This order of accuracy is close to that of numerical schemes used in industrial applications. Hence, the commutativity can be assumed within this framework, which leads to the simplification of the residual terms:

$$\begin{cases} A_{1,i} = A_{3,i} = A_{4,i} = 0 \\ A_{2,i} = (\nabla \cdot \bar{\rho} \tau_{sgs}, e_i) \end{cases} \quad (3.24)$$

where  $\tau_{sgs}$  is the subgrid stress (SGS) tensor.

Thus, in the compressible regime, the filtered Navier-Stokes equations expresses as:

$$\begin{cases} \frac{\partial}{\partial t} \bar{\rho} + \frac{\partial}{\partial x_j} (\bar{\rho} \tilde{U}_j) & = 0 \\ \frac{\partial}{\partial t} (\bar{\rho} \tilde{U}_i) + \frac{\partial}{\partial x_j} (\bar{\rho} \tilde{U}_j \tilde{U}_i) & = -\frac{\partial}{\partial x_i} \bar{p} + \frac{\partial}{\partial x_j} \bar{\sigma}_{ij} - \frac{\partial}{\partial x_j} \bar{\rho} \tau_{sgs,ij} \end{cases} \quad (3.25)$$

where  $\bar{\sigma}_{ij} = 2\mu(\tilde{S}_{ij} - \frac{1}{3}\tilde{S}_{kk}\delta_{ij})$  is the filtered viscous stress strain tensor with  $\tilde{S}_{ij} = \frac{1}{2}(\frac{\partial \tilde{U}_i}{\partial x_j} + \frac{\partial \tilde{U}_j}{\partial x_i})$  the filtered strain rate tensor, and:

$$\tau_{sgs,ij} = \widetilde{U_i U_j} - \tilde{U}_i \tilde{U}_j \quad (3.26)$$

The subgrid stress tensor represents all the interactions between the filtered and subgrid scales [39]:

$$\begin{cases} \tau_{sgs,ij} = L_{ij} + C_{ij} + R_{ij} \\ L_{ij} = \widetilde{U_i U_j} - \tilde{U}_i \tilde{U}_j \\ C_{ij} = \widetilde{u_i'' U_j} + \widetilde{u_j'' U_i} \\ R_{ij} = \widetilde{u_i'' u_j''} \end{cases} \quad (3.27)$$

- the Leonard tensor  $L_{ij}$  contains only the filtered velocities. It represents the interaction among the large scales.
- the cross tensor  $C_{ij}$  represents the interaction between the filtered and the subgrid scales.
- the Reynolds stress tensor  $R_{ij}$  represents the interaction between the subgrid scales.

Even if only  $\widetilde{U_i U_j}$  is unknown in  $\tau_{sgs}$ , the subgrid stress tensor is entirely modeled. There are two possible ways to model  $\tau_{sgs}$ :

- Structural models that assess the subgrid stress without introducing the subgrid viscosity concept [103].
- Functional models that assess the residual stress using the Boussinesq hypothesis:

$$\tau_{ij,sgs} = -2\nu_{sgs}\tilde{S}_{ij} + \frac{1}{3}\tau_{kk,sgs}\delta_{ij}, \quad (3.28)$$

where  $\nu_{sgs}$  is the subgrid viscosity.

Many subgrid models are generally developed using the Kolmogorov assumption, and assumes that the subgrid production and the dissipation rate are equal. This requires to be well in the inertial sub-region of the turbulence energy spectrum.

Different mesh resolution criteria have been proposed for LES. For example, Pope [104] recommended that the filter-width should cover at least 80% of the resolved fraction of the energy spectrum. If the filter-width is close to the energy containing area, the hypothesis of equilibrium of the subgrid scales is not necessarily verified and thus the dissipation rate can be different from the subgrid turbulent production, which results in a misestimate of the subgrid viscosity [104].

### 3.3.2 Temporal LES (TLES)

While LES has been mostly used with spatial filtering, some authors attempted to replace it by a temporal filter, leading to the so-called Temporal LES (TLES). The reasons that motivated this choice include the following [19]:

- In contrast with spatial filters, the width of the temporal filter can be taken uniform in the domain, which ensures the commutativity with spatial derivatives [42]. However, this is of limited interest, since the purpose of LES/TLES is to adapt the filter width to local flow conditions.
- Dakhoul and Bedford [23] showed that, unlike temporal filtering, spatial filtering is inconsistent in flows that comprise time-dependent point sources.
- By using temporal filtering, the linkage with RANS solutions can be properly defined in stationary flows. Indeed, the statistical average is the limit of the temporal filter when the temporal filter width goes to infinity [38]. This property motivates the use of temporal filters in the following chapters.

The finite time filtering for turbulence was originally proposed by Boussinesq [107]. Few works were dedicated to the time filtering of turbulence. Dakhoul and Bedford [23] and Aldama [2] proposed spatio-temporal filtering while Meneveau *et al.* [85] developed a Lagrangian time-domain filter for LES. For its part, Pruet [19] proposed the temporal LES using temporal filtering in the Eulerian time domain [106].

In what follows, we focus on Pruet's work on the development of the TLES concept. The scale separation operator corresponds to a causal temporal filter in the Eulerian-time

domain [19]:

$$\mathcal{F}(f)(x, t) = \int_{-\infty}^t f(\tau, x) G(\tau - t, T_w) d\tau, \quad (3.29)$$

where  $G$  is the kernel that must satisfy:

$$G(t, T_w) = \frac{1}{T_w} g\left(\frac{t}{T_w}\right), \quad (3.30)$$

where  $T_w$  is the temporal filter width and  $g$  is any integrable function such that:

$$\begin{cases} g(0) & = 1 \\ \lim_{t \rightarrow -\infty} g(t) & = 0 \end{cases} \quad (3.31)$$

The Temporally Filtered Navier-Stokes Equations (TFNS) are formally identical to the spatially filtered Navier-Stokes Equations (3.25). The difference lies in the interpretation of the filtered fields, which correspond in TLES to temporally filtered quantities rather than spatially filtered quantities as in LES.

The residual stress, also called the subfilter stress in the temporal framework, is formally identical to the one obtained in LES:

$$\tau_{SFS,ij} = \widetilde{U_i U_j} - \widetilde{U}_i \widetilde{U}_j \quad (3.32)$$

Another interesting feature of filtering in the time-domain is that when  $T_w$  tends to  $+\infty$  in stationary flows,  $\tau_{SFS}$  asymptotically approaches the RANS Reynolds stress [106].

As far as we know, only the Temporal Approximate Deconvolution Model (TADM) exist in the literature to model the subfilter stresses [106]. Indeed, in stationary flows, the statistical quantities are independent of time and the statistical average is equivalent to the long-time average. Since temporal filtered quantities tend to the long-time averaged quantities when the filter width  $T_w$  goes to infinity, the TLES equations tend to the RANS equations.

### 3.3.3 Limitations of LES in industrial applications

The high computational cost of LES remains the main factor limiting its widespread use. Indeed, in wall-bounded flows, the grid requirement of LES scales with the friction Reynolds number as  $Re_\tau^2$ , which is today unfeasible for most industrial applications [104].

The high computational cost of LES is essentially related to the resolution of the boundary layers:

- the turbulent scales in the boundary layers are rather small. For example, Davidson [24] recommends a grid resolution expressed in wall-units of:  $y^+ = 1$  for the wall-normal direction,  $x^+ = 100$  for the streamwise direction and  $z^+ = 30$  for the spanwise direction.
- LES requires small CFL values to reduce error due to the temporal discretization. Thus, the grid resolution requirement near the wall induces small time-steps, which increases the overall turnaround time of the simulation.

Similarly to RANS, Wall-Modeled LES (WMLES) uses wall-functions to reduce the computational cost of the simulation. The grid requirement in WMLES increases weakly as  $\ln(Re_\tau)$  instead of  $Re_\tau^2$  for wall-resolved LES. Despite the continuous efforts that have been dedicated to develop wall-models, developing sufficiently general model is still a challenge [18, 20, 59, 101]. These wall-models are generally adaptations of RANS wall-functions or 1D simplifications of RANS models which have shown limited accuracy in the prediction of the wall friction [60, 79, 96]. This is potentially due to the inconsistency between LES fields, which relies on the spatial filtering and wall functions that provide statistical averaged quantities rather compatible with the RANS framework.

Next Section introduces hybrid RANS/LES models that present a promising alternative to WMLES.

## 3.4 Hybrid RANS/LES turbulence models

### 3.4.1 Concept

Despite the numerous studies that outline the advantages of LES over RANS modeling [25, 122, 123] and the relevance of LES to simulate ICE flows [115], Section 3.3.3 showed that the stringent mesh requirement of LES still limits its widespread use in the industry. The hybrid RANS/LES concept was proposed within this context. Hybrid models decrease the computational cost of LES by using RANS where LES is too expensive or where a statistical description of the flow is sufficient. This is made possible thanks to the RANS and LES equations which are formally identical, even if they represent variables of different

physical natures (statistically averaged and spatially filtered quantities, respectively). In the framework of eddy viscosity models, the Boussinesq relation is applicable for both approaches to model the residual stress:

$$\tau_{ij} = -2\nu_t \tilde{S}_{ij} + \frac{1}{3} \tau_{kk} \delta_{ij}. \quad (3.33)$$

where  $\nu_t$  can be expressed from a dimensional interpretation as:

$$\nu_t = u'' l. \quad (3.34)$$

where  $u''$  is a velocity scale and  $l$  is a length scale.

The difference between RANS and LES lies in the interpretation of  $\nu_t$ :

- in RANS,  $u''$  and  $l$  are computed from integral scales of turbulence in such a way that  $\nu_t$  models the effects of all the turbulent fluctuations.
- in LES,  $u''$  and  $l$  are based on the local grid step so that  $\nu_t$  models the effects of the subgrid scales upon the filtered scales.

Hybrid RANS/LES methods aim to propose turbulence models that are able to switch between the two approaches. Many efforts have been dedicated to the development of hybrid methods during the last decades. They resulted in the development of a wide variety of models which differ, first by the way how the transition between RANS and LES is operated and second by the theoretical background.

### 3.4.2 Classification

Sagaut *et al.* proposed the following classification of hybrid methods [116]:

- Zonal hybrid methods rely on a discontinuous treatment at the RANS-LES interface. The RANS and LES regions are predefined by the user, and RANS and LES models are used in each region. The LES content has to be explicitly reconstructed at the inlet of a LES region to take into account the lack of resolved fluctuations in the RANS region. The difficulties of this approach concern the definition of the different areas and treatment of the interface between RANS and LES.
- Global methods or seamless methods are based on one set of equations and continuous treatment between RANS and LES zones. In particular, these approaches

usually treat the near-wall region with a RANS model and operate in LES where the mesh resolution is suitable by reducing the Reynolds-stresses of the original RANS model.

For global methods, the RANS-LES transition raises a conceptual weakness, as RANS and LES use operators of different nature. Some hybrid models address this issue by using LES in the time-domain (TLES), the so-called hybrid RANS/TLES models [28, 80, 81, 129], in which the RANS-LES transition can be properly defined in statistically stationary flows [38]. This work focuses on the seamless Hybrid Temporal-LES (HTLES) approach which belongs to this category (see Section 4).

## **3.5 Literature review of CFD applied to ICE flows**

This Section aims to provide a review of CFD studies that have been conducted in ICE flows and their main findings for RANS, LES and hybrid RANS/LES. The first two Sections provide the fundamentals of ICE flows and their main characteristics. Then, a literature review of the turbulence modeling approaches that have been applied to ICE flows is provided.

### **3.5.1 Characteristics of in-cylinder flows**

The in-cylinder flow is a crucial element that enhances engine efficiency. As an example, it was found that typical flow motions can promote rapid and stable combustion in spark-ignited engines [11, 76].

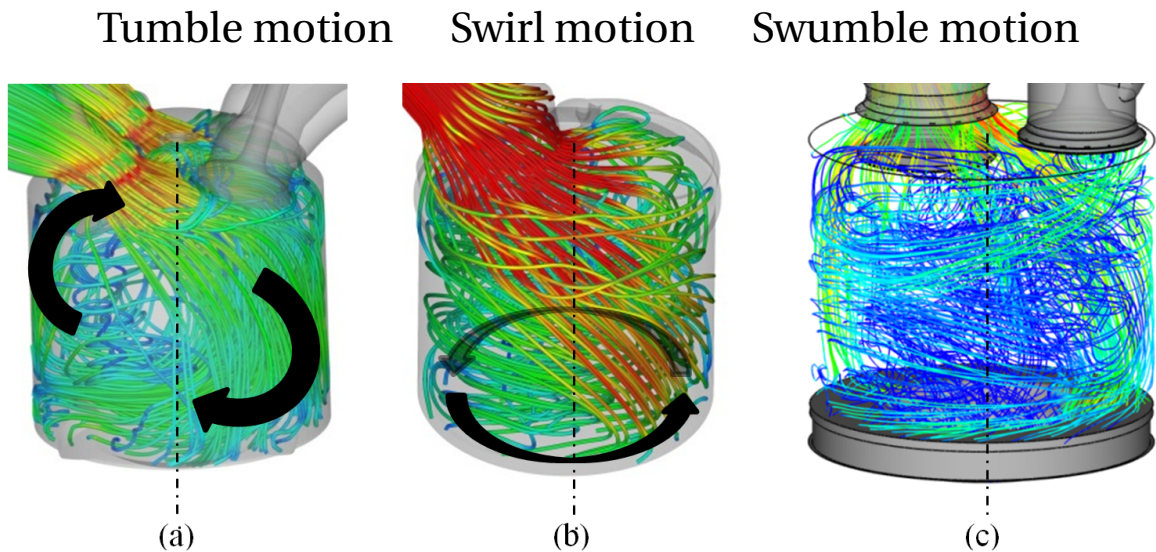


**Fig. 3.1** Typical ICE flow motions

Three typical flow-motions are encountered in ICE (see Figure 3.1):

- Tumble is the rotational motion around an axis perpendicular to the cylinder axis. This flow motion, typical of SI engine, is generated during the intake stroke by a dedicated shape of the intake ducts and valves leading to a specific angle of the incoming charge motion. This induces a flow separation that overfeeds one portion of the intake valve, forming the rotational motion. Indeed, the tumble motion stores the kinetic energy generated during the intake. During compression, the rotational motion – or tumble – is compressed and breaks down into small-scale turbulent fluctuations shortly before ignition, increasing turbulence. The increased turbulence wrinkles the flame, which increases the burning rate and reduces the combustion duration.
- Swirl is a rotational flow around the cylinder axis, which is typical of Diesel engines. This flow is created during the intake stroke, thanks to the intake ducts oriented tangentially to the cylinder. The swirl is then partially dissipated by wall friction and fuel injections.
- Swumble is a combination swirl and tumble. It offers the opportunity to be compatible with variable distribution systems. It allows reaching high turbulence levels at TDC even with very early or late closure of the intake valves.

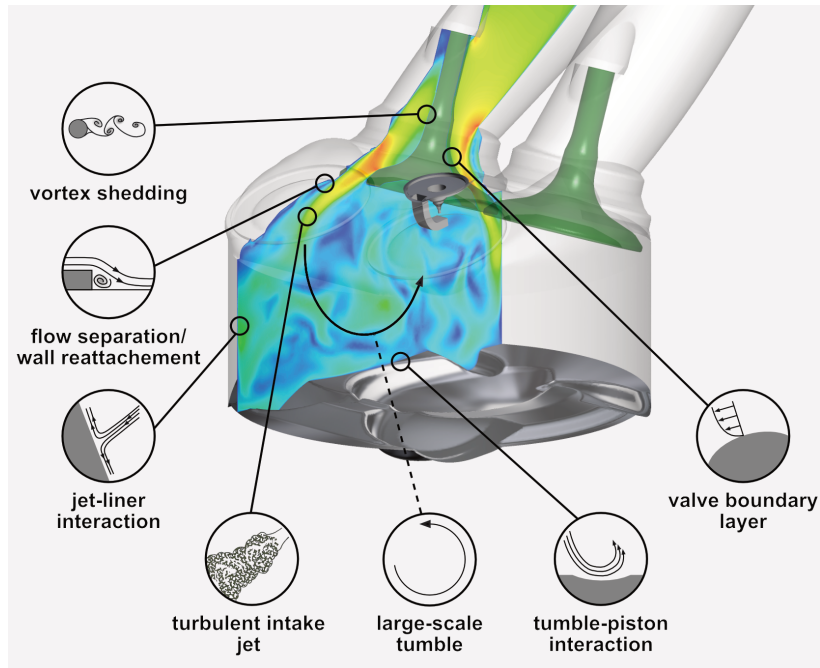


**Fig. 3.2** Illustration of some aerodynamic characteristics of a tumble type flow [15].

Up to now, the tumble motion is the most used in SI engines. Figure 3.2 illustrates some aerodynamic characteristics of a tumble flow. Several phenomena characterize the generation of the tumble motion. The flow is turbulent with a Reynolds number between 10,000 and 30,000 [115] and time-varying. The flow generated downstream of the intake valve gives rise to a turbulent jet flow with a turbulent free shear [49]. The resulting flow deflects on the cylinder liner and thereby interacts with the boundary layers [60, 79].

### 3.5.2 Cycle-to-Cycle Variations (CCV)

ICE development faces a strongly limiting issue, namely Cycle-To-Cycle variations (CCV). This phenomenon refers to the significant change in the overall flow characteristics from one cycle to another. That means that different flow conditions may occur at the same crank angle of consecutive cycles.

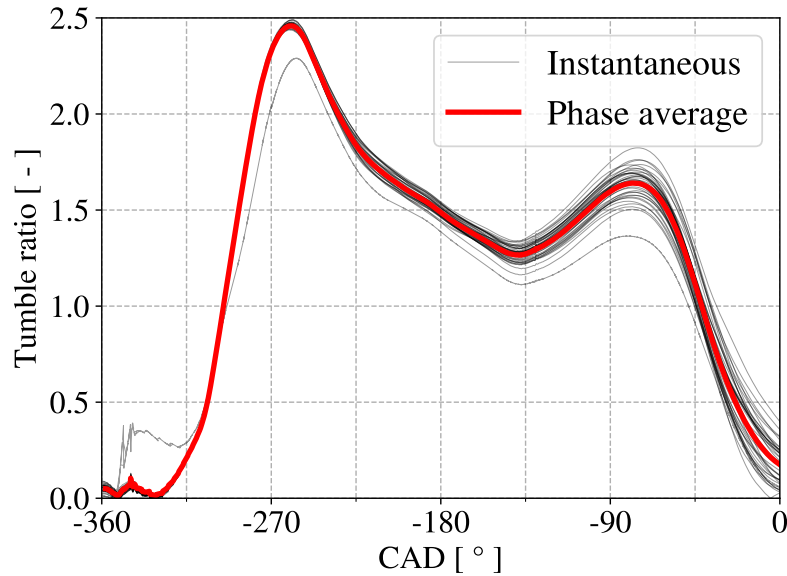


**Fig. 3.3** Cycle variability of the tumble ratio in the non-reacting Darmstadt engine obtained from a LES performed in Section 7.3.2.3.

Figure 3.3 shows an example of these variations for the tumble ratio, which was calculated as the ratio of the flow angular speed about the perpendicular axis to the tumble at the center of mass of the cylinder over the engine crankshaft angular speed, found in a LES of a non-reacting optical engine. A significant variation in the tumble characteristics can be observed from one cycle to another. Several studies showed that these CCV can cause losses in efficiency or, at worst, critical operating states (knock) [51]. There have been ongoing experimental studies to understand the occurrence of CCV in SI engines [51, 73, 100, 121]. It is proven that these variations are the consequences of the interaction of multiple phenomena. The in-cylinder aerodynamics, air-fuel mixture, mixture velocity differences near the spark plug and variations of spark discharge characteristics are amongst them. Indeed, the interaction of all these phenomena is not yet fully understood. Therefore, we still do not know the appropriate countermeasures to avoid their occurrence altogether.

### 3.5.3 Overview of RANS and LES simulations of ICE

In the frame of ICE, RANS provides phase-averaged flow quantities, which is sufficient for assessing stable and repeatable operating points. RANS has been used to evaluate specific ICE components or even the whole engine [35]. In [108], Qi *et al.* used RANS simulations to optimize the intake port design of a SI engine, increasing the tumble ratio by 20% during

intake. Comparisons between experimental findings and numerical results exhibit good agreement either for spark-ignited engines [8] or for compression ignited engines [22]. Nevertheless, due to its averaged nature, RANS can hardly capture phenomena such as CCV, even if recent work suggests that RANS could be relevant for a qualitative assessment [117].

Alternatively, LES offers significant advantages over RANS modeling approaches. By resolving the large eddies, LES accurately predicts unsteady phenomena such as the occurrence of knock and CCV [5, 13, 32, 49, 75, 93, 94, 114, 115]. Nonetheless, the use of LES is still limited in industrial applications due to its high computational cost, especially near the wall boundaries (see Section 3.3.3). LES is also constraining when it comes to obtaining averaged flow quantities in ICE. Since LES provides instantaneous flow fields, statistical averaging requires to simulate many cycles, which increases the overall simulation time.

Wall-modeling (WMLES) significantly decreases the computational cost of LES by using wall-functions to model boundary layers (see Section 3.3.3). Nevertheless, WMLES in ICE flows has shown limited accuracy in predicting wall fluxes (of both shear and heat) [2017, 96]. One of the reasons for this is the inconsistency between the resolved LES fields and the wall-functions, which were generally developed to provide statistically averaged quantities for RANS. Besides that, Ma *et al.* [79] have shown that, during compression, the boundary layer enters a state of non-equilibrium in which the standard wall-functions fail to predict the wall shear stress. These wall functions also showed a grid-dependent character if the first mesh node was situated used outside the viscous sublayer [60, 79]. The author also proposed a non-equilibrium wall-function, which reduced the relative error of wall fluxes to less than 20% compared with the experimental findings.

Apart from the near-wall mesh resolution constraint, the stringent grid requirement in LES is also related to the Kolmogorov hypothesis used in several subgrid models [31, 115]. The use of turbulence models that resolve more information about turbulence, such as two-equation models [66] or ultimately RSM models [26], can help solving large eddies that may embody some of the energy containing vortices (VLES). Hence, these models can resolve turbulent scales in relatively coarse meshes, reducing the simulation computational cost [115].

Another practical disadvantage of 0-equation LES models (algebraic models) is that they do not provide subgrid turbulent kinetic energy, which is often used for combustion, scalar mixing, and spray models [115].

### 3.5.4 Hybrid RANS/LES models applied to ICE

Hybrid RANS/LES methods offer a favorable response to the weaknesses of RANS and LES mentioned in Section 3.5.3. These methods use RANS where LES is too expensive or not necessary. They often model the subgrid scales using transport equations of turbulent quantities, making it possible to resolve large eddies with a relative coarse mesh.

#### 3.5.4.1 Zonal approaches

In a zonal approach, the user splits the computational domain into different zones and manually selects the turbulence model for each one. The moving wall boundaries and time-varying flow in ICE make the use of zonal approaches difficult. Few studies used zonal approaches in ICE flows up to now. Keskinen *et al.* used the HLR zonal approach [54] to simulate a cold flow engine-like configuration with moving piston [60, 95]. The model combines the low Reynolds  $k - \varepsilon$  [78] for RANS with the  $\sigma$  subgrid model [97] for LES zones. The RANS-LES interface was defined using a non-dimensional wall-normal distance of  $y^+ = O(100)$ . Results in terms of mean and rms velocity and heat transfer showed good agreement with DNS and were found to be more accurate than with WMLES. The same model was applied to investigate the origins of CCV and their effects on the combustion in a lean-burn SI engine [40, 41].

#### 3.5.4.2 Seamless approaches

Seamless approaches are easier to use in ICE flows as the model switches between RANS and scale-resolving modes automatically. One may refer to the comparative study performed by Buhl *et al.* of some seamless approaches, such as the Scale Adaptive Simulation (SAS) and Detached-Eddy Simulation (DES) in a two-stroke engine, which consists of intake and exhaust strokes [13, 14]. Some applications of the seamless approach in ICE flows are detailed in the following.

##### **Detached-Eddy Simulation (DES)**

Up to now, DES is the most used seamless approach in ICE [13, 48–50, 70]. Two-equation DES uses the same set of equations as RANS models, except for the dissipation term in the  $k$ -equation, which includes a modified length scale that activates outside the

boundary layer and makes the model able to mimic a Smagorinsky LES subgrid model [122]. The dissipation term depends on the local grid step rather than the integral scales of turbulence, which is the case in RANS. Travin *et al.* applied this approach to the  $k - \omega$  SST model. The dissipation term in the  $k$ -equation was modified to take into account the DES lengthscale:

$$\varepsilon_{SST} = \beta^* k \omega = \frac{k^{3/2}}{L_t} \rightarrow \varepsilon_{DES} = \frac{k^{3/2}}{L_{DES}} \quad (3.35)$$

where  $\beta^* = 0.09$  and  $L_{DES}$  switches between the turbulence integral length scale  $L_t = \frac{k}{\beta^* \omega}$  and grid-dependent length scale  $c_{DES} \Delta$  as,

$$L_{DES} = \min(L_t, c_{DES} \Delta) \quad (3.36)$$

$c_{DES} = 0.65$  is a coefficient calibrated so that DES exhibits the same turbulent dissipation as the Smagorinsky subgrid model in a Homogeneous Isotropic Turbulence. Nonetheless, several studies using DES outlined some issues:

- Premature boundary-layer separation, also called Grid Induced Separation (GIS) [87]: for fine grids, the switch from RANS to LES can take place somewhere inside the boundary layer. This phenomenon leads to the underestimation of the turbulent viscosity in the boundary layer, which provokes a premature separation [87].
- Grey area between RANS and LES regions: high viscosity of RANS can propagate to the LES region, resulting in a non-physical delay in the development of resolved eddies.
- Log-layers mismatch: the application of DES in a channel flow showed that if the RANS-to-LES transition occurs in the log layer, its results in the two mismatched log layers — one from the RANS branch, and the other from the LES branch.

This phenomenon leads to the misprediction of the velocity in the logarithmic layer [24].

Different efforts have been devoted to improving DES models, such as the Delayed-DES (DDES) [45]: in order to prevent grid-induced separation, shielding functions are introduced, which aims at protecting the boundary layer from the LES mode by delaying the transition between RANS and LES. The shielding function adjusts the thickness of the RANS region to a large portion of the boundary layer. However, due to the sudden RANS-LES transition, the log-layer mismatch problem remains.

This approach has shown satisfactory results in various applications. Krastev *et al.* [70] used DES in the steady flow rig (see Section 5.6.3.2). The SST DES formulation was applied to the tumble engine (presented in Section 6) to investigate the formation and compression of a tumble motion [50]. Hasse *et al.* [48] examined the SST DES on a fine mesh. It examined its predictions in terms of CCV, mean and rms velocity fields in a motored single-cylinder engine, showing good agreement with experimental findings. Further investigations of DES by the same authors [49] showed competitive results compared to LES in realistic ICE geometries. Nevertheless, the issues related to the RANS-LES transition uncertainties were not investigated.

### Zonal-DES (ZDES)

The Zonal-DES (ZDES) [25] is despite its name is a seamless approach that has been substantially investigated by Krastev *et al.* in ICE applications. The particularity of ZDES compared to other DES approaches is that it allows the user to impose the RANS mode in chosen regions irrespective of the mesh. The particularity of ZDES compared to other DES approaches is that it allows the user to impose the RANS mode in chosen regions irrespective of the mesh. ZDES based on the RNG  $k - \varepsilon$  RANS model [99] and DES of Krastev *et al.* [70] was investigated in engine-like geometries in [67–69, 71, 72]. Results in terms of mean and rms velocity were satisfactory. The RANS and DES modes have been successfully activated thanks to their manual prescription.

### Scale Adaptive Simulation (SAS)

SAS aims to enhance RANS models' ability to resolve large-scale motions (such as separated flow regions) by using a source term in the  $\omega$ -equation that decreases the turbulent viscosity where resolved vortices are detected, i.e., when RANS locally switches to URANS (Unsteady RANS). The presence of resolved vortices is detected using the Von-Karman lengthscale [90]:

$$L_{vK} = \kappa \frac{\sqrt{2\bar{S}_{ij}\bar{S}_{ij}}}{\sqrt{\frac{\partial^2 \bar{U}_i}{\partial x_k^2} \frac{\partial^2 \bar{U}_i}{\partial x_j^2}}} \quad (3.37)$$

The von-karman lengthscale is used in a source term  $Q_{SAS}$  in the  $\omega$ -equation of the  $k$ - $\omega$  SST model [88] (see Appendix 8.2):

$$Q_{SAS} = \max\left[\rho \xi_2 \kappa S^2 \left(\frac{L_t}{L_{vK}}\right)^2 - C \frac{2\rho k}{\sigma \Phi} \max\left(\frac{1}{\omega^2} \frac{\partial \omega}{\partial x_j} \frac{\partial \omega}{\partial x_j}, \frac{1}{k^2} \frac{\partial k}{\partial x_j} \frac{\partial \omega}{\partial x_j}\right), 0\right] \quad (3.38)$$

where  $\xi_2 = 3.51$ ,  $\sigma_\phi = 2/3$ ,  $C = 2$ ,  $S = \sqrt{2S_{ij}S_{ij}}$  and  $L_t = \frac{k^{3/2}}{\varepsilon}$  is the characteristic turbulent length scale. SAS decreases the turbulent viscosity in URANS regions, according to the following process [24].  $L_{VK}$  gets small values in URANS regions, increasing  $Q_{SAS}$ . The source term increases  $\omega$ , which in turn decreases the turbulent viscosity  $\nu_t$ , helping the model to resolve a larger portion of large-scale motions.

In SAS, the grid size does not appear in the formulation. Hence, this model is rather considered a scale-resolving URANS model than a hybrid RANS-LES method [116].

Results of SAS in ICE configurations [13, 14, 16, 17] showed improvements compared to RANS models in terms of mean and rms velocity predictions. The relatively low flow instabilities within the intake and exhaust ports almost make SAS operate in RANS entirely within these regions [13]. In the combustion chamber, it has been shown that SAS is fully capable of capturing CCV and large-scale motions [16]. Imberdis *et al.* [53] performed a comparative study of SAS with experimental findings and DES in a 1.6 l Volkswagen Fuel Stratified Injection.

### Very Large-Eddy Simulation (VLES)

VLES is a seamless approach that transforms RANS to Hybrid RANS/LES models by adding a damping function to the Reynolds stresses. The damping function reduces the Reynolds stresses of RANS in regions where the mesh resolution is sufficient to resolve a part of the instantaneous turbulent spectrum:

$$\tau_{VLES} = \alpha \tau_{RANS} \quad (3.39)$$

where  $\alpha$  is an empirical damping function defined as [124]:

$$\alpha = [1 - \exp(-\beta \frac{\Delta}{L_k})]^n \quad (3.40)$$

$\beta$  and  $n$  are modeling parameters,  $\Delta$  is the grid spacing and  $L_k$  is the Kolmogorov length-scale. If  $\frac{L_k}{\Delta}$  tends to 0 then  $\alpha$  is zeroed and the simulation operates in DNS mode. At the other limit ( $\lim_{\Delta} \frac{L_k}{\Delta} \rightarrow +\infty$ ), the RANS Reynolds stresses are recovered and the model operates in RANS. Between the two limits, the model resolves a part of the turbulent scales. Nevertheless, this model presents some issues related to the damping function, such as [116]:

- the model is unable to operate in RANS simulation unless the mesh is unreasonably coarse.
- the original damping function is too diffusive in the LES region [46]. Therefore, VLES does not ensure to provide the real LES modeling as provided by LES subgrid models.

Alternative formulations of the damping function have been proposed to tackle these issues, and have been applied to simulate in-cylinder flows. They showed improvements with respect to RANS in terms of the predictive capabilities of the mean and rms velocity fields in the compressed tumble engine [10] and in the Darmstadt engine [6] [20]. Further improvements of VLES for engine flows were proposed in the so-called Dynamic Length-Scale Resolution Model (DLRM) [102, 133]. DLRM was applied in the compressed tumble. The mean and rms velocity fields were compared with PIV findings, and RANS and LES results. The results of DLRM in a relative coarse mesh provided reasonably good predictions of both mean and rms velocities that have been found fairly similar to LES and better than RANS. The grid dependency of the results has also been investigated showing enhancements in the prediction of the simulation.

### Partially averaged Navier-Stokes (PANS)

The PANS approach uses an undefined partial filtering operator which separates the flow in two parts. Each flow quantity expresses as the sum of the resolved scales and unresolved scales  $f = f_{res} + f_u$ .

PANS [44] is based on the definition of the two ratios  $f_k = \frac{k_u}{k}$  and  $f_\varepsilon = \frac{\varepsilon_u}{\varepsilon}$ , which are the ratio of unresolved to total turbulent energy and the ratio of unresolved to total dissipation, respectively. By definition of the PANS approach, these two ratios are constant in the flow domain. Therefore, the equations for  $k_u$  and  $\varepsilon_u$  are simply derived by using  $\frac{\partial k_u}{\partial t} = f_k \frac{\partial k}{\partial t}$  and  $\frac{\partial \varepsilon_u}{\partial t} = f_\varepsilon \frac{\partial \varepsilon}{\partial t}$ , which yields:

$$\begin{cases} \frac{\partial}{\partial t} k_u + U_j \frac{\partial}{\partial x_j} k_u &= P_u - \varepsilon_u + \frac{\partial}{\partial x_j} \left[ \left( \nu + \frac{\nu_t}{\sigma_{k,u}} \right) \frac{\partial k_u}{\partial x_i} \right] \\ \frac{\partial}{\partial t} \varepsilon_u + \bar{U}_j \frac{\partial}{\partial x_j} \varepsilon_u &= C_{\varepsilon 1} \tilde{P}_u \frac{\varepsilon_u}{k_u} - C_{\varepsilon 2}^* \frac{\varepsilon_u^2}{k_u} + \frac{\partial}{\partial x_j} \left[ \left( \nu + \frac{\nu_t}{\sigma_{k,u}} \right) \frac{\partial \varepsilon_u}{\partial x_i} \right] \end{cases} \quad (3.41)$$

the only parameters that differ from RANS equations are  $C_{\varepsilon 2}$  and  $\sigma_{k,u,\varepsilon_u}$ , which are computed dynamically:

$$C_{\varepsilon 2}^* = C_{\varepsilon 1} + \frac{f_k}{f_\varepsilon} (C_{\varepsilon 2} - C_{\varepsilon 1}); \sigma_{k,u,\varepsilon_u} = \frac{\sigma_{k,\varepsilon} f_k^2}{f_\varepsilon} \quad (3.42)$$

$C_{\varepsilon 1}$  and  $C_{\varepsilon 2}$  are the parameters of the  $k - \varepsilon$  model.  $C_{\varepsilon 2}^*$  takes into account the resolution parameters  $f_k = \frac{k}{k_u}$  and  $f_\varepsilon = \frac{\varepsilon}{\varepsilon_u}$  is assumed equal to one according to the assumption that the resolved dissipation is negligible [63].

In the original formulation [44],  $f_k$  was considered a constant, by definition of the approach. However, in order to make possible a switch from a RANS to a LES mode in different regions,  $f_k$  is estimated during the computation by comparing the grid step to the integral length scale of turbulence [43], and the additional terms that should appear in Equation (3.41) due to the spatial derivatives of  $f_k$  are neglected.

Investigations of PANS predictions in ICE have been briefly addressed in a relatively coarse mesh in [43] predicting CCVs with a relative error of 30% as compared to the experimental findings.

## **Part II**

# **Development of a hybrid RANS/LES model for ICE flows**



# Chapter 4

## Improvement of the HTLES model for wall-bounded flows

### 4.1 Introduction

The development of hybrid turbulence models faces numerous challenges. The proposal of a theoretical justification of the coexistence of RANS and LES which are of different nature, as well as the development of a versatile model able to switch its modeling approach to RANS, VLES and LES automatically, are amongst them. The Hybrid Temporal LES (HTLES) [80] was developed within this context. It converts any RANS model to a hybrid model by modifying its set of equations using the statistical multiscale approach in the frequency time domain, offering several advantages. First, in the time domain LES expresses using temporal filtering, namely Temporal-LES (TLES) (see Section 3.3.2) [106]. An interesting feature of filtering in the time domain is that the LES solution, which consists of a temporally filtered quantity, is consistent with RANS in stationary turbulence, since in this case the Reynolds average is equivalent to a temporal average [38]. Second, the derivation of the equations of the modeled scales in the frequency domain allows modeling complex turbulence processes, which makes the model able to perform RANS, VLES, and LES.

This Chapter is organized as follows. First, the theoretical framework of hybrid RANS/TLES models is introduced. Second, details of the HTLES model used in this study and its implementation in the CONVERGE CFD code are presented. After that,

the focus is placed on the behavior of HTLES close to the walls, introducing a shielding function which is adjoined to HTLES so that RANS is systematically used in these regions. Finally, a validation of HTLES in a channel flow is provided.

## 4.2 Hybrid RANS/Temporal-LES approach

### 4.2.1 Introduction

The coexistence of RANS and LES fields in hybrid RANS/LES models raises a conceptual weakness, as they use operators of different nature, the statistical operator and a spatial convolution filter, respectively. Concerning the latter, the linkage with RANS is only meaningful in the case of statistically homogeneous turbulence, as the spatial filter tends to the statistical average when the spatial filter width goes to infinity[37].

In contrast, in statistically stationary turbulence, the statistical average is equivalent to a temporal average (ergodicity hypothesis) such that it is the limit of the temporal filter when the temporal filter width goes to infinity [38]. Accordingly, the linkage between RANS and LES can be rigorously justified by using the Temporal LES (TLES), which uses temporal filtering to separate the resolved and modeled turbulent scales rather than spatial filtering [19]. Within this context, Fadai-Ghotbi *et al.* [28] proposed the first seamless hybrid RANS/TLES model, the so-called Temporal-PITM, which is an adaption of the Partially Integrated Transport Model (PITM) [21, 118] to the temporal filtering context.

### 4.2.2 Turbulence spectrum in the time domain

In Section 2.2, the turbulent cascade of the Homogeneous Isotropic Turbulence (HIT) was described in the wavenumber space. Tennekes [126] showed that the turbulence spectrum in the wavenumber and frequency domains are equivalent, meaning the turbulence cascade process can be similarly described in the frequency time domain. For homogeneous isotropic turbulence, within the inertial subrange, the turbulent energy spectrum expresses according to the Kolmogorov hypothesis in terms of wavenumber  $\kappa$  as:

$$E(\kappa) = C_\kappa \varepsilon^{2/3} \kappa^{-5/3} \quad (4.1)$$

where the Kolmogorov constant  $C_\kappa$  is around 1.5.

The Kolmogorov spectrum can be transposed to the frequency time domain using the developments performed by Tennekes [125] who showed that the frequencies observed at a fixed point (Eulerian description) are related to the advection (sweeping) of small scales by large scales. Therefore, the frequency of a turbulent fluctuation  $\omega$  can be related to its corresponding wavenumber using the dispersion relation:

$$\omega = U_s \kappa , \quad (4.2)$$

where the sweeping velocity  $U_s$  is the estimate of the convection velocity due to the energetic eddies [125]:

$$U_s = \bar{U} + \gamma \sqrt{k}, \quad (4.3)$$

where  $\bar{U}$  is the local mean velocity magnitude,  $\gamma$  is a coefficient fixed at 1,  $k$  is the total turbulent kinetic energy. The turbulence temporal spectrum is obtained by a change of the variable  $\kappa$  using the dispersion relation in:

$$dk = E(\kappa) d\kappa = E_T(\omega) d\omega , \quad (4.4)$$

yielding the equilibrium Eulerian spectrum:

$$E_T(\omega) = C_\kappa \varepsilon^{2/3} U_s^{2/3} \omega^{-5/3} . \quad (4.5)$$

In HIT, the mean flow velocity is zero, reducing  $U_s$  to:

$$U_s = \sqrt{k} . \quad (4.6)$$

Hence, the turbulence Eulerian spectrum of HIT in the frequency domain expresses as:

$$E_T(\omega) = C_\kappa \varepsilon^{2/3} k^{1/3} \omega^{-5/3} . \quad (4.7)$$

### 4.2.3 Temporal-PITM

The T-PITM [28] is a seamless hybrid RANS/TLES approach based on a splitting of the turbulence spectrum in the frequency domain. It consists in splitting the frequencies into three parts as illustrated in Figure 4.1:

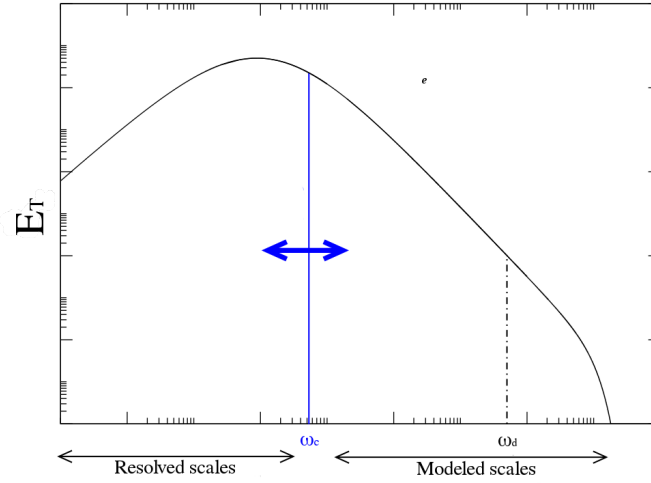


**Fig. 4.1** Decomposition of the turbulence spectrum according to the T-PITM approach [28]

- $[0, \omega_c]$  comprises the frequencies of the resolved turbulent fluctuations.
- $[\omega_c, \omega_d]$  and  $[\omega_d, \infty]$  comprise the frequencies of the unresolved turbulent fluctuations. Their effect upon the resolved frequencies is modeled.

$\omega_c$  is the cutoff frequency, which separates the resolved and the modeled frequencies of turbulence.  $\omega_d$  is a frequency taken large enough so that the turbulence energy contained in  $[\omega_d, \infty]$  is negligible.

In the T-PITM method, the resolved frequencies are treated in a similar way to TLES, meaning that they are resolved by the simulation using a temporal filter, which filter width is controlled by  $\omega_c$ . The unresolved frequencies correspond to the high frequencies ( $\omega > \omega_c$ ) that are filtered-out by the temporal filter, namely the subfilter scales  $sfs$  (the modeled scales).

The governing equations of the unresolved frequencies are derived using integrations of the Eulerian temporal energy spectrum over  $[\omega_c, \omega_d]$  and  $[\omega_d, \infty]$  [28] in a similar way to the statistical multiscale approach [57, 119], yielding equations that are similar to the incompressible  $k - \varepsilon$  RANS model:

$$\begin{cases} \frac{\partial k_{sfs}}{\partial t} + \tilde{U}_j \frac{\partial k_{sfs}}{\partial x_j} = & P_{sfs} - \varepsilon + D_{sfs} \\ \frac{\partial \varepsilon}{\partial t} + \tilde{U}_j \frac{\partial \varepsilon}{\partial x_j} = & C_{\varepsilon 1} \frac{\varepsilon}{k_{sfs}} P_{sfs} - C_{\varepsilon 2}^* \frac{\varepsilon^2}{k_{sfs}} + D_{\varepsilon sfs} \end{cases}, \quad (4.8)$$

where  $k_{sfs}$  is the subfilter turbulent kinetic energy,  $\tilde{U}_j$  is  $j$ -th component of the resolved velocity,  $P_{sfs}$  and  $D_{sfs}$  are the subfilter parts of the production and diffusion of the total turbulent kinetic energy.  $\varepsilon$  is the turbulent dissipation rate, and  $C_{\varepsilon 1} = 1.44$ .

The only difference with the  $k - \varepsilon$  RANS model concerns the coefficient  $C_{\varepsilon 2}$  in the destruction term of the  $\varepsilon$ -equation (equal to 1.92 in RANS), which is dynamically computed using  $C_{\varepsilon 2}^* = (C_{\varepsilon 2} - C_{\varepsilon 1})r + C_{\varepsilon 1}$ , allowing to control the level of the subfilter turbulent kinetic energy  $k_{sfs}$  and thus the transition from a RANS to a LES behavior. The main parameter is the energy ratio  $r = \frac{\overline{k_{sfs}}}{k}$ , the average of the subfilter turbulent kinetic energy to total turbulent kinetic energy, which is equal to 1 in RANS regions and less than 1 in LES regions. This ratio is linked to the cutoff frequency  $\omega_c$  in a way that will be detailed in Section 4.3.

Among the benefits of T-PITM is the ability to resolve turbulent fluctuations without the constraint of  $\omega_c$  being placed in the inertial subrange of the turbulence energy spectra as it is required in TLES, allowing to perform Very Large-Eddy Simulation (VLES).

Nevertheless, the indirect control of the subfilter stresses through  $\varepsilon$  showed some difficulties to sustain the resolved turbulent fluctuations, also called the pseudo-laminarization, during the computation of some flows, such as the flows that are not dominated by the Kelvin-Helmholtz instability [34].

#### 4.2.4 The Hybrid Temporal-LES approach (HTLES)

Friess *et al.* [34] proposed a solution to reduce the pseudo-laminarization issue in the TPITM method by deriving an equivalent approach in which the control of the subfilter turbulent kinetic is directly operated via the dissipation term in the turbulent kinetic energy in the same spirit as for the Detached-Eddy simulation (DES) method [130], the so-called Hybrid Temporal LES (HTLES) approach:

$$\begin{cases} \frac{\partial k_{sfs}}{\partial t} + \tilde{U}_j \frac{\partial k_{sfs}}{\partial x_j} = & P_{sfs} - \psi \varepsilon + D_{sfs} \\ \frac{\partial \varepsilon}{\partial t} + \tilde{U}_j \frac{\partial \varepsilon}{\partial x_j} = & C_{\varepsilon 1} \frac{\varepsilon}{k_{sfs}} P_{sfs} - C_{\varepsilon 2} \frac{\varepsilon^2}{k_{sfs}} + D_{\varepsilon} \end{cases}, \quad (4.9)$$

where  $\psi$  is the coefficient which is added to the dissipation term to control the part of the subfilter turbulent kinetic energy.  $\psi$  is defined as:

$$\psi = \frac{k_{sfs}}{T\varepsilon} \quad (4.10)$$

As mentioned above, this modification of the form of the system of equations aims to avoid pseudo-laminarisation problems, while maintaining the essential properties of the model, i.e. keeping the same control of the energy partition between the resolved and unresolved parts. One can think that if both systems are based on the same underlying RANS model (for example, here, a  $k - \varepsilon$  model) and give the same energy partition, their solutions will be very close to each other, especially at the statistical level. This idea was expressed by Friess *et al.* [34] in the form of the following postulate: *"Two hybrid approaches based on the same closure, but using a different method of control of the energy partition, yield similar low-order statistics of the resolved velocity fields provided that they yield the same level of subfilter energy."*

By definition [34], two approaches are called  $H$ -equivalent ( $H$  for hybrid) if they provide the same level of  $\overline{k_{sfs}}$  for the same filter width, and if they tend to the same RANS model when the filter width tends to  $+\infty$ .

In order to establish an equivalence between HTLES and TPITM, the perturbation method was used [6]. This method consists in introducing a small perturbation to the energy control parameter in the system of equations of each of the two methods. In TPITM, the perturbation corresponds to  $\delta C_{\varepsilon 2}^*$  while in HTLES it corresponds to  $\delta\psi$ . It is then possible to study for the two systems what is the infinitesimal variation  $\delta k_{sfs}$  of the subfilter turbulent kinetic energy induced by these variations in the parameters. Using this method, Friess *et al.* [34] demonstrated, in some simplified situations, that HTLES is equivalent to TPITM if the time-scale  $T$  is defined as :

$$T = \frac{r}{1 + \left(\frac{C_{\varepsilon 2}}{C_{\varepsilon 1}} - 1\right)(1 - r \frac{C_{\varepsilon 1}}{C_{\varepsilon 2}})} \frac{k}{\varepsilon} \quad (4.11)$$



where  $\beta$  is a constant fixed at 0.667, calibrated in order to exhibit the correct amount of dissipation in the case of decaying homogeneous turbulence [129]. Equation (4.16) was derived using the integration of the Equilibrium Eulerian (see Equation (4.5)) spectrum over the unresolved frequencies  $[\omega_c, \infty]$  [129]:

$$r = \frac{1}{k} \int_{\omega_c}^{+\infty} C_\kappa \varepsilon^{2/3} U_s^{2/3} \omega^{-5/3} d\omega. \quad (4.17)$$

The upper-bound was added to in order to avoid wrong values of  $r$  were the equilibrium assumption is not valid such as in the near-wall regions.

$r$  allows the model to vary locally and seamlessly from RANS, i.e,  $r = 1$ , in this case  $T \rightarrow \frac{k}{\varepsilon}$  we retrieve RANS equations, to LES if  $r < 0.2$ .  $r > 0.2$  means that less than 80% of the total turbulent kinetic energy is resolved indicating to the model to operate in VLES [104].

The cutoff frequency  $\omega_c$  is chosen as the highest frequency that can be represented by the numerical scheme:

$$\omega_c = \min\left(\frac{\pi}{dt}, \frac{U_s \pi}{\Delta}\right) \quad (4.18)$$

- The first cutoff frequency  $\pi/dt$  corresponds to the Nyquist frequency related to the time step  $dt$ .
- The second cutoff frequency is imposed by the spatial resolution  $\Delta = \max(dx, dy, dz)$ , since the highest frequency that can be observed in a computation is the Eulerian frequency of the smallest resolved eddies [125]  $\frac{U_s \pi}{\Delta}$ , where the sweeping velocity  $U_s = \bar{U} + \gamma \sqrt{k}$ .

The HTLES approach controls the resolved turbulent fluctuations directly in the  $k$ -equation using the energy ratio  $r$ , which depends on the spatial and the temporal resolutions through  $\omega_c$ . Such an approach can lead to a model where the RANS-LES transition strongly depends on the mesh, yielding to a transition that can occur too close to the walls [29]. Section 4.4 aims to adjoin a shielding function to HTLES so that RANS is systematically activated at the walls, and that the RANS-LES transition depends on the wall-distance rather than  $r$ .

### 4.3.2 Implementation in the CONVERGE CFD code

#### 4.3.2.1 Presentation of the CFD code

HTLES has been implemented in the CONVERGE code [112], which is widely used for ICE simulations. CONVERGE is a cell-centered code using the finite-volume method to solve the equations for compressible flows.

#### Mesh management

CONVERGE includes a mesh module that generates the mesh internally during the simulation. The mesh is generated using a Cartesian mesh block, the grid spacing of which is specified by the user for each direction ( $dx$ ,  $dy$ ,  $dz$ ). The geometry is immersed in the Cartesian block and the cells at the geometry surfaces are trimmed using a cut-cell technique developed by Senecal *et al.* [120]. As shown in Figure 4.2, the trimmed cells with a volume of less than 30% of their adjacent Cartesian cell are paired together, resulting in a single node.

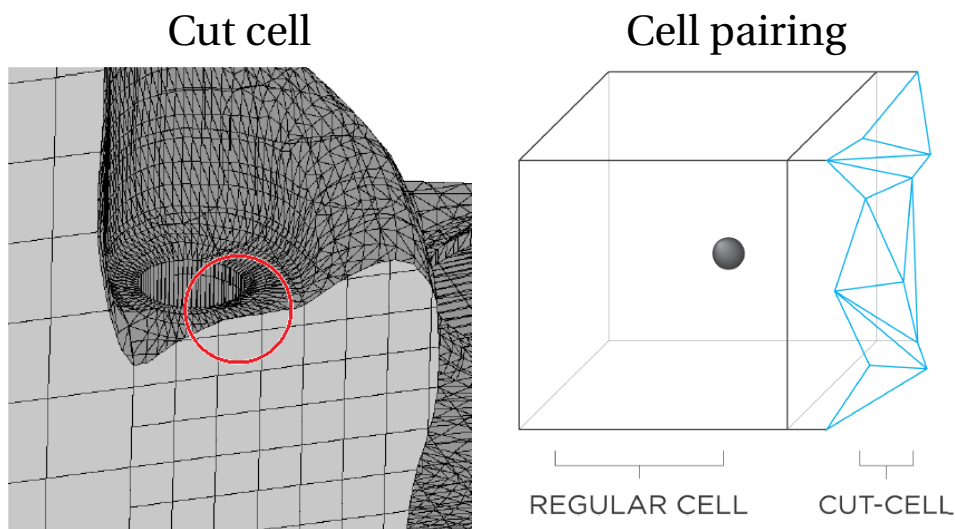


**Fig. 4.2** Illustration of the cut-cell technique (encircled by the red line) and cell pairing in CONVERGE [112].

CONVERGE offers the possibility to refine the mesh for specified regions either permanently or during finite periods of time. Nevertheless, the refinement options are limited. Indeed, CONVERGE only applies refinements ratios by powers of 2, i.e.,  $dx_{refined} = dx/2^n$  where  $n$  is an integer specified by the user. Furthermore, CONVERGE uses isotropic mesh

refinement, which means that any refinement is systematically applied to all three directions:

$$\begin{cases} dx_{refined} = dx/2^n \\ dy_{refined} = dy/2^n, \\ dz_{refined} = dz/2^n \end{cases} \quad (4.19)$$

Isotropic mesh refinement is limiting in situations where the mesh refinement is only required in a specific direction. This is particularly true for the resolution of boundary layers in RANS, which only requires a stringent mesh refinement in the normal direction of the wall. In general, boundary layer resolution using isotropic mesh refinement dramatically increases the total number of cells. Therefore, all simulations in the present thesis use wall modeling.

For stationary geometries, CONVERGE generates the mesh once at start of the simulation et repeats the process at each applied or removed refinement.

For moving geometries, CONVERGE generates the mesh at each time step by using the method mentioned above. Details about how new cells resulting from a moving wall are treated are not released.

## Numerics

The pressure-velocity coupling is achieved using a modified Pressure Implicit with Splitting of Operator (PISO) method [ISSA198640]. The convection and diffusion terms are approximated by second-order central differencing, and they are advanced in time using the first-order implicit Euler time scheme. The Redlich-Kwong equation of state [109] is used for gas to couple the density, pressure and temperature.

All computed variables values are stored at the cell centers (collocated grid). The use of collocated quantities can result in a decoupling of the pressure and velocity. This decoupling can produce fluctuations in the pressure and velocity solution that appear in a checkerboard pattern. The Rhie-Chow [111] interpolation scheme is used to prevent pressure and velocity decoupling and checkerboarding effects.

A step-flux limiter is applied to convective fluxes in order to prevent nonphysical oscillations (also known as "wiggles") that can appear when the second-order differencing scheme is used. It detects where the wiggles occur and downgrades locally the spatial

scheme to the first-order upwind scheme which is more stable numerically:

$$f_{cen,limited} = f_{up} + \psi(f_{cen} - f_{up}), \quad (4.20)$$

where  $f_{cen}$  corresponds to flux of the central differencing scheme,  $f_{up}$  is the flux of the upwind scheme, and  $f_{cen,limited}$  is the limited flux.  $\psi$  is the flux limiter. For example for the velocity  $U_i$ , if:

$$|(U_i - U_{i-1}) - (U_{i+1} - U_i)| < monotone\_tolerance$$

$\psi = 0$  else  $\psi = 1$ .

where  $i$  indicates the cell,  $i + 1$  is the cell to the right,  $i - 1$  is the cell to the left, and  $x$  is the spatial location. The parameter *monotone\_tolerance* defines the threshold at which the limiter is activated.

#### 4.3.2.2 Implementation of HTLES

HTLES was implemented by modifying the dissipation term of the  $k$ -equation of the Shear Stress Model (SST), which is already available in CONVERGE:

Modeling approach	RANS SST	HTLES
Dissipation term	$-\beta^* \rho k \omega$	$-\frac{\rho k_{sfs}}{T}$

The time scale  $T$  used in the dissipation term is computed at each time step and each cell using Equation (4.11), and the energy ratio  $r$  is controlled by Equation (4.16).

The statistically averaged quantities in Equations (4.11) and (4.16) can be calculated using time averaging. Nevertheless, we chose to approximate them using an exponential temporal filter [106], as the statistical average is the limit of the temporal filter when the filter width goes to infinity in stationary flows [37]. This filter was chosen because it could be adapted to ICE cyclic flows by using it as a moving average. Further details of the exponential temporal filter and its adaption for cyclic ICE flows are provided in Section 5.5.

Each mean quantity in HTLES is calculated by resolving the differential form of the filter:

$$\frac{d\bar{f}}{dt} = \frac{1}{T_w}(\bar{f} - f), \quad (4.21)$$

where  $f$  is the quantity to be time filtered,  $\bar{f}$  is the time filtered quantity. The temporal filter width  $T_w$  is the time period over which the past solutions are weighted. It should be long enough so that  $\bar{f}$  tends to its average. In our simulations  $T_w$  was chosen equal to the simulation runtime  $t$ . This results in a simulation that takes place in two phases: it begins with a transitional phase during which the model adjusts its inputs by collecting the averaged quantities, then it enters a second phase from which the model inputs are established and the results can be exploited.

It worth noting that the exponential temporal filter is used to approximate the mean quantities in the model and does not have any relationship with the temporal filtering framework of HTLES.

## 4.4 Development and validation of a shielding to enforce RANS at walls

### 4.4.1 The elliptic shielding

With HTLES in wall-bounded flows using Equation (4.16), the energy ratio  $r$  strongly depends on the grid resolution (through  $\omega_c$ ). Therefore, depending on the mesh, the RANS-LES transition can occur too close to the wall as shown by Figure 4.3.

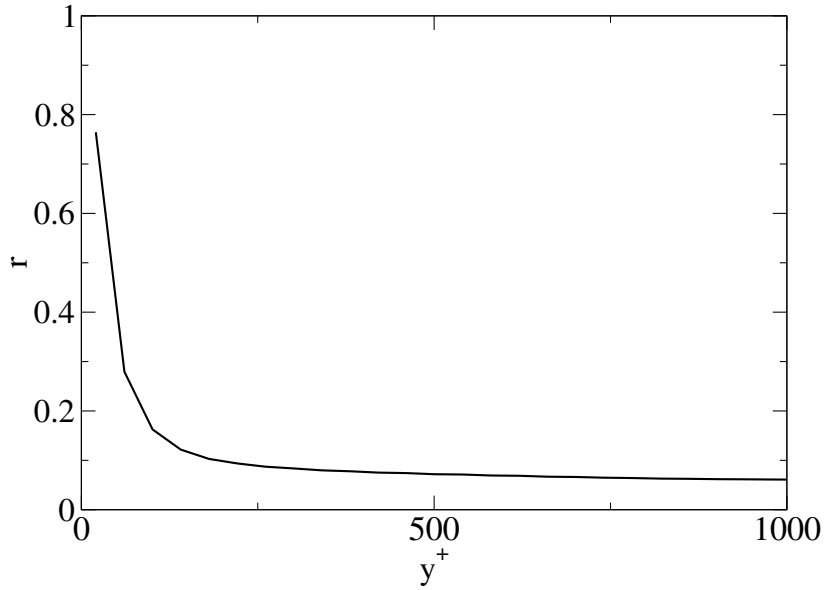


**Fig. 4.3 Channel Flow:** Profile of the energy ratio  $r$  along the wall-normal direction.

This phenomenon results in the reduction in the subfilter viscosity in the RANS region, which degrades the RANS model. This can lead to poor flow prediction in this region, such as premature boundary layer separation, also known as Grid Induced Separation (GIS) [122]. The shielding functions were introduced in this context. They aim to protect the RANS region by ensuring RANS at the walls and moving the RANS-LES transition away from the walls.

Accordingly, in the same way as the PITM approach [29], a shielding function  $\alpha$  based on the elliptic blending theory [82] is added to  $r$  such that the RANS-LES transition is controlled by the wall-distance rather than the cutoff frequency  $\omega_c$ :

$$r = \min \left( 1, (1 - \alpha^2) + \alpha^2 \frac{1}{\beta} \left( \frac{U_s}{\sqrt{k}} \right)^{\frac{2}{3}} \left( \frac{\omega_c k}{\varepsilon} \right)^{-\frac{2}{3}} \right), \quad (4.22)$$

$\alpha$  is equal to zero at walls which makes HTLES operate in RANS, and it goes smoothly to unity with the wall-distance so that the energy ratio given by Equation (4.16) is used far from walls.  $\alpha$  is the solution of:

$$\alpha - L_{sf}^2 \nabla^2 \alpha = 1, \quad (4.23)$$

$L_{sfs}$  is the modeled length scale:

$$L_{sfs} = C_L \max \left( \frac{k_{sfs}^{\frac{3}{2}}}{\varepsilon}, r^{\frac{3}{2}} C_\eta \frac{\nu^{\frac{3}{4}}}{\varepsilon^{\frac{1}{4}}} \right). \quad (4.24)$$

$L_{sfs}$  controls the shielding thickness  $\alpha$ .  $C_L$  is set to 0.161 according to [29]. In order to define a shielding thickness that is weakly dependent on the mesh, we chose to set  $L_{sfs}$  through  $C_\eta$ . Indeed,  $C_\eta$  is associated with the Kolmogorov lengthscale which is grid-independent.

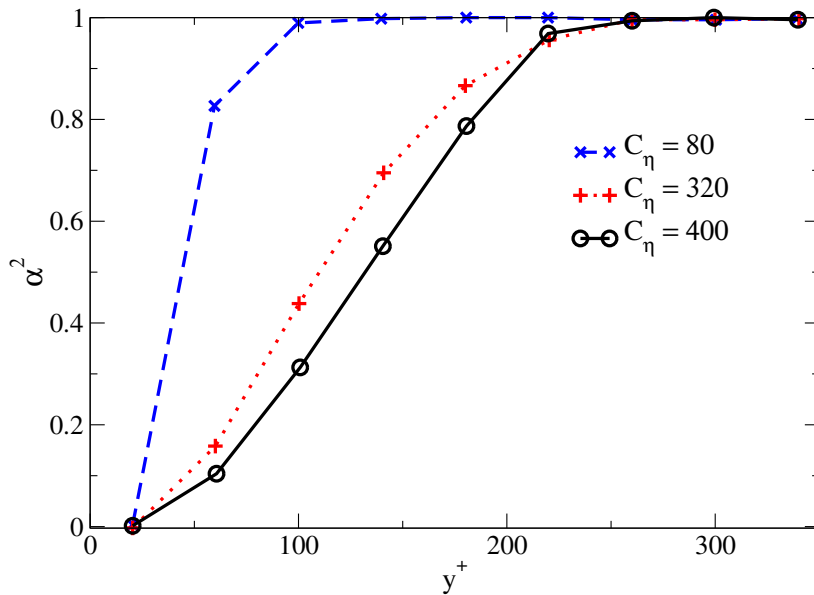


**Fig. 4.4 Channel Flow:** Profiles of  $\alpha^2$  over the altitude for three different values of  $C_\eta$ .

Figure 4.4 shows the profiles of  $\alpha^2$  along the wall-distance yielded by three simulations with different values of  $C_\eta$  in a channel flow (described in Section 4.4.2). For  $C_\eta = 80$ , the shielding thickness in wall-units is approximately equal to 100, while for  $C_\eta = 320$  and  $C_\eta = 400$ , it is almost equal to 250. HTLES of the channel flow using a thick shielding showed that the simulation degenerates everywhere in RANS. Therefore, we chose  $C_\eta = 80$  in order to have a relatively thin shielding helping to prevent this phenomenon.

Further analysis of the effect of the shielding will be examined the following Section.

## 4.4.2 Validation in a Channel Flow

### 4.4.2.1 Presentation of the configuration

The configuration consists of a flow at a constant pressure gradient between two infinite parallel walls, as schematized in Figure 4.5.

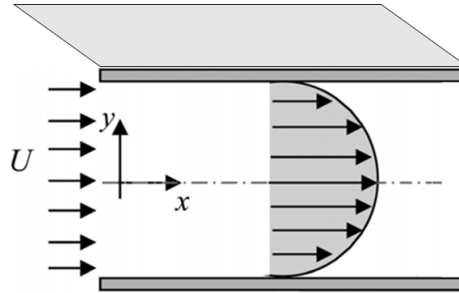


**Fig. 4.5 Channel Flow:** Illustration of the configuration.

Except for the pressure, the flow is periodic in the  $x$ -direction. A streamwise source term equal to 176 Pa/m is added to the momentum equation in the  $x$ -direction in order to sustain the flow.

Parameter	Value
Fluid	Air
Temperature [K]	320
Pressure [atm]	1
Channel half height $\delta$ [mm]	12.5

**Table 4.1 Channel Flow:** Main specifications.

The Reynolds number based on the friction velocity  $u_\tau$  is 1,000 and the reference data are extracted from DNS (Lee and Moser [77]). Further details of the configuration are summarized in Table 4.1.

The shear-stress at the cells adjacent to the walls is computed using the automatic wall function for RANS and HTLES [86] and the Werner and Wengle wall function [131] for LES.

The streamwise boundaries use periodic boundary conditions. For the spanwise boundaries, the configuration assumes that the channel's width is very large. The use of

periodic boundary conditions for spanwise boundaries enable to reproduce such configurations in a reduced domain's width. Nevertheless, in the used CONVERGE version the periodicity can only be defined in one direction. As periodicity is already used for the streamwise boundaries, we had to find an alternative to periodic conditions for the spanwise boundaries. For this purpose, we tested slip walls in a computational domain with a width equal to twice the channel height in order to reduce the impact of the boundary conditions on the simulation results. This alternative was validated by examining the results of HTLES in this configuration, knowing that in channel flows, the flow is statistically homogeneous in the spanwise direction.

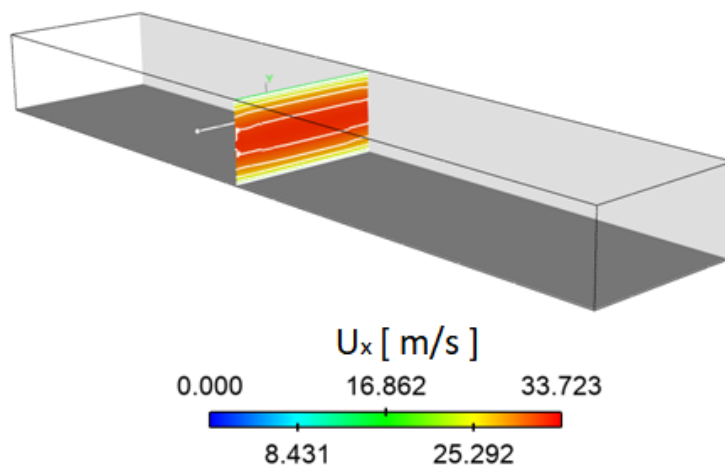


**Fig. 4.6 Channel Flow:** Contours and iso contours (white lines) of the mean axial velocity yielded by HTLES at a streamwise plane cut of the domain.

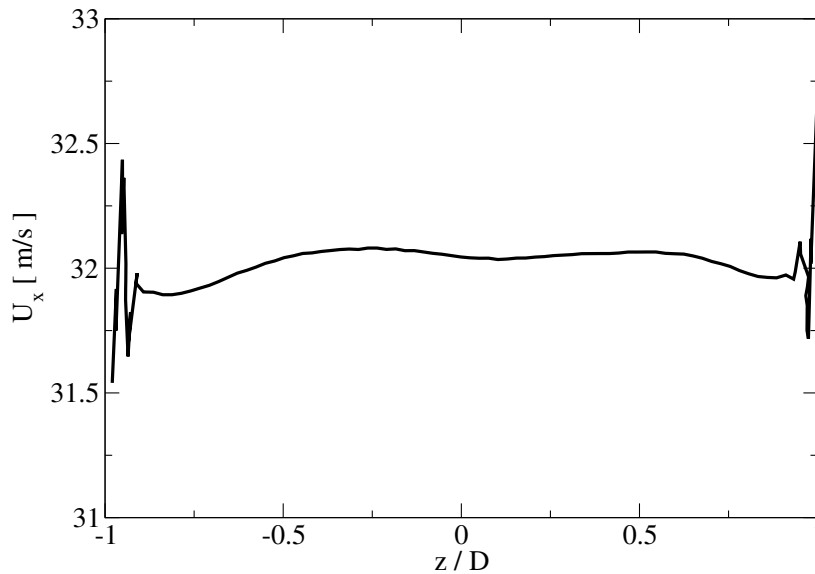


**Fig. 4.7 Channel Flow:** Profile of the mean axial velocity over the spanwise direction at centerline yielded by HTLES.

Figure 4.6 shows the isocontours of the mean axial velocity in a streamwise plane. The isocontours are quasi parallel showing a quasi homogeneous mean velocity in the spanwise direction. Nevertheless, Figure 4.7 shows that some velocity fluctuations appear close to the spanwise boundaries. They are suspected to be provoked by the anisotropic instantaneous velocities that are blocked by the spanwise boundaries. Furthermore, the mean axial velocity slightly varies in the core region that is also suspected to be the result of inevitable effects of the spanwise boundaries. Another test not presented here, using a domain width equal to three times the channel height, did not significantly reduce these problems. As this computational cost significantly increased with no real enhancement, we decided to keep the domain with a width that is two times larger than in DNS.

The simulations are performed on a mesh which contains  $N_x \times N_y \times N_z = 500 \times 50 \times 100$  hexahedra with a uniform distribution, yielding a mesh composed of 50 cells in the wall-normal direction. It should be noted that the boundary layer could not be resolved due to the limitations induced by the mesh management in CONVERGE (see section 4.3.2.1). Indeed, CONVERGE can only apply refinement ratios by powers of 2 that are systematically applied in all three directions, which dramatically increases the total number of cells if the mesh is refined to resolve the boundary layer. Therefore, the boundary layer is modeled using wall functions. The height of the cells adjacent to the walls has been chosen to target  $y^+ = 30$  so that it lies in the log layer of the wall functions (see Section 3.2.3).

The flow is initialized using a coarse DNS, performed on the same grid and using a first-order upwind scheme to prevent HTLES from degenerating into RANS, which occurred when a statistically averaged velocity field is used for initialization. A physical time of 2 s was simulated, which corresponds to 200 convective times ( $t_x = \frac{L_x}{U_{bulk}}$ ). Mean quantities are collected over a time period of 180 convective times and are also averaged in the spanwise direction over a distance equal to the channel height.

#### 4.4.2.2 Results of HTLES

In this section, the impact of the elliptic shielding (ES) on the HTLES predictions is investigated by comparing the results of two HTLES simulations with and without the ES.

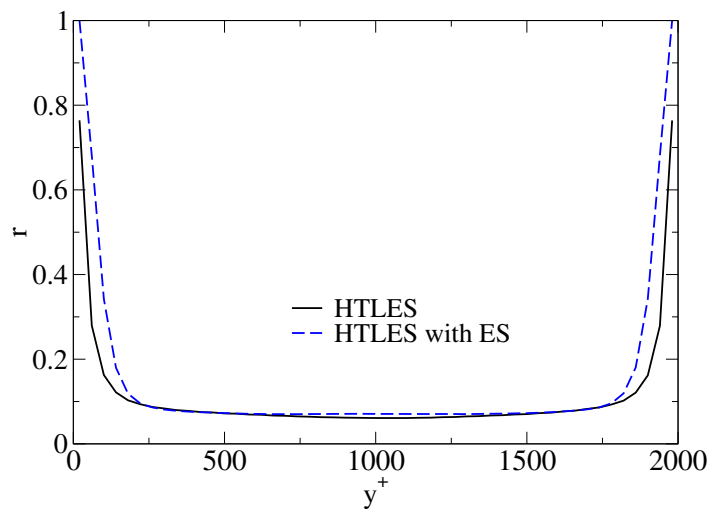


**Fig. 4.8 Channel Flow:** Profiles of the energy ratio  $r$  along the wall-normal direction.

Profiles of the energy ratio  $r$  yielded by each simulation are given in Figure 4.8. Both simulations give quasi similar profiles for wall-distance larger than  $y^+ > 250$ . Differences between the two simulations are observed near the wall. First, the simulation using the ES exhibits large values of the energy ratio compared to the simulation without ES, shifting the RANS-LES transition farther from the wall. Second, the energy ratio is forced to unity at the cell adjacent to the wall which preserves the RANS mode near the wall.

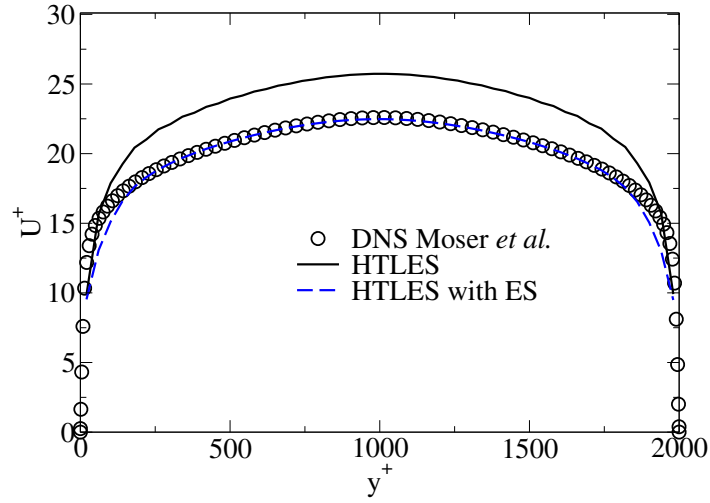


**Fig. 4.9 Channel Flow:** Impact of the elliptic shielding on the dimensionless velocity profiles for the channel flow  $Re_\tau = 1,000$ .

Figure 4.9 shows the dimensionless axial velocity  $U^+ = \frac{U_x}{u_\tau}$ , as a function of the wall distance in wall units  $y^+$  of the channel given by HTLES with and without the elliptic shielding (ES). The simulation without the ES shows a significant overestimation of the velocity magnitudes in comparison to DNS. Indeed, in the simulation without ES, the RANS-LES transition occurs too close to the wall where the mesh is not sufficiently fine to perform LES, resulting in a misprediction of the flow.

The simulation using the ES yields a velocity profile, which is in better agreement with DNS in the core region. Nevertheless, the velocity profiles close to the walls show a slight underestimation, which can be provoked by different reasons, such as the mesh which is not sufficiently fine to simulate the abrupt RANS-LES transition as indicated by the energy ratio  $r$ . In order to investigate examine this issue, the mesh should be refined in the boundary layers which we could not perform due to the CONVERGE mesh refinement limits mentioned in Section 4.4.2.1.

	DNS	HTLES	HTLES with the ES
Flow rate [ $m^3/s$ ]	0.71	0.79	0.69
Relative error $\varepsilon_D$ [%]	-	+11.0	-2.3

**Table 4.2 Channel Flow:** Flow rates given by the HTLES with and without the ES.

The flow rates yielded by each simulation are listed in Table 4.3. HTLES without the ES shows a relative error of +11% compared with DNS data, while HTLES with the ES reduces the relative error to  $-2.3\%$ .

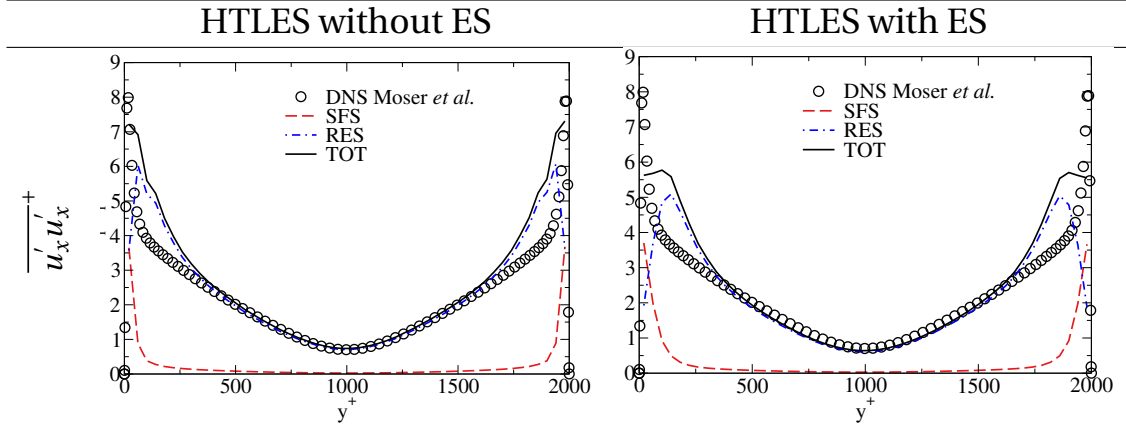


**Fig. 4.10 Channel Flow:** Profile of the streamwise component of the Reynolds stress tensor: resolved  $\overline{u'_x u'_x}^+$  (**RES**), modeled  $\overline{\tau_{xx}}^+$  (**SFS**) and total  $TOT = RES + SFS$ .

The streamwise component of the Reynolds stress tensor given by HTLES with and without the ES is depicted in Figure 4.10. The Reynolds stress is computed as the sum of:

- the resolved stress:

$$\overline{u'_x u'_x}^+ = \frac{\overline{(\tilde{U}_x - \bar{U}_x)(\tilde{U}_x - \bar{U}_x)}}{u_\tau^2}. \quad (4.25)$$

- the subfilter stress, which is estimated using the Boussinesq approximation:

$$\overline{\tau_{xx}}^+ = \frac{-2\nu_{sfs} \frac{\partial \tilde{U}_x}{\partial x} + \frac{2}{3} k_{sfs}}{u_\tau^2}. \quad (4.26)$$

The impact of the ES on the streamwise Reynolds stress can be seen in the near-wall region, where the resolved and the subfilter fluctuations given by the simulation without the ES are of the same order of magnitude. The scale-resolving mode is activated too close to the wall due to small values of  $r$  (see Figure 4.8). In HTLES with the ES, the subfilter contribution is increased near the wall and thus the scale-resolving region is slightly shifted away from the wall. The peak that appears close to the walls is deteriorated in HTLES with ES since the simulation tends to the RANS mode, which does not reproduce this peak accurately.

Although the targeted  $r$  plotted in Figure 4.8 goes to 1 at the wall, it is observed in Figure 4.10 that a significant part of the energy of the streamwise fluctuations is resolved. These fluctuations are induced by the fluctuating resolved scales coming from the core region and penetrating in the RANS region. To study in more detail the difference between the targeted  $r$  and what is observed in the simulation, two quantities should be examined:

- The target energy ratio  $r$ : is the energy ratio given by Equation (4.22) that enters Equation (4.11) and thus drives the transition from RANS to LES of the HTLES approach.
- The observed energy ratio  $r_{observable}$ : which is obtained by post-processing the results using Equation:

$$r_{observable} = \frac{\overline{k_{sfs}}}{k} \quad (4.27)$$

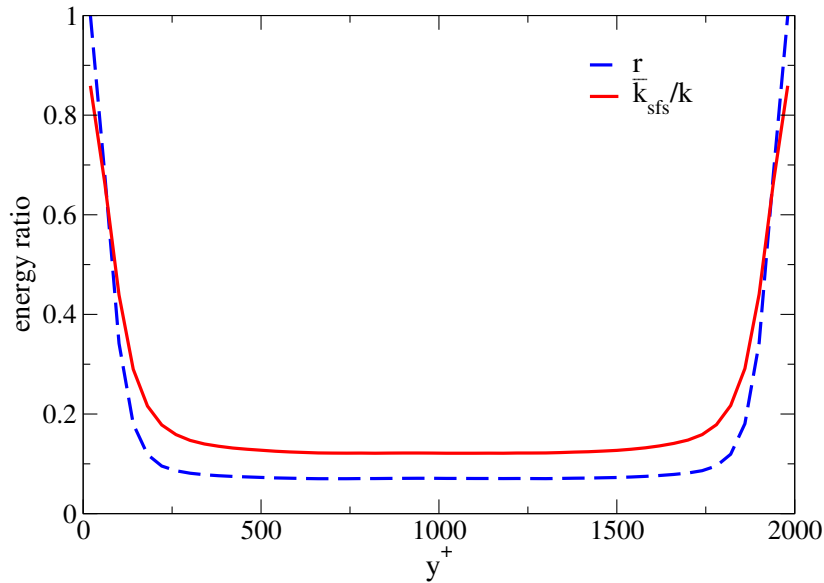


**Fig. 4.11 Channel Flow:** Comparison of the targeted and the observed energy ratio  $r$ .

Figure 4.11 compares the target ratio and the observed one. At the walls, the target ratio is equal to one and is higher than the observed ratio. It then decreases along the wall-distance and reaches smaller values than the observed ratio in the core region. Indeed, it is worth mentioning that there is no mechanism in the simulation that ensures that the observed ratio is identical to the target ratio.

#### 4.4.2.3 Comparison with RANS and LES

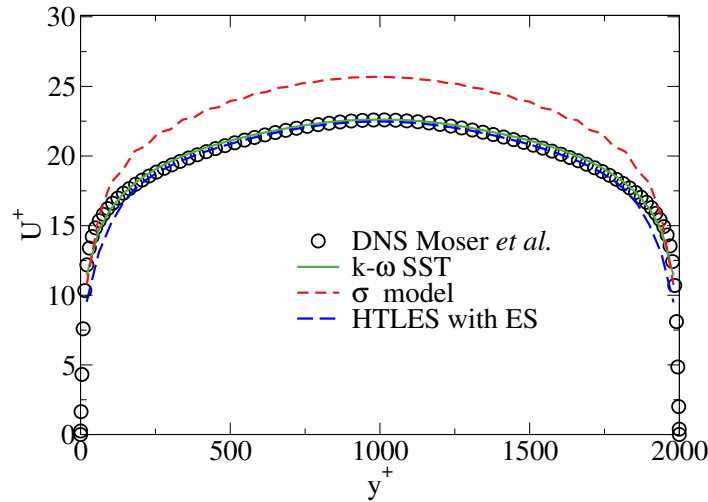


**Fig. 4.12 Channel Flow:** Comparison of the mean axial velocity along the wall-normal direction between RANS, LES and HTLES.

RANS and LES, using the  $k - \omega$  SST model [88] and the  $\sigma$  subgrid model [97] respectively, are also performed in the channel flow using the same mesh. The velocity profiles are compared with HTLES and DNS data in Figure 4.12. RANS shows accurate velocity profiles in this configuration, and the flow rate is almost the same as DNS with a relative error of  $-0.4\%$ , as listed in Table 4.3. The velocity profile given by LES shows the same overestimation of the flow rate as HTLES without the ES. Similar conclusions were already outlined in [96] when using wall functions in the channel flow.

	DNS	RANS	LES	HTLES ES
Flow rate [ $m^3/s$ ]	0.71	0.70	0.79	0.69
Relative error $\varepsilon_D$ [%]	-	-0.4	10.7	-2.3

**Table 4.3 Channel Flow:** Comparison of the flow rates given by RANS, HTLES and LES to DNS data

These results show the interest in using hybrid methods. Indeed, in LES even if the wall-function is used, the simulation fails to accurately predict the flow if the mesh in the vicinity of the boundary layer is relatively coarse. Hybrid methods resolve this problem by using RANS in these regions and LES in the core region.

# Chapter 5

## Development of EWA-HTLES for non-stationary flows

### 5.1 Introduction

Chapter 4 introduced the HTLES approach in statistically stationary turbulence. The approach transforms the  $k-\omega$  SST RANS model into a hybrid turbulence model by modifying the dissipation term in the  $k$ -equation using statistically averaged turbulence quantities. The difficulty of using HTLES in more general flows is related to this point. Indeed, in LES regions HTLES resolves a part of the turbulent fluctuations and, therefore does not provide statistical turbulent quantities. Therefore, the resolved turbulent quantities must be statistically averaged in order to be used as inputs of the HTLES models. As shown in Section 4.3, in stationary configurations, the averaged quantities can be approximated by applying a time filter, the so-called Exponentially Weighted Average (EWA) to the simulated flow fields, using a sufficiently large filter width, as the temporal filter tends to the statistical average when the temporal filter width goes to infinity [37]. However, in cyclic engine flows, the statistical average corresponds to the phase average which is time-dependent. As a consequence, the phase-averaged quantities cannot be calculated as in stationary flows by applying a temporal filter to the resolved flow fields with a large filter width as this will suppress the time-dependent character of the signal.

This Chapter proposes an extension of the HTLES approach to these flows by approximating the statistically averaged HTLES inputs using a temporal filtering with some

adaptations introduced for cyclic engine flows. The first two Sections detail the main characteristics of ICE flows and the difficulties of applying HTLES to such flows. Then, Section 5.4 lists some approaches studied in this work to extend the HTLES approach to cyclic engine flows. Section 5.5 focuses on the selected approach, namely EWA-HTLES. Finally, Section 5.6 provides validations of EWA-HTLES in two stationary configurations: the Channel Flow at  $Re_\tau = 1,000$  [77] and the Steady Flow Rig [127]. The aim of these applications is to validate HTLES in simple configurations before applying it to more complex non-stationary configurations in the next Chapters.

## 5.2 Main features of four-stroke ICE flows

This work focuses on the application of HTLES to four-stroke ICE flows. These flows, already detailed in Section 1.2, are characterized by a cycle with moving valves and pistons and time-dependent boundary conditions, resulting in a flow with statistical averages that vary periodically over time, i.e., phase averages. Two characteristic frequencies can be introduced to distinguish the variations in time of the statistics from the turbulent time scales:

- A low frequency  $f_0 = 1/T_0$  which characterizes the temporal evolution of the phase average, where  $T_0$  is the period of the cycle.
- A high frequency  $f_\tau = 1/\tau_t$  related to turbulent fluctuations.  $\tau_t$  is the integral time scale of the turbulence.

## 5.3 Difficulties to use HTLES in cyclic engine flows

The HTLES approach transforms the  $k - \omega$  SST into a hybrid turbulence model by introducing a time scale  $T$  in the dissipation term of the  $k$ -equation (see Equation (4.12)):

$$T = \frac{r}{1 + \left(\frac{C_{\epsilon 2}}{C_{\epsilon 1}} - 1\right)(1 - r \frac{C_{\epsilon 1}}{C_{\epsilon 2}})} \frac{k}{\epsilon}. \quad (5.1)$$

where:

$$\left\{ \begin{array}{l} \varepsilon = \\ k = \\ r = \end{array} \right. \begin{array}{l} \beta^* \overline{k_{sf_s} \bar{\omega}} \\ \overline{k_{sf_s} + k_{res}} \\ \min \left( 1, (1 - \alpha^2) + \alpha^2 \frac{1}{\beta} \left( \frac{U_s}{\sqrt{k}} \right)^{\frac{2}{3}} \left( \frac{\omega_c k}{\varepsilon} \right)^{-\frac{2}{3}} \right) \end{array} \quad \begin{array}{l} (5.2a) \\ (5.2b) \\ (5.2c) \end{array}$$

In cyclic flows, the calculation of these quantities requires the knowledge of the phase average of:

- the resolved velocity  $\tilde{U}_i$  ( $i \in \llbracket x, y, z \rrbracket$ ) in order to compute the fluctuating velocity.
- the subfilter turbulent kinetic energy  $k_{sf_s}$ .
- the resolved turbulent kinetic energy  $k_{res}$ .
- the turbulence frequency  $\omega$ .

Nevertheless, except in RANS regions, the HTLES approach provides turbulent flow fields and not phase-averaged quantities. To calculate these phase averages, a straightforward approach would be to perform a transient phase consisting of several cycles during which phase averages are calculated and stored over short periods of time. Once the phase averages have reached a state of convergence they can be read and used by the model. However, this approach cannot be used because it would considerably increase the computational cost of the simulation and hence reduce the interest of using HTLES. Therefore, the extension of HTLES to cyclic engine flows relies on the formulation of a method allowing to approximate the statistically averaged inputs of the model ( $\overline{\tilde{U}_i}$  ( $i \in \llbracket x, y, z \rrbracket$ ),  $\overline{k_{sf_s}}$ ,  $\overline{k_{res}}$ ,  $\overline{\omega}$ ) without having to actually calculate them.

## 5.4 Possible solutions

Different solutions were examined to extend HTLES to cyclic engines flows. The next Sections detail some of the approaches that were identified and explored in the present work.

### 5.4.1 Mapping a RANS solution

In this approach a pre-calculation of a complete cycle is performed using a RANS model to obtain estimates of the statistically averaged fields of  $U_i$ ,  $\varepsilon$  and  $k$ , which are stored at short time intervals. Then, the turbulence model switches to HTLES and reads the stored statistically averaged flow quantities obtained from RANS and uses them to calculate the energy ratio  $r$ , and the time scale  $T$ .

This approach has not been tested in this work for the following reasons. First, the need to perform a RANS pre-calculation and to store the statistical average of the flow fields at short time intervals will considerably increase the complexity of the model implementation. Second, storing the 3D statistical fields requires a high memory space. The process of reading the 3D statistical fields frequently takes considerable time to perform. Finally, the statistical averages provided by RANS may be inaccurate in some complex flows [56].

This approach will significantly increase the complexity of the simulation. It was decided not to use it.

### 5.4.2 Test of HTLES without averaged inputs

This approach has been proposed by drawing inspiration from the work of Basara *et al.* [43] on the application of the hybrid PANS method. The authors were confronted to the similar difficulty encountered in HTLES where they had to average some turbulent quantities used in the PANS equations. The authors avoided this difficulty by using instantaneous resolved flow fields instead of statistically averaged quantities. In this work, we tested a similar approach for HTLES using the instantaneous flow fields resolved by the simulation for  $k_{sfS}$ ,  $k_{res}$  and  $\omega$  instead of statistically averaged quantities to compute the energy ratio  $r$  and the time scale  $T$ . The only mean quantity left in the model is the mean resolved velocity  $\overline{U}_i$  which is needed to compute the resolved turbulent kinetic energy :

$$k_{res} = \frac{1}{2}(\tilde{U}_i - \overline{U}_i)(\tilde{U}_i - \overline{U}_i) . \quad (5.3)$$

This approach has been tested in stationary configurations, showing almost similar predictions compared to the original HTLES. This approach, in combination with the

developed elliptic shielding described in Section 4.4, has been the subject of the following publication [1]:

Development and validation of a hybrid temporal LES model in the perspective of applications to internal combustion engines.

*Afailal A. H., Galpin J., Velghe A. and Manceau R.*

*Oil Gas Sci. Technol. – Rev. IFP Energies nouvelles, 74 (2019) 56.*

However, in this approach, it is still necessary to evaluate the mean velocity field. Therefore, it is not applicable to non-stationary flows.

It has also been envisaged to avoid computation of the statistical average of  $\tilde{U}_i$  by directly solving a transport equation that models the quantity  $k_{res}$ , as was proposed for the PANS method [4, 43]:

$$\frac{\partial}{\partial t} k_{res} + \tilde{U}_j \frac{\partial}{\partial x_j} k_{res} = \frac{k_{res}}{k_m} (P - \varepsilon) + \frac{\partial}{\partial x_j} \left[ \left( \nu + \frac{\nu_m}{\sigma_{ku}} \right) \frac{\partial k_m}{\partial x_j} \right]. \quad (5.4)$$

where  $P$  and  $\varepsilon$  are the production and dissipation terms of the modeled turbulent kinetic energy  $k_m$ ,  $\nu_m$  is the modeled turbulent viscosity and  $\sigma_{ku} = \sigma_k \frac{f_k^2}{f_\varepsilon}$ ,  $\sigma_k$  is a coefficient equal to 1,  $f_k$  is the energy ratio and  $f_\varepsilon = \frac{\varepsilon_u}{\varepsilon}$  is the turbulent dissipation rate of the modeled scales over the total turbulent dissipation rate  $\varepsilon$ .

However, the resolved turbulent kinetic energy predicted by Equation (5.4) showed significant discrepancies with the reference data in [43]. Section 5.4.3 presents another alternative, which has been tested to estimate the total turbulent kinetic energy using a recursive method.

### 5.4.3 Recursive method

The recursive method is the continuation of the approach of Section 5.4.2, which uses instantaneous resolved flow fields to compute HTLES inputs. The only difference concerns the computation of the total turbulent kinetic energy  $k$ , which is computed by a recursive method without computing the resolved turbulent kinetic energy  $k_{res}$ , thereby avoiding the need to compute the mean of the resolved velocity.

The total turbulent kinetic energy is calculated recursively, using the definition of the energy ratio  $r = \frac{\overline{k_{sfs}}}{k}$ . At any instant of the simulation  $t = t_n$ , the total kinetic energy writes:

$$k = \frac{\overline{k_{sfs}}}{r}. \quad (5.5)$$

As  $r$  is not known at  $t_n$ , it is assumed that the variation of  $r$  between  $t_{n-1} = t_n - dt$  and  $t_n$  can be neglected as long as small CFL numbers are used. Therefore,  $k$  is calculated using  $r$  from the previous time-step  $t_{n-1}$  in Equation (5.5).

HTLES with the recursive approach has been tested in the Channel Flow at  $Re_\tau = 1,000$  detailed in Section 4.4.2. The velocity and pressure fields were initialized from instantaneous fields of a coarse DNS to prevent HTLES from degenerating into RANS, which occurs when a statistically averaged velocity field is used as an initialization. The energy ratio  $r$  and the time scale  $T$  were initially calculated using  $k$  and  $\varepsilon$  profiles interpolated from a  $k - \omega$  SST RANS solution. The  $k$  and  $\omega$  fields were initialized using fields set to zero as no solution in the code has been found to simultaneously map two fields coming from different simulations (fields from DNS for the pressure and velocity, and fields from RANS for  $k$  and  $\omega$ ).

In a first approach, the direct use of Equation (5.5) proved to give an unstable behavior. This unstable behavior turned out to be the result of small values of  $r$  in some areas, which, according to Equation (5.5), gave locally high values of  $k$ . This phenomenon amplifies in time and propagates to the whole flow field, leading in turn to a wrong prediction of  $r$  and  $T$  and ultimately causing the simulation to diverge.

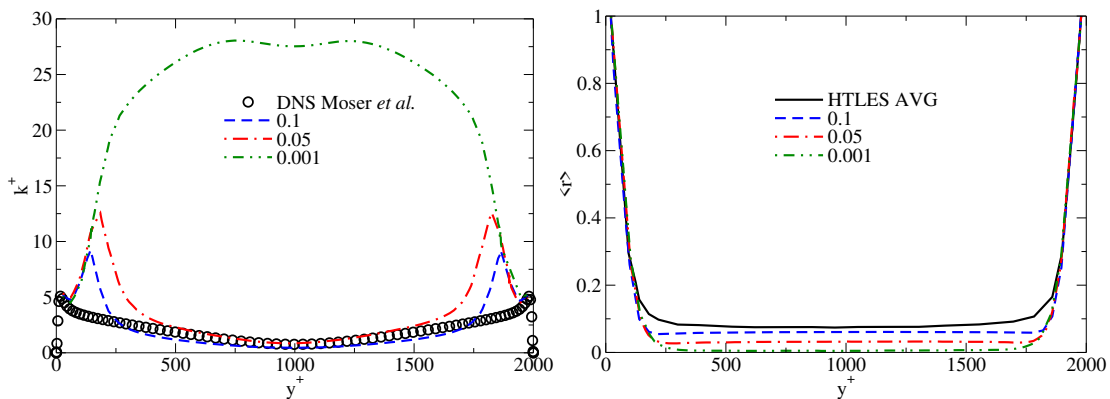


**Fig. 5.1 Channel Flow:** Profiles predicted by the recursive HTLES with three different values for the lower bound - **Left:**  $k = \frac{k_{sfs}}{r}$  - **Right:** energy ratio  $r$ .

In order to avoid this instability, we investigated the possibility of introducing a lower bound  $r_{min}$  in Equation (5.5):

$$k = \frac{k_{sfs}}{\max(r_{min}, r)}. \quad (5.6)$$

First, a value of  $r_{min} = 0.1$  was tested, which is close to the minimum value observed in the original HTLES, described in Chapter 4 (referred to as HTLES AVG). Second, two less stringent values of  $r_{min} = 0.05$  and  $r_{min} = 0.001$  were also tested. The three corresponding simulations were indeed able to reach a converged state. Figure 5.1-*left* shows the profiles of the kinetic energy predicted by Equation (5.6). The simulation using  $r_{min} = 0.001$  gives a completely wrong profile compared with DNS, whereas the simulations with  $r_{min} = 0.05$  and  $r_{min} = 0.1$  are in better agreement with DNS in the center of the channel. However, the near-wall predictions show significant deviations from DNS, with a pronounced peak that the latter does not show. This peak is less pronounced in the simulation using the stringent  $r_{min}$  value of 0.1, which avoids having small values of  $r$  and therefore large values of  $k$  according to Equation (5.6).

In any case, the results seem to significantly depend on the value of  $r_{min}$ . Attempts to derive a lower limit for  $r$  based on physical parameters have not been successful, as it turned out that an a priori knowledge of the integral length scale  $L_{int}$  is required. Indeed, since the turbulent length scales computed during the simulation  $\frac{k^{3/2}}{\epsilon}$  are supposed to be less than  $L_{int}$ :

$$\frac{k^{3/2}}{\epsilon} \leq L_{int}, \quad (5.7)$$

A bound can be formulated for  $r$  by using  $L_{int}$  in Equation (5.2c) as:

$$r_{min} = \min \left( 1, (1 - \alpha^2) + \alpha^2 \frac{1}{\beta} U_s^{\frac{2}{3}} (\omega_c L_{int})^{-\frac{2}{3}} \right) \quad (5.8)$$

This approach could not provide an acceptable estimate of the total turbulent kinetic. Furthermore for approaches that uses instantaneous variables for the model inputs (recursive and the approach discussed in Section 5.4.2), there is no solid theoretical explanation that supports the use of the model without averaging its inputs. In order to keep the model as close as possible to its original formulation, the approach detailed in 5.5 preserves the averaged quantities in the model inputs, and approximates them using temporal filtering with some adaptations that makes it applicable for cyclic flows.

## 5.5 EWA-HTLES

This section introduces a temporal filter that aims at approximating the statistically averaged quantities  $\overline{\tilde{U}_i}$  ( $i \in \llbracket x, y, z \rrbracket$ ),  $\overline{k_{sf}}$ ,  $\overline{k_{res}}$ , used as HTLES inputs during the simulation. The proposed temporal filter adjusts its temporal filter width locally in time and space according to the turbulence time scales and the cycle period. The application of this filter to the resolved quantities aims at separating the periodic component due to the cycle from the turbulent fluctuations.

### 5.5.1 Exponentially Weighted Average (EWA)

#### 5.5.1.1 Definition

The Exponentially Weighted Average (EWA) is as a low-pass temporal filter that removes the high frequency content from each flow field quantity  $f$  by weighting its past values according to the integral operator:

$$\overline{f}(x, t) = \int_{-\infty}^t W(\tau - t, T_w) f(x, \tau) d\tau, \quad (5.9)$$

where  $\widehat{f}(x, t)$  denotes the time-filtered quantity of  $f$  at any position  $x$  at instant  $t$ , and  $T_w$  is the temporal filter-width.  $W$  is the kernel function of EWA, it defines the way the past flow fields are weighted:

$$W(t, T_w) = \frac{1}{T_w} e^{-\frac{t}{T_w}}. \quad (5.10)$$

Calculating  $\overline{f}$  using the integral form in Equation (5.9) requires storing a long history of the flow fields that need to be filtered. One of the main reasons why the EWA was chosen in this study is that its differential formulation is known [106]:

$$\frac{d\overline{f}}{dt} = \frac{1}{T_w} (\overline{f} - f). \quad (5.11)$$

Therefore, EWA quantities can be calculated by solving the EWA differential equation, eliminating any storage constraints.

### 5.5.1.2 Requirements of the temporal filter width

This Section defines the requirements of EWA so that it can be used in cyclic engine flows. The main properties of the filter can be examined using its transfer function in the Fourier space:

$$H(z) = \frac{\hat{Y}(z)}{\hat{X}(z)}. \quad (5.12)$$

The transfer function determines the output of the filter  $\hat{Y}$  depending on the input  $\hat{X}$  for any  $z \in \mathbb{C}$ . For EWA this function is [106]:

$$H(\Omega') = \frac{1}{1 + i\Omega'}, \quad (5.13)$$

where  $\Omega' = \omega T_w$  is the dimensionless frequency.

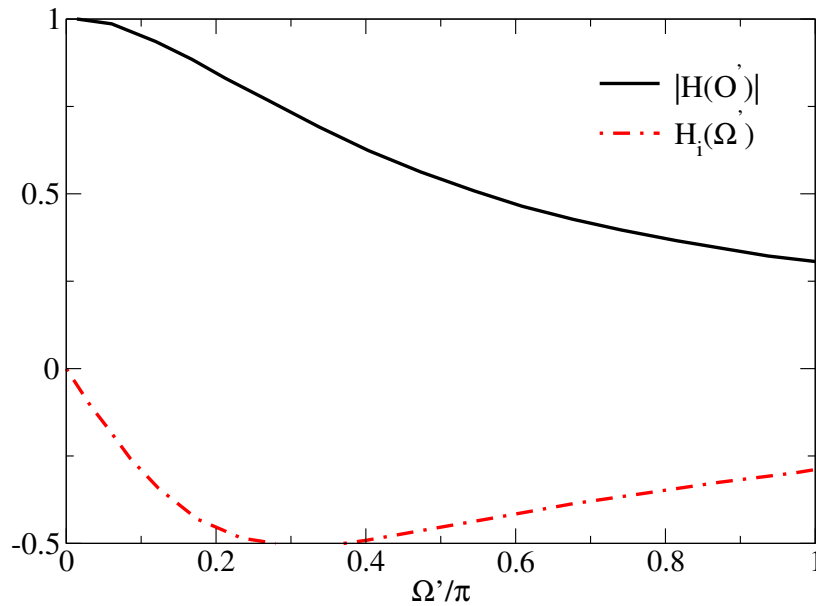


**Fig. 5.2** Transfer function of EWA.

Figure 5.2 shows the evolution of  $|H(\Omega')|$  the magnitude and  $H_i(\Omega')$  the imaginary part of the transfer function as a function of  $\Omega'$ .  $|H(\Omega')|$  shows the magnitude response of the filter and  $H_i$  is linked to the phase shift induced by the EWA.  $|H(\Omega')|$  significantly decreases with increasing frequency  $\Omega'$ , showing the low-pass character of the EWA. The imaginary part of the transfer function  $H_i$  shows how the phase shift induced by EWA varies significantly with the increase in frequency  $\Omega'$ .

The cutoff frequency  $\omega_{co}$  is defined as the frequency at which the response gain is half :

$$|H(e^{i\omega_{co}})|^2 = \frac{1}{2} . \quad (5.14)$$

In EWA, it expresses as:

$$\omega_{co} = \arccos\left(\frac{T_w^2 + 2T_w - 2}{2(T_w - 1)}\right) \quad (5.15)$$

To be able to use EWA to provide averaged quantities to HTLES during the simulation, the cutoff frequency should be  $\omega_0 \ll \omega_{co} \ll \omega_t$  so that :

- The EWA filters out the turbulent frequencies without eliminating the frequency of the phase-averaged motion.
- The phase shift induced by EWA between the time-filtered and the instantaneous flow fields is kept as low as possible.

## 5.5.2 Definition of the temporal filter width

This section proposes an expression for the temporal filter width  $T_w$  for EWA that meets the requirements listed in Section 5.5.1.2.  $T_w$  was determined by performing analyses on two synthetic turbulent signals. The first part determines an expression for the temporal filter width based on the turbulent integral time scale to filter out turbulent fluctuations from a stationary synthetic turbulent signal. The second part focuses on the phase shift induced by EWA. It determines the upper limit for the temporal filter width in a sinusoidal synthetic signal to keep the phase shift low. Based on this analysis, an expression for the temporal filter width for EWA-HTLES in cyclic flows is proposed at the end of this Section.

### 5.5.2.1 Stationary synthetic turbulence signal

#### Generation of the synthetic signal

The synthetic turbulent signal as a function of time is generated using  $N$  modes from an imposed turbulence spectrum  $E$  and random phases  $\phi_n$ :

$$U(t) = \sum_{n=1}^N A_n \cos(\omega_n t + \phi_n) , \quad (5.16)$$

where  $N = \frac{\omega_N - \omega_0}{\Delta\omega}$  is the number of modes,  $\omega_0 = 0.05$ ,  $\omega_N = 1.5 Re_t^{3/4}$ ,  $Re_t$  is the turbulent Reynolds number, and  $\Delta\omega = 0.1$ .  $A_n$  is the amplitude of the mode  $n$ .

The energy of mode  $n$ ,  $u_n^2 = \frac{1}{2} A_n^2$ , is determined from a turbulence spectrum  $E$ . It is equal to  $\frac{2}{3} E(\omega_n) \Delta\omega$  such that the sum of the energies of all the modes is equal to the integral of the spectrum. Accordingly:

$$A_n = \sqrt{\frac{4}{3} E(\omega_n) \Delta\omega} \quad (5.17)$$

In order to generate the signal a model for the turbulence spectrum is required. For this purpose, the Kraichnan spectrum [65] was selected:

$$E(\kappa) = C \varepsilon^{2/3} \kappa^{-5/3} f_\eta(\kappa), \quad (5.18)$$

where  $C$  is a coefficient,  $\varepsilon$  is the turbulent dissipation,  $\kappa$  is the wavenumber and  $f_\eta(\kappa) = \exp(-\beta\kappa\eta)$  with  $\beta = 2.1$  [104].

The spectrum is expressed in the frequency domain using the change of the variable:

$$dk = E(\kappa) d\kappa = E_T(\omega) d\omega, \quad (5.19)$$

and using the dispersion relation (Eulerian description, see Section 4.2.2):

$$\omega = U_s \kappa, \quad (5.20)$$

Accordingly, the Kraichnan spectrum in the frequency domain writes:

$$E_T(\omega) = C \varepsilon^{2/3} U_s^{2/3} \omega^{-5/3} f_\eta(\omega). \quad (5.21)$$

However this relation is not valid for low frequencies. Indeed, by definition of  $E$ ,  $E(0)$  must be equal to  $\frac{2k\tau_t}{\pi}$ , where  $\tau_t$  is the integral time scale.  $\tau_t$  can be modeled as  $\frac{L}{U_s}$ , such that  $\tau_t = \frac{k}{\varepsilon}$  if the mean velocity is zero, and  $\tau_t = \frac{k^{3/2}}{\varepsilon U}$  at the limit of large velocities (Taylor's hypothesis).

In order to make sure that the value  $E(0)$  is correct and that Relation 5.21 is recovered for large frequencies, a function  $f_T(\omega)$  must be introduced in  $E_T$ , such that:

$$E_T(\omega) = C \varepsilon^{2/3} U_s^{2/3} \omega^{-5/3} f_\eta(\omega) f_T(\omega), \quad (5.22)$$

where  $f_T(\omega)$  can be written as:

$$f_T(\omega) = \frac{2}{\pi} \frac{1}{(1 + (\omega L U_s^{-1})^{-5/3})} \quad (5.23)$$

For what follows, the turbulent quantities are expressed in their non-dimensional form by using:

- The integral length scale  $L = \frac{k^{3/2}}{\varepsilon}$  as a length unit.
- The integral time scale  $\tau_t = \frac{L}{\sqrt{k}} = \frac{k}{\varepsilon}$  as a time unit.

The two following quantities are used to express the Kraichnan spectrum in its dimensionless form:

- The sweeping turbulent intensity  $I_s = \frac{\sqrt{k}}{U_s}$ .
- The turbulent Reynolds number  $Re_t = \frac{\sqrt{k}L}{\nu}$

The following dimensionless quantities are introduced:  $\tilde{E} = \frac{E_T}{L\sqrt{k}}$ ,  $\tilde{\omega} = \frac{\omega L}{\sqrt{k}}$ ,  $\tilde{\varepsilon} = 1$  and  $\tilde{U}_s = \frac{1}{I_s}$ .

Accordingly, the Kraichnan spectrum in its dimensionless form becomes:

$$\left\{ \begin{array}{l} \tilde{E}(\tilde{\omega}) = \\ f_\eta(\tilde{\omega}) = \\ f_T(\tilde{\omega}) = \end{array} \right. \begin{array}{l} C I_s^{-2/3} \tilde{\omega}^{-5/3} f_T(\tilde{\omega}) f_\eta(\tilde{\omega}) \\ \exp(-\beta \frac{\tilde{\omega} I_s}{Re_t^{3/4}}) \\ \frac{2}{\pi} \frac{1}{(1 + (\tilde{\omega} I_s)^{-5/3})} \end{array} \quad \begin{array}{l} (5.24a) \\ (5.24b) \\ (5.24c) \end{array}$$

From Equation 5.24, one can observe that the spectrum is defined by  $Re_t$  and  $I_s$ .

$Re_t$  is set to 1,000. This value is large enough to make the separation between the integral scales and the dissipative scales significant. Since the objective, in what follows, is to examine the behavior of EWA with large filter widths (hence with small cutoff frequencies  $\omega_{co}$ ) capable of filtering the most energetic part of the spectrum, there is no real necessity to further increase  $Re_t$  as this will only add high frequencies that contain low amounts of energy.

$I_s$  is chosen in such a way that the generated signal represents a situation similar to a Homogeneous Isotropic Turbulence (HTI). In this case,  $\overline{U} = 0$ , thereby the sweeping velocity reduces to  $U_s = \sqrt{k}$  and  $I_s$  is equal to unity.

$C$  was set to 0.87 in such a way that  $\tilde{k} = \int_0^{+\infty} \tilde{E}(\tilde{\omega}) d\tilde{\omega}$  is equal to one for  $Re_t = 1,000$ .  $C$  is quasi independent from the variations of  $I_s$  but slightly depends on  $Re_t$ . It tends to 0.79 when  $Re_t$  goes to infinity.

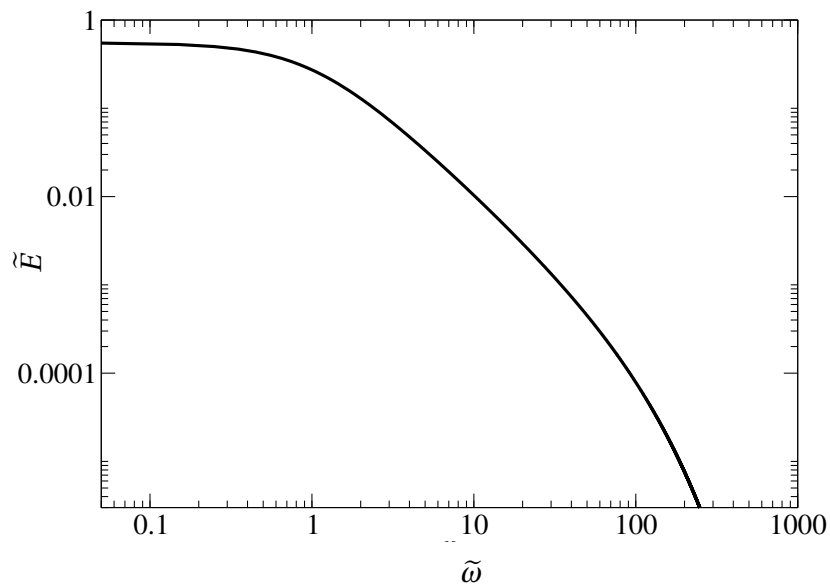


**Fig. 5.3 Synthetic signal:** Kraichnan turbulence spectrum in the frequency domain.

Figure 5.3 shows its profile as a function of  $\omega$ . The resulting synthetic signal is shown in Figure 5.4, its statistical average is equal to zero.

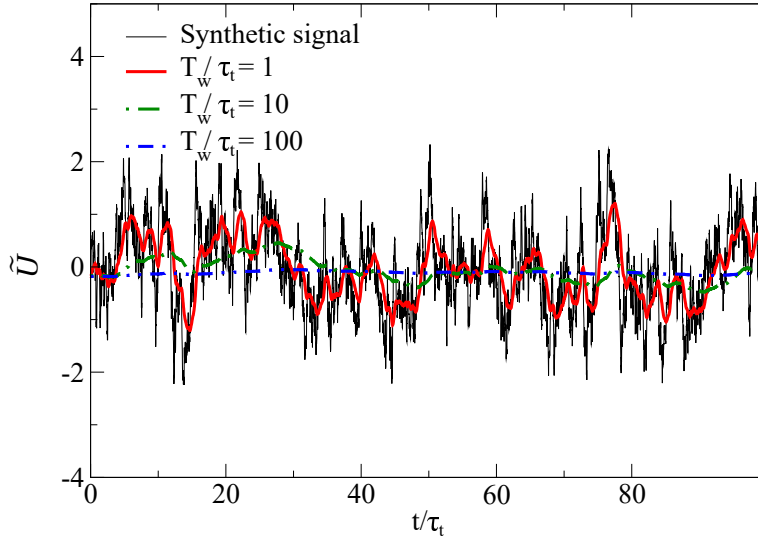


**Fig. 5.4 Synthetic signal:** Time evolution of the synthetic signal and the filtered signal for different temporal filter-widths.

### Application of EWA

The EWA is applied to the synthetic signal using three different temporal filter widths  $T_w$  to determine the required filter width. The resulting signals as a function of time for each  $T_w$  are shown in Figure 5.4. The results obtained with  $T_w = \tau_t$  show that EWA hardly filters turbulent fluctuations. Better results are obtained with  $T_w = 10\tau_t$  which shows a significant reduction of the remaining turbulent fluctuations in comparison with the results obtained with  $T_w = \tau_t$ . The results obtained with  $T_w = 100\tau_t$  are almost similar to the statistical average which is equal to zero.

To quantitatively evaluate the impact of the temporal filter width on the evaluation of the turbulent kinetic energy, the turbulent kinetic energy is computed using the filtered velocity  $\tilde{U}$  obtained with different filter widths:

$$\tilde{k} = \frac{3}{2} \langle (\tilde{U} - \overline{\tilde{U}})(\tilde{U} - \overline{\tilde{U}}) \rangle, \quad (5.25)$$

where  $\langle \dots \rangle$  is the statistical average.

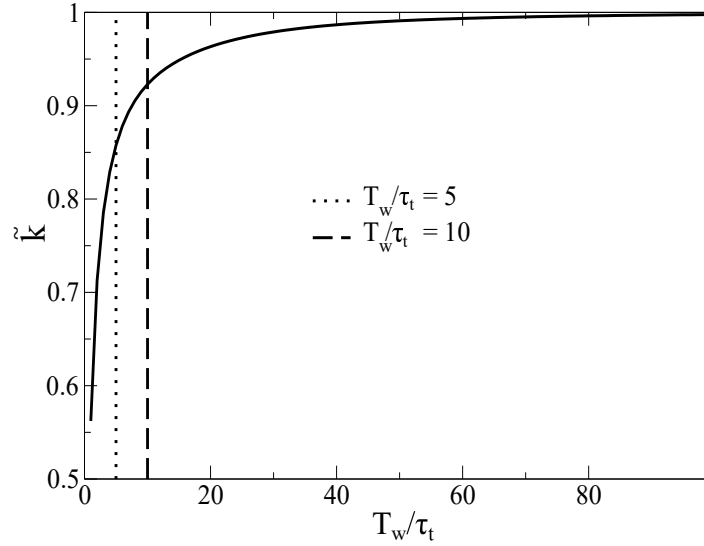


**Fig. 5.5 Synthetic signal:** Evolution of  $\tilde{k}$  for different values of the temporal filter widths.

Figure 5.5 shows the evolution of the turbulent kinetic energy given by Equation (5.25) as function of the filter width. The turbulent kinetic energy increases with the temporal filter width and tends towards the statistical average.

This analysis shows that for a temporal filter width of the order of  $10 \tau_t$ , the underestimation of the turbulent kinetic energy is lower than 10%. An underestimation of 10% appears admissible considering the results that will be shown in Section 5.6.2.1, which show that as long as the underestimation is lower than 30% the impact on the model predictions is not significant.

Therefore, in this work, we have chosen to calculate the temporal filter width as:

$$T_w = 10\tau_t. \quad (5.26)$$

### 5.5.2.2 Adjustment for sinusoidal signals

The goal in this Section is to investigate how well the EWA approximates the phase average in the case of synthetic turbulence superimposed on a sinusoidal signal. This signal was selected as it represents a simple model for cyclic conditions.

To this aim, a signal was generated by superposing the synthetic turbulence signal introduced in Section 5.5.2.1 onto a low frequency sinusoidal signal with a period  $\tilde{T}_0 = 1,000$ . Table 5.1 lists the main specifications of the resulting signal and its time-evolution is shown in Figure 5.6.

Sine frequency	1/1,000
Frequency of the integral scales	1
Sine amplitude $\tilde{U}_{amp}$	10
Turbulence intensity $\sqrt{\frac{2}{3}k}/\tilde{U}_{amp}$	8%

**Table 5.1 Sinusoidal synthetic signal:** Main dimensionless specifications.

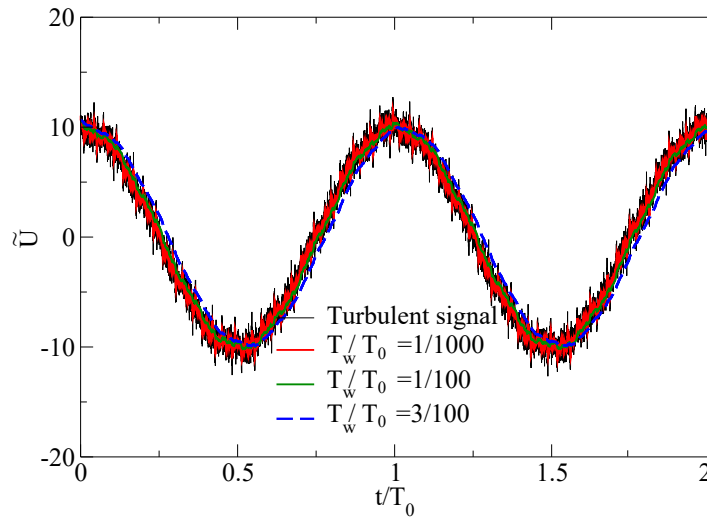


**Fig. 5.6 Sinusoidal synthetic signal:** Time evolution of the sinusoidal synthetic signal and the filtered signal for different temporal filter widths.

EWA is first applied to the signal to approximate its statistical average, which corresponds to the sine. Figure 5.6 shows the time evolution of the filtered signal for three temporal filter widths  $T_w$ . A phase shift and a slight underestimation of the magnitude are observed on the filtered signal when  $T_w$  is increased.

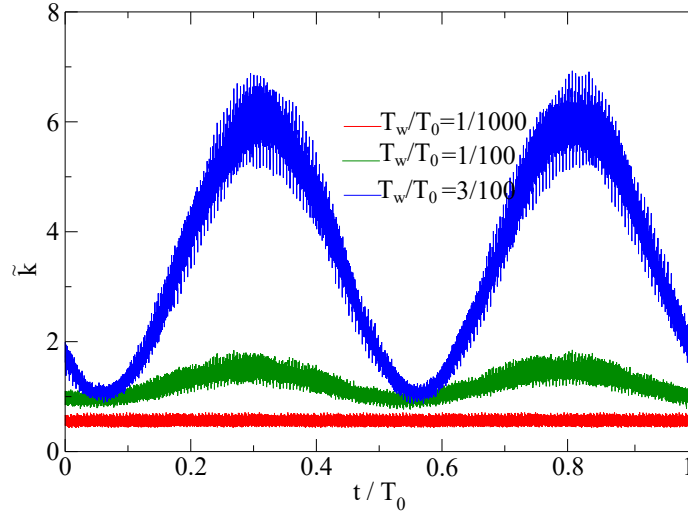


**Fig. 5.7 Sinusoidal synthetic signal:** Phase averaged  $\tilde{k}$  over 100 sine period for different  $T_w$  values.

If a phase average is applied, the signal is decomposed into the average part (the sine) and the fluctuations (the synthetic signal (5.16)). The turbulent kinetic energy of the signal is equal to that of the synthetic signal, which is equal to one. Therefore, applying the EWA to the signal and computing the turbulent energy using (5.25) allows us to evaluate the quality of the approximation of the phase average.

Figure 5.7 shows the time evolution of the turbulent kinetic energy estimated using the filtered velocity for three different filter widths.

For  $\frac{T_w}{T_0} = 1/1000$ , the turbulent kinetic energy is quasi equal to 0.6 all along the cycle. Indeed, the filter width is too short ( $T_w = \tau_t$ ) correctly to filter out turbulent fluctuations, leading to the underestimation of the turbulent kinetic energy as seen in the previous Section. For  $\frac{T_w}{T_0} = 1/100$ , the results show a turbulent kinetic energy that oscillates between 0.9 and 1.4. The observed oscillations are the results of the phase shift induced by EWA. Indeed, the phase shift between the signal and the filtered velocity causes oscillations in the calculation of  $\tilde{U} - \bar{U}$  that enters Equation 5.25. Therefore, a part of the energy of the sinusoidal signal is erroneously counted in the turbulent energy. It is worth noting that the turbulent kinetic energy is relatively well predicted as the temporal filter width is equal to  $10 \times \tau_t$ , which has been shown in Section 5.5.2.1 to be long enough to give an acceptable estimate of the turbulent kinetic energy. For  $\frac{T_w}{T_0} = 3/100$ , the phase shift induced by EWA becomes significantly large, leading to a completely wrong estimation of  $\tilde{U} - \bar{U}$ .

The results show that the use of a filter width of  $\frac{T_w}{T_0} = 1/100$  provides a good compromise between an acceptable estimate of the turbulent kinetic energy and a relatively small phase shift. Nevertheless, it must be noted that the studied case corresponds to an ideal situation to apply EWA, as the turbulent time scale  $\tau_t$  and the sinusoid period  $T_0$  are well separated ( $\frac{T_0}{\tau_t} = 1,000$ ). As an example, a test of EWA on a more stringent case in which the ratio  $\frac{T_0}{\tau_t}$  was only equal to 100 showed that using a filter width equal to  $\frac{T_0}{100}$  resulted in a significant underestimation of the turbulent kinetic energy.

However, in all the cases, a filter width larger than  $T_0/100$  leads to unacceptable results conclude as in Figure 5.7. From this analysis, we found that to keep the phase shift induced by EWA acceptable, an upper bound has to be used for  $T_w$ :

$$\max(T_w) = \frac{T_0}{100}, \quad (5.27)$$

which expresses in ICE using the engine's speed  $\Omega$  in *rpm*:

$$\max(T_w) = \frac{6}{10\Omega}. \quad (5.28)$$

Consequently, the temporal filter width that will be used for cyclic engine flows is:

$$T_w = \min(10\tau_t, \frac{6}{10\Omega}). \quad (5.29)$$

### 5.5.3 Expression of the temporal filter width in EWA-HTLES

The temporal filter-width found in the synthetic turbulent study was chosen for EWA-HTLES:

$$T_w = \min(10\tau_t, \frac{6 \text{ pm}}{10\Omega}). \quad (5.30)$$

The turbulent integral time scale  $\tau_t$  can be calculated using the total turbulent kinetic energy  $k$  and turbulent dissipation rate  $\varepsilon$  as:

$$\tau_t = \frac{k}{\varepsilon}. \quad (5.31)$$

In HTLES, the turbulent dissipation is defined as:

$$\varepsilon = \frac{\beta^* \overline{k_{sfs}}}{T}, \quad (5.32)$$



with:

$$\left\{ \begin{array}{l} k_{res} = \frac{1}{2}(\tilde{U}_i - \overline{U}_i)(\tilde{U}_i - \overline{U}_i) \\ \omega_c = \min\left(\frac{\pi}{dt}, \frac{U_s \pi}{\Delta}\right) \\ U_s = \tilde{U} + \gamma \sqrt{k_{sfs}} \\ \Delta = \max(dx, dy, dz) \end{array} \right. \quad (5.39)$$

The elliptic shielding factor  $\alpha$  is obtained by solving:

$$\alpha - L_{sfs}^2 \nabla^2 \alpha = 1, \quad (5.40)$$

where:

$$L_{sfs} = C_L \max\left(\frac{k_{sfs}^{\frac{3}{2}}}{\varepsilon}, r^{\frac{3}{2}} C_\eta \frac{v^{\frac{3}{4}}}{\varepsilon^{\frac{1}{4}}}\right) \quad (5.41)$$

The set of coefficients of HTLES and the elliptic shielding are listed in Table 5.2.

$\gamma$	$\beta$	$C_L$	$C_\eta$
1	0.667	0.161	80

**Table 5.2** Coefficients of the HTLES approach.

The time-filtered quantities are computed by solving the ordinary following differential equations:

$$\left\{ \begin{array}{l} \frac{d\overline{\tilde{U}_i}}{dt} = \frac{1}{T_w}(\overline{\tilde{U}_i} - \tilde{U}_i) \\ \frac{d\overline{k_{sfs}}}{dt} = \frac{1}{T_w}(\overline{k_{sfs}} - k_{sfs}) \\ \frac{d\overline{k_{res}}}{dt} = \frac{1}{T_w}(\overline{k_{res}} - k_{res}) \\ \frac{d\overline{\omega}}{dt} = \frac{1}{T_w}(\overline{\omega} - \omega) \end{array} \right. \quad (5.42)$$

The temporal filter width expresses as:

$$T_w = \min\left(10 \frac{T}{\beta^* r}, \frac{6}{10\Omega}\right). \quad (5.43)$$

The subfilter viscosity expresses as:

$$\nu_{sfs} = \frac{a_1 k_{sfs}}{\max(a_1 \omega, F_2 S)} \quad (5.44)$$

All parameters and coefficients of the  $k - \omega$  SST RANS model can be found in Appendix 8.2.

## 5.6 Validation of EWA-HTLES on stationary configurations

Before applying EWA-HTLES to cyclic ICE flows, it is important to validate the approach in stationary flows and to compare the results with those of the original HTLES in order to verify that the modifications introduced to the model do not degrade its predictions. For this purpose, EWA-HTLES was validated in two stationary configurations: The Channel Flow at  $Re_\tau = 1,000$ , and the flow in a cylinder over a fixed valve with an abrupt expansion, the so-called steady flow rig [127]. For each configuration, the results yielded by EWA-HTLES are compared with the original HTLES (HTLES AVG). The modeled turbulence is examined by analyzing resolved turbulent quantities, and the predictions of the model are validated by comparing them to the reference data.

### 5.6.1 Simulation set-up

All simulations in this Chapter use the same set-up described hereafter.

#### 5.6.1.1 Numerical configuration

All simulations, RANS, HTLES and LES, use the same numerical parameters and meshes in order to compare solely the impact of the turbulence model on the simulation results. The set of the numerical parameters used for the simulations is summarized in Table 5.3. Definitions of these parameters are detailed in Section 4.3.2.1.

Temporal scheme	First-order implicit Euler
Convective and acoustic CFL	0.7, 50
Fourier number	2
Convective scheme	Second-order central differencing scheme
Flux limiter	Step at 0.1

**Table 5.3 Stationary configurations:** Set of the numerical parameters used for RANS, HTLES and LES.

### 5.6.1.2 Turbulence modeling

Four turbulence models are used in what follows. Table 5.4 lists the turbulence models used for each turbulence modeling approach. For HTLES, the simulations were performed using EWA-HTLES and HTLES AVG which is detailed in Section 4.3.

RANS	$k-\omega$ SST [88]
HTLES	EWA-HTLES and HTLES AVG [129]
LES	$\sigma$ sub-grid model [97]

**Table 5.4 Stationary configurations:** Turbulence models used for RANS, HTLES and LES.

### 5.6.1.3 Wall boundary conditions

In order to avoid the resolution of thermal and aerodynamic boundary layers, wall functions are used. The shear stress is calculated using the automatic wall-functions [86] for RANS and HTLES, and the Werner and Wengle wall-functions [131] for LES. The heat transfer is calculated using the O'Rourke wall-functions [47].

## 5.6.2 Channel Flow

The present section provides the validation of EWA-HTLES in the Channel Flow at  $Re_\tau = 1,000$ . Details of the configuration and the initialization are provided in Section 4.4.2. First, Section 5.6.2.1 examines the sensitivity of HTLES predictions to the model inputs. Section 5.6.2.2 provides an analysis of EWA. Then, the results of EWA-HTLES are compared to those obtained by HTLES AVG.

### 5.6.2.1 Preliminary investigation on the sensitivity of the HTLES results to the model inputs

In previous Sections, it was shown that the use of EWA to approximate the statistical average can lead to underestimate the turbulent energy. The present Section focuses on the impact of underestimating  $k$  on the simulation predictions. This may be, for example, a scenario in which EWA hardly filters the turbulent fluctuations (see Section 5.5.2.1).

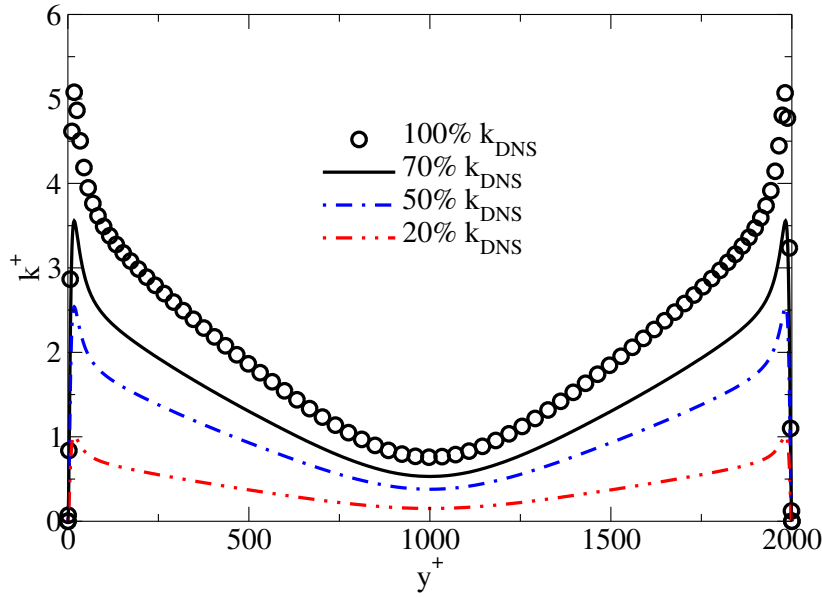


**Fig. 5.8 Channel Flow:** Profiles of the imposed turbulent kinetic energy over the wall-distance.

The underestimation of  $k$  is reproduced hereafter by imposing four different fields of  $k$  in the HTLES Equations (5.37) and (5.38):

$$\left\{ \begin{array}{l} T = \frac{r}{1 + \left(\frac{C_{\varepsilon 2}}{C_{\varepsilon 1}} - 1\right)\left(1 - r\frac{C_{\varepsilon 1}}{C_{\varepsilon 2}}\right)} \frac{k}{\varepsilon} \\ r = \min\left(1, (1 - \alpha^2) + \alpha^2 \frac{1}{\beta} \left(\frac{U_s}{\sqrt{k}}\right)^{\frac{2}{3}} \left(\frac{\omega_c k}{\varepsilon}\right)^{-\frac{2}{3}}\right) \end{array} \right. \quad (5.45)$$

The first simulation, chosen as the reference, uses the turbulent kinetic energy profile given by DNS. The other three simulations use respectively 70%, 50%, and 20% of the turbulent kinetic energy of the DNS. The profiles over the wall-distance of  $k$  for each scenario are shown in Figure 5.8. Four simulations using the presented profiles, respectively, for  $k$  have been performed, and their results are analyzed in the following.

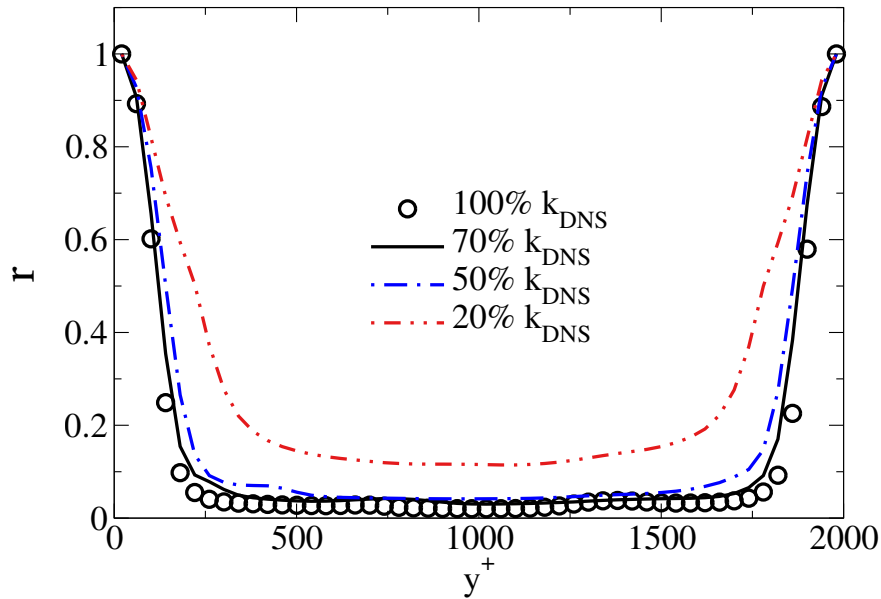


**Fig. 5.9 Channel Flow:** Profiles of the energy ratio  $r$  along the wall-distance predicted by HTLES for the four different imposed profiles of  $k$ .

Profiles of the energy ratio  $r$  over the wall-distance obtained by each simulation are compared in Figure 5.9. In the simulation using  $k = 100\% k_{DNS}$ , the energy ratio is equal to one at the walls and decreases considerably with the wall-distance until reaching its minimum values in the core region. The predictions given by the simulation using  $k = 70\% k_{DNS}$  show almost no difference compared to results obtained with  $k = 100\% k_{DNS}$ . Slight differences starts to be observed when using  $k = 50\% k_{DNS}$  featuring a slight overestimation of the energy ratio  $r$ . The results are significantly deteriorated when using  $k = 20\% k_{DNS}$ , where the energy ratio is significantly overestimated almost everywhere.

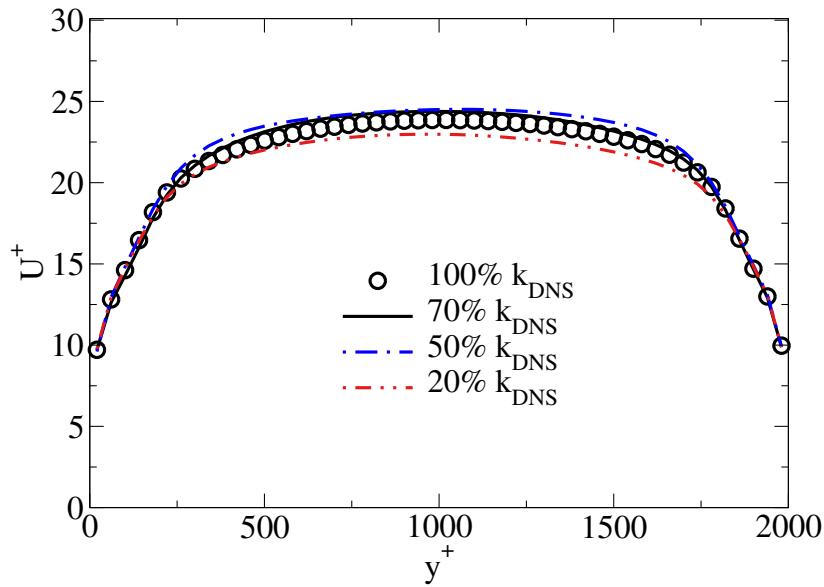


**Fig. 5.10 Channel Flow:** Profiles of the mean axial velocity  $U^+ = \frac{\bar{U}_x}{u_\tau}$  along the wall-distance predicted by HTLES for the four different imposed profiles of  $k$ .

The profiles of the mean axial velocity predicted by the four simulations are shown in Figure 5.10. The four simulations give an almost similar velocity profile near the wall for  $y^+ < 500$  and  $y^+ > 1500$ . In the core region, the predictions of the simulations using  $k = 70\% k_{DNS}$  and  $k = 100\% k_{DNS}$  are fairly similar, while the simulations using  $k = 50\% k_{DNS}$  and  $k = 20\% k_{DNS}$  slightly misestimate the mean velocity magnitudes.

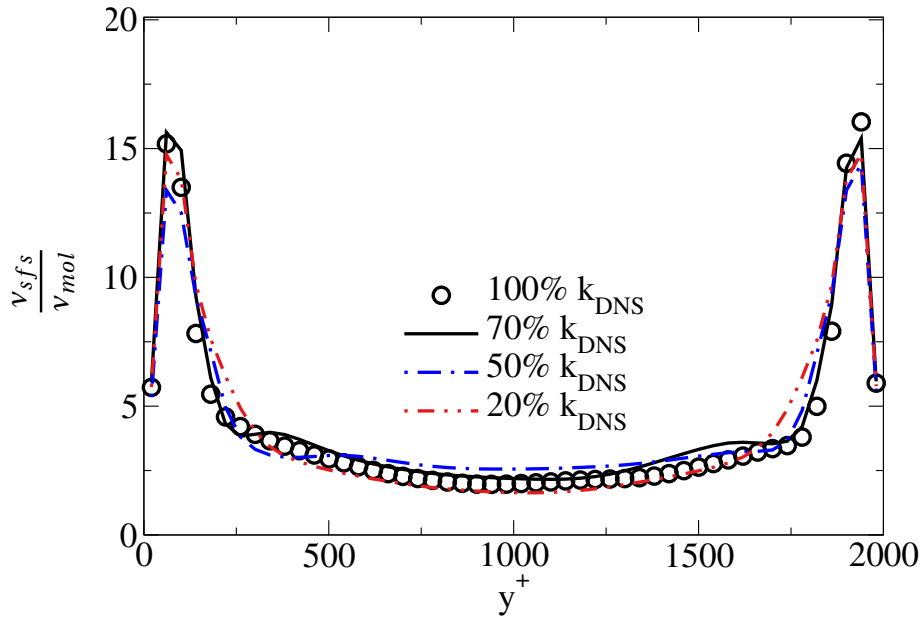


**Fig. 5.11 Channel Flow:** Profiles of the mean viscosity ratio along the wall-distance predicted by HTLES for the four different imposed profiles of  $k$ .

Figure 5.11 shows the profiles of the ratio of the modeled viscosity to the molecular viscosity obtained by the four simulations. As expected, the viscosity ratio increases in the near-wall regions and decreases at the walls according to the RANS mode. The viscosity ratio for  $y^+ < 100$  and  $y^+ > 1900$  is predicted quite similarly by all four simulations, as the elliptical shielding enforces RANS in this region and all simulations tend toward the  $k - \omega$  SST RANS model at the walls. The mean viscosity ratio away from the walls decreases significantly and is quite similar between the four simulations, in spite of the significant differences in  $r$  and  $k$  used as the model inputs.

The four simulations show that the results are very slightly dependent on the total turbulent kinetic energy used in the inputs. The extreme case of underestimating the total turbulent kinetic energy by 80% resulted in major overestimation of the energy ratio. Despite this, the impact is not as significant on the mean axial velocity predictions, which remains relatively similar to the other simulations. The velocity profiles are predicted relatively better in the simulations using 50%, 70% of  $k_{DNS}$ , showing almost similar predictions to the reference simulation using 100%  $k_{DNS}$ . Finally, the impact is minimal on the viscosity ratio predictions, which are quite similar between the four simulations.

These results show that the exact calculation of the total turbulent kinetic energy  $k$  does not have a significant impact on the results. Therefore, even the application of EWA

instead of the statistical average only provides an estimate of  $k$ , HTLES predictions are not significantly affected by the use of EWA.

### 5.6.2.2 Analysis of the temporal filter

The EWA used in EWA-HTLES is analyzed in the following by examining its filter width and the resulting time-filtered velocity.

As the configuration is stationary, the upper limit introduced for cyclic flows is not used (see Equation (5.30)). However, at any simulation time  $t$ , an upper limit has been added to  $T_w$  to avoid giving too much weight to the arbitrary initial conditions:

$$T_w(t) = \min\left(10\frac{T}{\beta^* r}, t\right). \quad (5.46)$$

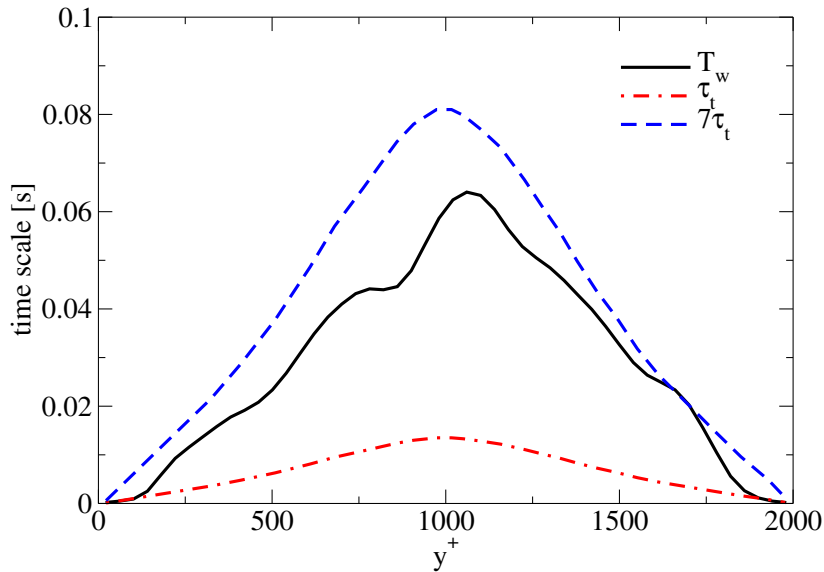


**Fig. 5.12 Channel Flow:** Comparison of the profile of an instantaneous temporal filter-width  $T_w$  with the turbulence integral time scales.

Figure 5.12 compares profiles of  $T_w$  and the turbulence integral time scale  $\tau_t$  estimated from a RANS simulation. The profile of  $T_w$  fluctuates slightly as it is computed from the instantaneous resolved fields. The resulting values are quite similar to the values indicated by  $7 \times \tau_t$ , which has been proven in the analysis of the synthetic signal in Section 5.5.2.1 to give acceptable estimates of statistical averages. This is verified in the following by

comparing the time-filtered axial velocity to the statistically averaged axial velocity shown in Figure 5.13

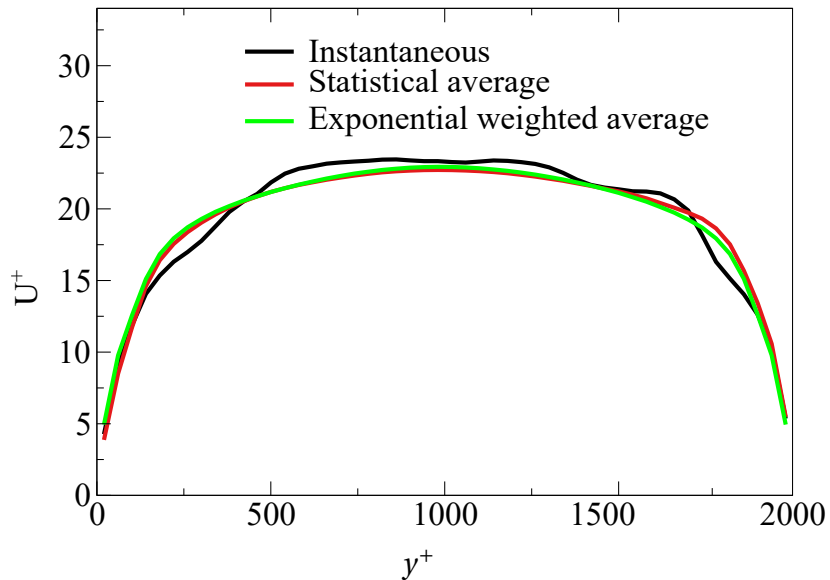


**Fig. 5.13 Channel Flow:** Comparison of the profiles of the instantaneous, the time-filtered and the statistical average axial velocities over the wall-distance

The results show that EWA provides a time-filtered velocity profile almost similar to the one given by the statistical average.

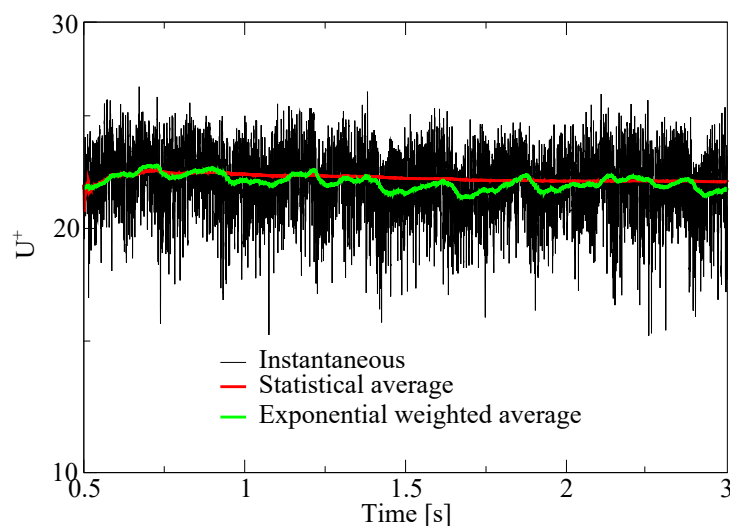


**Fig. 5.14 Channel Flow:** Time evolution at a monitoring point located at half height of the channel of the instantaneous, the time-filtered and the statistically averaged axial velocities.

Figure 5.14 shows the time evolution at mid-channel height of each of the above velocities. It can be observed that EWA filters out a significant part of the turbulent fluctuations. A small part of the turbulent fluctuations remains in the time-filtered velocity as the filter width of the temporal filter is not sufficiently large.

### 5.6.2.3 Comparison with the original HTLES

The predictions of EWA-HTLES are now assessed by comparing its results with DNS data and results given by HTLES AVG.

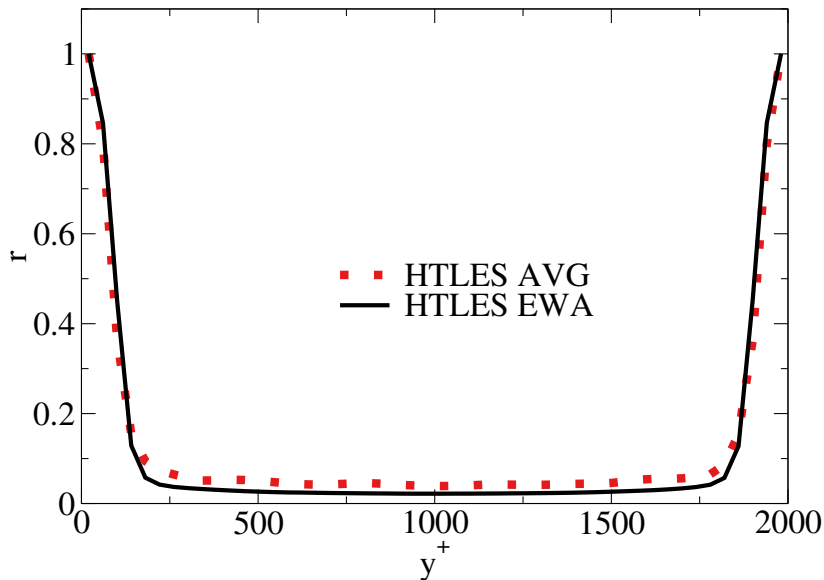


**Fig. 5.15 Channel Flow:** Comparison of the profiles of the energy ratio  $r$  over the wall-distance yielded by EWA-HTLES and HTLES AVG.

First of all, HTLES AVG and EWA-HTLES results are compared by studying their predictions of energy ratio profiles, as shown in Figure 5.15. Both simulations prescribe an energy ratio  $r$  of one at the walls. The energy ratio decreases similarly with the wall-distance, ensuring a similar transition from RANS to LES for the two simulations. In the central region, the energy ratio values remain very similar for the two simulations, even if HTLES AVG gives slightly higher values.

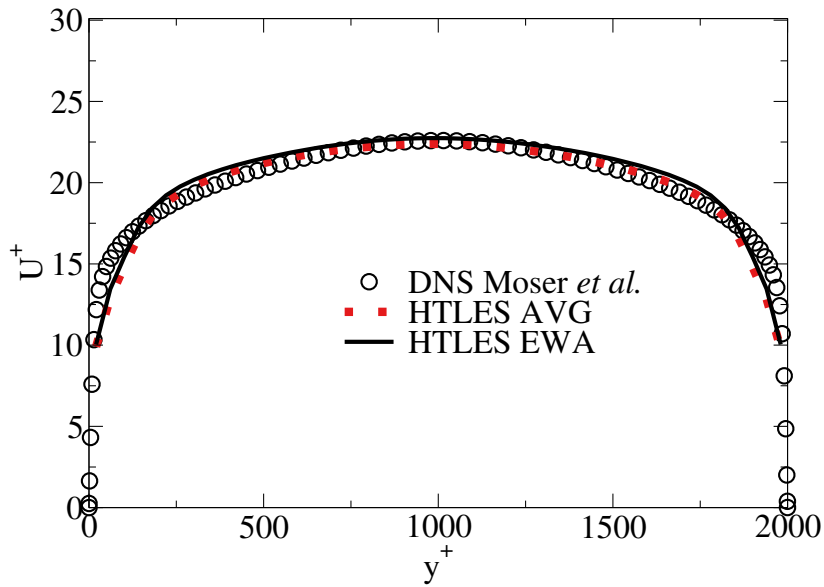


**Fig. 5.16 Channel Flow:** Comparison of the profiles the dimensionless axial velocity  $\frac{\bar{U}_x}{u_\tau}$  over the wall-distance yielded by DNS, EWA-HTLES and HTLES AVG.

Figure 5.16 compares the mean axial velocity profile yielded by DNS, and HTLES AVG and EWA-HTLES. As expected, both simulations yield very similar predictions which are in good agreement with DNS.

	DNS	HTLES AVG	EWA-HTLES
Flow rate [ $m^3/s$ ]	0.71	0.70	0.71
Relative error $\varepsilon_D$ [%]	-	-1.4	0.0

**Table 5.5 Channel Flow:** Flow rates yielded by DNS and HTLES.

The flow rates shown by each simulation are listed in Table 5.5. They indicate that the two simulations yield almost the same flow rate as DNS with a relative error of  $-1\%$  and  $-0\%$ , respectively.

The results of EWA-HTLES and HTLES AVG are similar, showing that the use of EWA had almost no effect on HTLES' predictions in this case. The next Section focuses on a similar comparative study but in a stationary configuration closer to the engine configurations.

### 5.6.3 Steady Flow Rig

#### 5.6.3.1 Configuration

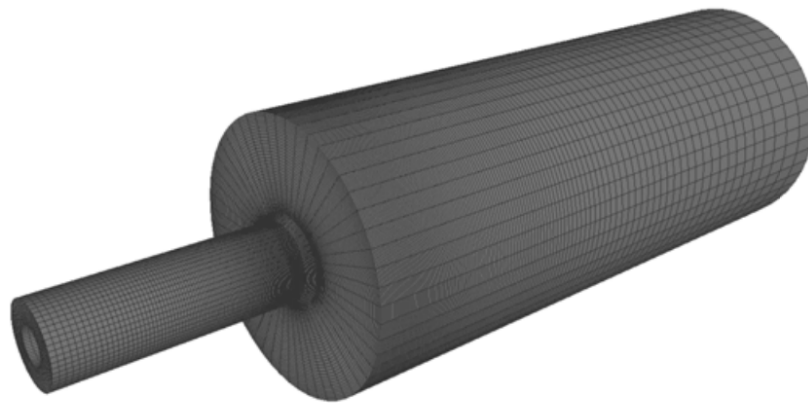


Fig. 5.17 Steady Flow Rig: Computational domain.

The steady flow rig represents a simplified in-cylinder flow around a valve with a fixed lift. The gas is injected in the intake port, which consists of a cylinder and a fixed valve placed axisymmetrically inside the jet nozzle. The flow exiting through the valve opening, a jet flow separates giving rise to a recirculating flow. The computational domain is depicted in Figure 5.17 and an overview of the geometry with its dimensions is illustrated in Figure 5.18.

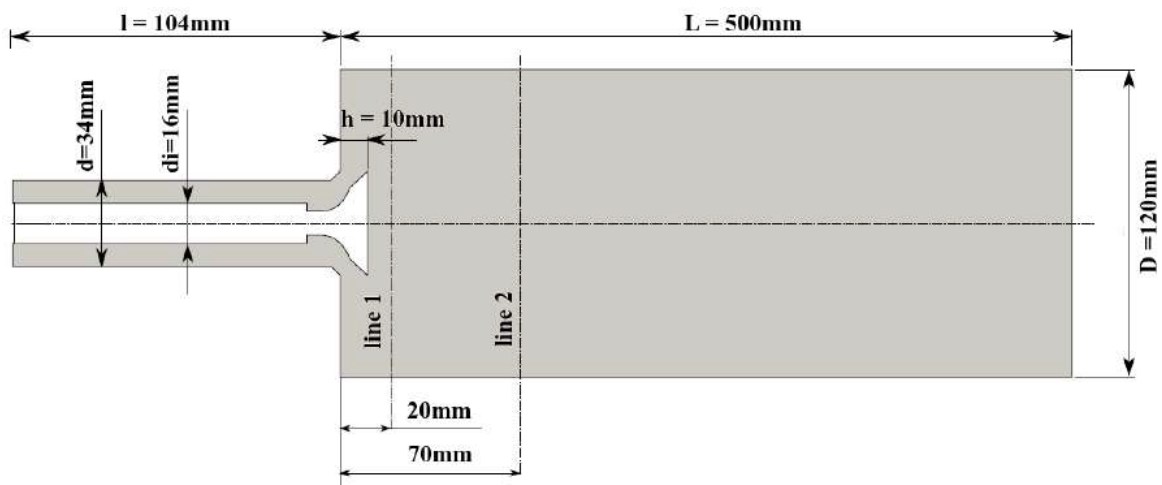
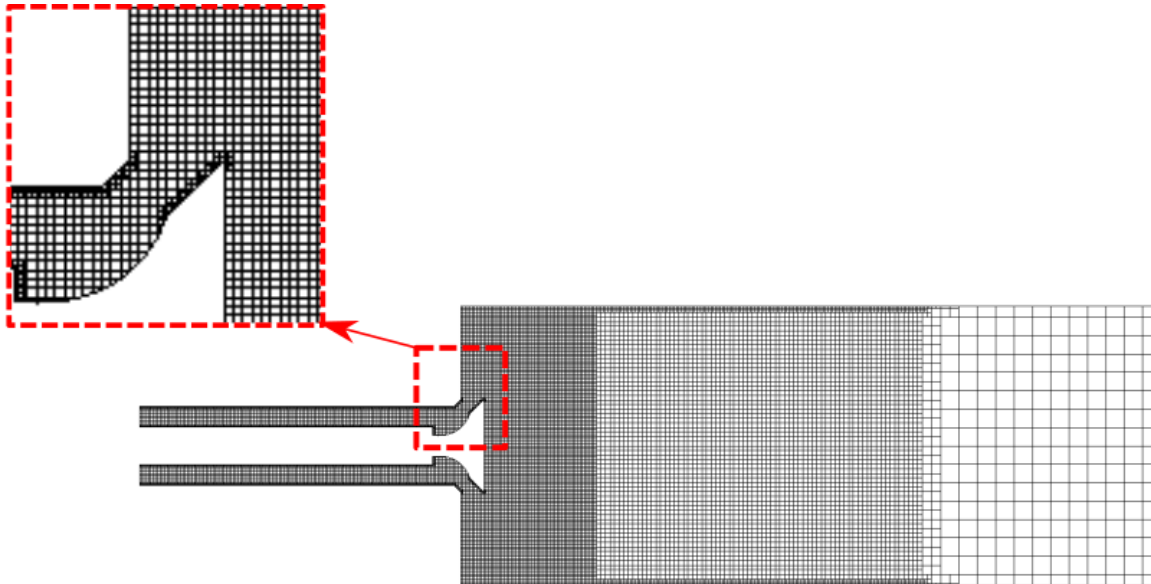


Fig. 5.18 Steady Flow Rig: Schematic and geometrical parameters.

Working Gas	$N_2$
Gas Temperature	300 K
Reynolds number $Re_D$	30,000
Mass Flow rate	$0.06 \text{ kg}\cdot\text{s}^{-1}$
Static pressure at the exit	1 bar

**Table 5.6 Steady Flow Rig:** Main specifications.

Laser Doppler Anemometry (LDA) measurements were investigated by Thobois *et al.* [127], which provide the mean and RMS for axial as well as radial velocity along profiles located 20 and 70 millimeters from the abrupt expansion (see Figure 5.18).



**Fig. 5.19 Steady Flow Rig:** Cut-plane of the hexahedral mesh.

The mesh is composed of 1,402,628 cells. It is generated using hexahedra far from the walls, while the cells near the walls are cut by the outer surface of the geometry using the cut-cell technique [120]. Figure 5.19 shows a cut-plane in the central plane of the resulting mesh: the grid step in the core of the domain is 2 mm; a refinement of 1 mm is embedded at the inlet pipe and the head of the valve where the jet develops; at the outlet a coarse grid size of 8 mm is used as a sponge layer to avoid the reflection of acoustic waves inside the chamber. At the walls, the grid resolution is refined in such a way that the wall distance is less than 100 in wall units.

The boundary conditions were imposed in accordance with the experimental conditions listed in Table 5.6. At the inlet, a constant flat velocity profile with  $U_{bulk} = 65 m \cdot s^{-1}$  is imposed so that the experimental mass flow rate is recovered. The static pressure is imposed at the outlet.

For RANS and LES, the flow fields were initialized with the working gas at rest at a pressure of 1 *bar* and a temperature of 300 *K*. In RANS,  $k$  and  $\omega$  were initialized with zero fields. The final RANS solution was used to initialize the flow fields in HTLES. The energy ratio  $r$  and the time scale  $T$  were initially computed by using RANS flow fields.

A physical time of 2 *s* was simulated. For each simulation, a transient phase of  $t = 0.3$  *s* is performed during which the initial conditions are driven out from the computation domain, this phase duration is equivalent to 8 flow through times; then the statistics for RANS, HTLES and LES are collected during a period of 44 flow through times which is equivalent to 1.7 *s*.

### 5.6.3.2 Results

Results of the simulations are provided in three parts. First, EWA-HTLES is validated by comparing its results with the ones predicted by HTLES AVG. Second, Section 5.6.3.2 gives a more detailed analysis of how turbulence is modeled by EWA-HTLES. Then, the last part compares the flow predictions of EWA-HTLES with the LDA measurements and RANS and LES results.

#### Validation of EWA-HTLES

The EWA-HTLES is validated in the following by comparing its predictions in terms of RMS and mean velocity, and pressure with the experimental data and HTLES AVG results.

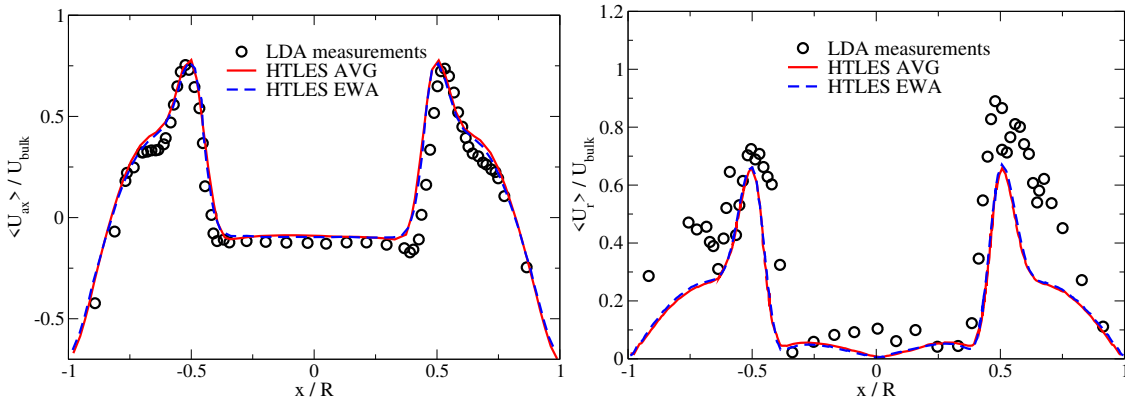


**Fig. 5.20 Steady Flow Rig:** Comparison of the dimensionless mean velocity yielded by LDA measurements, EWA-HTLES and HTLES AVG along *line 1*. -**Left:** Axial component. -**Right:** Radial component.

The mean axial and radial velocity profiles along *line 1* yielded by EWA-HTLES and HTLES AVG are compared with LDA measurements in Figure 5.20. For the axial component, the profiles of the two simulations are quasi identical showing good prediction in comparison with LDA measurements in terms of the profile and magnitude of the near wall velocity. In the core region ( $-0.5 < x/R < 0.5$ ), the magnitude of the velocity predicted by the two simulations is very close to the experimental data. For the radial component, the results of the two simulations remain very similar. The experimental results close to the walls give scattered data, which makes it difficult to make a comparison with the predictions of the simulations. Nevertheless, the latter quite well reproduce the experimental results out of this region.

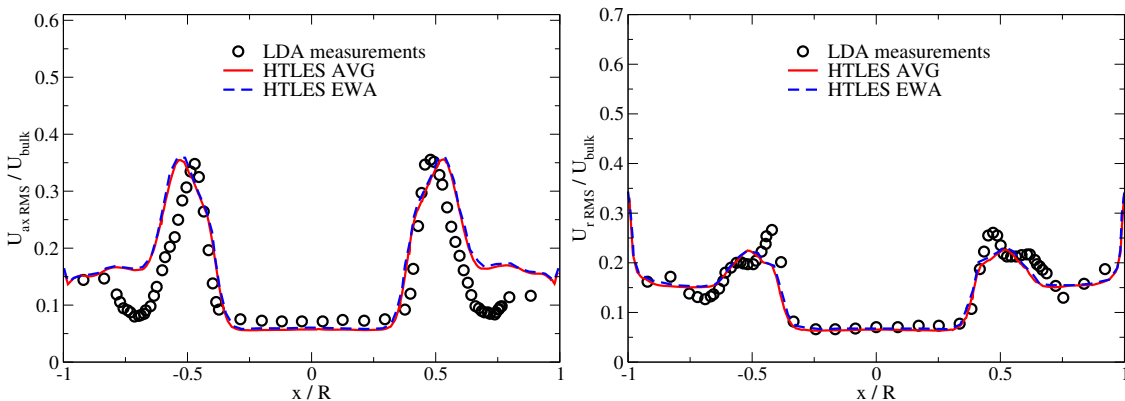


**Fig. 5.21 Steady Flow Rig:** Comparison of dimensionless RMS velocity yielded by LDA measurements and EWA-HTLES and HTLES AVG along *line 1*. -**Left:** Axial component. -**Right:** Radial component.

Profiles of the axial and radial RMS velocity along *line 1* are compared with LDA measurements in Figure 5.21. For the axial component, the two simulations slightly overestimate the RMS magnitude near the walls. The peak at  $|x/R| \approx 0.5$  shown in the experimental data is well predicted by the two simulations and the predictions in the core region ( $-0.5 < x/R < 0.5$ ) are very similar to LDA measurements. The two simulations give better predictions of the radial RMS component, except the peak at  $|x/R| \approx 0.5$  which is missed by the two simulations.

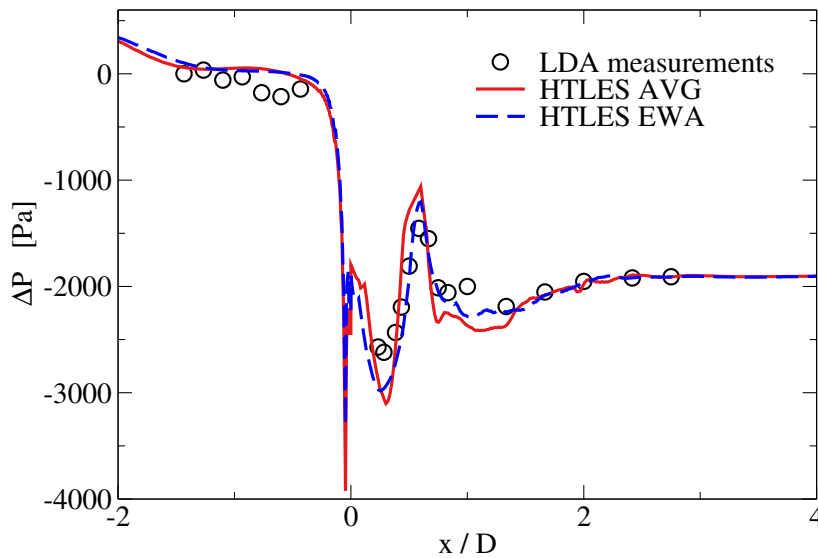


**Fig. 5.22 Steady Flow Rig:** Comparison of the static pressure over the axial distance  $x$  yielded by the experiment and EWA-HTLES and HTLES AVG.

Figure 5.22 shows the axial profile of the static pressure at the wall at  $t = 2$  s. Both simulations reproduce quite well the stiff pressure decrease at  $x = 0$  due to the sudden expansion, and the recirculation zone featured by a slight pressure increase at  $x/D = 1$ . Some slight differences between the two simulations are observed for  $x/D > 0$ , but they are believed to be related to the instantaneous turbulent fluctuations. Analysis of the pressure drop between the position downstream the valve and the outlet domain is provided in Section 5.6.3.2.

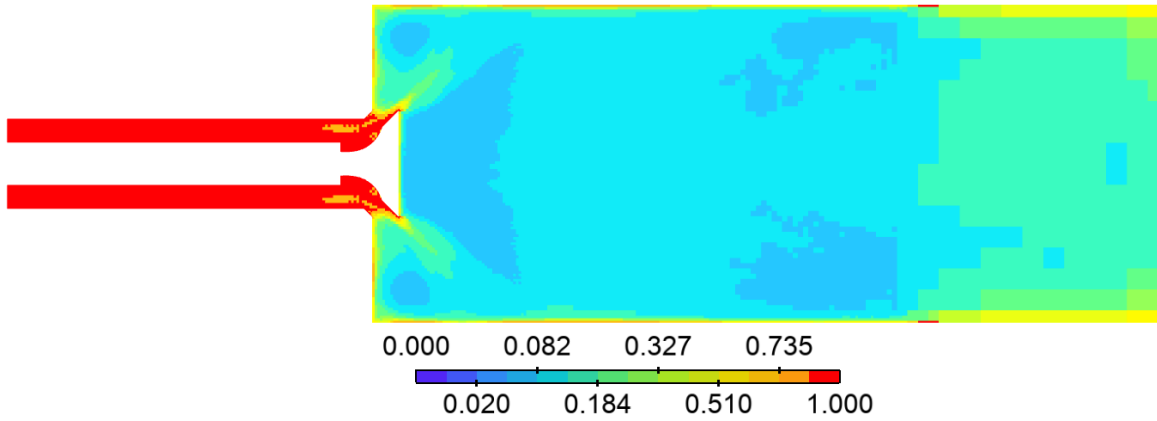
### Modeled turbulence in EWA-HTLES

The turbulence modeling in EWA-HTLES is examined hereafter by analyzing the subfilter turbulent kinetic energy, the resolved velocity field and the modeled RMS velocity yielded by the model.

First of all, the amount of the turbulent kinetic energy that is modeled by EWA-HTLES is assessed by examining the ratio of the mean subfilter to the total turbulent kinetic energy  $\frac{\overline{k_{sfs}}}{k}$ .  $\overline{k_{sfs}}$  corresponds to the subfilter kinetic energy yielded by the HTLES  $k$ -equation which was statistically averaged for in the post processing, and the total turbulent kinetic energy  $k$  is post-processed from the mean of the resolved velocity  $\overline{\tilde{U}_i}$  as:

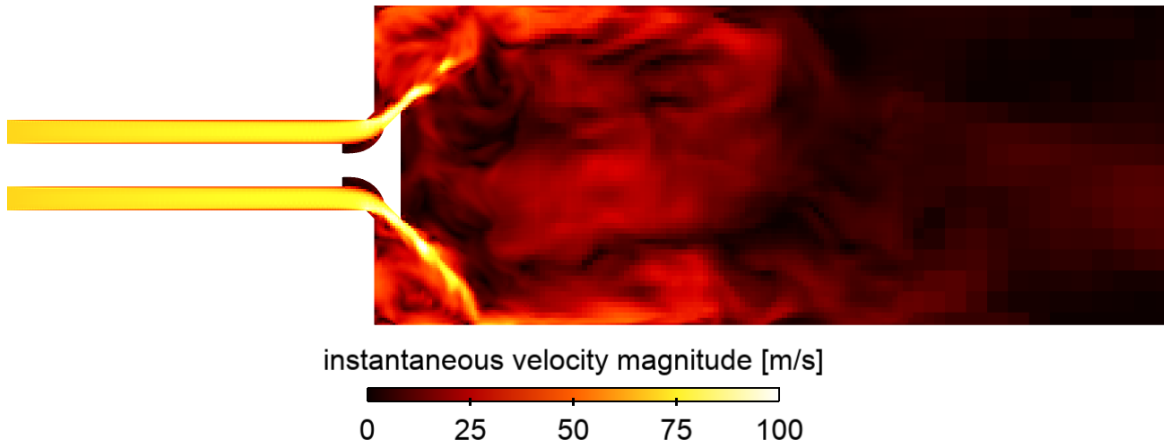
$$\begin{cases} k = \overline{k_{sfs} + k_{res}} \\ k_{res} = \frac{1}{2}(\tilde{U}_i - \overline{\tilde{U}_i})(\tilde{U}_i - \overline{\tilde{U}_i}) \end{cases}, \quad (5.47)$$

This is therefore the "observed" energy ratio, which is, as explained above, to be distinguished from the "target" ratio  $r$ , that enters the model equations.



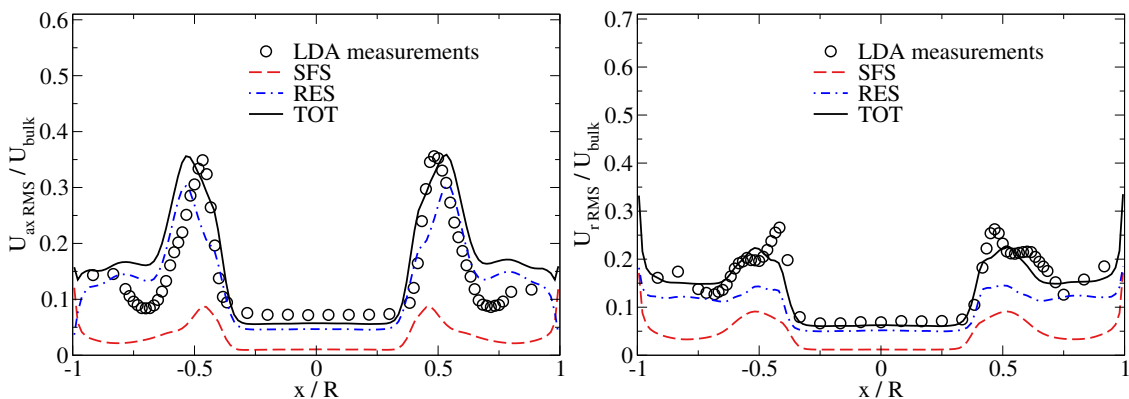
**Fig. 5.23 Steady Flow Rig:** Contours of the mean subfilter to the total turbulent kinetic energy  $\frac{\overline{k_{sfs}}}{k}$  in the central plane yielded by EWA-HTLES.

Figure 5.23 shows the contours of  $\frac{\overline{k_{sfs}}}{k}$  in the central plane. In the upstream pipe,  $\frac{\overline{k_{sfs}}}{k}$  is equal to unity showing that all the turbulent fluctuations are modeled, i.e.,  $k_{res} = 0$ , (RANS). Downstream the valve, the flow separates and is dominated by large turbulent scales. Therefore, EWA-HTLES reduces the amount of the modeled turbulent fluctuations in the core region to less than  $\frac{\overline{k_{sfs}}}{k} < 0.2$  allowing to perform LES.  $\frac{\overline{k_{sfs}}}{k}$  increases slightly to 0.3 at the exit of the domain where the mesh is coarsened, showing that the model switches to VLES (VLES being defined here as a coarse LES for which  $\frac{\overline{k_{sfs}}}{k} > 0.2$ ). At the walls, even if the elliptic shielding enforces the target energy ratio  $r$  to 1, around 50% of the turbulent kinetic energy is still resolved. This is related to the flow resolved in the core in LES, which penetrates the near-wall region.



**Fig. 5.24 Steady Flow Rig:** Instantaneous contours of the velocity magnitude computed in EWA-HTLES at  $t = 2$  s

The contours of the instantaneous velocity magnitude predicted by EWA-HTLES are illustrated in Figure 5.24. As expected, the instantaneous velocity is congruent with the  $\frac{k_{sfs}}{k}$  contours. The resolved field is smooth and fairly similar to RANS within the upstream pipe, while the resolved field is fluctuating in the downstream region which confirms that a significant part of the turbulent fluctuations is solved.



**Fig. 5.25 Steady Flow Rig:** Decomposition of the dimensionless RMS velocity along *line 1* into two components, *RES* the resolved part and *SFS* the modeled part. **-Left:** axial RMS velocity. **-Right:** radial RMS velocity.

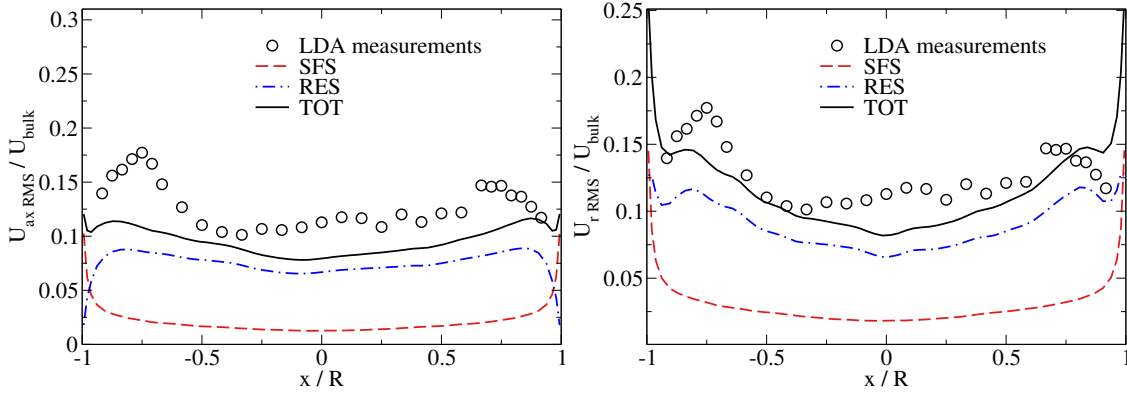


**Fig. 5.26 Steady Flow Rig:** Decomposition of the dimensionless RMS velocity along *line 2* into two components, *RES* the resolved part and *SFS* the modeled part. **-Left:** axial RMS velocity. **-Right:** radial RMS velocity.

To further examine the turbulent fluctuations, profiles of the RMS velocity for both axial and radial components along *line 1* and *line 2* are decomposed into the resolved and sub-filter parts, respectively, in Figures 5.25 and 5.26:

- the resolved RMS velocity fluctuations calculated from the resolved velocity  $\tilde{U}_i$  as:

$$u_{i\ RMS}^{(res)} = \sqrt{(\tilde{U}_i - \bar{\tilde{U}}_i)(\tilde{U}_i - \bar{\tilde{U}}_i)}. \quad (5.48)$$

- the subfilter RMS velocity estimated using the Boussinesq hypothesis:

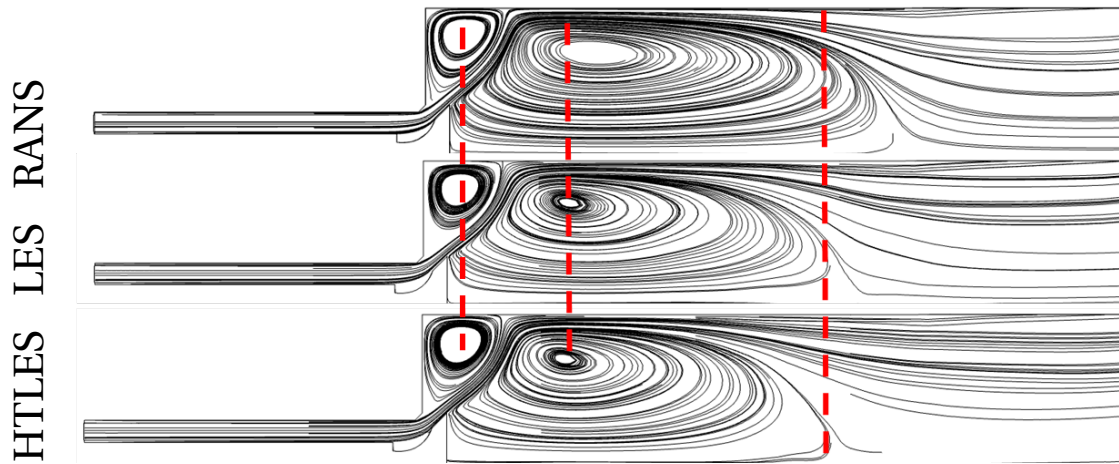
$$u_{i\ RMS}^{(sfs)} = \sqrt{-2\nu_{sfs} \frac{\partial \tilde{U}_i}{\partial x} + \frac{2}{3} k_{sfs}}, \quad (5.49)$$

where  $i$  is either  $ax$  for the axial or  $r$  for the radial component.

For both the axial and radial RMS components, the profiles show sub-filter fluctuations increase at the walls and decrease in the core region featuring magnitudes that remain non negligible compared to the resolved ones. The plots of the resolved RMS velocities show that the axial component vanishes at the wall along both *lines 1* and *2*, as expected. However, the radial component surprisingly does not vanish at the wall along both lines. The same issue was observed in RANS and LES simulations, pointing whether a difficulty of the code to impose velocities tangential to the walls.

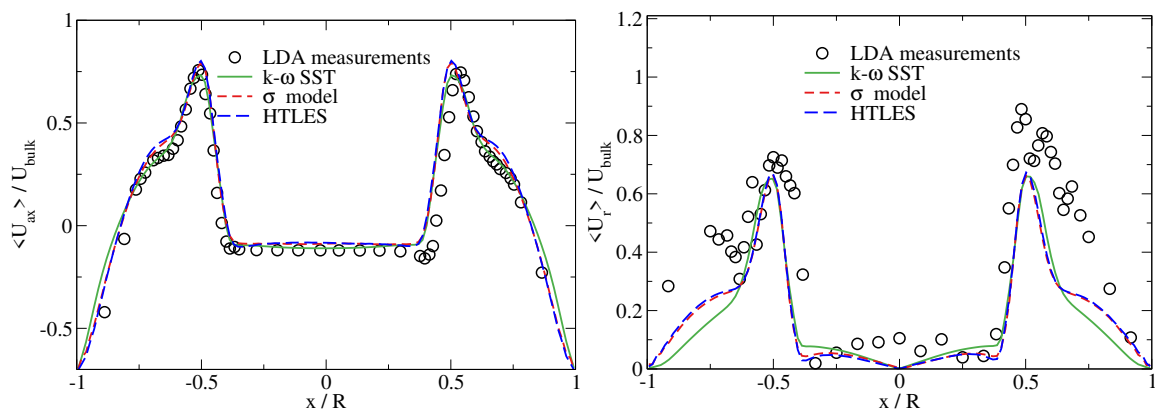
### Comparison with RANS and LES

The predictions in terms of RMS and mean velocity given by HTLES, RANS and LES are compared hereafter with the experimental data.



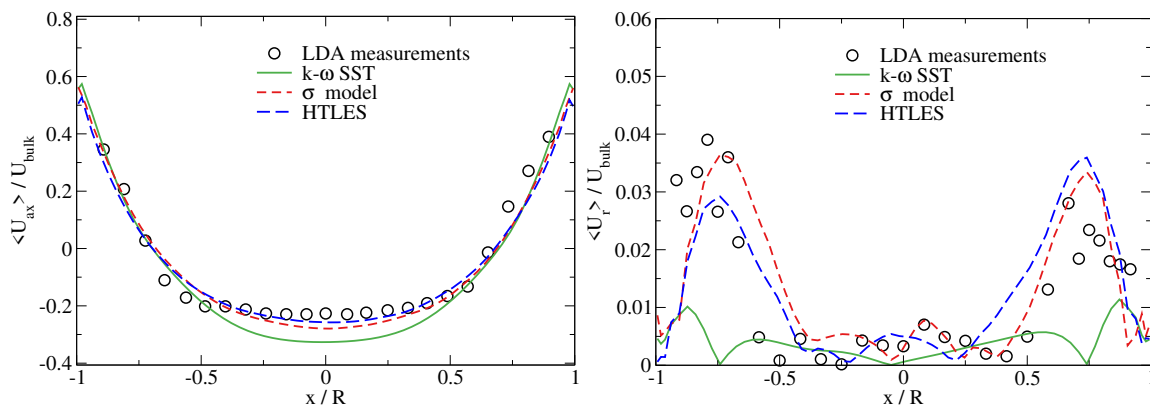
**Fig. 5.27 Steady Flow Rig:** Cut plane of the mean streamlines obtained with RANS, LES and HTLES.

Figure 5.27 shows a section at the center of the computational domain of the mean streamlines for RANS, LES and HTLES. A pipe flow develops upstream of the valve. The three simulations similarly reproduce the topology of the first recirculation region, with the same center location identified by a dashed line. Nevertheless, RANS predicts the second recirculation longer than for LES and HTLES, which show fairly similar predictions. Comparison of the mean velocity profiles along *line 1* and *line 2* (see Figure 5.18) yielded by the simulations and LDA measurements analyzed next will determine which simulation is closest to the experiment.



**Fig. 5.28 Steady Flow Rig:** Comparison of dimensionless mean velocity along *line 1* yielded by LDA measurements and RANS, HTLES and LES. **-Left:** axial component. **-Right:** radial component.

Profiles of the axial and radial mean velocity along *line 1* given by LDA measurements, and RANS, HTLES and LES are compared in Figure 5.28. All the simulations give fairly similar profiles of the axial velocity at this location. The velocity magnitudes and the shape of the profiles are in good agreement with the experiment. Differences between the simulations can be observed on the radial velocity profiles. HTLES and LES show similar radial profiles and provide a good prediction of the radial velocity profiles within the recirculation region ( $0.5 < \frac{r}{R} < 0.5$ ), whereas RANS underestimates the radial velocity within the recirculation. The experimental data exhibit high a significant scatter at this location, hence no clear conclusion can be drawn regarding velocity magnitudes.



**Fig. 5.29 Steady Flow Rig:** Comparison of dimensionless mean velocity along *line 2* yielded by LDA measurements and RANS, HTLES and LES. **-Left:** axial component. **-Right:** radial component.

The mean averaged velocity profiles along *line 2* are compared in Figure 5.29. Similar axial velocity profiles are obtained in HTLES and LES, which are in good agreement with the experiment data. RANS overestimates the axial velocity in the central region where  $-0.5 < \frac{r}{R} < 0.5$ , showing that the larger recirculation is predicted in RANS. For the radial component, one can notice the small velocity magnitudes at this location. Despite the axisymmetric configuration, both experimental and simulation data are not fully symmetrical. The asymmetry in experimental data can be related to an intrinsic uncertainty of the measurement device due to the small velocity magnitudes, while the asymmetry in the simulations can be related to insufficiently converged statistics. HTLES and LES still provide results fairly similar to the experimental data, whereas RANS underestimates the radial velocity at this location.

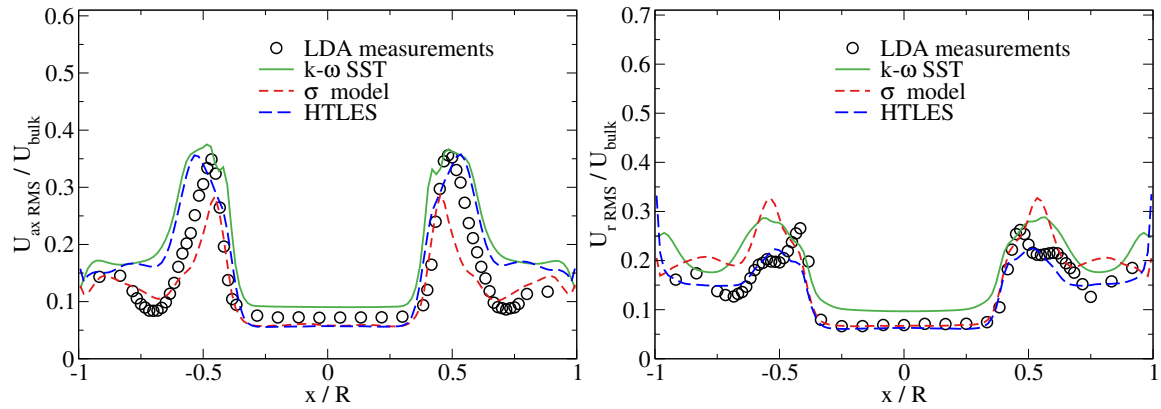


**Fig. 5.30 Steady Flow Rig:** Comparison of dimensionless RMS velocity along *line 1* yielded by LDA measurements and RANS, HTLES and LES. - **Left:** axial component. - **Right:** radial component.

rms velocity results are compared hereafter. RANS results are obtained using the Boussinesq hypothesis (see Equation (5.49)) while LES results are computed using the resolved turbulent fluctuations only (see Equation (5.48)). For HTLES, both the sub-filter and the resolved parts are taken into account (sum of Equation (5.49) and Equation (5.48))

The RMS velocity profiles along *line 1* predicted by RANS, HTLES and LES are compared with LDA measurements in Figure 5.30. All simulations show acceptable results compared with the experimental data. HTLES provides results similar to RANS close to the walls and quasi identical to LES in the core region. RANS exhibits higher levels of fluctuations in the core region than HTLES and LES results.

It is observed in Figure 5.30 that RANS and LES both overestimate the peak of  $U_{r,RMS}$  at the location of the annular jet  $\frac{r}{R} \pm 0.5$  and mispredicts its location. HTLES reproduces better the shape of the profile everywhere except for the peak that is completely missed.

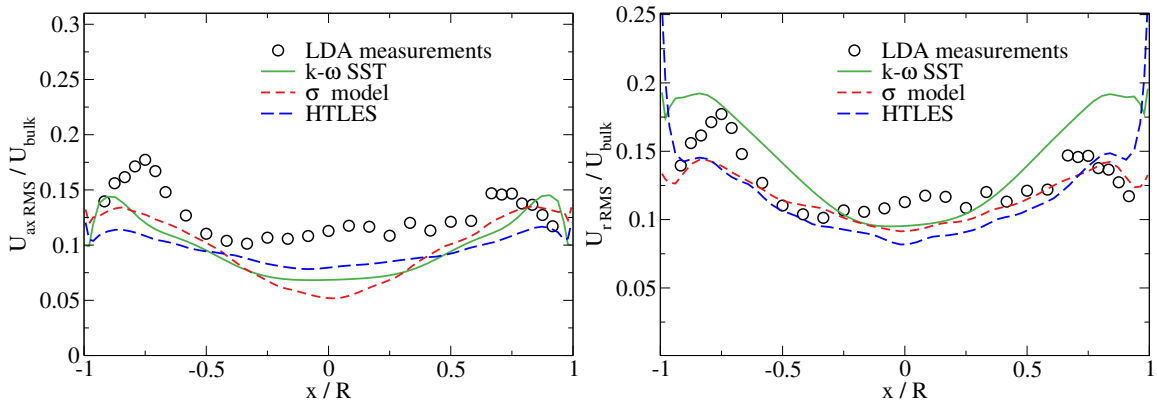


**Fig. 5.31 Steady Flow Rig:** Comparison of dimensionless RMS axial velocity along *line 2* yielded by LDA measurements and RANS, HTLES and LES. - **Left:** axial component. - **Right:** radial component.

Figure 5.31 shows the profiles along *line 2* for the axial and radial RMS velocities. All simulations predict fairly similarly the axial RMS velocity profile at this location. The profiles given by the simulations show good agreement with respect to LDA measurements even if they unanimously slightly under-predict the RMS magnitudes. For the radial component, RANS results slightly overpredict the RMS magnitudes in comparison to the experiment, and to HTLES and LES which yield fairly similar predictions. However, at the walls the RMS magnitudes yielded by HTLES are overestimated as a result of the fact that a part of the turbulent fluctuations which is still resolved (see Figure 5.21) even if RANS is imposed at the walls, i.e,  $r = 1$ .

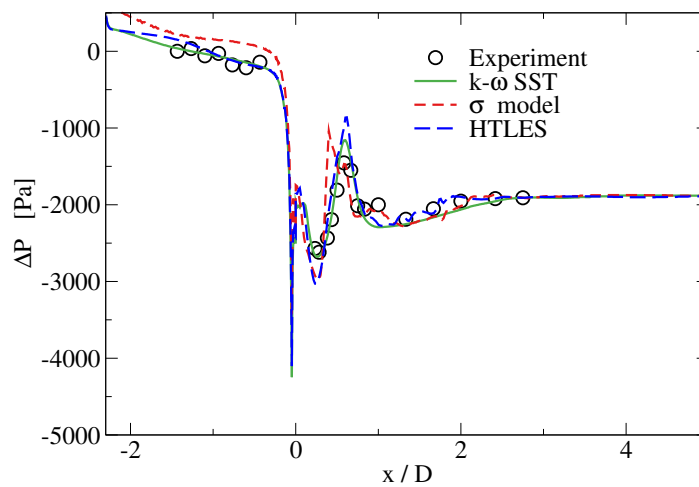


**Fig. 5.32 Steady Flow Rig:** Comparison of the axial profile of static pressure yielded by the experiment and RANS, HTLES and LES.

	EXP	RANS	HTLES	LES
$\Delta P$ [Pa]	1766	1713	1705	1957
Relative error $\varepsilon_D$ [%]	–	-3	-3	+11

**Table 5.7 Steady Flow Rig:** Comparison of the pressure drop given by the experiment and RANS, HTLES and LES.

Figure 5.32 compares the axial profile of the static pressure at the wall at  $t = 2$  s. All the simulations reproduce the stiff pressure decrease at  $x = 0$  due to the sudden expansion, and the slight pressure increase at  $x/D = 1$ . Despite this good qualitative agreement, the global pressure drop defined as the difference of pressure between the position upstream the valve and outlet of the domain is different between the three simulations. While RANS and HTLES provide a prediction close to the experiment with a relative error of  $-3\%$  (see Table 5.7), LES is less accurate with a relative error of  $+11\%$ .

This application shows one of the interests of using the HTLES approach over wall-modeled LES. Indeed, to obtain a good estimate of  $\Delta P$  with LES, a much more refined grid would be necessary, especially in the pipe and around the valves [96]. The advantage in HTLES is that the model switches to RANS in these regions, which allows to have good results with a relatively coarse mesh.

## 5.7 Conclusions

This Chapter provided an extension of the HTLES approach, which was initially developed for statistically stationary turbulence, i.e., non-cyclic flows. The main difficulty of using HTLES in such flows comes from calculating the statistically averaged quantities of the model inputs that are unknown during the simulation. To cope with this problem, four approaches were investigated in this work. They can be classified into two categories depending on the way they calculate the model inputs:

- Approaches that use the instantaneous resolved flow quantities without statistical averaging in the HTLES inputs.
- Approaches that propose an approximation of the statistically averaged HTLES inputs.

Even if some approaches belonging to the first category were shown not to spoil the model predictions in comparison with the original HTLES [1], they were not selected because there is no solid theoretical explanation that could support the use of the model without using a statistical average of its inputs. The selected approach belongs to the second category. It approximates the statistically averaged quantities of the HTLES inputs in cyclic flows by weighting the history of the resolved flow fields using a temporal filter with an exponential kernel (EWA) that adapts its filter-width locally in time and space. The temporally filtered quantities are calculated by solving the ordinary differential equation of the temporal filter for each averaged quantity. An expression for the temporal filter-width based on the turbulence integral time scale was proposed in such a way that the temporal filter is able to filter the turbulent fluctuations without eliminating the time-varying character of the statistical average of the flow fields. Validations of this approach were provided in the Channel Flow and the Steady Flow Rig showing satisfactory results and almost no difference with the original HTLES.

## **Part III**

### **Validation of HTLES on engine flows**



This part is dedicated to the validation of the developed EWA-HTLES in cyclic flows (for the sake of simplicity, it will be referred as HTLES) in two non-reacting engine configurations: the compressed tumble [10] and the Darmstadt engine [5]. The former is an academic engine with a simplified squared geometry of the compression chamber, and the latter is an engine with a realistic SI engine geometry. These two configurations operate following a four-stroke cycle under motored conditions, which features aerodynamics typical to SI engines such as the tumble motion formation, compression, and Cycle-To-Cycle Variabilities (CCV). For both configurations, an experimental database of measurements is available and is used for the validation of HTLES.



# Chapter 6

## Compressed tumble

The compressed tumble [9, 10, 83] is a simplified configuration that is representative of the working conditions of a realistic engine. It comprises moving parts and fully unsteady aerodynamic phenomena encountered in SI engines, such as the tumble generation and breakdown. This configuration is not intended to reproduce all the complexity of in-cylinder flows but focuses on the tumble vortex evolution during its generation and compression.

This Chapter is organized as follows. The description of the experimental and numerical set-up of the compressed tumble are detailed in Sections 6.1.1 and 6.2. Section 6.4 shows some adjustments that had to be added to the piston law. After that, the convergence of the two first statistical moments given by the simulations is examined in Section 6.7. Then, HTLES results for two operating modes of the engine are analyzed compared to PIV, to RANS and to LES simulations in Sections 6.5 and 6.6, featuring different aspects such as the analysis of HTLES modeling parameters, flow predictions, and the grid dependency of HTLES results.

### 6.1 Presentation

#### 6.1.1 Configuration and computational domain

The compressed engine configuration is shown in Figure 6.1a. It consists of a cubic compression chamber linked to a plenum via a rectangular channel. The compression

chamber comprises a square piston (see Figure 6.1b), which performs a back-and-forth motion at 206 *RPM*. The channel plays the role of the intake and exhaust ports. It is equipped with a rectangular guillotine, which plays the role of the intake and exhaust valves, opening during intake and exhaust and closing during compression and expansion, similar to the operation of a four-stroke engine.

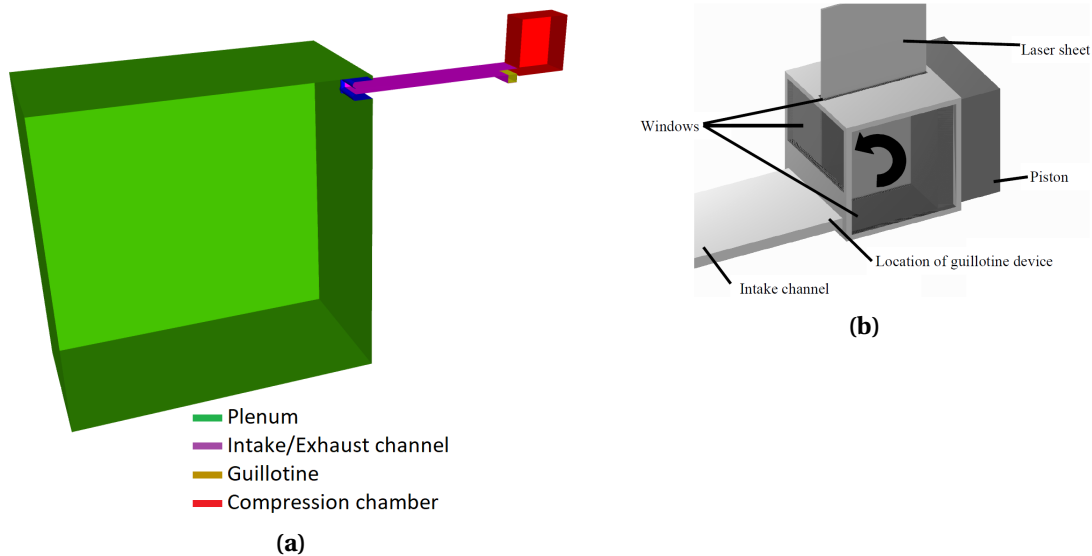


**Fig. 6.1 Compressed Tumble:** (a) Sketch of the computational domain. (b) Zoom in on the compression chamber [10].

The computational domain was chosen as close as possible to the experimental set-up [10], except from the plenum, which was expanded in our simulations in order to ensure a quasi-steady background pressure during the whole operation. Table 6.1 lists the dimensions of each part of the engine.

Parts	Plenum	Channel	Compression chamber
Length [ <i>mm</i> ]	560	314	Time-dependent (see Section 6.4)
Height [ <i>mm</i> ]		10	100
Width [ <i>mm</i> ]		96	100

**Table 6.1 Compressed Tumble:** Dimensions of the compressed tumble.

### 6.1.2 Simulated operating conditions

The experiment measurements were performed under two different volumetric compression ratios (CR): 4 and 10. This work focuses on the configuration with  $CR = 4$ . Two operating modes of the engine were examined:

- Uncompressed configuration: which features a two-stroke cycle composed of an intake and an exhaust strokes. In this configuration the guillotine is maintained fully opened during the cycle.
- Compressed configuration: which features a non-fired four-stroke cycle. In this configuration the guillotine seals the compression chamber with the channel during the compression and the expansion strokes.

For ICE flows, the piston travel is used, rather than time, to identify the advancement in the cycle. The unit of measure of the piston travel is the Crank Angle Degree (CAD). One revolution of the piston is equal to 360 CAD. In what follows, the intake stroke starts at  $-360$  CAD and each stroke lasts 180 CAD. The Bottom Dead Center (BDC) refers to the farthest position of the piston to the cylinder head, and the Top Dead Center (TDC) is the its closest position to the cylinder head.

## 6.2 Numerical set-up

### 6.2.1 Mesh configurations

Three meshes are used in this work, which all consist of isotropic hexahedral elements. They were chosen in such a way that the spatial resolution is higher in the channel and in the compression chamber and lower in the plenum, where a qualitative simulation using RANS or VLES is sufficient.

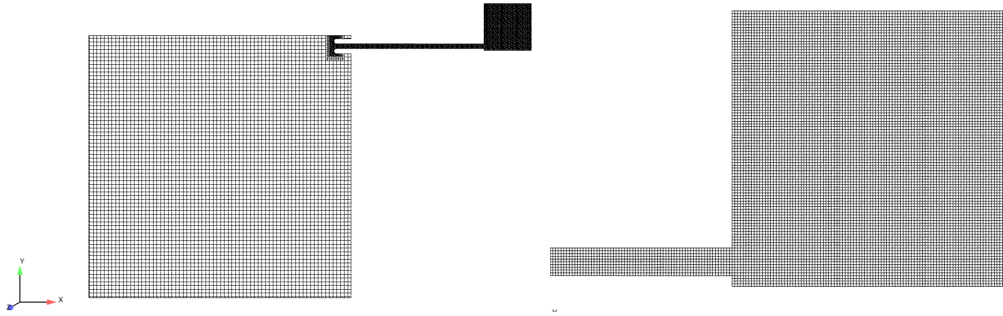


**Fig. 6.2 Compressed Tumble:** Cut-plane in the symmetry plane of the domain at BDC. - **Left:** The whole computational domain. - **Right:** Zoom in on the compression chamber.

The reference mesh, denoted as  $M2$ , is shown in Figure 6.2. Its grid resolution in each region is listed in Table 6.2. In the channel, the mesh is composed of 10 cells along the height of the channel.

Mesh configuration	M1	M2	M3
Plenum [mm]	12	8	
Channel [mm]	1.5	1	
Compression chamber [mm]	1.5	1	
Refinement of the jet region	No	No	Yes
Intake jet region [mm]	1.5	1	0.5

**Table 6.2 Compressed Tumble:** Grid resolutions of  $M1$ ,  $M2$ , and  $M3$  in each region.

Two other meshes,  $M1$  and  $M3$  shown in Figure 6.3, are used in Section 6.5.4 to investigate the grid dependency of the HTLES results. Table 6.2 provides their grid resolutions.  $M1$  is a coarse mesh that uses the same meshing strategy as  $M2$  but with a lower resolution.  $M3$  is a finer mesh that is identical to  $M2$  apart from the intake jet region, which uses a higher resolution.

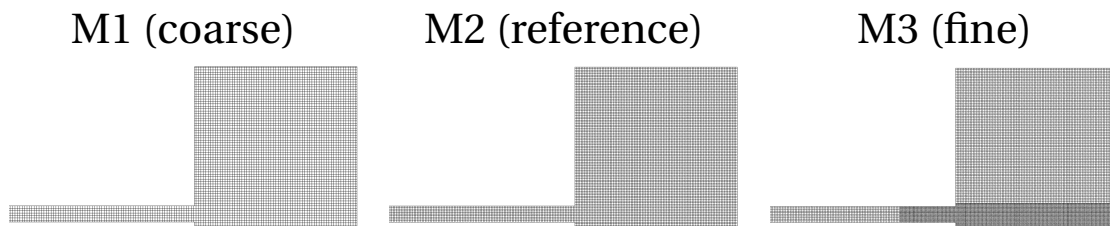


**Fig. 6.3 Compressed Tumble flow:** Cut-plane in the symmetry plane of three meshes.

### 6.2.2 Numerical parameters

The set of numerical parameters used for all simulations is summarized in Table 7.3. The acoustic CFL was increased, attempting not to resolve the acoustic flow.

Temporal scheme	First-order implicit Euler
Convective scheme	Second-order central differencing scheme
Flux limiter	Step at 0.1
Convective, acoustic CFL	0.7, 90
Fourier Number	2

**Table 6.3 Compressed Tumble:** Numerical parameters.

All simulations – RANS, HTLES and LES – were performed using the same numerical parameters and meshes in order to compare solely the impact of the turbulence model on the results.

### 6.2.3 Turbulence modeling

The turbulence models used for RANS, HTLES and LES are detailed in Table 6.4.

RANS	$k - \omega$ SST [88]
HTLES	EWA-HTLES
LES	$\sigma$ subgrid model [97]

**Table 6.4 Compressed Tumble:** Turbulence models used for RANS, HTLES and LES.

For EWA-HTLES, the model computes its inputs using temporal filtering. The temporal filter width corresponds to the expression proposed in Section 5.5.3:

$$T_w = \min\left(10 \frac{T}{\beta^* r}, \frac{6}{10\Omega}\right). \quad (6.1)$$

Concerning LES, the Smagorinsky model with a coefficient of  $C_s = 0.2$  had to be used for the uncompressed configuration instead of the  $\sigma$  model, due to a zero division in the sub-grid viscosity.

### 6.2.4 Boundary conditions and initialization

The moving piston and guillotine are managed in CONVERGE using the cut-cell technique described in Section 4.2. The piston follows a quasi sinusoidal motion, and the guillotine lift is set in such a way that it opens during the intake and exhaust strokes, and closes during the compression and expansion strokes. Borée *et al.* provided the experimental measurements of the piston and the guillotine laws (see Figure 6.4). In our simulations, using these laws resulted in important oscillations in the velocity and pressure results that are not observed in the experiment. Section 6.4 investigates the involvement of the piston law in the generation of these oscillations and introduces some adjustment to reduce them.

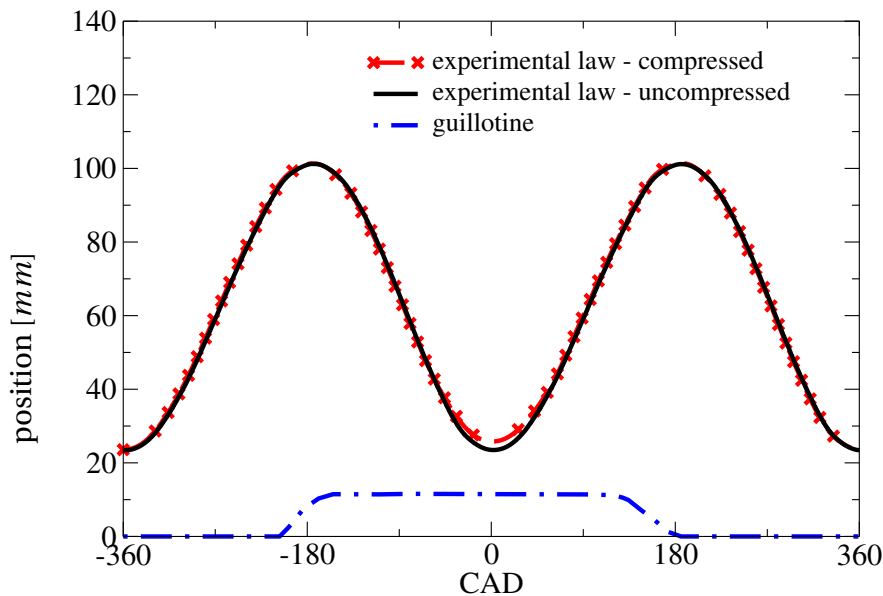


**Fig. 6.4 Compressed Tumble:** Time evolution of the guillotine lift and the piston law.

The temperature at the piston and the cylinder walls were set to  $T = 295.6\text{ K}$  and  $T = 291.6\text{ K}$ , respectively.

The boundary layers are modeled using wall functions. For the heat transfer, the O'Rourke wall function [3] is used, while the shear stress is computed using the automatic wall function [86] for RANS and HTLES, and the Werner and Wengle wall function [131] for LES.

For RANS and LES, the computational domain is initialized with air at  $291\text{ K}$ . The initial velocity and pressure are set to 0 and 1 *bar*, respectively. For HTLES, the first cycle

is simulated using the RANS mode by imposing  $r = 1$  and  $k_{res} = 0$ , then HTLES is activated from the second cycle on.

### 6.3 Post-processing of simulation results and experimental data

Experimental measurements at different crank angles of the cycle for both the uncompressed and compressed configurations are provided by the PIV measurements conducted by Borée *et al.* [10]. PIV measurements of 120 consecutive cycles were collected in the symmetry plane that is represented by the PIV laser sheet in Figure 7.8.

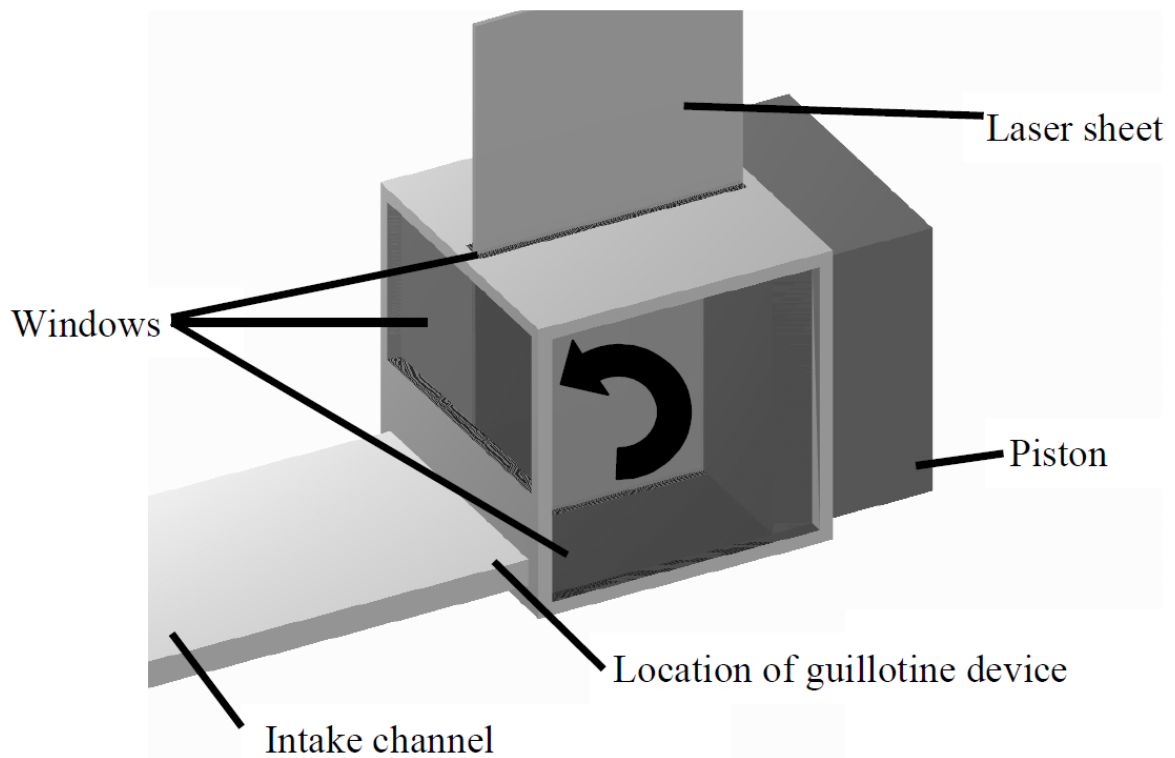


**Fig. 6.5 Compressed Tumble:** Sketch of the compression chamber and PIV laser sheet, Figure extracted from [10].

The coordinate system and its original position are shown in Figure 6.6. The x axis corresponds to the horizontal direction and the y axis to the vertical direction.

All the extracted 2D results (including those extracted from PIV and 3D simulations) provided in this work are given in the optically accessible area shown in Figure 6.6. The 1D results were extracted along lines located at five increasing distances from the cylinder head, as schematized in Figure 6.6. Their exact coordinates at each instant are given in Table 6.5. The vertical profiles were set in such a way that they cross the tumble rotational core.

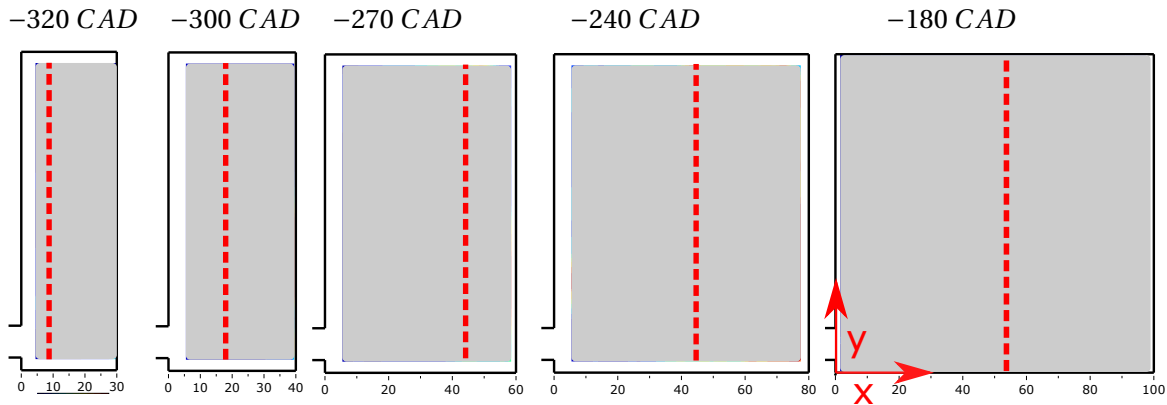


**Fig. 6.6 Compressed Tumble:** Coordinate system, schematic of the optically accessible area (grey), and the vertical lines over which are extracted the 1D profiles.

Instant [CAD]	$x$ -coordinate of the vertical line [mm]
-320	9
-300	19
-270	30
-240	44
-180	54

**Table 6.5 Compressed Tumble:**  $x$ -coordinate of the 1D vertical profiles.

The two first simulated cycles are discarded because slight variations in the time evolution of in-cylinder pressure (related to the initial conditions) were observed. HTLES and LES resolved fields are phase averaged using 40 consecutive cycles, which are sufficient to obtain a reasonable estimate of the two first statistical moments, as shown in Section 6.7. The way the statistics are calculated for HTLES and LES is also provided in Section 6.7. It is worth noting that in HTLES, both the subfilter stresses and the resolved fluctuations are included in the calculation of the mean velocity fluctuations. For RANS, the velocity is extracted from the third cycle, and the velocity fluctuations are approximated using the

Boussinesq viscosity hypothesis:

$$\overline{u'_i u'_j} = -\nu_t \left( \frac{\partial \tilde{U}_i}{\partial x_j} + \frac{\partial \tilde{U}_j}{\partial x_i} + \frac{2}{3} \frac{\partial \tilde{U}_k}{\partial x_k} \delta_{ij} \right) - \frac{2}{3} k \delta_{ij}, \quad (6.2)$$

where  $i$  can be either  $x$  or  $y$ ,  $\nu_t$  is the turbulent viscosity and  $k$  is the turbulent kinetic energy.

## 6.4 Exploring the influence of the piston law

The first simulations of the uncompressed configuration showed significant oscillations in velocity and pressure that are not observed in the experiment. This section focuses on the involvement of the piston law on the generation of these oscillations. To this end, three piston laws are examined, and their impacts on the simulation results are analyzed. First, the three examined piston laws are detailed. Their main characteristics are provided through the analysis of their first two time derivatives. Then, the three piston laws are used in three RANS simulations to assess the impact of each of these laws on the velocity and pressure.

The following analysis is performed in the uncompressed configuration. Three piston laws are explored:

- The experimental law: which was measured by Borée *et al.* [10].
- The sinusoidal law: which is an approximation of the experimental law [128]:

$$a(t) = b - \frac{V_p}{\Omega} (1 + \cos(\Omega t)), \quad (6.3)$$

where  $a(t)$  is the time evolution of the distance between the piston and the cylinder head,  $\Omega$  is the angular speed of the engine, and  $V_p = 0.809 \text{ m/s}$  is the maximum piston velocity.  $b = 100 \text{ mm}$  is the BDC.

- The smoothed law: which is proposed in this work, and which consists in a linear interpolation of the experimental law on a much smaller number of data points compared to the experimental law (100 versus 6,000).

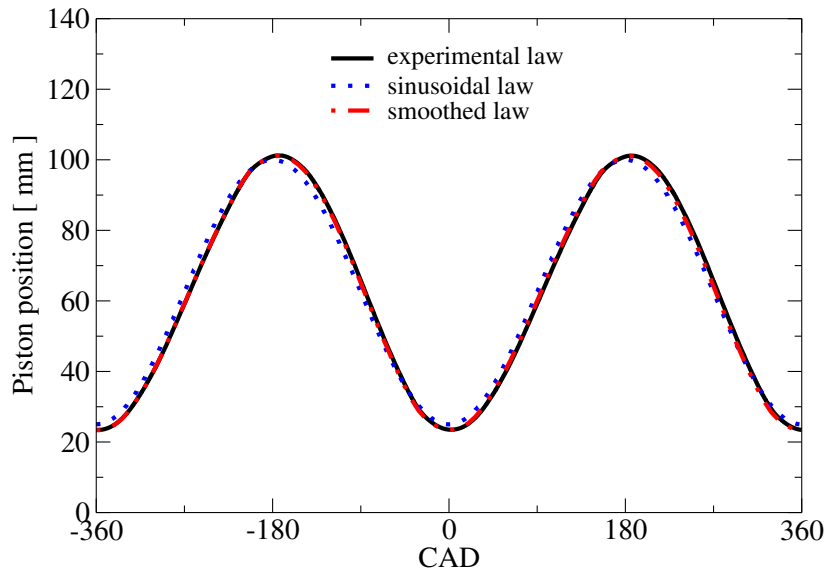
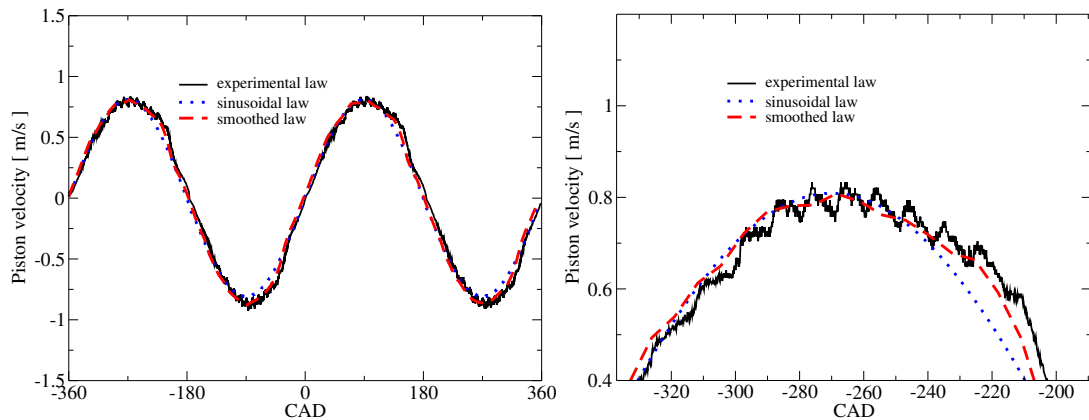


**Fig. 6.7 Compressed Tumble:** Time evolution of three piston laws for the uncompressed configuration.

Figure 6.7 reproduces the time evolution of the three piston laws. The sinusoidal law shows some differences with the experimental law in terms of TDC, BDC (see Table 6.6) and their timings. The smoothed law yields quasi identical piston positions than the experimental law.

Configuration	Sinusoidal law	Experimental law uncompressed
TDC [ $mm$ ]	25	23.4
BDC [ $mm$ ]	100	101.20

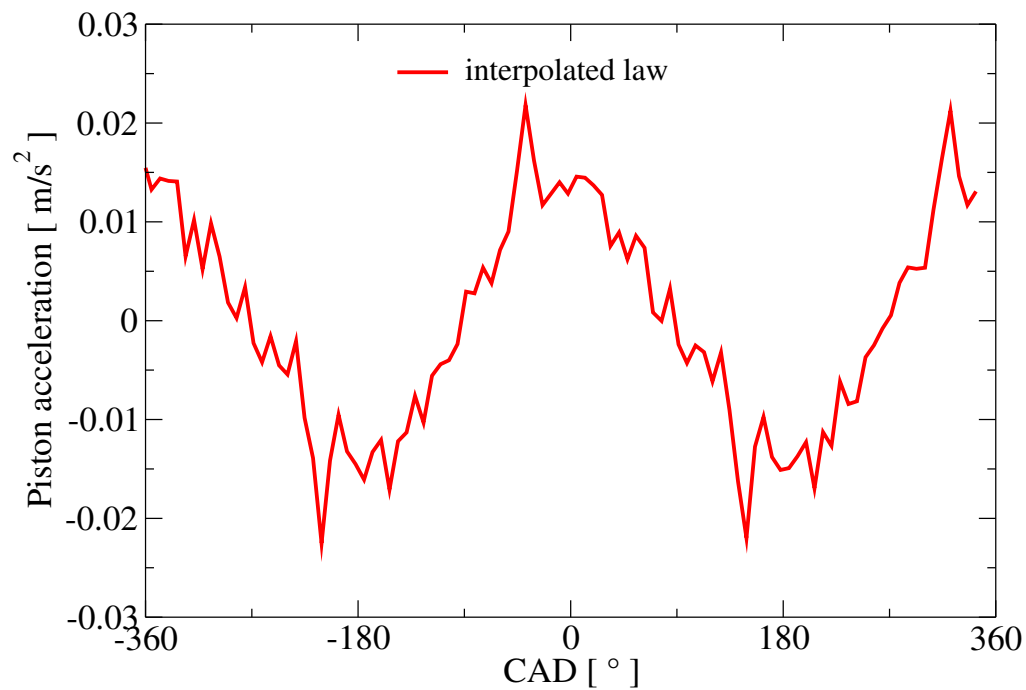
**Table 6.6 Compressed Tumble:** Specifications of the sinusoidal and the experimental piston motion laws.



**Fig. 6.8 Compressed Tumble:** -Left: Time evolution of the piston velocity of three laws for the uncompressed configuration. - Right: Zoom in where the velocity is maximum during the intake.

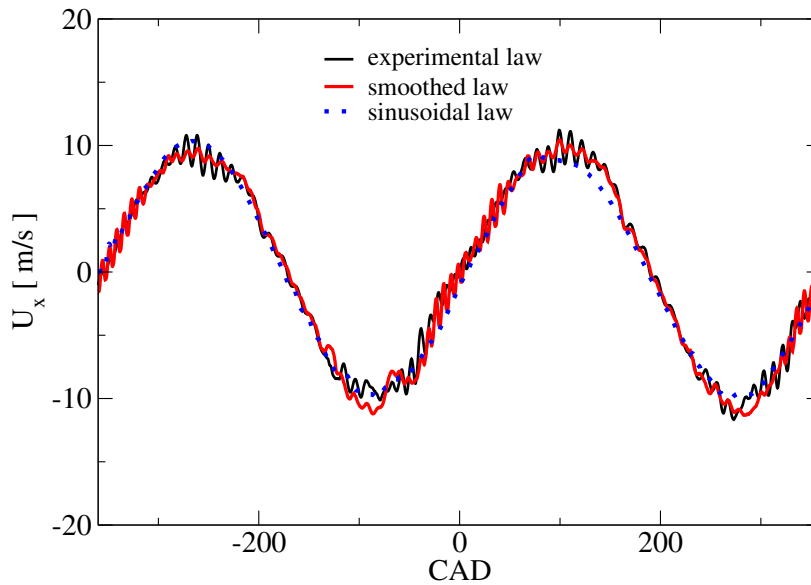
The first time derivative of the three piston laws (piston velocity) is given in Figure 6.8. The experimental law features some small fluctuations that amplifies where the piston velocity is at its extrema. These fluctuations were already outlined in [84]. They consist of fluctuations of 5% of the maximum velocity of the piston  $V_p$ , and have a frequency of about 37 Hz. These fluctuations were shown to be the consequence of piston vibrations, which are due to a mechanical play between the mechanical parts that connect the piston to the motoring device. These vibrations gave rise to a slight pulsating effect in the intake jet flow in the experiment [84].

The sinusoidal law yields an acceptable approximation of the experimental velocity but shows some local differences as can be seen in the zoomed in Figure 6.8-*right*. As can be observed, the smoothed law reproduces similarly the experimental piston velocity with almost no fluctuation. Nonetheless, the smoothed law does not remove completely the fluctuations from the experimental law, as they can still be seen in the piston acceleration (see Figure 6.9).



**Fig. 6.9 Compressed Tumble:** Time evolution of the acceleration of the piston along the cycle calculated from the smoothed law.

The three pistons laws have been tested in three RANS simulations. The results of each simulation are compared in what follows.



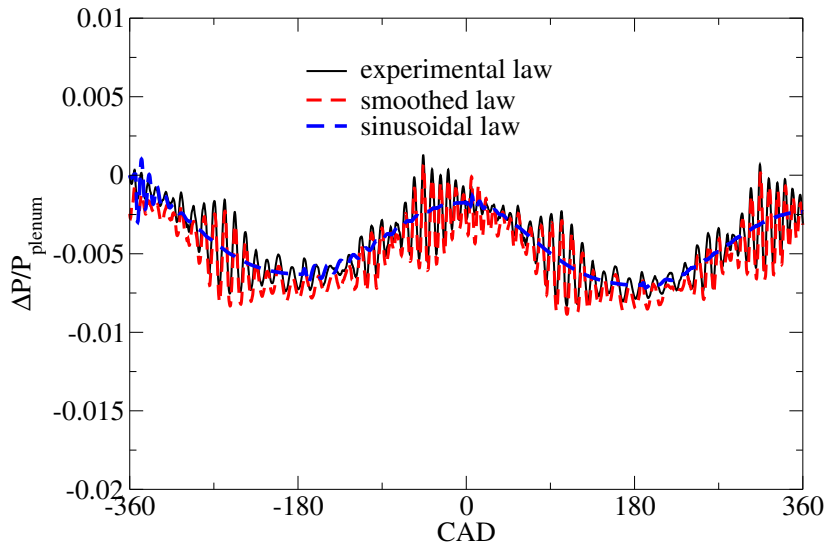
**Fig. 6.10 Compressed Tumble:** Comparison of the time evolution of horizontal velocity at a monitoring point at half height of the channel obtained with three piston laws in RANS.

Figure 6.10 compares the time evolution, in the channel, of the horizontal velocity obtained with each law. It shows the results of two consecutive intake-exhaust cycles.

All simulations show that, during the intake, the flow velocity increases until reaching its maximum, around  $-270 \text{ CAD}$ . After that, the velocity decreases as the piston slows down. After  $-180 \text{ CAD}$ , the piston reverses its trajectory, pushing the flow out from the chamber. This results in negative velocities in the channel until  $0 \text{ CAD}$ , which is the end of the cycle.

In the simulation with the experimental law, the horizontal velocity shows an oscillating behavior during the whole cycle. These oscillations increase when the piston vibrates the most. They have a frequency of  $110 \text{ Hz}$ , which is superior to the frequency of the fluctuations present in the piston law ( $37 \text{ Hz}$ ). In the simulation using the smoothed law, the results show less oscillations than in the experimental law. The remaining oscillations are potentially due to the piston fluctuations that could not be eliminated.

The sinusoidal law shows no oscillation during the whole cycle. This clearly shows the involvement of the piston vibrations in the generation of the oscillations observed when using the experimental law. Nevertheless, the flow evolution predicted by the sinusoidal law does not correspond precisely to the experimental law, especially at  $180 \text{ CAD}$ , where the flow velocity is underestimated.



**Fig. 6.11 Compressed Tumble:** Comparison of the time evolution of the pressure  $\Delta P = (P - P_{plenum})/P_{plenum}$  at a monitoring point at half height of the channel obtained with three piston laws in RANS.

Figure 6.10 shows that the oscillations also appear in pressure in both the experimental and the smoothed law, but remain relatively small (less than 1% of the statistic pressure of the plenum).

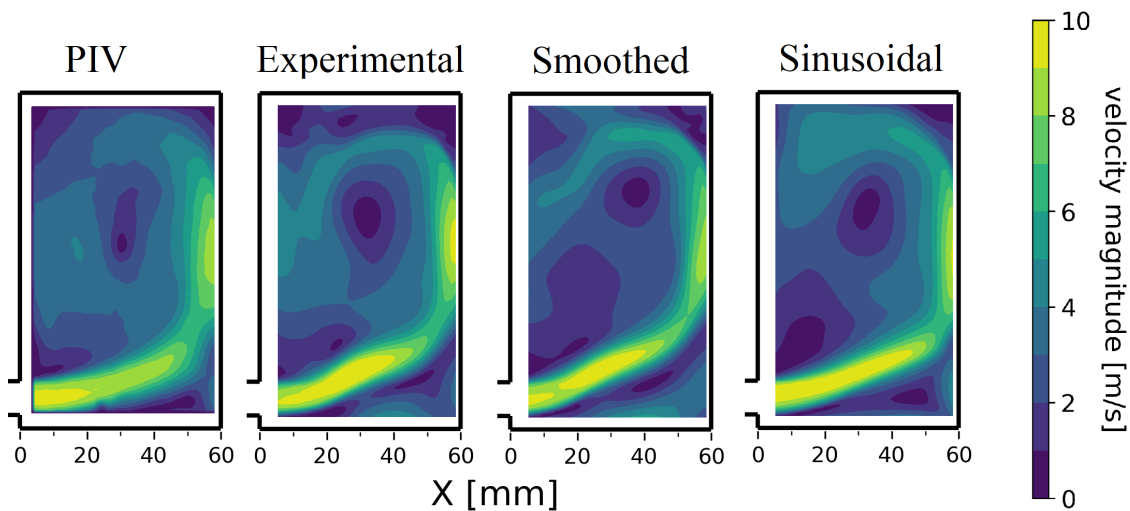


**Fig. 6.12 Compressed Tumble:** Contours of the velocity magnitude extracted from PIV and RANS using three different piston laws.

Figure 6.12 compares the velocity magnitude contours at  $-270$  CAD that are yielded by the three simulations using the three piston laws and PIV. This instant corresponds to

the instant where the piston vibrations are at their maximum. PIV shows that the intake jet streams toward the piston and deflects forming a tumble vortex in the core region. A small recirculating flow appears beneath the intake, in the corner formed by the lower cylinder liner, the piston and the intake jet.

In the simulation using the experimental law, the intake jet is clearly deflected upwards and has a stronger pulsating behavior than PIV. The pulsating effect and upward deflection of the intake jet are also observed in the smoothed law. Nevertheless, as proven by the analysis above, the pulsating effect is less strong in the smoothed law. In the simulation with the sinusoidal law, the intake jet is more regular and shows no pulsating effect. The intake jet penetration and the intake jet velocity magnitudes, however, are clearly overestimated.

The experimental law showed strong oscillations in the simulated fields. Even though the sinusoidal law allows to prevent pressure and velocity oscillations, this law was not retained in this work because it was shown to provide a slightly different motion than the experimental law. The smoothed law, for its part, allows to be as close as possible to the experimental conditions while partially reducing the undesirable oscillations. It was consequently selected in this work.

## 6.5 Results for the uncompressed configuration

The HTLES results are compared with PIV, and RANS and LES during the intake stroke. The comparison is organized in three parts. First, the simulation results in terms of mean velocity and velocity fluctuations are compared with the PIV findings, and RANS and LES. Next, the modeled turbulence in HTLES is examined at different instants of the intake. Then, the grid dependency is explored by comparing the HTLES results on three meshes.

### 6.5.1 Comparison with PIV, RANS and LES

The intake stroke starts at  $-360$  CAD. The piston moves away from the cylinder head, drawing the air into the compression chamber through the channel. The flow emanating from the channel separates from the wall forming a jet flow, which deflects on the piston wall. This yields two counter-rotating vortices: a small clockwise vortex appears beneath the jet flow and a counter-clockwise rotational movement appears in the core region, i.e.,

the tumble motion, the formation process of which is featured during all the intake stroke until  $-180$  CAD, where the piston is at BDC (the farthest piston position from the cylinder head). This Section aims at comparing the HTLES predictions of the tumble generation during the intake with the PIV findings, and RANS and LES. To this aim, Section 6.5.1.1 provides a comparative study of the mean velocities at different instants of the intake, then the mean velocity fluctuations are examined in Section 6.5.1.2.

## 6.5.1.1 Mean velocity

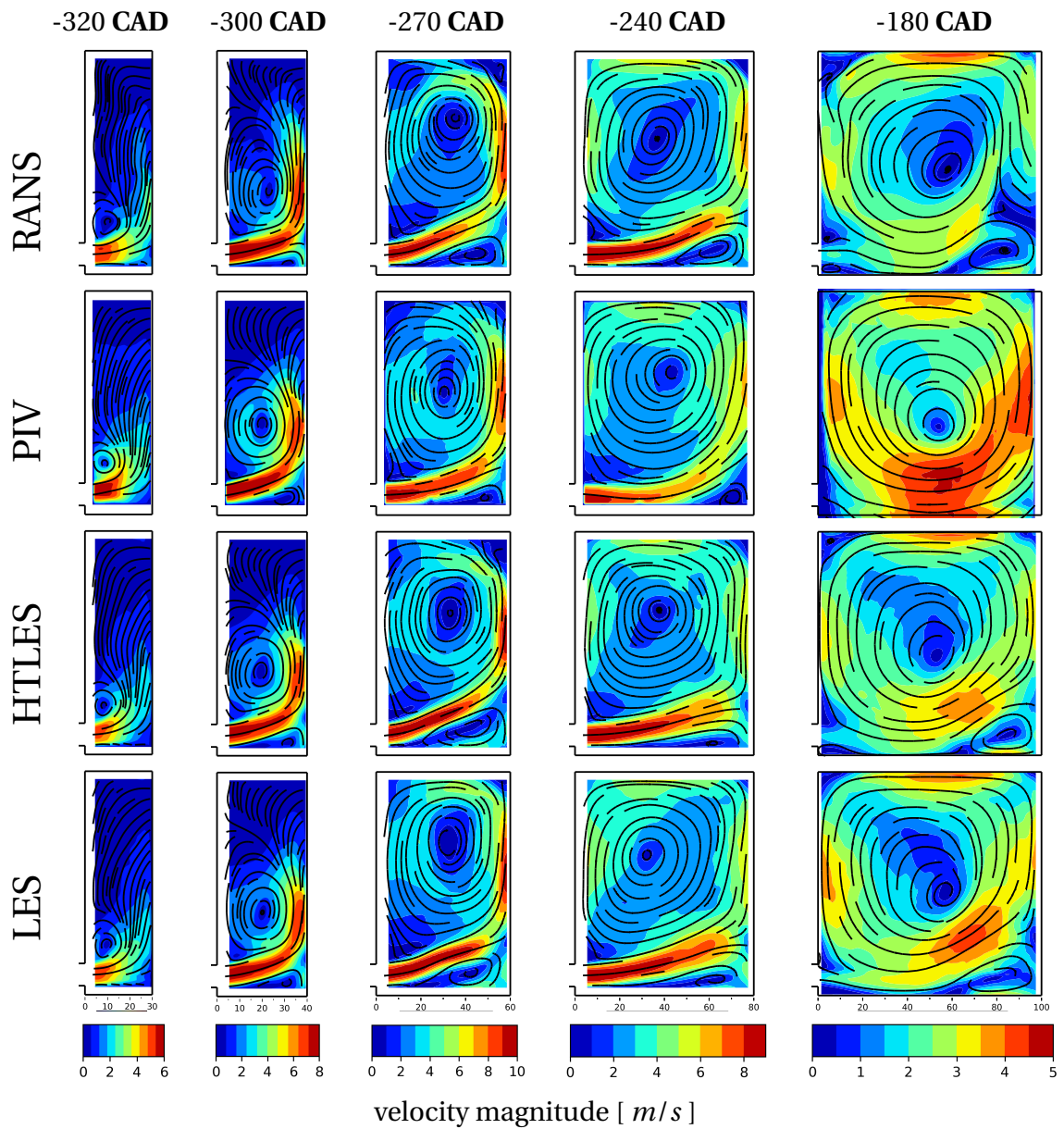


**Fig. 6.13 Compressed Tumble:** Contours and streamlines of the phase-averaged in-plane velocity in the symmetry plane of the compression chamber at 5 instants during the intake.

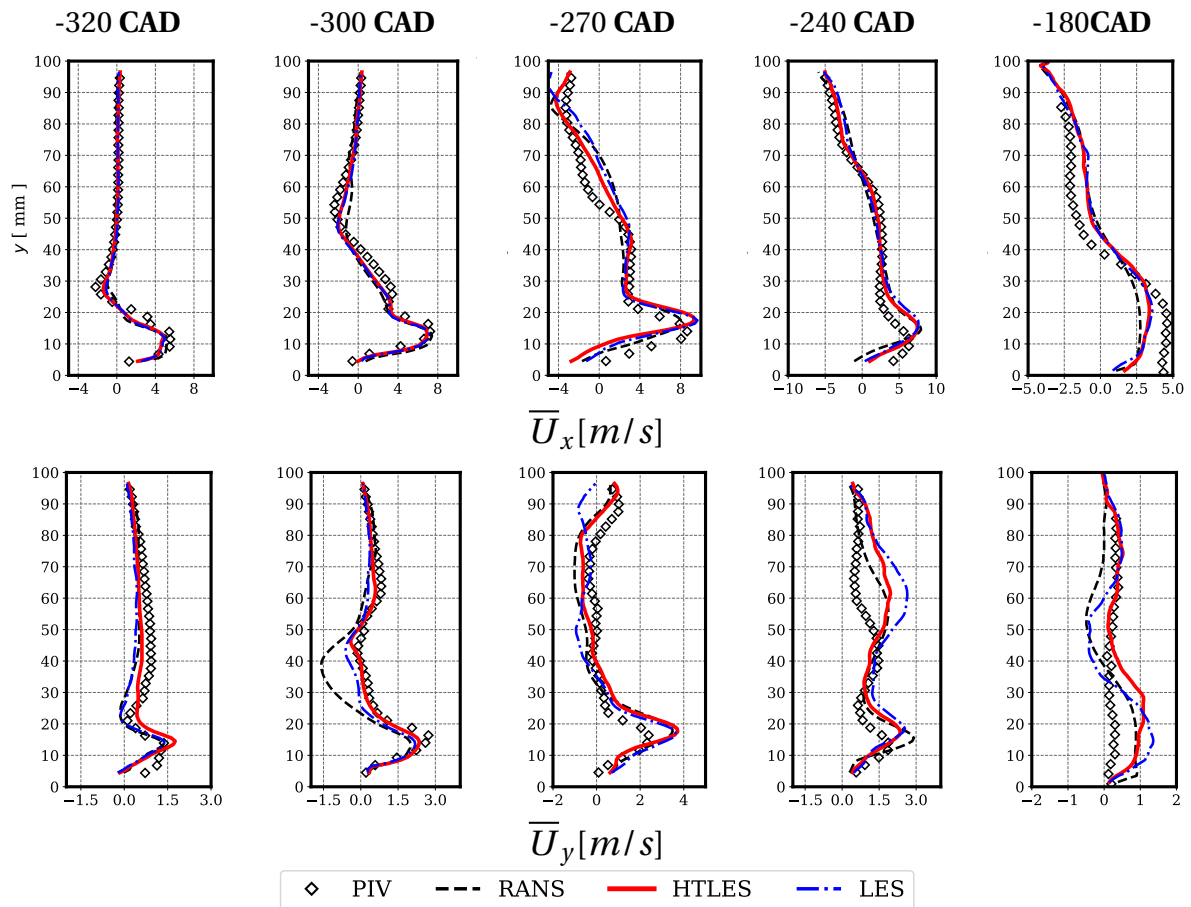


**Fig. 6.14 Compressed Tumble:** Vertical 1D profiles of the phase-averaged velocity at 5 instants of the intake.

Figure 6.13 compares the contours and streamlines of the in-plane phase-averaged velocity in the symmetry plane of the compression chamber predicted by RANS, LES and HTLES with the PIV data at 5 instants of the intake stroke. Figure 6.14 shows 1D extracts from these velocity fields obtained along a vertical line defined in Section 6.3.

The first shown instant, at  $-320\text{ CAD}$ , corresponds to the early intake. The motion of the piston moving away from the cylinder head draws air into the chamber, forming a jet that flows out of the channel. The emanating flow deflects on the piston and starts generating the tumble motion. All approaches predict a horizontal penetration of the intake jet that is close to the PIV findings. They predict a slightly higher upward deflection than in the experiment, as shown by the 1D velocity profiles. All simulations yield a fairly good approximation of the rotational motion compared to the PIV data, regarding the rotational core location and the size of the tumble. HTLES and LES appear to reproduce the

initiation of the tumble rotation better than RANS, which predicts a much less structured tumble vortex.

At  $-300$  CAD, the intake jet is deflected upwards by the piston and detaches from the lower cylinder wall. All three simulations correctly predict the recirculating flow. The leading edge of the intake jet, i.e. the tumble front, is close to the piston. While HTLES and LES predict its position fairly accurately in comparison to the PIV, RANS overestimates the penetration of the tumble front and underestimates the rotational flow, resulting in a rotational center of the tumble that is shifted to the bottom right side. The tumble rotational center can be identified in 1D velocity profiles where both velocity components are equal to zero, which corresponds in PIV to  $(x, y) = (19\text{mm}, 40\text{mm})$ . HTLES predicts a close value of  $y = (19\text{mm}, 39\text{mm})$ . The 1D profiles obtained by LES also show a good agreement with the PIV data, while RANS profiles are the least accurate as the tumble rotational center was not accurately predicted.

At the third shown instant, significant differences are apparent between all simulations and PIV. In the simulations, the intake jet exhibits a quite higher deflection towards the upper side, clearly visible in the 1D profiles of the horizontal velocity. As a result, the tumble vortex is shifted upwards compared to PIV, and a stronger recirculation zone can be observed in the lower right corner. Despite these noticeable differences, the vortex rotational speed is still close to the one found in PIV.

The upward deflection of the intake jet persists until the fourth shown instant in all the simulations. The 1D profiles of the horizontal velocity show that all the simulations overestimate the intake jet penetration. The bottom recirculation is better predicted in HTLES and LES predictions than in RANS. Regarding the rotational center of the tumble, RANS and HTLES fairly well predict its location, unlike LES, which yields a rotational center more shifted to the left side.

At  $-180$  CAD, which corresponds to the BDC, the intake jet is no longer apparent in the PIV fields. On their side, all simulations predict an intake jet that still exists but is a lot less intense. HTLES and LES also predict a secondary vortex in the lower right part, which is not apparent in the PIV. This vortex appears even more in the RANS. In addition, the PIV fields show a high velocity region in the lower part of the tumble vortex, which could be a remnant of the intake jet. This feature is much less apparent in the simulations. However, overall, the tumble vortex center and rotational speed are comparable to PIV in HTLES and LES, while RANS yields a clearly poorer prediction.

### 6.5.1.2 Mean velocity fluctuations

The mean fluctuations of each velocity component in the symmetry plane yielded by the simulations are compared with the PIV findings in the following.

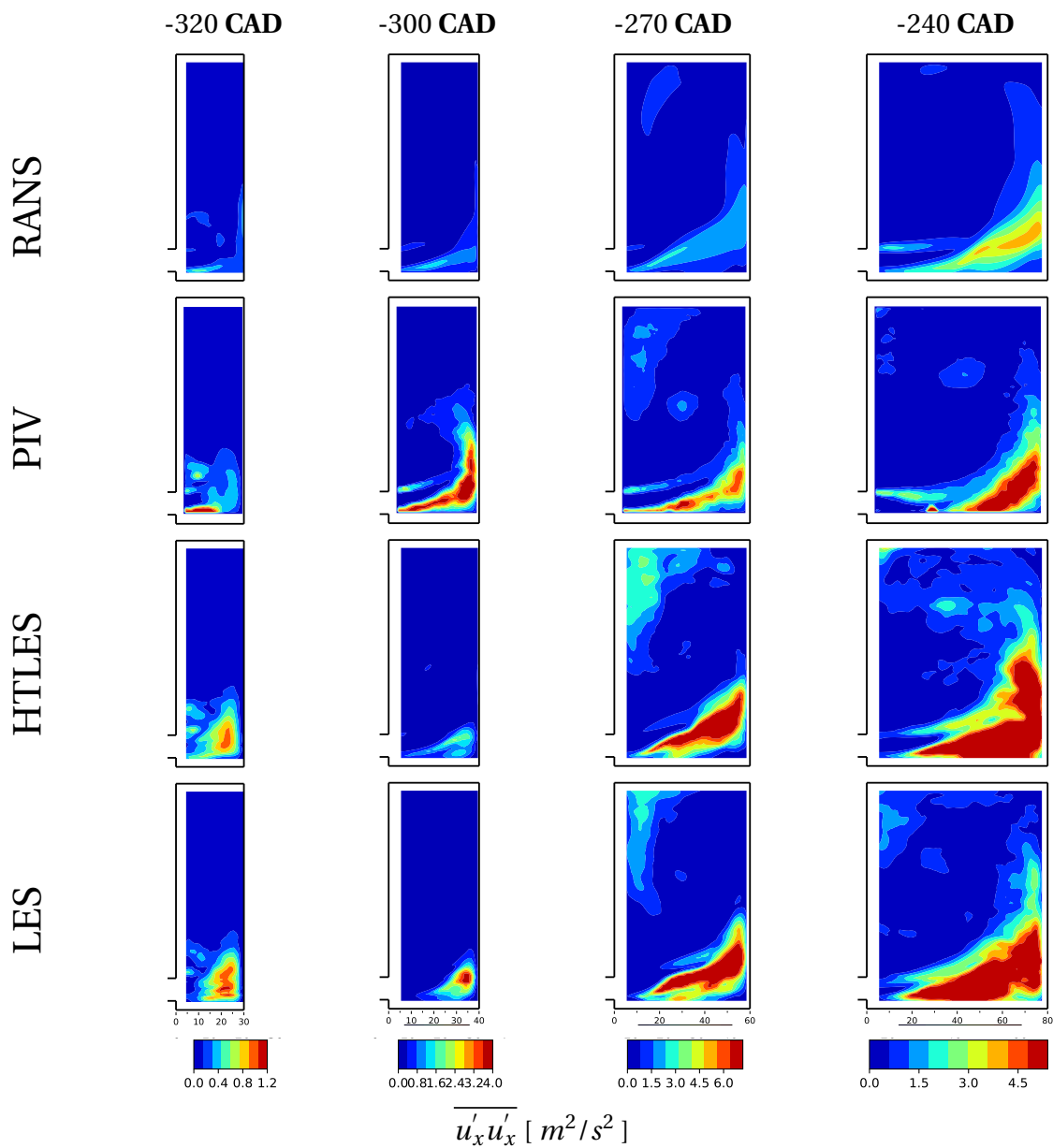


**Fig. 6.15 Compressed Tumble:** Contours of the mean velocity fluctuations  $\overline{u'_x u'_x}$  in the symmetry plane at 4 instants of the intake.

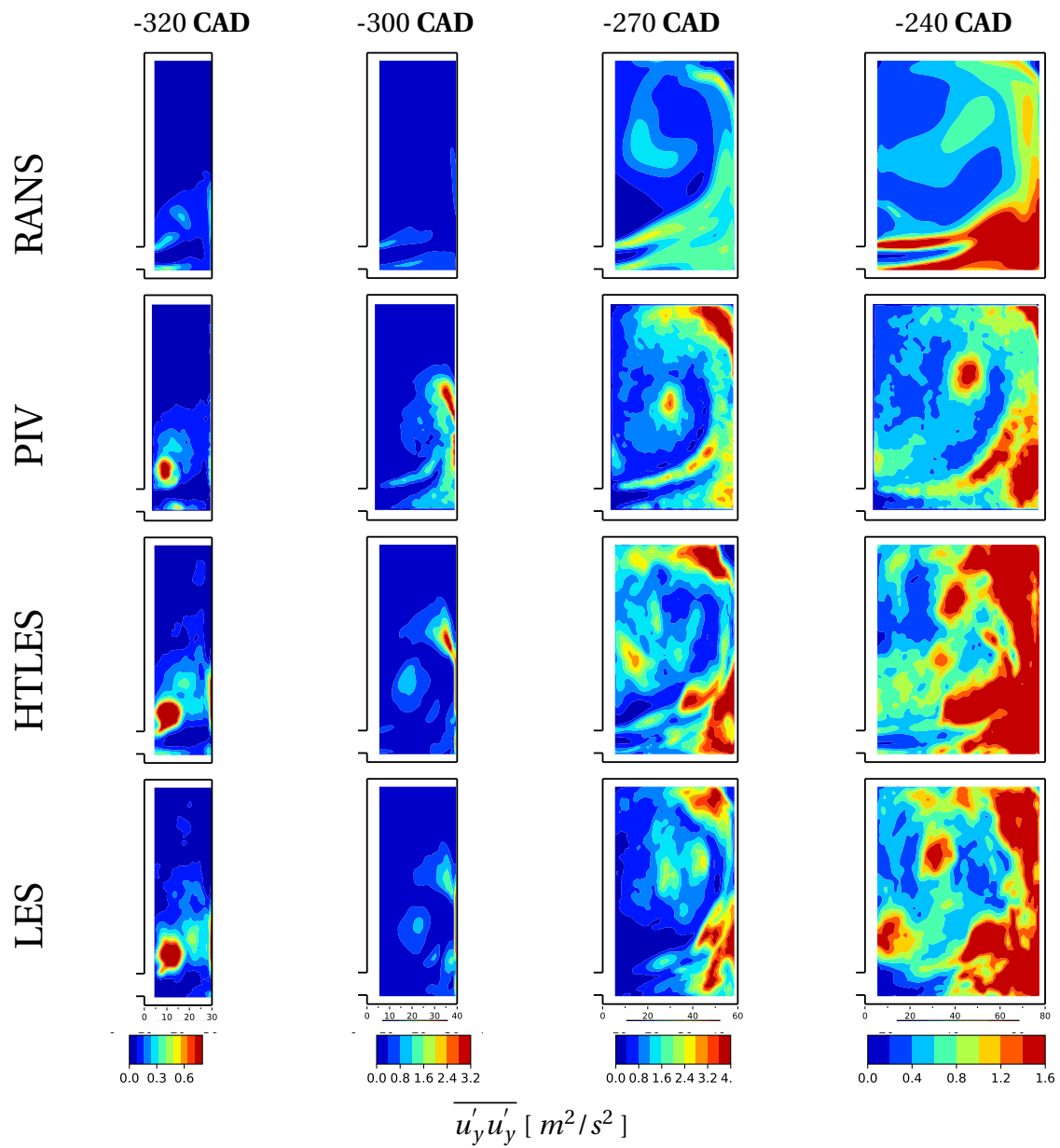


**Fig. 6.16 Compressed Tumble:** Contours of the mean velocity fluctuations  $\overline{u'_y u'_y}$  in the symmetry plane at 4 instants of the intake.

Figures 6.15 and 6.16 show the contours yielded by the simulations and the PIV findings of  $\overline{u'_x u'_x}$  and  $\overline{u'_y u'_y}$ , respectively. Their corresponding 1D vertical profiles are given in Figure 6.17.

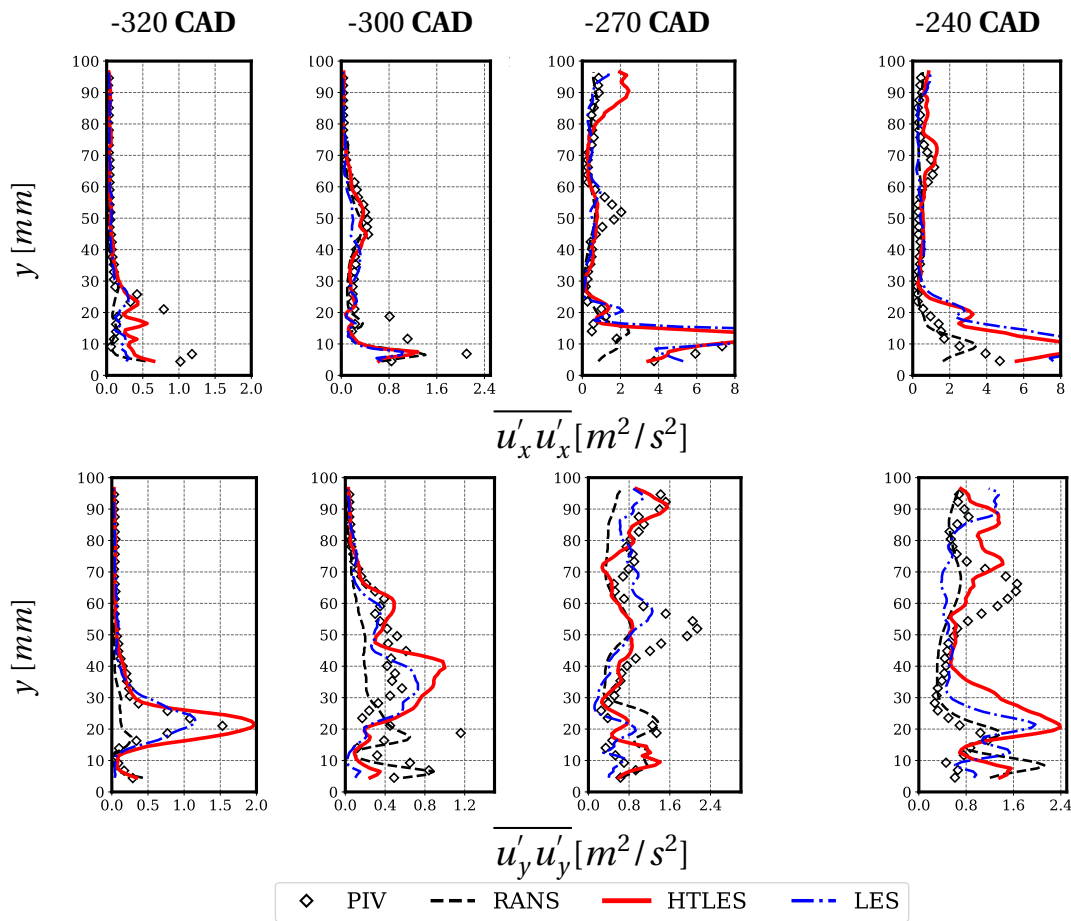


**Fig. 6.17 Compressed Tumble:** Vertical 1D profiles of the mean velocity fluctuations at 4 instants of the intake.

At  $-320 \text{ CAD}$ , the PIV data show that  $\overline{u'_x u'_x}$  reaches its highest values in the shear layer, around the intake jet and its penetration tip. Also, there is an increase in fluctuations in the center region of the secondary vortex that is generated above the jet close to the chamber head. HTLES and LES qualitatively reproduce this behavior, but strongly overestimate it quantitatively, especially around the jet tip. RANS yields a quite poor reproduction, both qualitatively and in terms of magnitude, which is strongly underestimated.

At  $-300 \text{ CAD}$ , all simulations underestimate the levels of fluctuations appearing in the jet shear layer and around the tip in PIV. Another region with noticeable fluctuations is predicted by HTLES and LES around the vortex center. Although the latter is also apparent in PIV, the experimental levels are smaller than the simulated ones, as shown by the 1D profiles.

At the third shown instant ( $-270$  CAD), the tumble front continues its formation and moves to the upper right side of the compression chamber. The tumble front region is characterized by an increase in fluctuations that are hardly predicted by RANS. Conversely, HTLES and LES predict this phenomenon fairly well in comparison to the PIV findings. Around the tumble rotational core, PIV features a local increase in the vertical velocity fluctuations that is less well defined in HTLES and LES, and partially captured in RANS. Below the intake jet, HTLES and LES show a substantial increase in the horizontal fluctuations, that are overestimated compared to PIV. This seems to be caused by the pulsating intake jet, which is exaggerated due to the velocity and pressure oscillations that only appear in the simulations, as reported in Section 6.4. It has been shown that these oscillations were caused by the vibrations included in the piston law.

The overestimation of velocity fluctuations under the intake jet persists in HTLES and LES until  $-240$  CAD. RANS qualitatively reproduces these fluctuations in the horizontal direction and overestimates the vertical fluctuations. The peak of fluctuations that appears around the tumble center is quite well detected in HTLES, as shown in 1D profiles. For the other simulations, the peak is either detected with a left shift (LES, as shown by the contours) or with an overestimation in magnitude (RANS).

Overall, HTLES and LES showed a better prediction of both mean velocities and mean fluctuations than RANS. The latter gave a qualitative prediction of the flow but significantly underestimated the fluctuations, especially in regions that are characterized by cyclic variabilities.

### 6.5.2 Analysis of EWA

This Section aims at examining the filter width  $T_w$  of EWA (see Section 5.5.3), which is used to approximate the mean inputs in HTLES:

$$T_w = \min\left(10 \frac{T}{\beta^* r}, \frac{T_0}{100}\right), \quad (6.4)$$

where  $T_0 = 0.29s$  is the period of one piston revolution. The quantity  $\frac{T}{\beta^* r}$  aims at approximating the turbulent integral time scale  $\tau_t$ .  $\frac{T_0}{100}$  is a fraction of the period of the engine cycle. It prevents large filter widths that induce large phase errors.

In what follows, the turbulent integral time scale  $\tau_t$  is examined in the compression chamber to estimate the filter width required in Equation (6.4). A qualitative estimation of  $\tau_t$  is extracted from a RANS simulation. Figure 6.18 shows the contours of ratio  $\tau_t/T_0$  are shown at three instants of the intake.

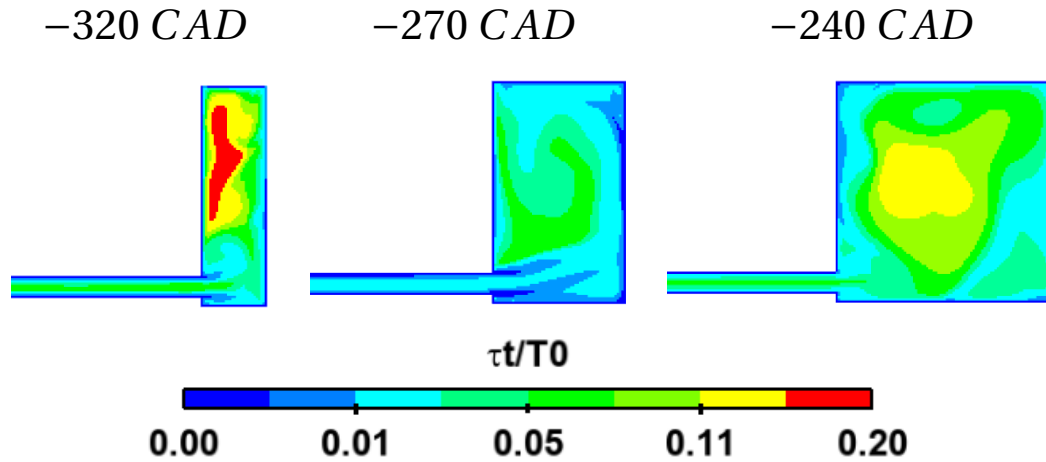


**Fig. 6.18 Compressed Tumble:** Contours of the integral time scale over  $T_0$  during intake.

At the three investigated instants, the integral time scale  $\tau_t$  inside the cylinder is greater than  $0.05 \times T_0 = 0.145 \text{ s}$  in a large part of the domain, which is larger than the fraction of the period of the engine cycle  $\frac{T_0}{100} = 2.9 \text{ ms}$ . As Equation (6.4) uses the smallest of the two time scales, the filter width  $T_w$  will be calculated using  $\frac{T_0}{100}$  almost everywhere.

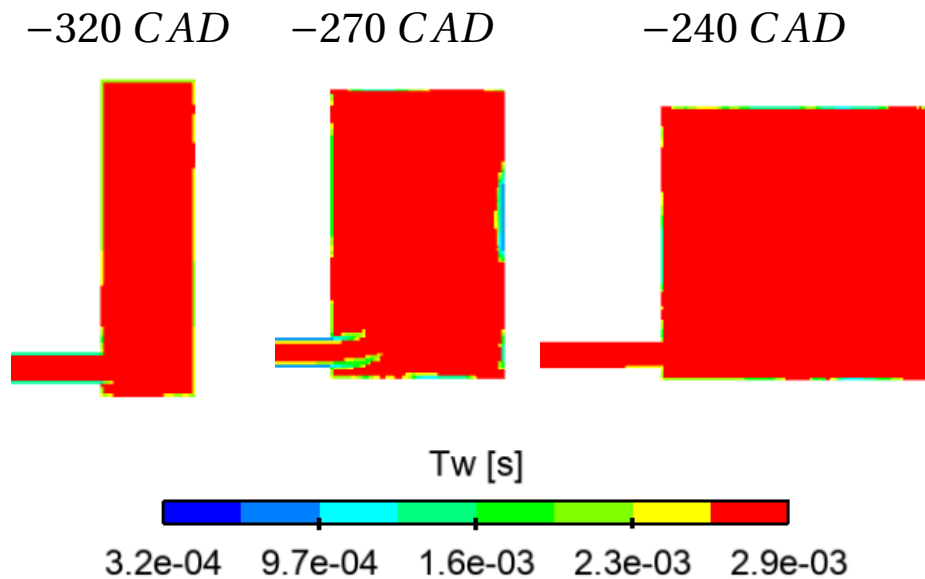


**Fig. 6.19 Compressed Tumble:** contours of the temporal filter-width  $T_w$  during intake.

Indeed, Figure 6.19 confirms the analysis given above as,  $T_w$  computed during the simulation corresponds to the fraction of the engine cycle almost everywhere. It is worth noting that even if the filter is not long enough to perfectly approximate the average inputs of the model, the simulations showed satisfactory predictions. These findings are in line with the observations made in the Channel Flow in Section 5.6.2.1, which showed that even if the EWA approach underestimates the total turbulent kinetic energy (through short time filtering), the model predictions were not significantly affected.

### 6.5.3 Modeled turbulence in HTLES

This Section aims at analyzing the modeled turbulence in HTLES during the tumble generation process. First, Section 6.5.3.2 examines the amount of subfiltered turbulent kinetic energy among the total turbulent kinetic energy. Then, Section 6.5.3.1 provides a visualization of the resolved fields using Q-criterion isosurfaces.

#### 6.5.3.1 Resolved flow structure

The resolved flow structures in HTLES are compared to those in RANS and HTLES using  $Q^+$ -criterion isosurfaces ( $Q^+ = Q \cdot L_y^2 / U_{bulk}^2$ ) with  $L_y = 100 \text{ mm}$  and  $U_{bulk} = 10 \text{ m/s}$ , iso surfaces at 3 in Figure 6.20. This allows to identify the flow structures captured by each simulation [58].

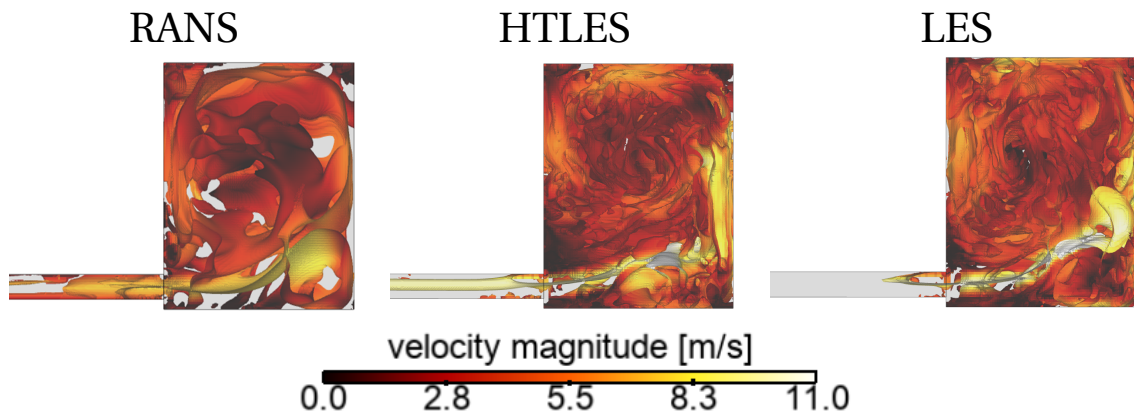


**Fig. 6.20 Compressed Tumble:**  $Q^+$  – criterion iso surfaces at 3 in the symmetry plane colored by the instantaneous velocity magnitude at  $-270 \text{ CAD}$ .

RANS results in the channel show elongated flow structures, which separate into two recirculating vortices in the compression chamber. The vortex close to the lower cylinder wall corresponds to the recirculating flow provoked by the jet flow separation, while the vortex in the core region corresponds to the tumble motion. Despite the refined mesh, RANS only captures the largest flow structures, which correspond to the phase average. Concerning LES results, no flow structures are observed in the channel, whether it be for the examined  $Q^+$  isosurface value or for other smaller values (not shown here). This indicates that the mesh resolution is not sufficiently fine to resolve the turbulent structures. In the compression chamber, LES captures the two vortices with their constituting turbulent structures, which are larger than the mesh. In HTLES, the isosurfaces have an elongated structure in the intake channel similar to that of the isosurfaces observed in RANS. Downstream from the channel, the resolved flow structures show similarities with LES, except near the walls where the resolved turbulent structures are more elongated due to the triggering of the RANS mode resulting in less resolution of the turbulent structures.

### 6.5.3.2 Targeted and observed energy ratio $r$

This Section aims at examining the amount of the modeled turbulent kinetic energy in HTLES during the intake. As shown in Section 4.4.2.2, such an analysis should include:

- The target energy ratio  $r$ : which is the parameter that drives the transition from RANS to LES in HTLES.
- The observed energy ratio  $r_{observed} = \frac{k_{sfs}}{k}$ : which is calculated from the simulation results and represents the response of the simulation to the targeted ratio.

These two parameters are examined during the intake.

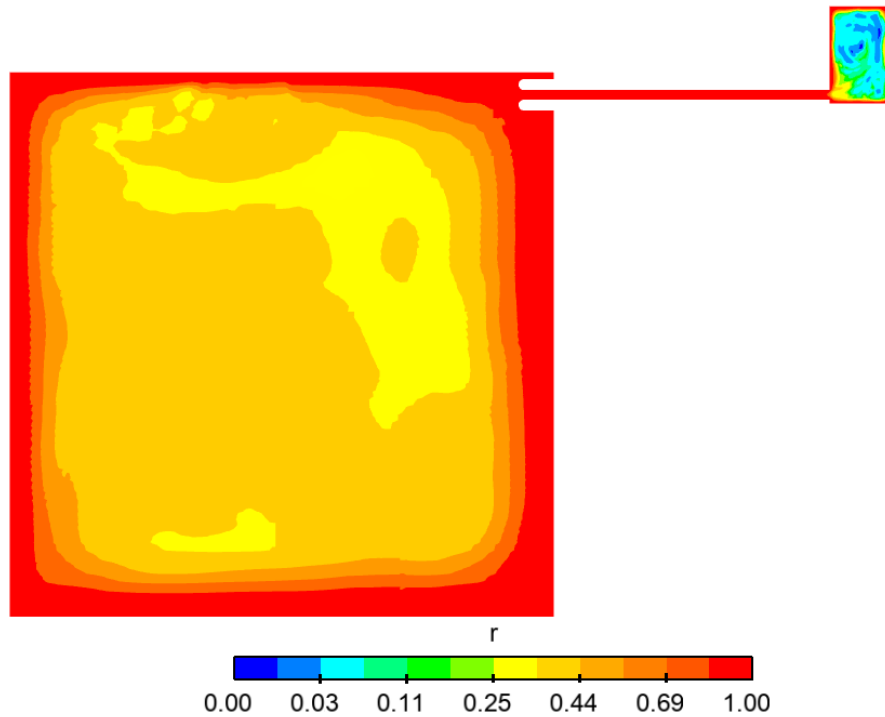


**Fig. 6.21 Compressed Tumble:** Contours of the target energy ratio in the symmetry plane at  $-270$  CAD ( $5^{th}$  cycle).

Figure 6.21 shows the instantaneous contours of the target energy ratio at  $-270$  CAD. The plenum is dominated by large values of  $r$  ( $r > 0.4$ ) as the mesh resolution was lowered, indicating to the model to operate in VLES. The elliptic shielding activates in the whole channel as the Reynolds number is relatively low, making HTLES recover RANS equations ( $T \rightarrow \frac{k}{\epsilon}$ ).

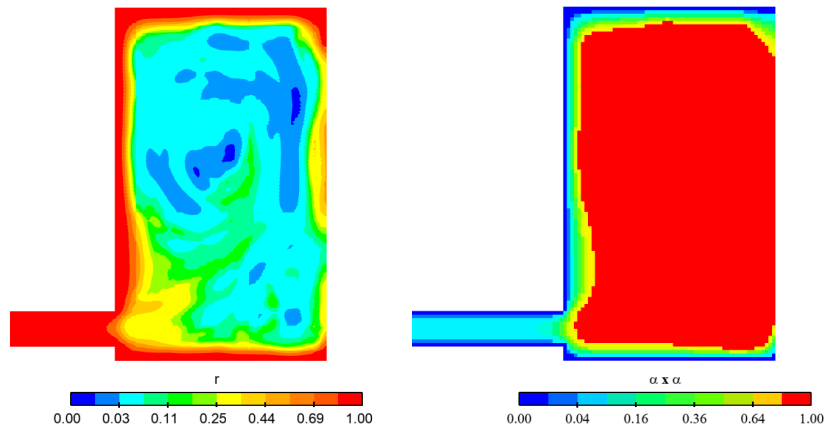


**Fig. 6.22 Compressed Tumble:** A zoom in on the compression chamber at  $-270$  CAD. - **Left:** Target energy ratio  $r$ . - **Right:**  $\alpha^2$ .

Figure 6.22 shows a zoom in on the compression chamber. The energy ratio  $r$  decreases from one at the fixed walls to small values in the core region, which vary locally between VLES and LES. At the piston, the model fails to ensure RANS. In order to identify where the problem lies, Figure 6.22-*right* shows the contours of the elliptic shielding  $\alpha^2$ . It decreases at the fixed wall showing that the shielding successfully activates. Nevertheless, this is not the case at the moving wall, where  $\alpha^2$  does not decrease. This turned out to be related to the Dirichlet boundary condition used for the resolution of the Poisson equation of  $\alpha$  (see Equation (5.40)) that could not be properly imposed for the moving walls. This issue is suspected to come from the module that manages the moving surfaces in CONVERGE.

Contours of  $r$  at other instants of the intake exhibited in Figure 6.23 show the same observations as those mentioned above.

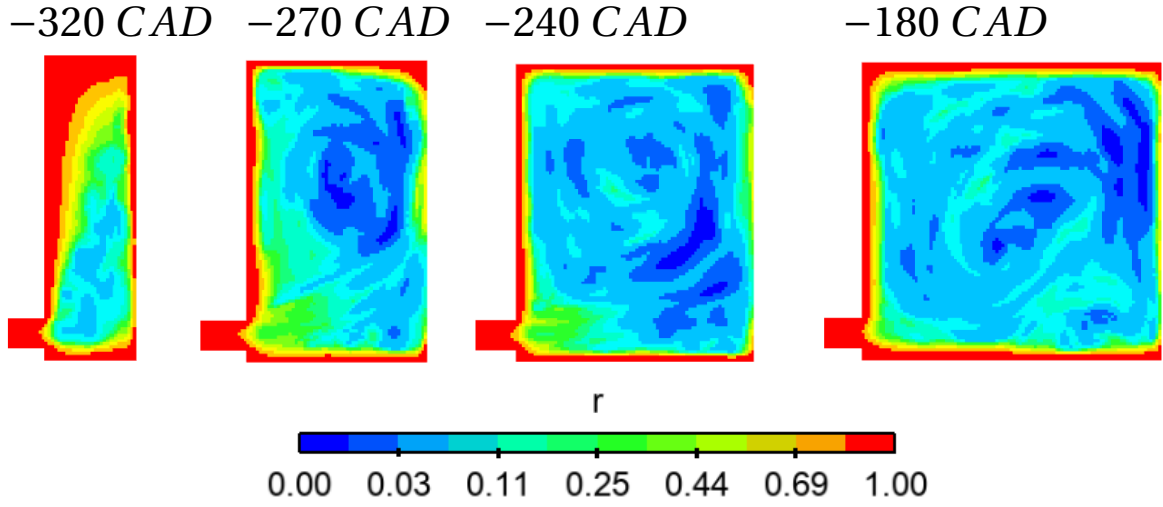


**Fig. 6.23 Compressed Tumble:** Contours of  $r$  in the symmetry plane at four instants during the intake.

The observed energy ratio is investigated by examining the post-processing of:

$$r_{observable} = \overline{k_{sfs}} / k, \quad (6.5)$$

where  $k_{sfs}$  corresponds to the subfilter kinetic energy yielded by the HTLES  $k$ -equation, which was phase-averaged for the post processing, and the total turbulent kinetic energy  $k$  is post-processed from the phase-averaged resolved velocity  $\overline{U}_i$  as:

$$\begin{cases} k = \overline{k_{sfs} + k_{res}} \\ k_{res} = \frac{1}{2}(\tilde{U}_i - \overline{U}_i)(\tilde{U}_i - \overline{U}_i) \end{cases} \quad (6.6)$$

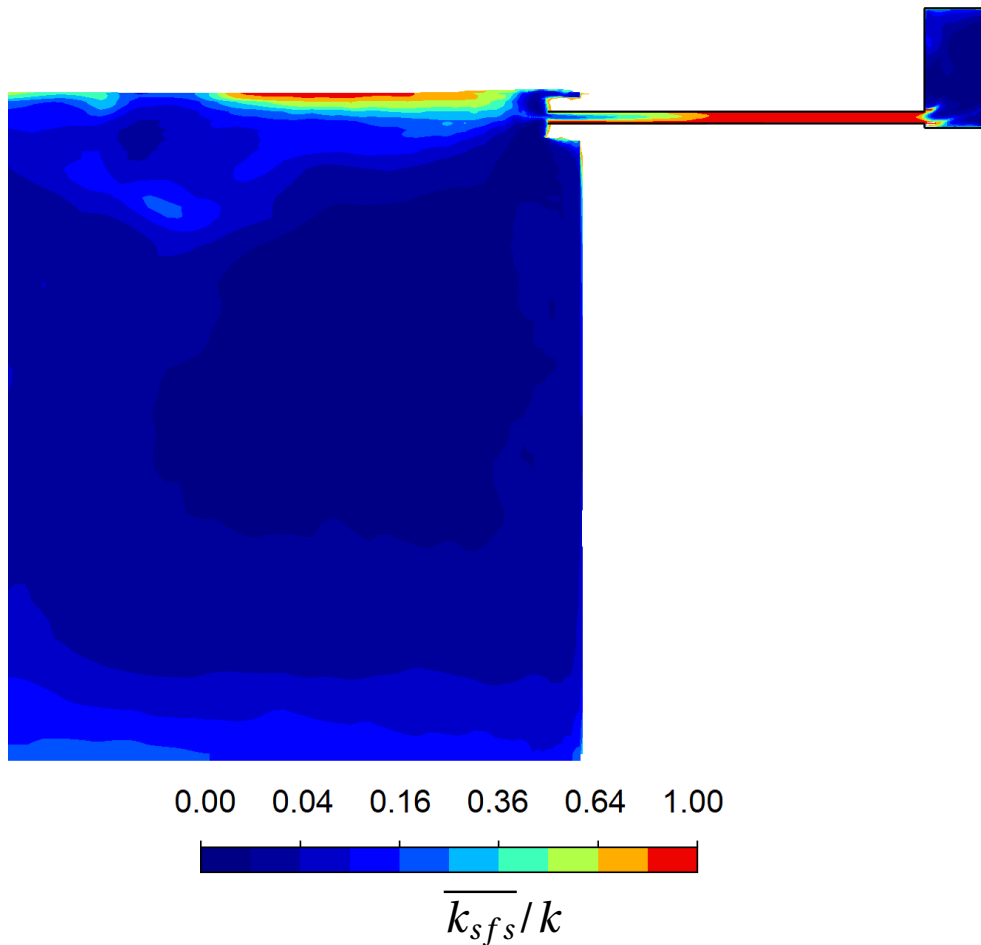


**Fig. 6.24 Compressed Tumble:** Contours of  $\overline{k_{sf_s}}/k$  in the symmetry plane at  $-270 CAD$ .

Figure 6.24 shows the observed energy ratio in the symmetry plane at  $-270 CAD$ . In the plenum, about 10% of the turbulent kinetic energy is modeled and shows a slight spacial variation. In the channel, similar levels than those observed in the plenum are observed at the entrance of the channel. Then, they progressively increase as we move from the plenum until reaching 1, which shows that all turbulent fluctuations are modeled. In the compression chamber, the observed ratio drastically decreases to less than 4% showing that the model operates in LES. At the fixed walls, even if the target energy ratio is equal to 1, a substantial amount of the turbulent kinetic energy is still resolved. As mentioned in the stationary configurations, this is related to the penetration of the resolved flow in the core region in LES, which penetrates the boundary layers.

### 6.5.3.3 Resolved and modeled velocity fluctuations

To further examine the modeled turbulent fluctuations, the velocity fluctuations at four instants of the intake are decomposed into the resolved and subfilter parts:

$$\overline{u'_i u'_i} = SFS + RES, \quad (6.7)$$

Details of this decomposition are provided in Section 6.7.

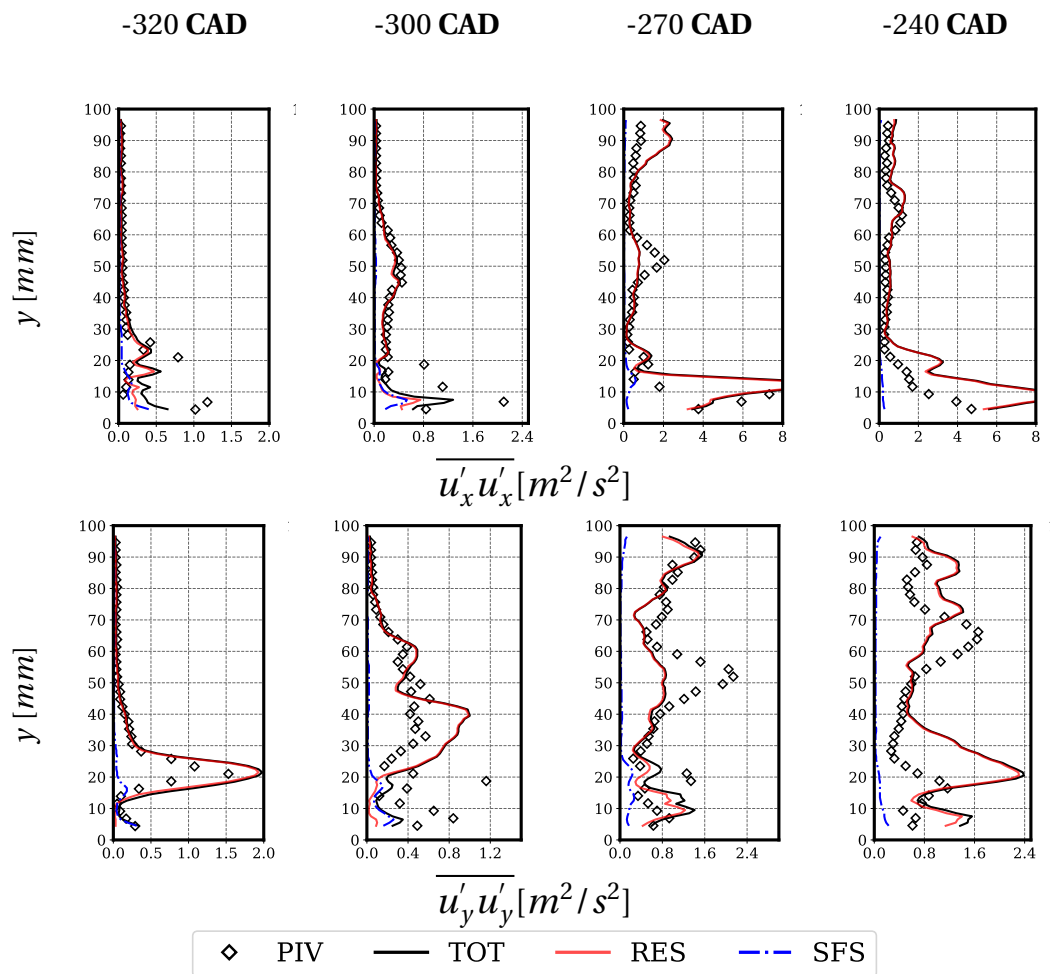


**Fig. 6.25 Compressed Tumble:** Decomposition of the velocity fluctuations into two components, the resolved part *RES* and the modeled part *SFS*.

1D vertical profiles of the resolved velocity fluctuations *RES*, the modeled velocity fluctuations *SFS* and the total velocity fluctuations *TOT* are shown in Figure 6.25. The modeled velocity fluctuations are quasi negligible in the core region, where almost all

velocity fluctuations are resolved and increase at the walls where the RANS mode is activated.

Despite  $r = 1$  near the walls, the resolved velocity fluctuations remain high where the flow is highly disturbed.

#### **6.5.4 Grid dependency**

The grid dependency of the HTLES predictions is examined by comparing the results on three meshes: the coarser mesh M1, the reference mesh M2 (the results of which were already shown in the former Sections) and a finer mesh M3. Details of each mesh are given in Section 6.2.1. First, the phase-averaged velocities are compared. Then, the mean velocity fluctuations are analyzed.

## 6.5.4.1 Mean velocity

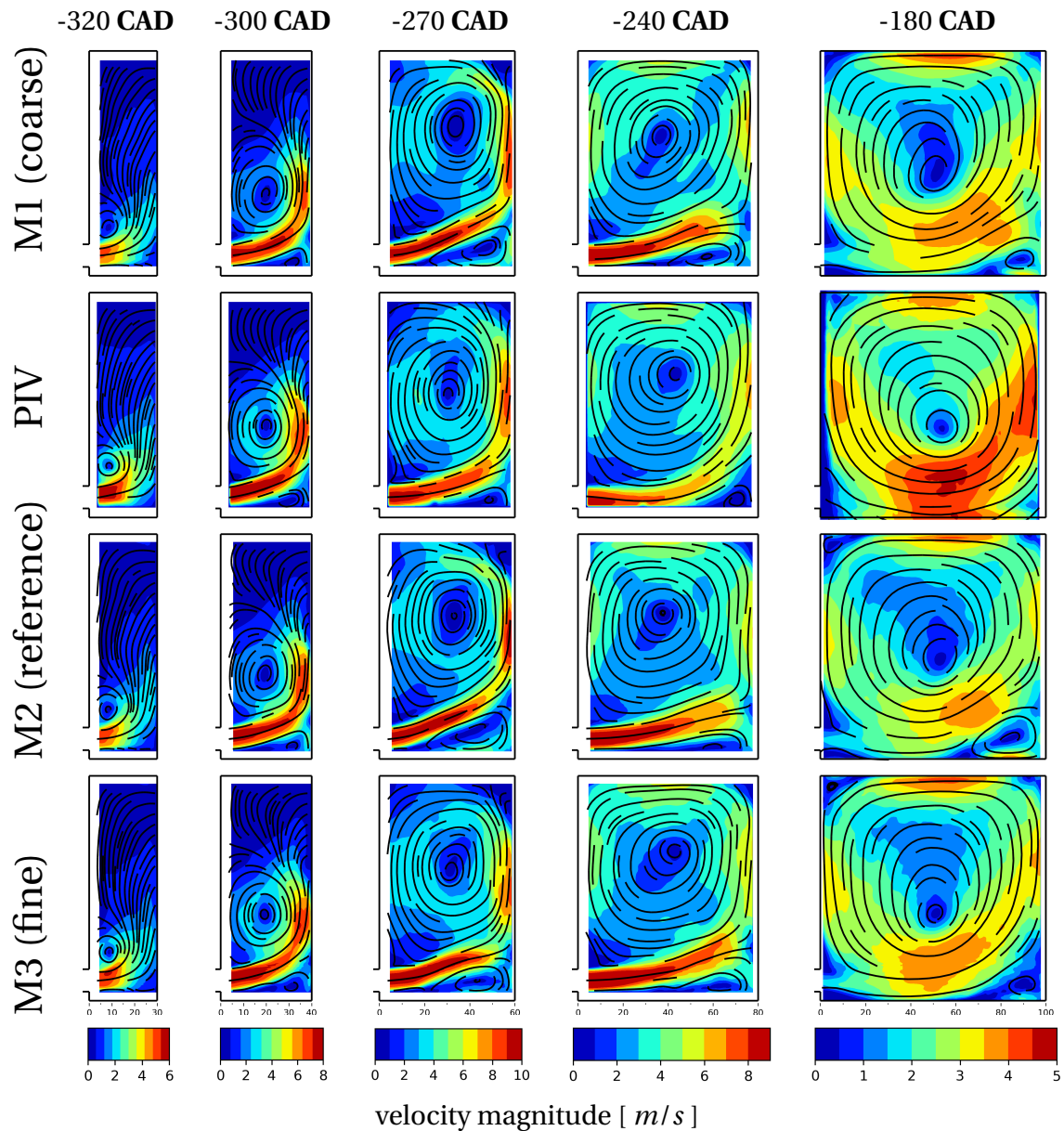


**Fig. 6.26 Compressed Tumble:** Comparison of the in-plane phase-averaged velocity during the intake predicted by HTLES using three meshes.

The contours and streamlines of the phase-averaged velocity predicted by HTLES using *M1*, *M2* and *M3* are compared with the PIV data in Figure 6.26. Their corresponding 1D vertical profiles are given in Figure 6.27.

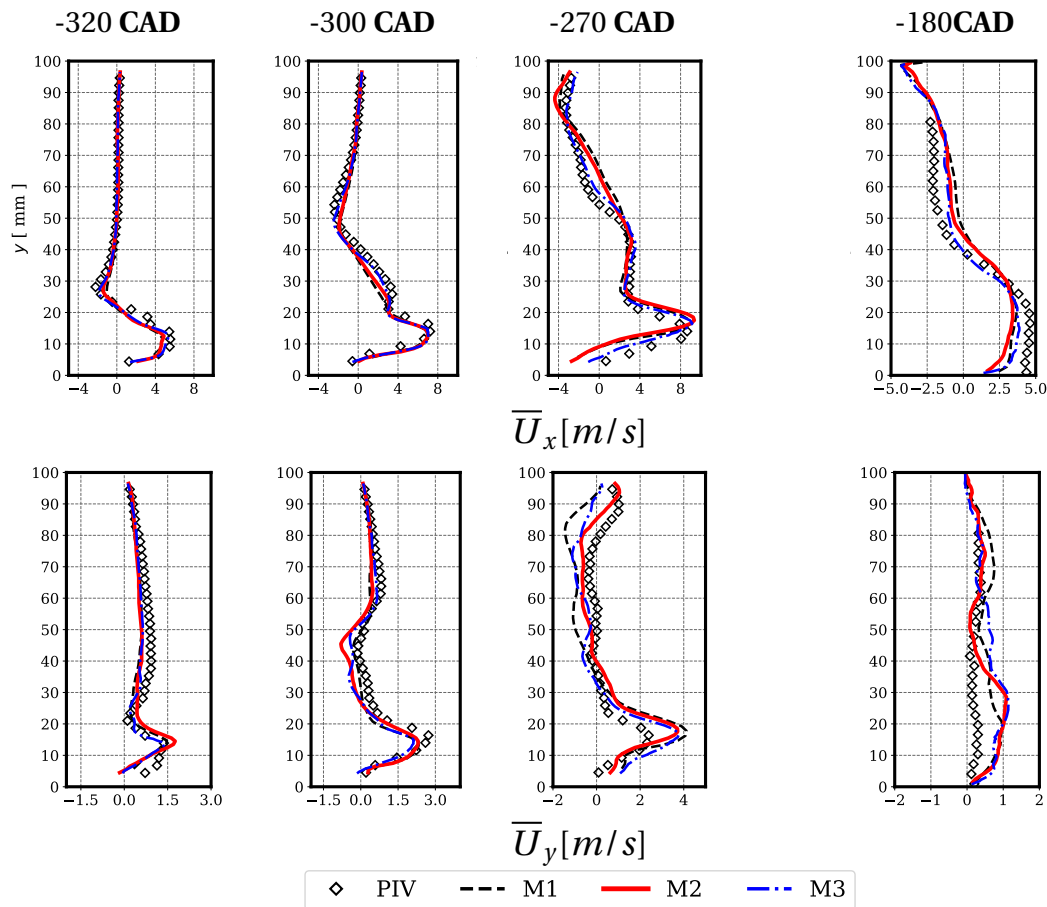


**Fig. 6.27 Compressed Tumble:** Vertical 1D profiles of the phase-averaged velocity during the intake predicted by HTLES using three meshes: M1 (**finer**), M2 (**reference**) and M3 (**coarser**).

The impact of the mesh resolution in the intake jet can be seen from the first shown instant at  $-320\text{ CAD}$ . The 1D profile of the horizontal velocity is slightly improved in M3. However, the mesh refinement does not improve the deflection of the intake jet, as shown by the profiles of the vertical velocity, which is underestimated in the three simulations in comparison to PIV. From the predicted streamlines, one can see that the center of rotation is well located in all three simulations, even if the mesh refinement slightly enhances the simulation results, which agree well with the PIV findings. The more accurate prediction of the intake jet penetration is given by the simulation using M3, which enhances the prediction of the rotational speed of the tumble that is no longer underestimated as it is in M1 and M2.

The second shown instant (at  $-300\text{ CAD}$ ), shows no significant differences between the three simulations, except for the rotational speed, which is accurately predicted in M3.

At  $-270$  CAD, the overestimation of the upward deflection of the intake jet appears for all three meshes as can be observed in the velocity streamlines. A slight improvement is nonetheless visible in *M3*. This results in a better formation of the tumble in *M3*, which can be observed by examining the rotational speed, the rotational core of the tumble and the tumble front. Concerning the latter, one can observe that the high velocity extent corresponding to the tumble front is more accurately predicted in *M3* than in *M1* and *M2*.

At the fourth shown instant ( $-240$  CAD), the simulations predict fairly similar tumble characteristics, apart from the rotational core, which is in better agreement with PIV in *M3*.

At  $-180$  CAD, the simulation using *M3* predicts slightly better the high velocity regions as a result of an overall better prediction of the tumble characteristics at former instants. The bottom recirculation, which is only shown in the simulations, is slightly reduced in *M3*.

## 6.5.4.2 Mean velocity fluctuations

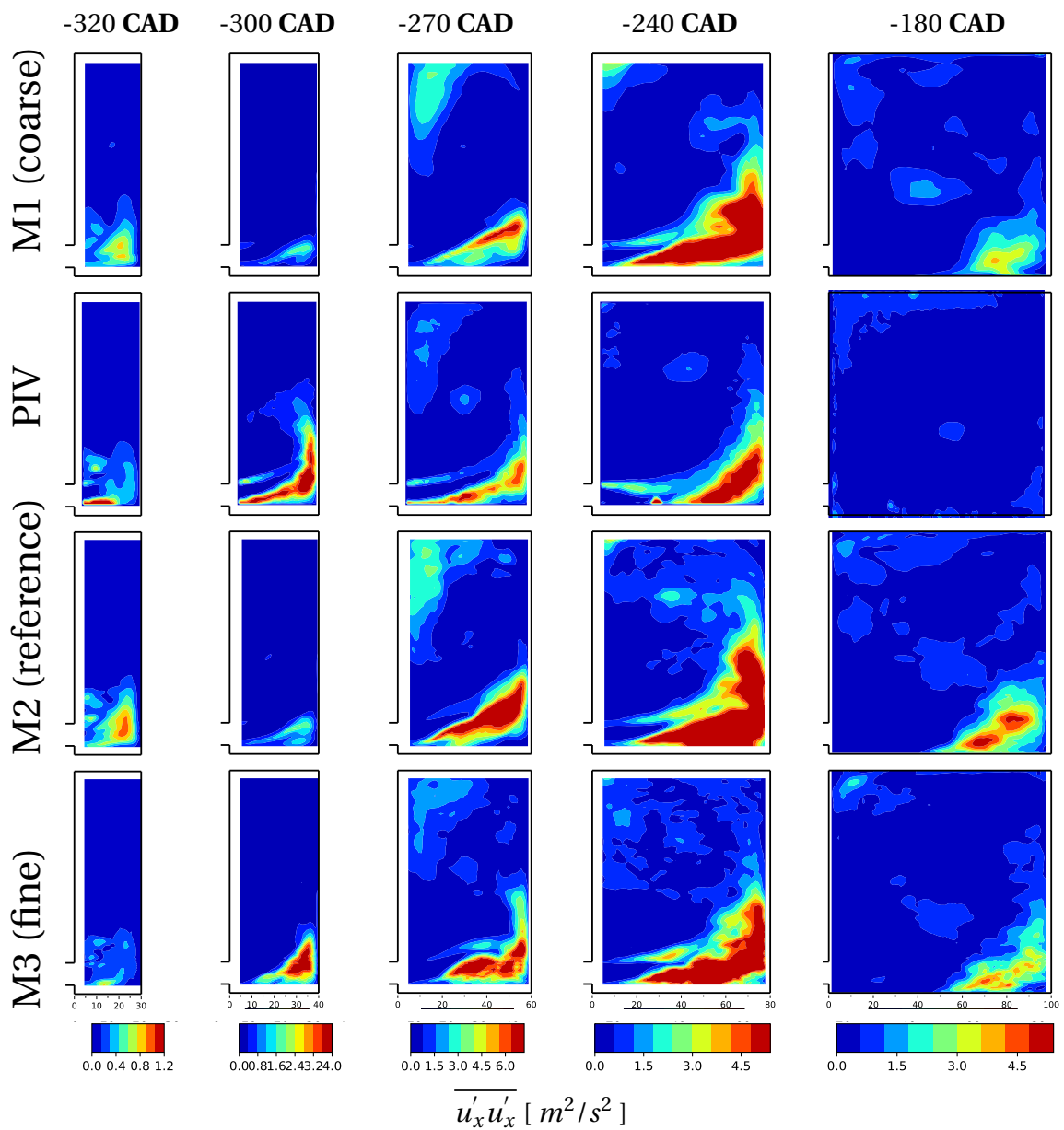


**Fig. 6.28 Compressed Tumble:** contours of the mean velocity fluctuations  $\overline{u'_x u'_x}$  during the intake predicted by HTLES using three meshes.

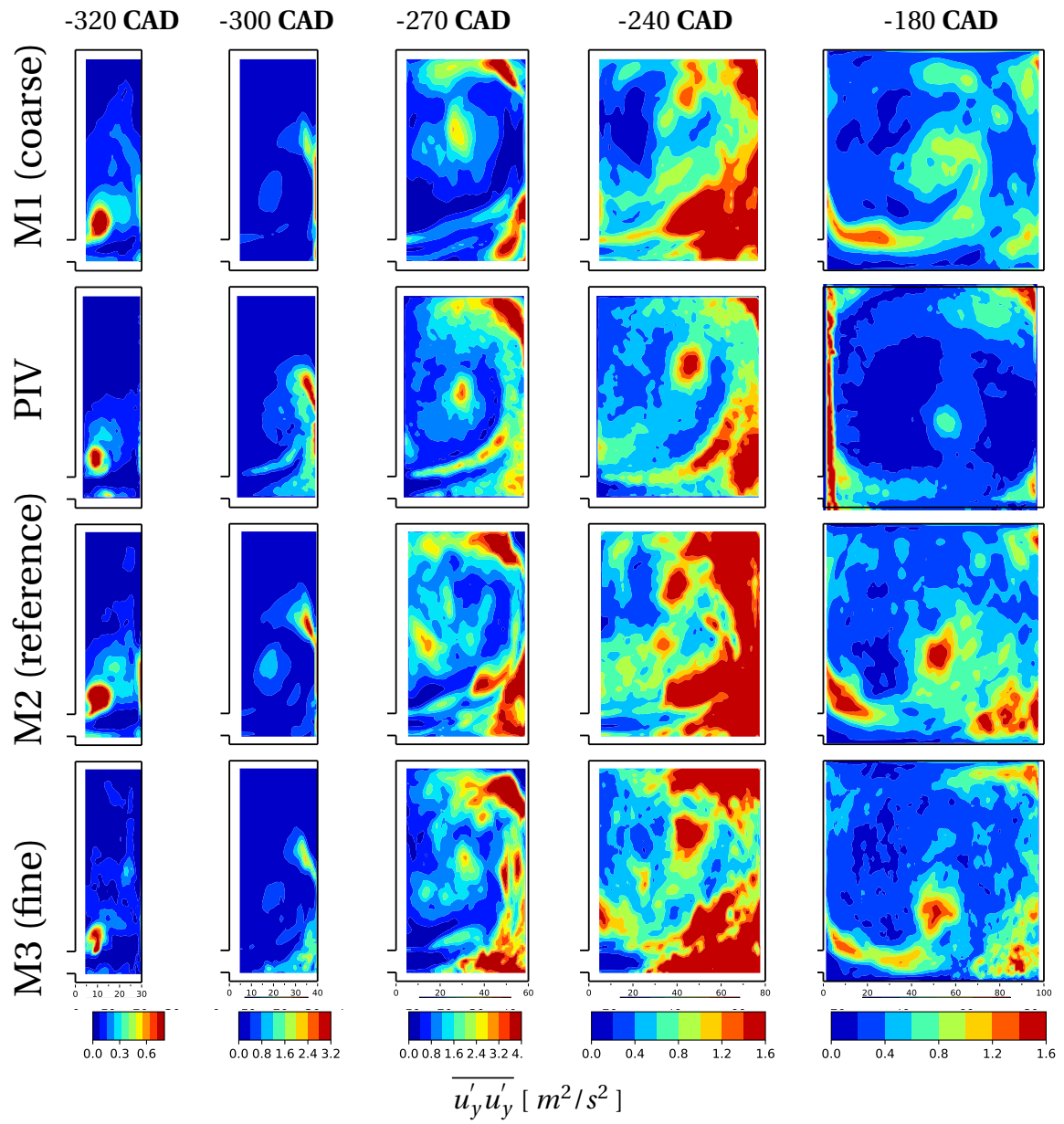


**Fig. 6.29 Compressed Tumble:** Contours of the mean velocity fluctuations  $\overline{u'_y u'_y}$  during the intake predicted by HTLES using three meshes.

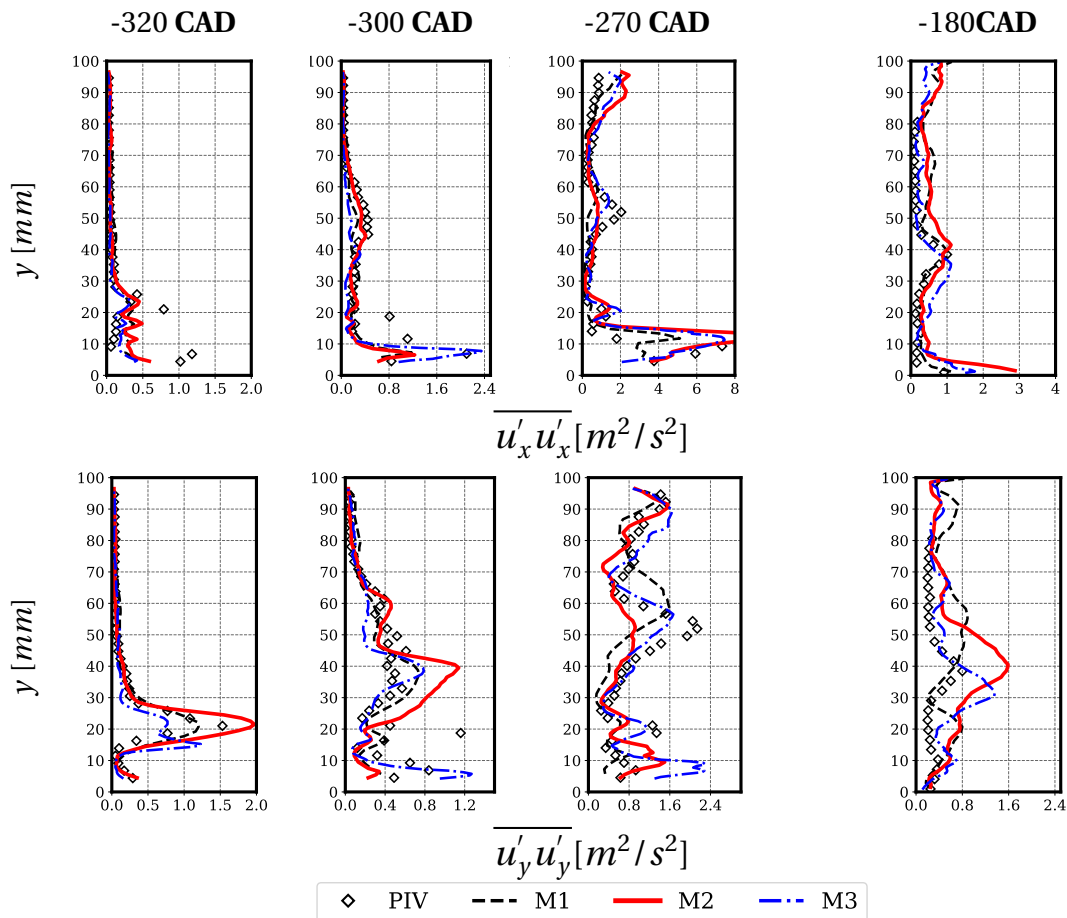


**Fig. 6.30 Compressed Tumble:** 1D vertical profiles of the mean velocity fluctuations during intake predicted by HTLES using three meshes: M1 (**finer**), M2 (**reference**) and M3 (**coarser**).

The simulation results of the mean fluctuations of the horizontal and vertical velocity components are shown in Figure 6.28 and 6.29, respectively. Their corresponding 1D vertical profiles are shown in Figure 6.30. At the first shown instant, the contours of  $\overline{u'_x u'_x}$  show high fluctuation regions at the tip of the intake jet, in simulations using *M1* and *M2*. The mesh refinement in the intake jet region in *M3* prevents this discrepancy with PIV. Improvements using *M3* can also be observed in the contours of  $\overline{u'_y u'_y}$ , where the fluctuation region around the rotational core is more accurately predicted than in the simulations using *M2* and *M1*, which slightly overestimate its extent as compared to PIV. The high fluctuations that appear in the shear layers of the intake jet, at  $-300$  CAD, are better predicted in *M3*. Concerning the tumble front fluctuations, the contours of  $\overline{u'_y u'_y}$  show that all simulations capture fairly accurately the increase in the velocity fluctuations. The third shown instant corresponds to  $-270$  CAD. At this instant, the simulations using

*M1* and *M3* yield smaller recirculations beneath the jet flow than in *M2*, yielding less fluctuations in  $\overline{u'_x u'_x}$  within this region. The tumble front fluctuations are better predicted in *M3* while *M1* and *M2* tend to slightly overestimate them in comparison with PIV. The tumble rotational core is well defined in *M3*.

## 6.6 Results for the compressed configuration

For the compressed case, which is the subject of this Section, the guillotine closes during the compression allowing the engine to feature a four-stroke cycle. During the intake, the process is similar to the configuration without the guillotine. Hence, the focus is put on the compression stroke during which the tumble is compressed.

Owing to the double duration of the four-stroke cycle, as compared to the uncompressed case, only 21 cycles could be simulated. The phase averages were computed on the last 18 cycles.

The analysis of the results is organized as follows. First, the in-cylinder pressure is compared with experimental findings. Then, the phase-averaged velocity and the mean velocity fluctuations are examined during the compression stroke.

### 6.6.1 In-cylinder pressure

Figure 6.31 compares the time evolution of the in-cylinder pressure predicted by RANS, HTLES and LES at the third cycle with the experimental measurements. As the engine works in non-fired conditions, the in-cylinder pressure profiles are similar from a cycle to another.

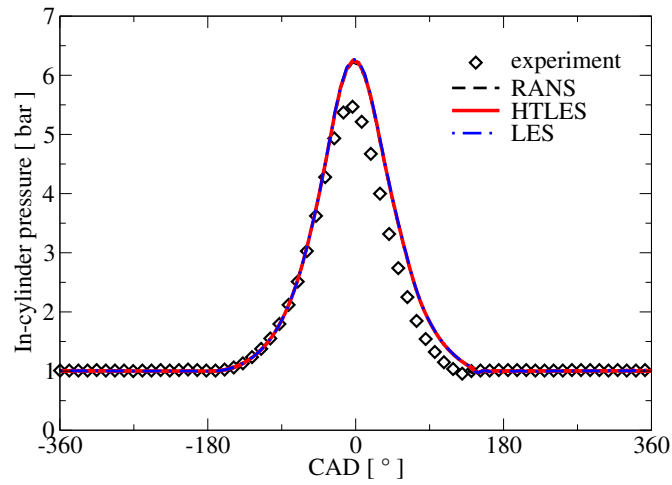


**Fig. 6.31 Compressed Tumble:** Time evolution of the in-cylinder pressure predicted by RANS, HTLES, and LES versus the experimental data.

The simulations reproduce accurately the pressure increase during the early stages of the compression. However, from  $-45$  CAD, the simulations yield a higher pressure than in the experiment and overpredicts the maximum pressure by 0.7 bar. Indeed, while the pressure peak is 5.5 bar in the experiment, it is 6.2 bar in the simulations. A mass leakage of 10% was observed in the experiment during the compression [10], possibly explaining the observed over-estimation of the peak pressure by 11% in the simulations that did not include a blow-by model.

## 6.6.2 Mean velocity

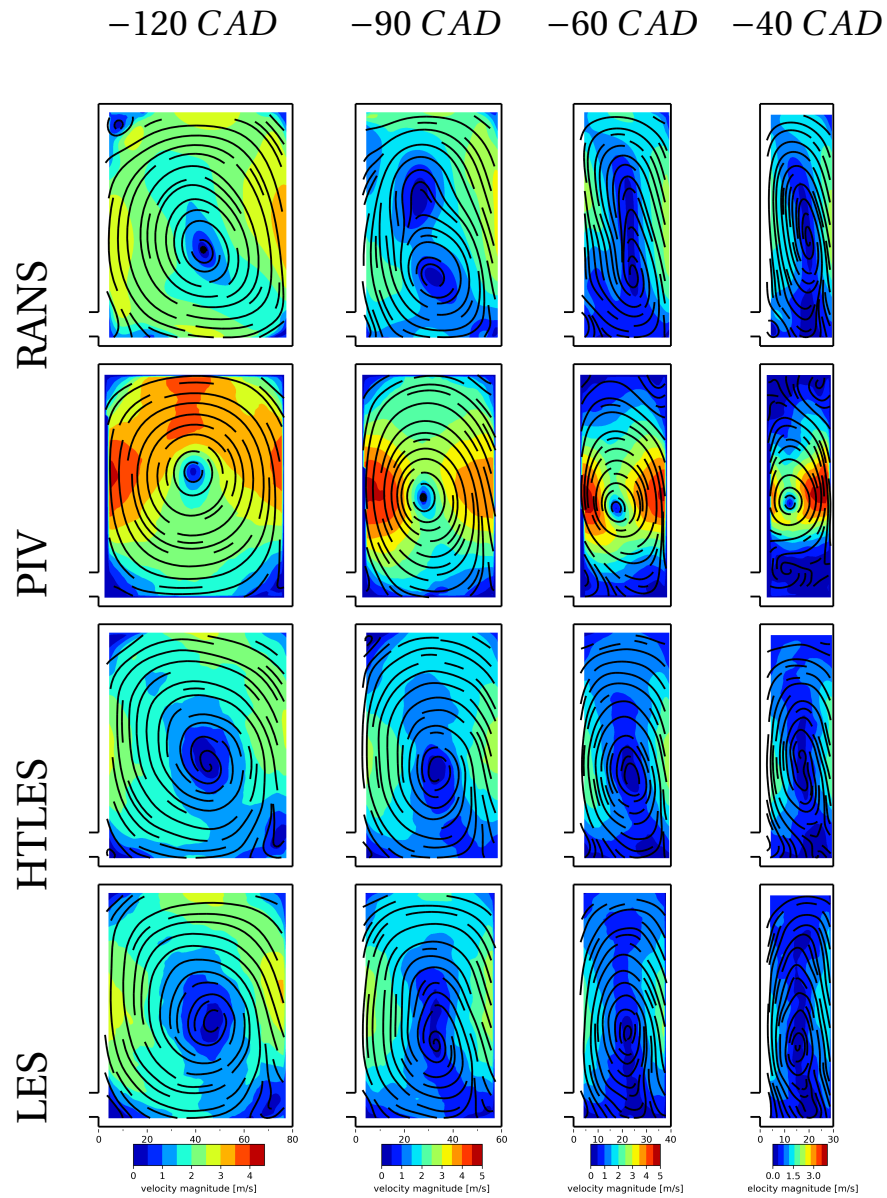


**Fig. 6.32 Compressed Tumble:** Contours and streamlines of the phase-averaged velocity during compression.

Contours and streamlines of the phase-averaged velocity for RANS, HTLES, LES and PIV at four instants during the compression are depicted in Figure 6.32. Figure 6.32 shows the vertical 1D profiles of the phase-averaged velocity and the mean velocity fluctuations, extracted halfway between the cylinder head and the piston.

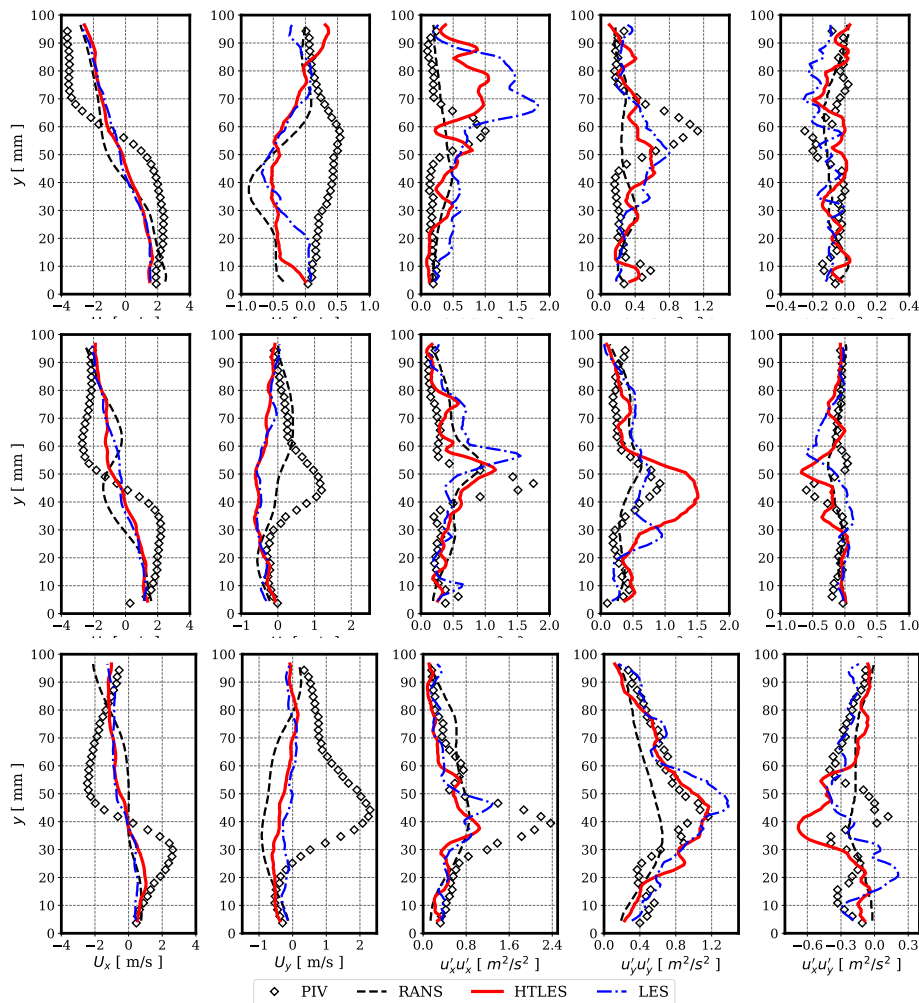


**Fig. 6.33 Compressed Tumble:** Vertical 1D profiles of the phase-averaged velocity and the velocity fluctuations during compression.

All simulations underestimate the tumble rotational speed, as it was underestimated at the end of the intake as shown in Section 6.5.1.1 for the compressed configuration.

At the first shown instant ( $-120$  CAD) the tumbling vortex center predicted by the simulations is situated closer to the piston than in PIV. The 1D profiles of the horizontal velocity are clearly underestimated in the simulations. The inaccurate location of the tumbling vortex can be observed on  $\overline{U}_y$ , which at certain locations has an opposite sign compared to PIV.

At  $-90$  CAD, the tumbling vortex starts to break down in RANS, while no similar phenomenon at this angle is apparent in PIV or in HTLES and LES. HTLES and LES yield

fairly similar results at this instant. At the end of the compression, none of the simulations succeeds to predict the tumbling vortex breakdown observed in the experiment.

### 6.6.3 Turbulence modeling during compression

This section aims at examining the differences between HTLES and LES in terms of turbulence modeling during compression by exploring the viscosity ratio  $\frac{\nu_{sf}}{\nu_{mol}}$  obtained by each approach. The analysis hereafter is based on the phase averages the viscosity ratios for a more organized vision.

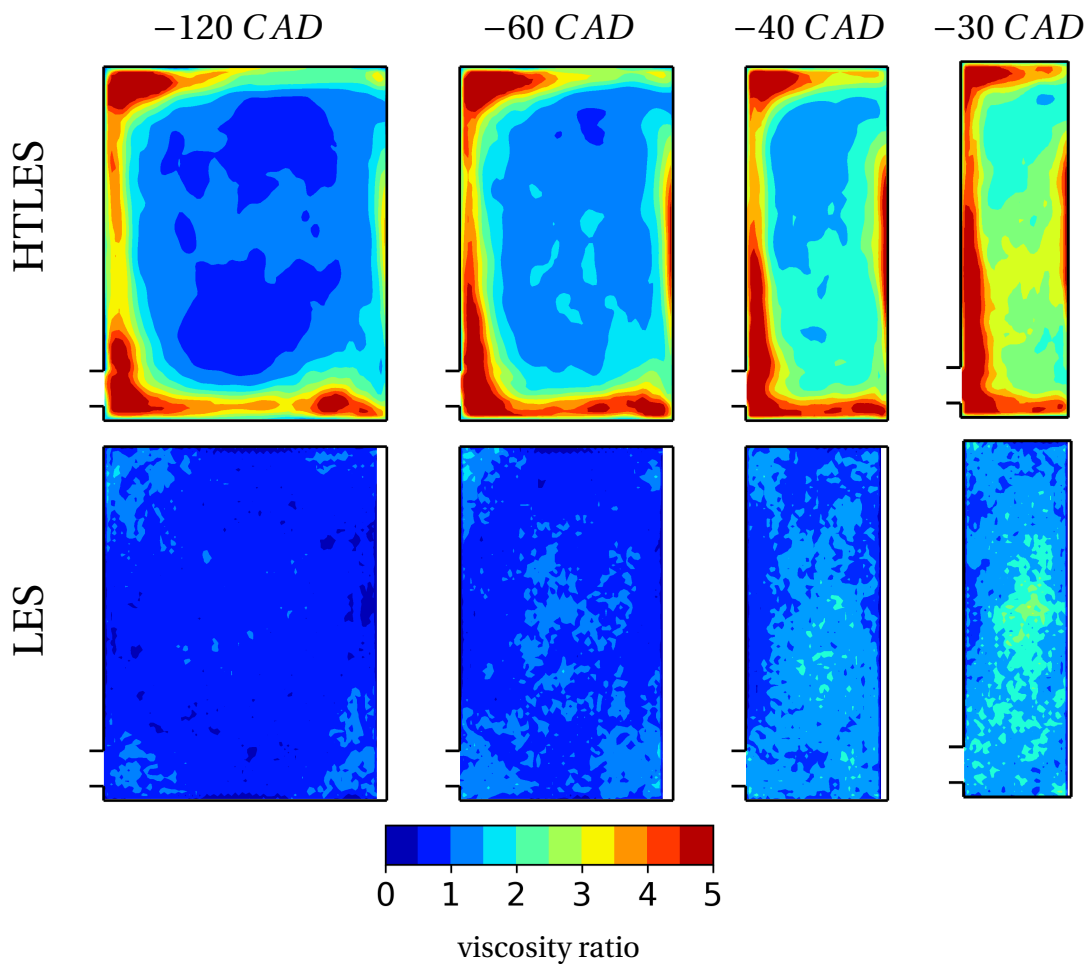


**Fig. 6.34 Compressed Tumble:** Contours of the phase-averaged viscosity ratio during compression in the symmetry plane.

Figure 6.34 shows the phase-averaged viscosity ratio  $\frac{\overline{\nu_{sfs}}}{\nu_{mol}}$  at four instants of the compression yielded by HTLES and LES. HTLES yields overall higher turbulent viscosity ratios than LES. At the fixed walls, the viscosity ratio increases as the RANS mode is triggered. A smaller increase is observed at the moving wall as the elliptic shielding fails to activate at the moving walls (see Section 6.5.3.2). In the core region, the subfilter viscosity decreases, as a larger proportion of the flow scales can be resolved. At the end of the compression, the turbulent scales become finer as the tumble breaks down, which makes HTLES increase the subfilter viscosity.

From a numerical point of view, the turbulent viscosity ratio can affect the simulation's numerical stability. As mentioned in Section 4.3.2.1, CONVERGE locally downgrades the spatial scheme from the second-order central differencing to the first-order upwind scheme to prevent non-physical oscillations (also known as "wiggles") that can appear when the second-order differencing scheme is used. Figure 6.35 shows the evolution of the number of upwinded cell faces during a randomly chosen cycle for RANS, LES, and HTLES.

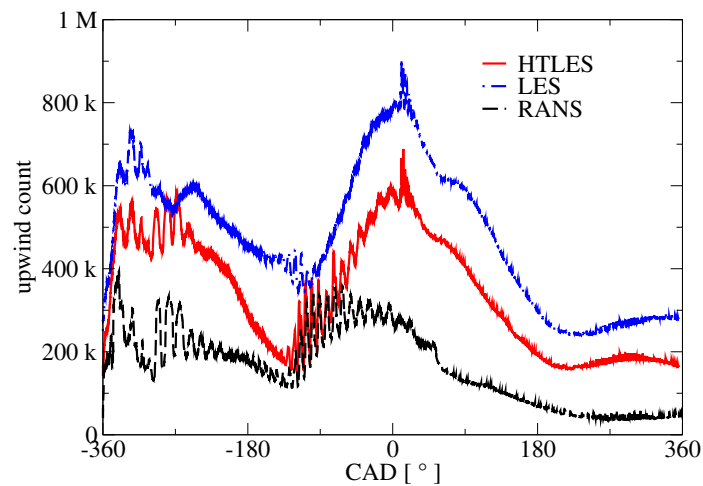


**Fig. 6.35 Compressed Tumble:** Time evolution of the number of the upwinded cell faces in RANS, HTLES and LES simulations.

RANS simulation yields the least number of upwinded cell faces, followed by HTLES then LES. This results from the more elevated the turbulent viscosity, the smaller the local gradients, which lowers the propensity to generate local numerical instability. From this

fact, HTLES reduces the upwinding by 40% compared to LES, as it partly operates in LES and RANS.

## 6.7 Statistical convergence

In order to examine the statistical convergence of the phase-averaged HTLES results, phase-averaged velocity and mean velocity fluctuation results are examined based on an increasing number of cycles used in the averaging process. The phase-averaged velocity for each crank angle (CA)  $\theta$  is computed as:

$$\bar{U}_i(\theta) = \frac{1}{N} \sum_{k=1}^N \tilde{U}_i^{(k)}(\theta), \quad (6.8)$$

where  $N$  is the number of included cycles,  $\tilde{U}_i^{(k)}(\theta)$  is the instantaneous resolved velocity at cycle  $k$ . The mean velocity fluctuations  $\overline{u'_i u'_j}$  are calculated as the sum of:

- the resolved velocity fluctuations calculated from the resolved velocity  $\bar{U}_i$  as:

$$RES = \overline{(\tilde{U}_i - \bar{U}_i)(\tilde{U}_i - \bar{U}_i)}. \quad (6.9)$$

- the subfilter velocity fluctuations estimated using the Boussinesq hypothesis:

$$SFS = \overline{-2\nu_{sfs} \frac{\partial \tilde{U}_i}{\partial x} + \frac{2}{3} k_{sfs}}, \quad (6.10)$$

where  $i$  is either  $x$  for the horizontal or  $y$  for the vertical component.

$$\overline{u'_i u'_j} = RES + SFS. \quad (6.11)$$

In the case of LES, only the resolved part is considered.

The convergence of the statistics is evaluated using two quantities. First, the evolution of the resolved kinetic energy in the symmetry plane with numbers of averaging cycles is examined. Then, 1D profiles of the mean velocity and mean velocity fluctuations obtained increasing numbers of averaging cycles are compared.

The kinetic energy for each velocity component is calculated using:

$$\sigma_{U_i}(\theta) = \frac{1}{N} \sum_{k=1}^N (\tilde{U}_i^{(k)}(\theta))^2. \quad (6.12)$$

Its value in the symmetry plane as a function of number of averaging cycles  $N$  is examined in Figure 6.36 at 3 different instants of the intake in the uncompressed engine. The black dashed lines represent the kinetic energies obtained using 80 averaging cycles.

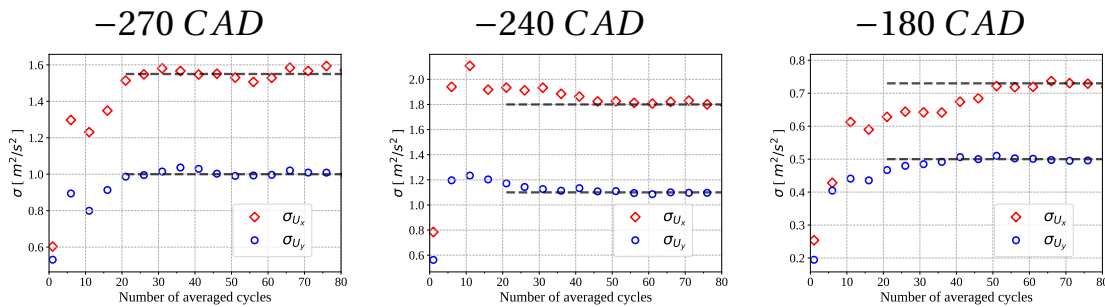


**Fig. 6.36 Compressed Tumble:** Evolution of the kinetic energy in the symmetry plane with numbers of averaging cycles at 3 instants of the intake stroke.

At the first shown instant, at  $-270 \text{ CAD}$ , the kinetic energy of both velocity components increases until 30 cycles and reaches a nearly constant plateau for higher numbers of cycles. At  $-240 \text{ CAD}$ , the variance of the  $x$  velocity component  $\sigma_{U_x}$  requires at least 40 cycles to stabilize, while for the  $y$  velocity component 30 cycles are sufficient to reach a converged state. The third shown instant corresponds to BDC, the variance of the  $x$ -component stabilizes around 40, but requires at least 50 cycles to stabilize. Concerning the variance of the  $y$ -component reaches the asymptote line around 40 averaged cycles.

The performed analysis shows that 40 cycles is enough to provide a converged kinetic energy for the three investigated instants.

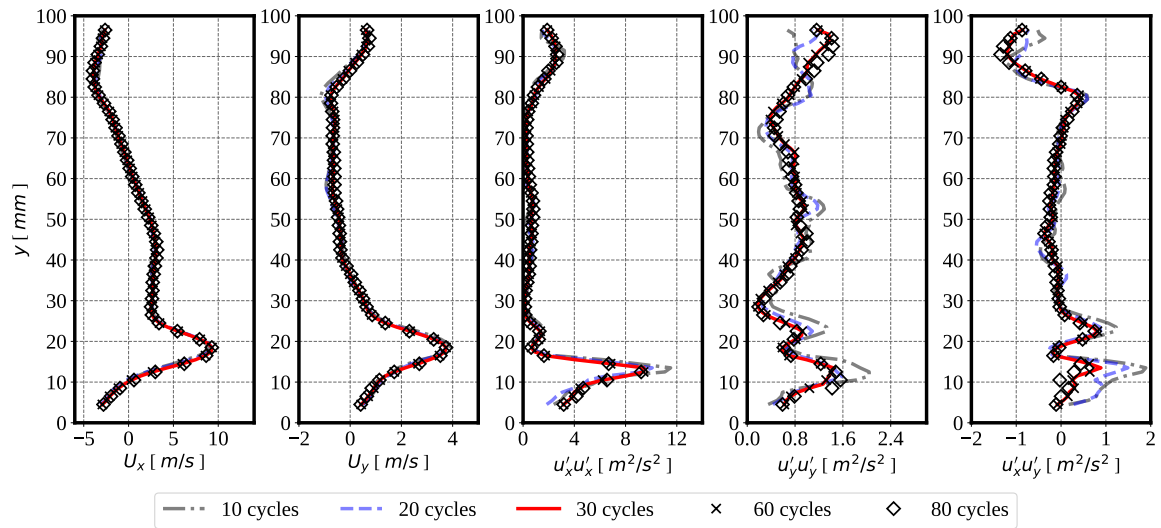


**Fig. 6.37 compressed tumble:** Vertical 1D profiles of the first two statistical moments at  $-270$  CAD.

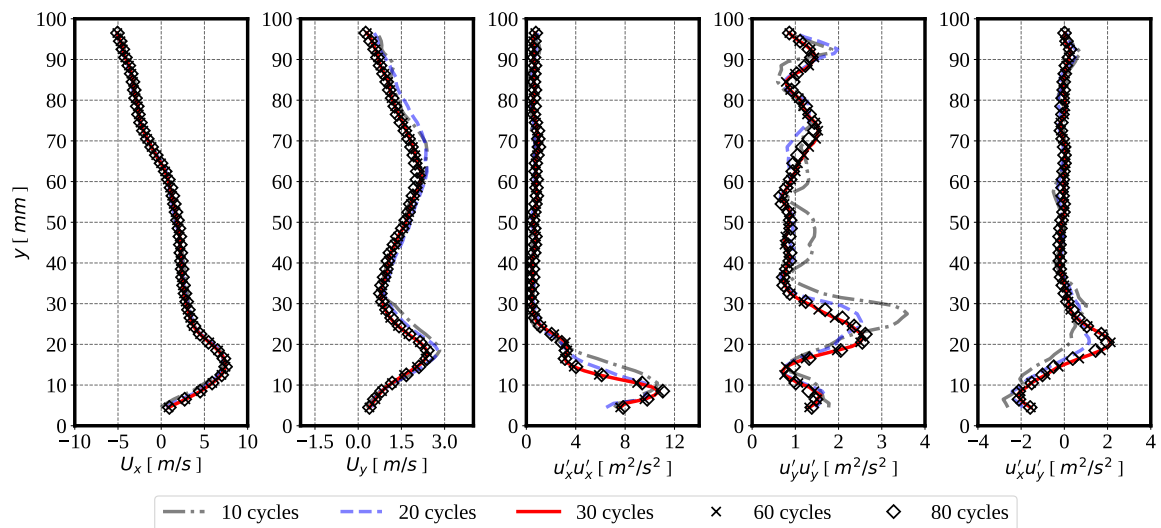


**Fig. 6.38 Compressed Tumble:** Vertical 1D profiles of the first two statistical moments at  $-240$  CAD.

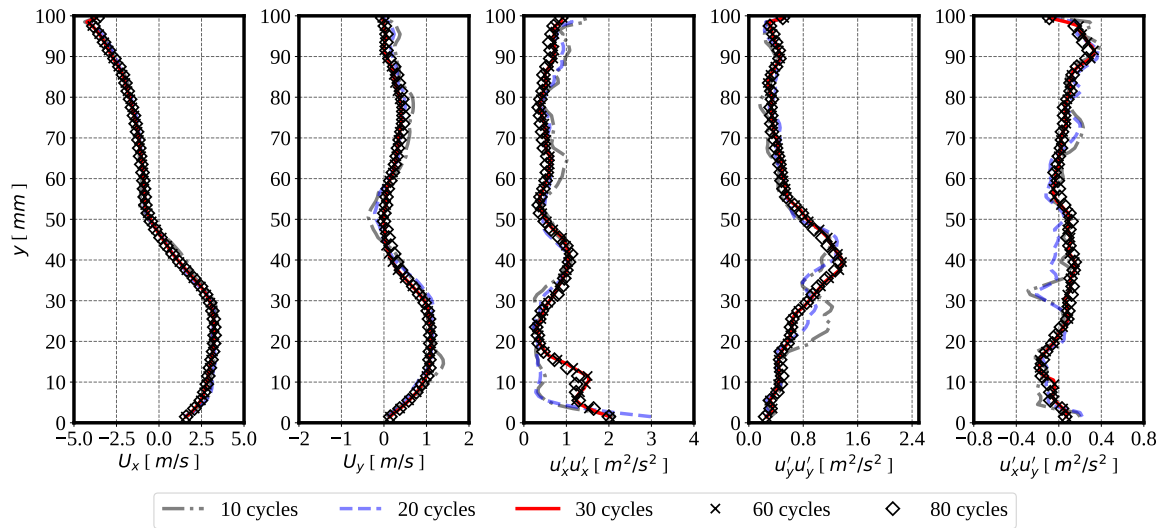


**Fig. 6.39 Compressed Tumble:** Vertical 1D profiles of the first two statistical moments at  $-180$  CAD.

To further investigate the phase average convergence, Figures 6.37, 6.38 and 6.39 show the vertical 1D profiles of the two first statistical moments profiles at three instants of the intake.

For the phase-averaged velocity, one can observe that, overall, the 1D profiles are similar up from 20 cycles. The mean velocity fluctuations require more cycles with at least 30 cycles to have converged results.

From these analyses, it is shown that using 40 averaging cycles are sufficient to have reasonable statistics. Accordingly, HTLES and LES results will be phase averaged on 40 cycles in order to compute the first two statistical moments. The convergence of LES was not checked separately, as it was found that LES results are quite comparable to those of HTLES.

## 6.8 Conclusions

A first validation of EWA-HTLES in engine flows was provided in the compressed tumble engine. Both the uncompressed and the compressed configurations were examined.

The first step was to examine the piston laws provided in the literature. It was shown that the experimental piston law contains small fluctuations, which provoked large oscillations in the velocity and pressure that were not observed in the experiment. A smoothed piston law was proposed to reduce these oscillations.

A total number of 43 consecutive cycles of the uncompressed configuration was simulated using HTLES and LES. The results were phase averaged from the third cycle for meaningful comparison with the PIV findings. A RANS simulation was also performed, the results of which were taken from the third cycle. The simulation results showed that HTLES and LES provided fairly similar predictions that were in good agreement with PIV. RANS results showed acceptable results in terms of velocity predictions but were less satisfactory in predicting the mean velocity fluctuations. Unlike RANS, HTLES and LES captured fairly well the increase in mean velocity fluctuations in regions characterized by CCV.

Nonetheless, all the simulation results were less satisfactory at the end of the intake. The exact reason that explains such discrepancies with PIV at this moment remained unsolved.

With regard to the turbulence modeling, it was shown that HTLES operates in RANS in the channel and in LES in the compression chamber. Even if the elliptic shielding was activated at the fixed walls of the cylinder, it was shown that a large portion of the turbulent fluctuations was still resolved due to the penetration of the scales resolved in LES in the boundary layers. The elliptic shielding could not be activated at the moving piston due to a problem related to moving boundary conditions that have not been solved. In the plenum, even if the energy ratio reached high values, the simulation still resolved a large portion of the turbulent fluctuations.

The grid dependency of HTLES was explored by using three meshes of different resolutions. It was shown that the results were not significantly affected when the mesh resolution was decreased. Nevertheless, refining the intake jet region improved the simulation predictions in terms of tumble characteristics and of mean velocity fluctuations. For the compressed configuration, 21 consecutive cycles were simulated using HTLES and LES. A RANS simulation was also performed, the results of which were extracted from the third cycle. All simulations showed important discrepancies with the experimental data. They gave higher peak pressures at the end of compression than the experiment due to a mass leakage that was present in the experiment and which was not included in our simulations. The flow predictions of the simulations were not satisfactory. Indeed, they

showed an important underestimation of the tumble speed during compression and an inaccurate representation of the process of the compression of the tumble, as the flow was not well predicted at the end of the intake.

# Chapter 7

## The Darmstadt engine

The validation of turbulence models for in-cylinder flows implies performing tests on realistic configurations with complex moving parts and non-stationary boundary conditions. In such conditions, unsteady phenomena, such as the formation and the breakdown of the tumbling motion and CCV, appear in the combustion chamber and need to be addressed adequately to accurately describe the engine functioning and predict its performance [51]. Baum *et al.* [5] acquired a detailed database of the flow in a motored single-cylinder engine with optical accesses.

This Chapter provides a first validation of EWA-HTLES in a non-fired realistic SI engine. The first Section introduces the Darmstadt Engine and its main specifications. Then, Section 7.2 provides the details of the used numerical parameters, meshes and turbulence models. The last Section aims at evaluating the HTLES predictions with regard to the intake and compression phases. The simulation results are compared with the PIV findings, and RANS and LES. The results are provided in four parts. The result analysis starts by examining the integral flow quantities. After that, the turbulence modeling in HTLES during the intake and compression phases is analyzed. After that, the mean and RMS velocities predicted by the simulations are compared with the PIV. Finally, the sensitivity of the simulation results to mesh is evaluated using two meshes.

## 7.1 Configuration and computational domain

The experimental configuration of the Darmstadt engine is illustrated in Figure 7.1. The intake system comprises different parts such as mass flow controllers (MFC), pneumatic valves (PV), and flow heaters (H) that allow conditioning the intake air in terms of pressure, temperature and gas composition. The plena P3 and P4 connected, respectively, to the intake and exhaust ports are used for sound reduction [5].

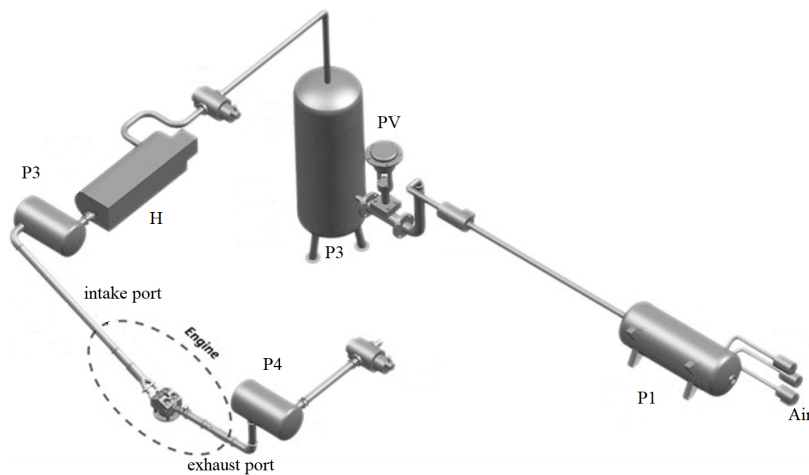


**Fig. 7.1 Darmstadt Engine:** Experimental setup [5].

The simulated part is restricted to the encircled part. It comprises the intake and exhaust ports and the engine. The intake port consists of a dualport, which is attached to the cylinder head and is designed in such a way that a high level of charge motion (*i.e.*, tumble) is introduced in the engine. The engine features a non-fired four-stroke cycle (see Section 1.2). CAD is used to measure time:

- intake stroke: from  $-360$  to  $-180$  *CAD*.
- compression stroke: from  $-180$  to  $0$  *CAD*.
- expansion stroke: from  $0$  to  $180$  *CAD*.
- exhaust stroke: from  $180$  to  $360$  *CAD*.

The engine consists of a single-cylinder Spark Ignited Direction Injection (SIDI) optical engine. The cylinder head has a four-valve pent-roof configuration. The main specifications of the engine are listed in Table 7.1.

Bore [ <i>mm</i> ]	86
Stroke [ <i>mm</i> ]	86
Clearance height [ <i>mm</i> ]	2.6
Conrod length [ <i>mm</i> ]	148
Intake valve opening instant [ <i>CAD</i> ]	325
Intake valve closing instant [ <i>CAD</i> ]	-125
Exhaust valve opening instant [ <i>CAD</i> ]	105
Exhaust valve closing instant [ <i>CAD</i> ]	-345
Engine speed [ <i>RPM</i> ]	800
Engine displacement [ <i>cm</i> <sup>3</sup> ]	499.6
Compression ratio [ – ]	8.5

**Table 7.1 Darmstadt Engine:** Main specifications.

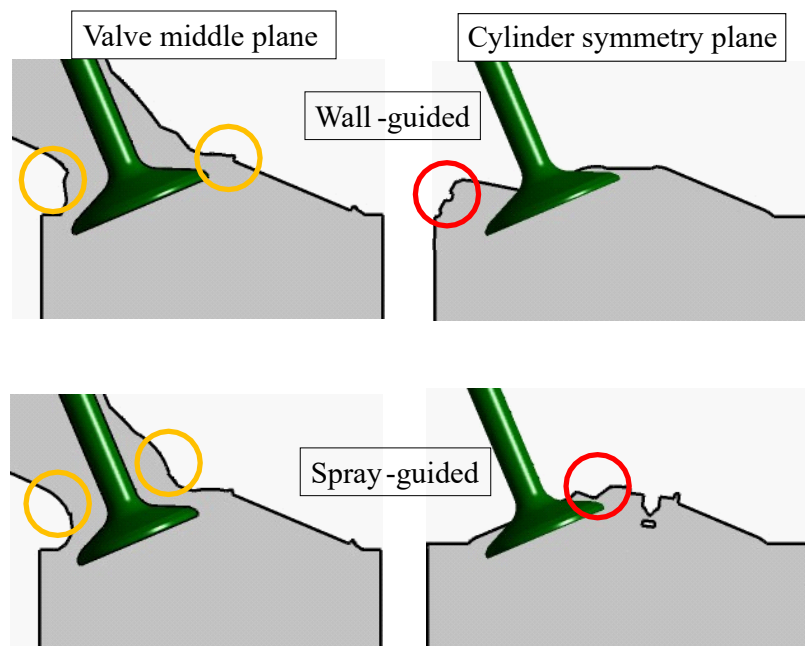


**Fig. 7.2 Darmstadt Engine:** Illustration of the two available configurations of the engine, Figure adapted from [15].

There are two different engine configurations of the Darmstadt engine: the Wall-Guided (WG) engine and the Spray-Guided (SG) engine (see Figure 7.2). Both engines are

identical in terms of their global parameters (see Table 7.1). Among differences between the two configurations are:

- the extremity of intake port which, as shown by the orange circles in the valve plane, has a sharper edge (separation edge) in the wall-guided than in the spray-guided engine.
- the intake valves, which have a smaller diameter of the valve disks in the spray-guided engine.
- the geometry of the cylinder head as shown by the red circles in the cylinder symmetry plane.

Other modifications related to the injector position are not discussed here as it is inactive in the experiment considered here. More details about each configuration can be found in [6, 12, 33]. The focus in what follows is restricted to the wall-guided engine. Its computational domain is illustrated in Figure 7.3

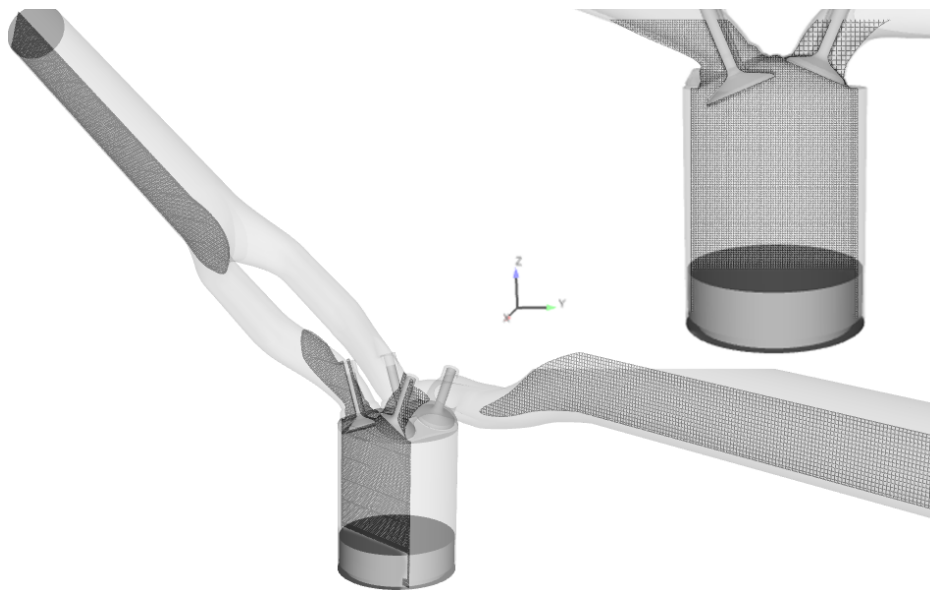


**Fig. 7.3 Darmstadt Engine:** Computational domain.

## 7.2 Numerical set-up

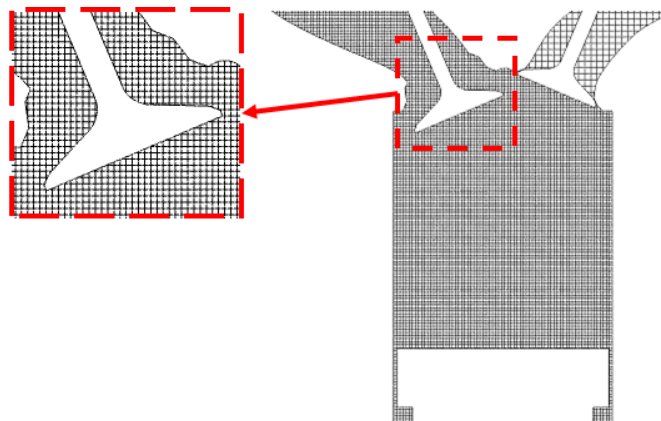
### 7.2.1 Mesh configuration

The mesh consists of hexahedral elements. It is set in such a way that the spatial resolution is higher in the combustion chamber during intake and compression, and in the intake port during intake, and lower in the rest of the domain where a qualitative simulation using RANS or VLES is sufficient. Details about the way the cell size changes depending on the region and the stroke is detailed in Table 7.2.

Phases of the cycle	Intake	Compression	Expansion	Exhaust
Intake port [ <i>mm</i> ]	1	2	2	2
Combustion chamber [ <i>mm</i> ]	1	1	2	2
Exhaust port [ <i>mm</i> ]	2	2	2	1

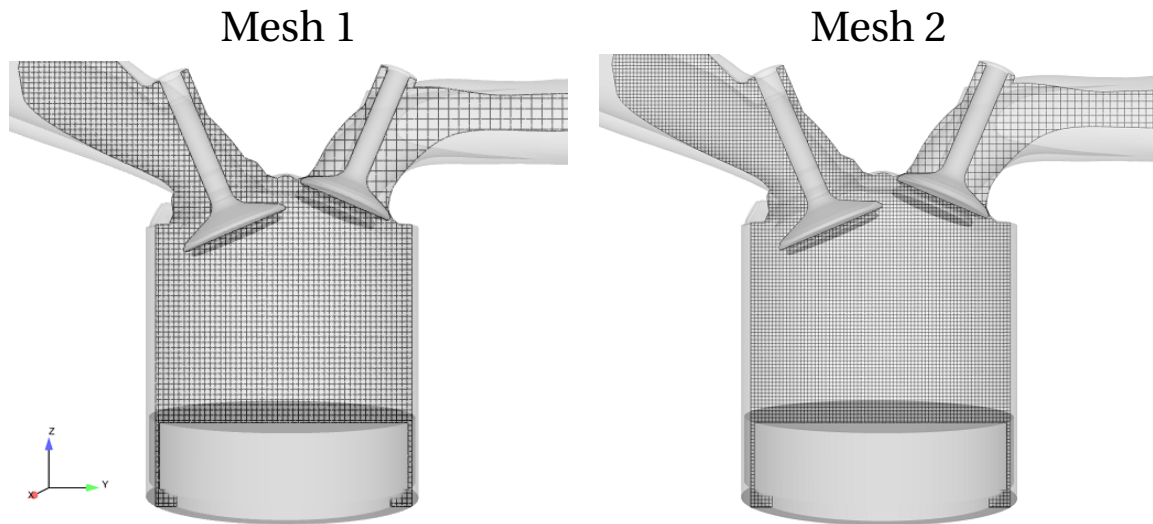
**Table 7.2 Darmstadt Engine:** Grid resolution for each region and each phase of the four-stroke cycle for Mesh 2.

Figure 7.4 illustrates a cut of the mesh in the symmetry plane of the intake valve with a zoom in on the valve region. It illustrates the mesh in the engine and the way the cells are trimmed at the valve boundaries using the cut-cell technique [103]. More details about the mesh management in CONVERGE at the wall boundaries and moving walls are provided in Section 4.3.2.1.



**Fig. 7.4 Darmstadt Engine:** A cut of M2 in the intake valve symmetry plane at the intake with a zoom in on the intake valve region.

Another mesh, which is coarser, is used for the grid dependency study in Section 7.3.5. It uses the same refinement strategy detailed in Table 7.2 but with a grid base which was downgraded from 2 mm to 3 mm. In order to distinguish both meshes, the coarse mesh is denoted as Mesh 1 and the fine mesh is denoted as Mesh 2. An illustration of both meshes at the intake is illustrated in Figure 7.5.



**Fig. 7.5 Darmstadt Engine:** Illustration of each mesh in the symmetry plane of the intake valve at  $-260\text{ CAD}$ .

## 7.2.2 Numerical parameters

The set of numerical parameters used for all simulations is summarized in Table 7.3.

Temporal scheme	First-order implicit Euler
Convective scheme	Second-order central differencing scheme
Flux limiter	Step at 0.1
Convective, acoustic CFL	0.7, 50
Fourier Number	2

**Table 7.3 Darmstadt Engine:** Numerical parameters.

All simulations – RANS, HTLES and LES – were performed using the same numerical parameters and meshes in order to compare solely the impact of the turbulence model on the results.

### 7.2.3 Turbulence modeling

The turbulence models are the same as those used for the Compressed Engine. Further details are provided in Section 6.2.3.

### 7.2.4 Boundary conditions and initialization

The kinematics of the moving boundaries are prescribed following the experimental data. The piston is driven following a sinusoidal movement (see Table 7.1). The lifts of the intake and exhaust valves follow the motion laws shown in Figure 7.6.

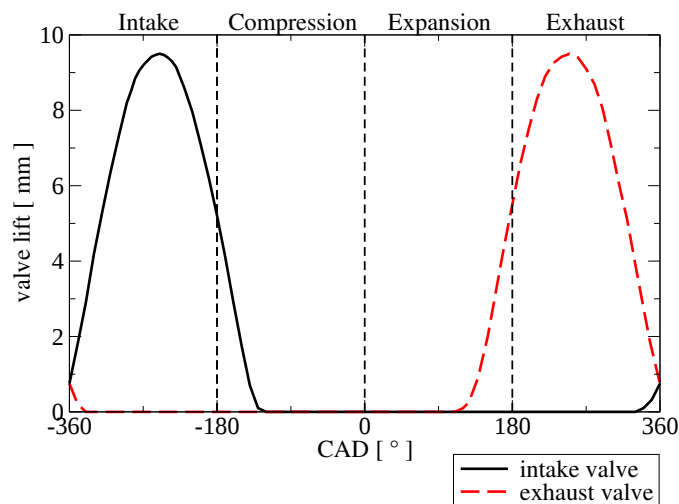


**Fig. 7.6 Darmstadt Engine:** Intake and exhaust valve lifts.

The static pressure at the inlet and the outlet is imposed with respect to the experimental measurements illustrated in Figure 7.7. The temperature at the inlet is set to 295 K and to 316.5 K at the outlet.

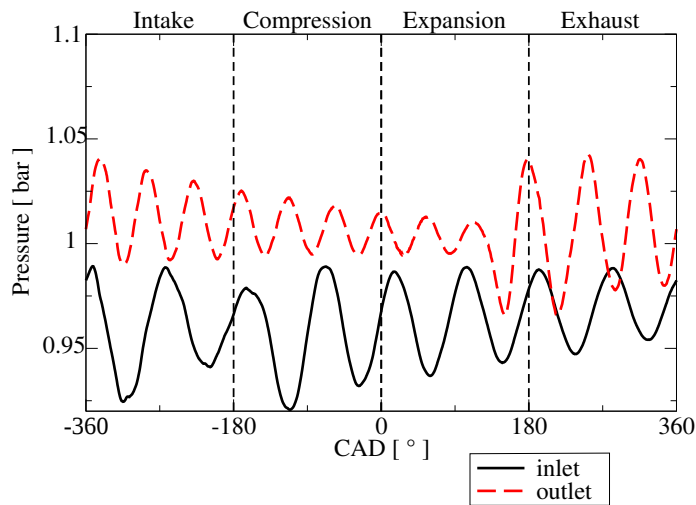


**Fig. 7.7 Darmstadt Engine:** Time evolution of the static pressure at the inlet of the intake port and at the outlet of the exhaust port.

For the wall boundaries, the prescribed temperatures correspond to the experimental data listed in Table 7.4.

	Temperature [ K ]
Engine walls	333
Intake port	295
Exhaust port	317

**Table 7.4 Darmstadt Engine:** Temperatures at the wall boundaries.

The heat transfer at the walls is modeled using the O'Rourke wall function [3], while the shear stress is computed using the automatic wall function [86] for RANS and HTLES, and the Werner wall function [131] for LES.

For the initialization, the computational domain is filled with air at 299 K and the initial velocity and pressure are set to zero and 1 bar, respectively.

Regarding HTLES, the first cycle is simulated using the RANS mode by imposing  $r = 1$  and  $k_{res} = 0$ , then HTLES is activated from the second cycle on.

## 7.3 Results of the intake and compression

The following Sections aim at evaluating the HTLES predictions with regard to the intake and compression phases. To this aim, the simulation results are compared with the experimental data, and with RANS and LES. The results are provided in four parts. Section 7.3.2 examines the integral flow quantities. Section 7.3.3 analyzes the turbulence modeling quantities, such as the energy ratio  $r$  and viscosity ratio. A deeper insight into the simulation results is provided by comparing the mean and RMS velocity with the PIV findings in Section 7.3.4. Finally, Section 7.3.5 focuses on the mesh dependency of the simulations by comparing their results in two meshes M1 and M2.

### 7.3.1 Post-processing of simulation results and experimental data

Experimental measurements of the first two statistical moments of the flow over 2700 cycles are provided by the PIV measurements conducted by Baum *et al.* [5]. The data are provided in the cross-section area that lies in the symmetry plane of the cylinder as shown in Figure 7.8-*right*.

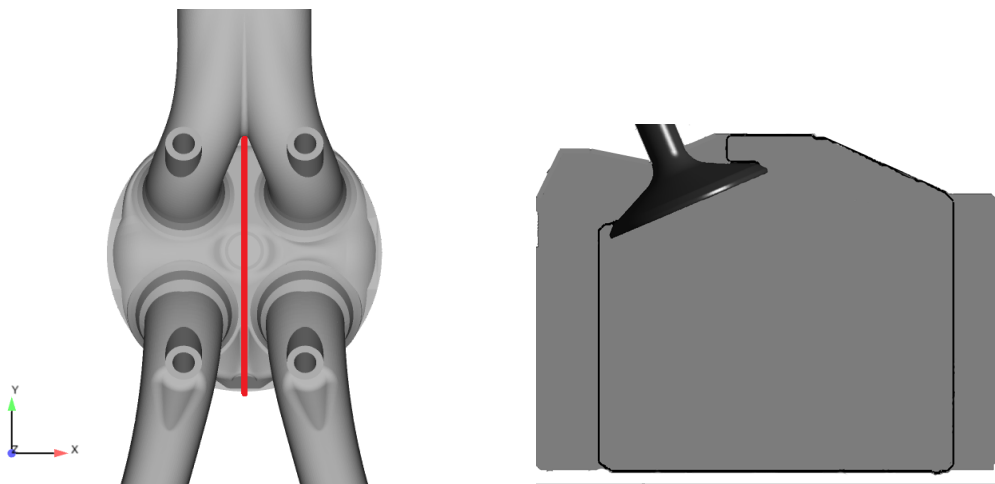


**Fig. 7.8 Darmstadt Engine:** -Left: Schematic of the cylinder symmetry plane (the red line). -Right: Contour of the optically accessible cross-section area.

All the 2D results (including PIV and 3D simulations) shown hereafter are shown in the cross-section area shown in Figure 7.8. The 1D profiles are extracted over the vertical centerline in the symmetry plane of the cylinder schematized in Figure 7.9.

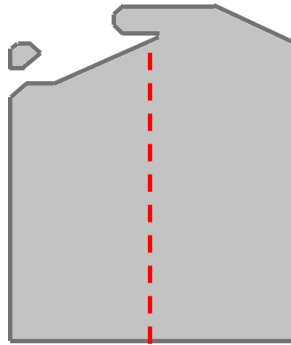


**Fig. 7.9 Darmstadt Engine:** Schematic of the vertical centerline in the cylinder symmetry plane over which are extracted 1D profiles.

HTLES and LES resolved fields are phase averaged using 40 consecutive cycles, which are sufficient to obtain a reasonable estimate of the two first statistical moments, as shown in Section 7.3.6. The first cycle was discarded to drive out the initial conditions, and the results were extracted from the second cycle as the in-cylinder pressure proved to be almost similar from the second cycle on.

The phase-averaged and RMS velocities are calculated as described in Section 6.7. In HTLES, the subfilter stresses were not included in the RMS calculation as they were not save them, due to a misconfiguration of the input files. The coordinate system and its origin position are shown in Figure 7.10. The x axis is normal to the cylinder symmetry plane and the z axis is aligned with the cylinder axis and is oriented towards the cylinder head.

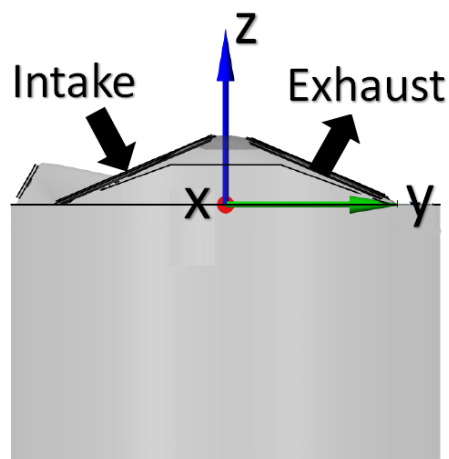


**Fig. 7.10 Darmstadt Engine:** Illustration of the coordinate system, and the origin position, Figure adapted from [15].

### 7.3.2 Results of the integral flow quantities

This Section examines three integral flow quantities. First, the in-cylinder pressure and trapped mass are compared with the experiment. Then, a qualitative analysis of the aerodynamic characteristics predicted by each simulation is performed by analyzing the tumble ratio (TR). The standard deviation of TR will be used as a qualitative means to quantify CCV.

#### 7.3.2.1 In-cylinder pressure

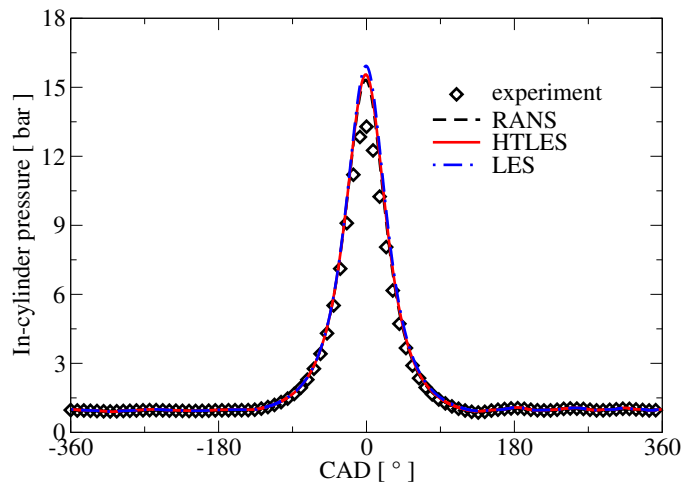


**Fig. 7.11 Darmstadt Engine:** Time evolution of the in-cylinder pressure.

Figure 7.11 compares the time evolution of in-cylinder pressure predicted by RANS, HTLES and LES with experimental data. As experiments exhibited a negligible cyclic variation of in-cylinder pressure, the HTLES and LES results are extracted from a randomly chosen cycle.

	Experiment	RANS	HTLES	LES
Peak pressure [ <i>bar</i> ]	13.2	15.2	15.4	15.8
Deviation [%]	-	15	16	20

**Table 7.5 Darmstadt Engine:** Experimental and predicted peak pressure at TDC.

All the simulations give fairly good predictions of the in-cylinder pressure along the cycle except around TDC. They overpredict the peak pressure as detailed for each simulation in Table 7.5. Similar observations were reported in [7, 55]. Baumann *et al.* [7] associated this overestimation to minimal inaccuracies in the description of the geometrical details. He managed to reduce the peak pressure by lowering the in-cylinder mass through the intake pressure so that the simulation matches the experimental peak pressure. Janas *et al.* [55] examined the blow-by possibility by performing 0D simulations of the compression and expansion of the engine. He showed that the geometrical compression ratio must be lowered from 8.5 to 7.5 to compensate the peak-pressure mismatch. This option was not retained for its side effects as it will require modifications of the engine geometry, that may influence the in-cylinder flow field the temperature evolution during compression. Furthermore, there is no meaningful blow-by in the experiment to justify such a choice.

Another possible reason could be a somewhat too high intake valve temperature imposed in our simulations, but this could not be verified in more detail due to the absence of a detailed experimental characterization. Since no exact explanation was found, no modification were added to simulation to match the experimental peak pressure. It is worth mentioning that this overestimation may not considerably affect the flow predictions as the engine works under motored conditions. Its effect would be more significant in the case of a fired engine [55].

### 7.3.2.2 Trapped mass

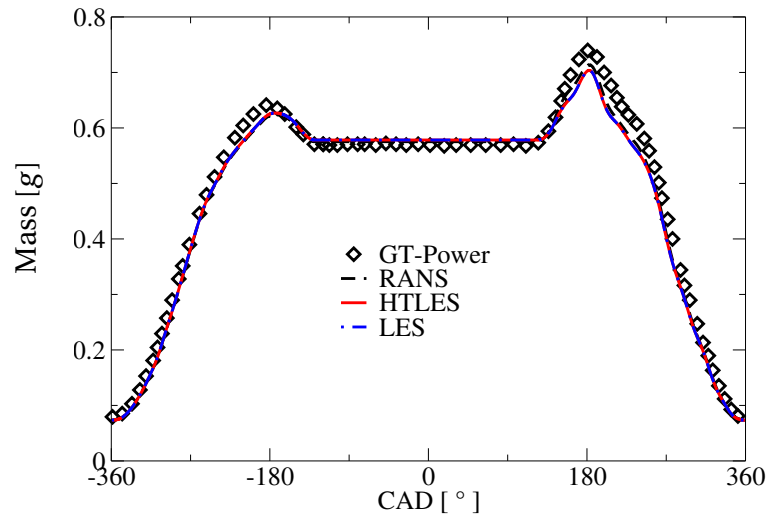


**Fig. 7.12 Darmstadt Engine:** Time evolution of the trapped mass predicted by 3D simulations and compared to a 1D CFD simulation using GT-Power.

Figure 7.12 compares the trapped mass predicted by our 3D simulation with results from a 1D GT-Power simulations [15] of the same engine. All 3D simulations yield the same evolution, independent of the used model with  $-16\%$  less trapped mass than the one given by GT-Power predictions. The 3D CFD results underestimated the 1D CFD curve during the intake and exhaust phase. During the closed phase of the cycle, the trapped mass yielded by 3D CFD is slightly higher than the one predicted by GT-Power. This might explain why our simulations overpredict the maximum in-cylinder pressure.

### 7.3.2.3 Tumble ratio and CCV

The development of the tumble around the  $x$ -direction during the cycle (the normal to the tumble plane) predicted by each simulation is examined hereafter. The tumble rate (TR) can be used as a qualitative means to quantify the intensity of the tumble[61]. TR is defined as the ratio of  $\omega_x$  the angular velocity of the flow about the  $x$ -direction to

$\omega_{crankshaft}$  the crank shaft angular velocity:

$$TR = \frac{\omega_x}{\omega_{crankshaft}} . \quad (7.1)$$

The angular velocity requires a reference point for its calculation. In CONVERGE, the reference point corresponds to the center of mass [112].

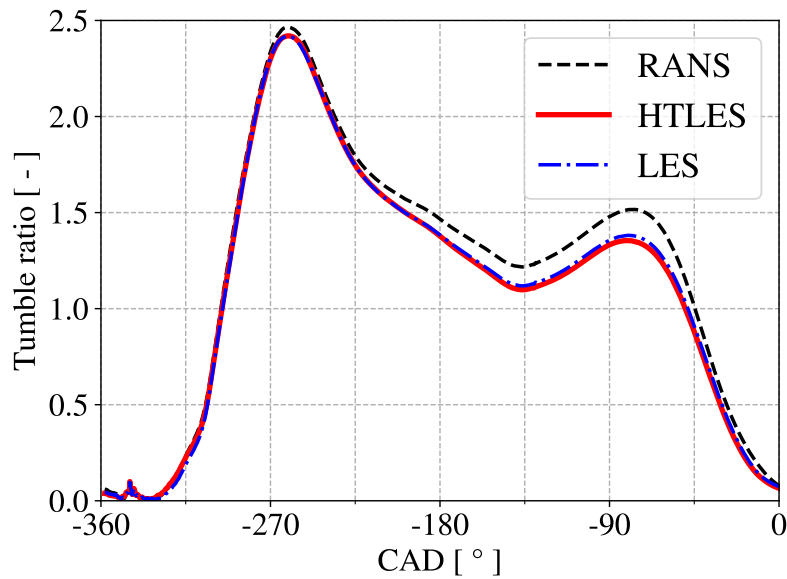


**Fig. 7.13 Darmstadt Engine:** Time evolution of TR predicted by the simulations.

The time evolution of TR yielded by HTLES, LES and RANS is shown in Figure 7.13. At the beginning of the intake stroke, the exhaust valves are partially open (see Figure 7.6) causing a small perturbation in TR. From  $-315$  CAD on, TR increases rapidly until reaching its first maximum value at  $-260$  CAD. After that, TR significantly decreases as the piston slows down, and the intake valves close. As the piston compresses the tumble vortex, TR increases and reaches its second peak at  $-76$  CAD, then vanishing due to the tumble breakdown process.

HTLES and LES provide quasi-similar results. RANS shows some differences, which appear from the first peak at  $-260$  CAD and progressively increases during the cycle, yielding a second peak of 12% larger than that predicted by HTLES and LES.

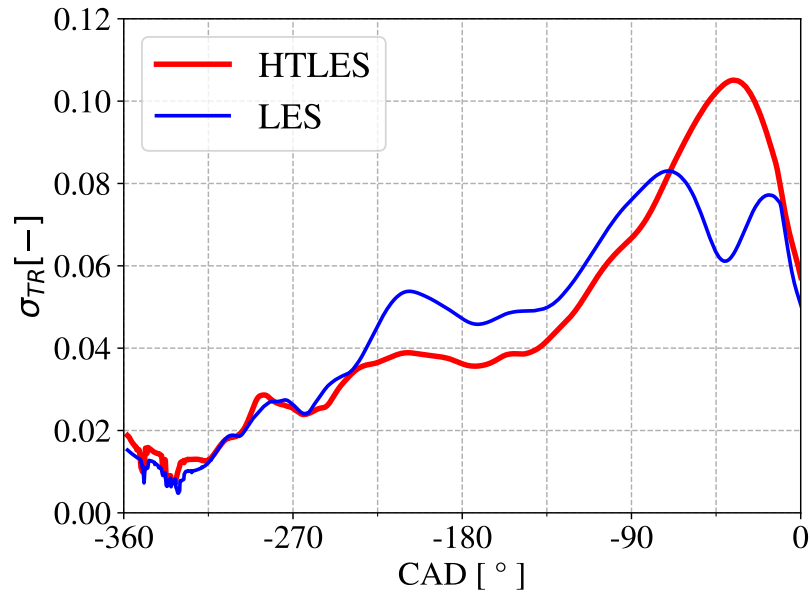


**Fig. 7.14 Darmstadt Engine:** Time evolution of the standard deviation of TR predicted by HTLES and LES.

The CCV predicted by HTLES and LES are qualitatively analyzed using the standard variation of TR  $\sigma_{TR}$ . Figure 7.14 shows the time evolution of  $\sigma_{TR}$  yielded by HTLES and LES. The cyclic variation of the first peak is very small, indicating an overall high reproducibility of the tumble generation during intake. The cyclic variability then gradually increases with time and becomes highest at the instant of the second peak resulting from the tumble breakdown due to compression. LES results presented in the same graph show fairly similar levels of  $\sigma_{TR}$  compared to HTLES. The observed differences seem to have a fluctuating behavior that may come from a not fully converged variance.

### 7.3.3 Qualitative assessment of modeled turbulence in HTLES

This Section provides an analysis of the way HTLES models turbulence during the intake and compression phases. The first Section focuses on turbulence modeling during the tumble generation. To this aim, the HTLES energy ratio  $r$  is examined. The resolved flow structures in HTLES are compared with those in RANS and LES by means of the  $Q$ -criterion. Finally, the focus is placed on the evolution of the turbulent viscosity during the intake and compression phases.

### 7.3.3.1 Turbulence modeling during the intake

In what follows, the parameter that controls the RANS-LES transition in HTLES, i.e, the energy ratio  $r$  (see Equations (5.38) and (5.37)) is examined at the intake stroke.

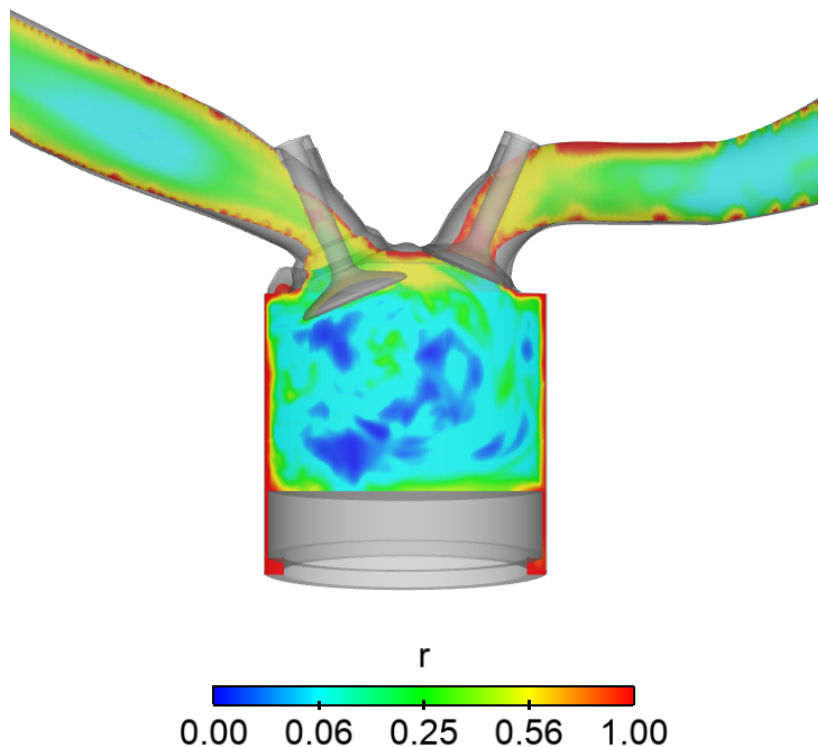


**Fig. 7.15 Darmstadt Engine:** Contours of the energy ratio  $r$  at  $-260$  CAD at an arbitrary cycle in the symmetry plane of the intake valve.

Figure 7.15 shows the instantaneous contours of the energy ratio  $r$  in the symmetry plane of the intake valve at  $-260$  CAD. At the fixed walls, the elliptic shielding ensures that  $r = 1$  so that RANS equations are recovered ( $T \rightarrow \frac{k}{\epsilon}$ ). Nevertheless, at the moving walls such as the valves and the piston the elliptic shielding fails to impose  $r = 1$ . This issue already highlighted in Section 6.5.3.2 comes from the boundary condition used for the elliptic shielding equation that could not be applied successfully for the moving walls in CONVERGE. The values of  $r$  in the intake port are around 0.25, indicating to HTLES to operate in VLES. In the combustion chamber, similar values around 0.25 are

observed close to the walls, while in the core region,  $r$  decreases to values smaller than 0.06 indicating to the model to operate locally in LES.

The resolved turbulent structures during the tumble formation are visualized using the Q-criterion isosurfaces. The HTLES results are compared with RANS and LES at  $-260$  CAD in Figure 7.16.

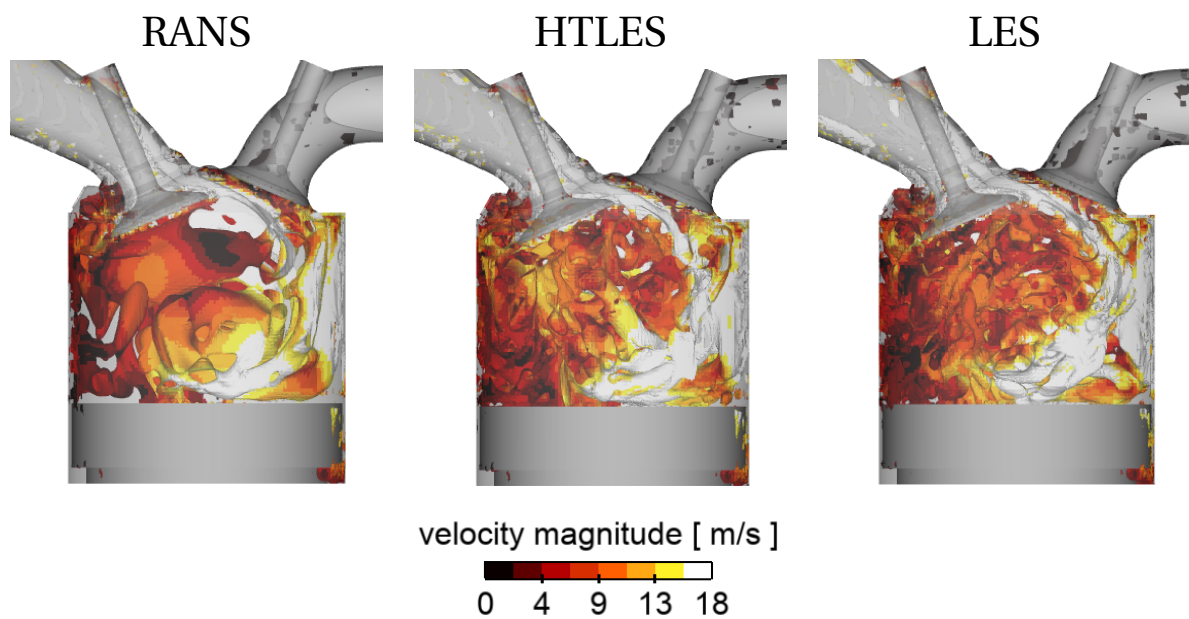


**Fig. 7.16 Darmstadt Engine:** Q-criterion iso surfaces at  $10^5 \text{ 1/s}^2$  in the symmetry plane of the intake valve colored by the instantaneous velocity magnitude at an arbitrary cycle.

Inside the cylinder, all approaches show an intake jet flow that develops over the valve and is deflected downwards by the cylinder, forming a tumbling vortex. The RANS simulation only predicts the phase-averaged large scale flow structures and naturally does not exhibit small flow structures. HTLES and LES exhibit an instantaneous range of large and finer flow structures. In HTLES, the resolved small structures are slightly more elongated than in LES, which corresponds to the VLES mode indicated by the energy ratio  $r$  in Figure 7.15.

### 7.3.3.2 Viscosity ratio

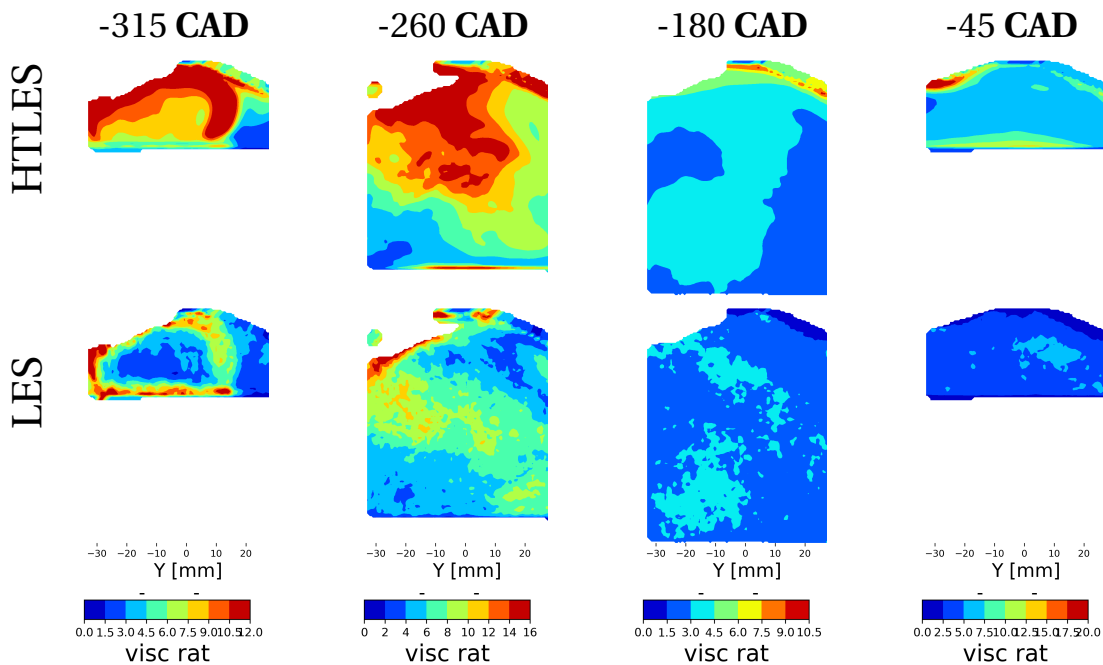


**Fig. 7.17 Darmstadt Engine:** Contours of the phase-averaged viscosity ratio on the tumble plane during intake and compression.

The phase-averaged viscosity ratio contours yielded by HTLES and LES at four instants of the intake and compression are depicted in Figure 7.17. It should be noted that the results were post-processed in the cross-section area shown in Figure 7.8--*right*. Therefore, the results close to the cylinder liner are not shown.

At the beginning of the intake, at  $-315\text{ CAD}$  and  $-260\text{ CAD}$ , the intake jet is at its early stages of generation, and the in-cylinder turbulent structures are rather small and less well resolved. HTLES predicts high viscosity ratios in the intake jet region compared to LES. At  $-180\text{ CAD}$ , the tumble generation of the tumble motion is nearly complete, and hence large turbulent scales dominate the flow. HTLES gives viscosity ratios of the same order of magnitude as LES. During compression, at  $-45\text{ CAD}$ , the tumble breaks down into small scales yielding a substantial increase in turbulence, requiring more turbulence modeling, i.e, higher viscosity ratios more visible in HTLES.

From a numerical perspective, as seen in the Tumble Engine in Section 6.6.3, CONVERGE locally downgrades the spatial scheme from the second-order central differencing to the first-order upwind scheme to prevent the wiggles that can appear when the second-

order differencing scheme is used. Figure 7.18 shows the evolution of the number of upwinded cell faces during a randomly chosen cycle for RANS, LES, and HTLES.

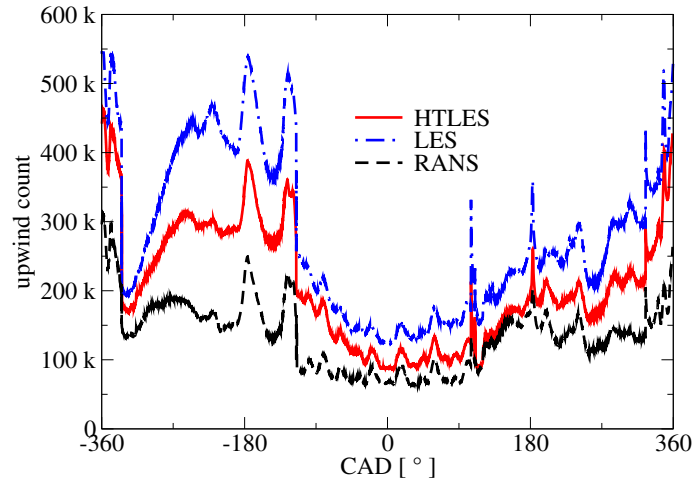


**Fig. 7.18 Darmstadt Engine:** Time evolution of the number of upwinded cell faces in CONVERGE.

One can observe that RANS exhibits the smallest number of upwinded cell faces, followed by HTLES, then LES, which yields the highest number of upwinded cell faces. This results from the more elevated the turbulent viscosity, the smaller the local gradients, which lowers the propensity to generate local numerical instability. From this fact, HTLES reduces the upwinding by 26% compared to LES, as it partly operates in LES and RANS.

### 7.3.4 Results of mean and RMS velocities

This Section compares the simulation predictions in terms of mean and RMS velocity with the PIV findings during the intake and compression.

As schematized in Figure 7.19, the flow evolves in three stages. During the intake, the intake valves opening and the piston descent allow a charge motion to be drawn in the cylinder forming a tumbling motion. Once the piston is at TDC, the intake valves close, and the piston moves upwards, leading to the tumble compression. Under the effect of compression, the tumble ends up breaking down into small scales. The tumble ratio analysis performed in Section 7.3.2.3 showed that the breakdown process starts from  $-76$  CAD on.

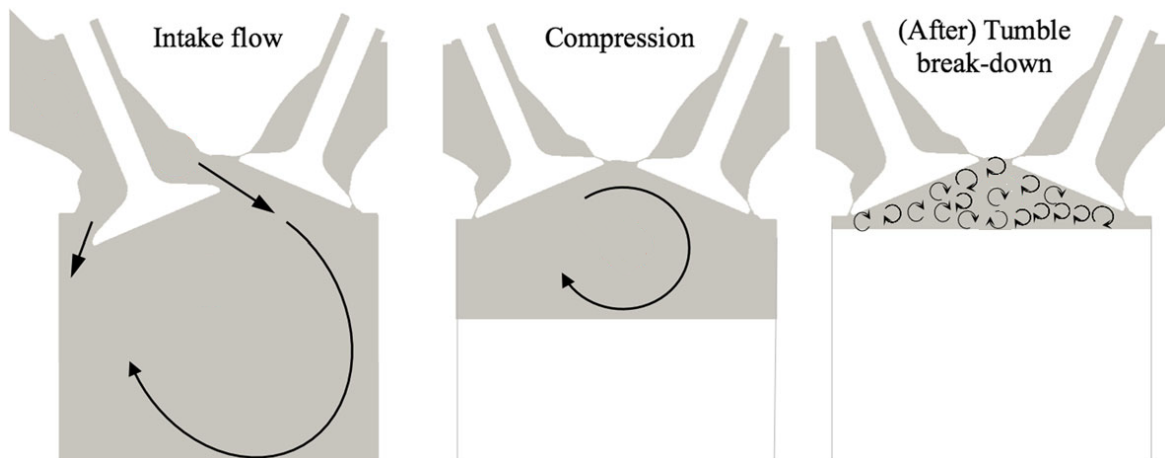


**Fig. 7.19 Darmstadt Engine:** Illustration of the flow evolution during intake and compression, Figure adapted from [55].

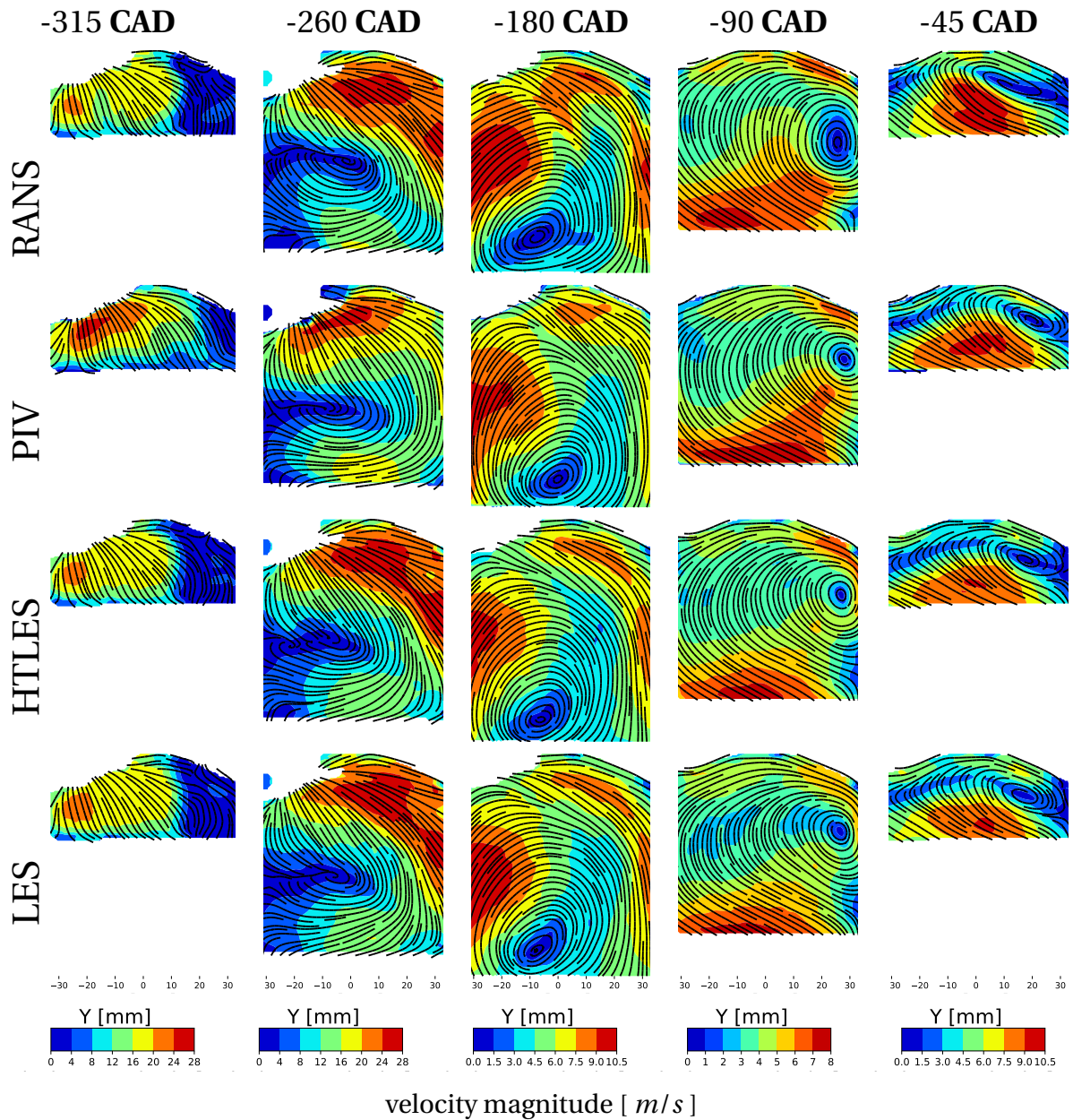


**Fig. 7.20 Darmstadt Engine:** Contours and streamlines of the phase-averaged 2D velocity magnitude in the cylinder symmetry plane at five instants during intake and compression.

Figure 7.20 compares the contours and streamlines of the phase-averaged velocity magnitudes predicted by RANS, LES and HTLES with PIV findings in the symmetry plane of the cylinder at five instants of the intake and compression phases. In Figure 7.21, the 1D profiles over the vertical centerline (illustrated in Figure 7.9) give a more in-depth insight into the phase-averaged velocity.

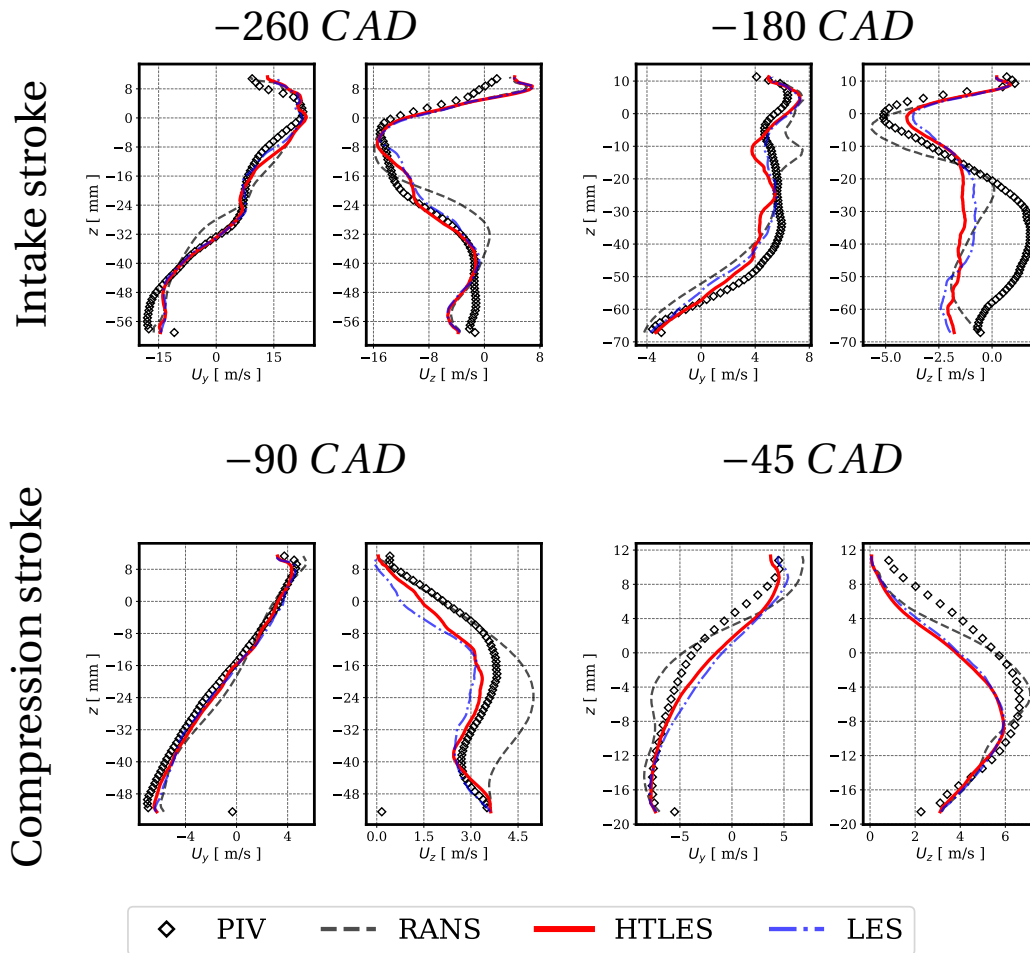


**Fig. 7.21 Darmstadt Engine:** 1D profiles of the phase-averaged velocity along the vertical centerline in cylinder symmetry line at four different instants.

The first shown instant at  $-315 \text{ CAD}$  corresponds to the early intake when the jet generated by the intake ports and valves reach the cylinder symmetry plane. The extend of the high-velocity region found in PIV is accurately reproduced by all presented simulations that yield very comparable results. However, the highest velocity magnitudes are underpredicted by all simulations.

The second instant at  $-260 \text{ CAD}$  corresponds to a high intake valve lift, characterized by a high intake jet velocity starting to generate the tumble motion. All simulations overestimate the extend of the highest velocity region found in PIV beneath the intake valves. This turned out to be due to an overestimation of the velocity in the  $z$ -direction shown by 1D profiles. Despite this discrepancy, all simulations predict the tumble motion fairly accurately in terms of tumble rotational core and angular penetration of the tumble

front. Concerning the latter, HTLES and LES yield a slightly lower penetration, indicating an underestimation of the tumble rotational speed. RANS predictions show besides an upward movement of the tumble front, which is not present in PIV.

The third instant corresponds to BDC, at a moment where the intake valves are closing, and the generation of the tumble motion is nearly complete. The PIV findings show that the tumble rotational core (corresponding to the low flow velocity region) has moved close to the piston. The high-velocity region at the left of the shown plane corresponding to the tumble front has moved towards the cylinder head. While all simulations qualitatively yield similar findings, some differences can be observed. RANS results do less well reproduce the PIV findings, with a rotational center situated further to the right and a less clearly defined tumble front. In addition, which high-velocity regions below the head and on the left of the cylinder are not found in PIV nor the other simulations. HTLES and LES predictions are similar and closer to PIV findings, despite a slight shift of the rotational center to the left and a slight underestimation of the rotational speed front penetration. The tumble rotational core can be localized where  $U_y$  and  $U_z$  are equal to zero simultaneously. Using the 1D profiles, this corresponds in PIV to  $(y, z) = (0, -80\text{mm})$ . At this location, all the simulations show magnitudes of  $U_z$  well above the PIV findings, which is a consequence of the mispredicted location of the tumble rotational core.

The two last shown instants correspond to the closed part of the cycle, during which the upward moving piston compresses the tumble motion. HTLES yields results that are the closest to PIV findings, despite underestimating the high-velocity region on the lower left side of the cylinder. LES produces quite similar results, but the streamlines show characteristics that slightly differ from PIV and HTLES. Finally, the compression of the less well-predicted tumble creation by RANS naturally leads to larger differences with PIV, even if the overall structure and level of velocity are well enough predicted.

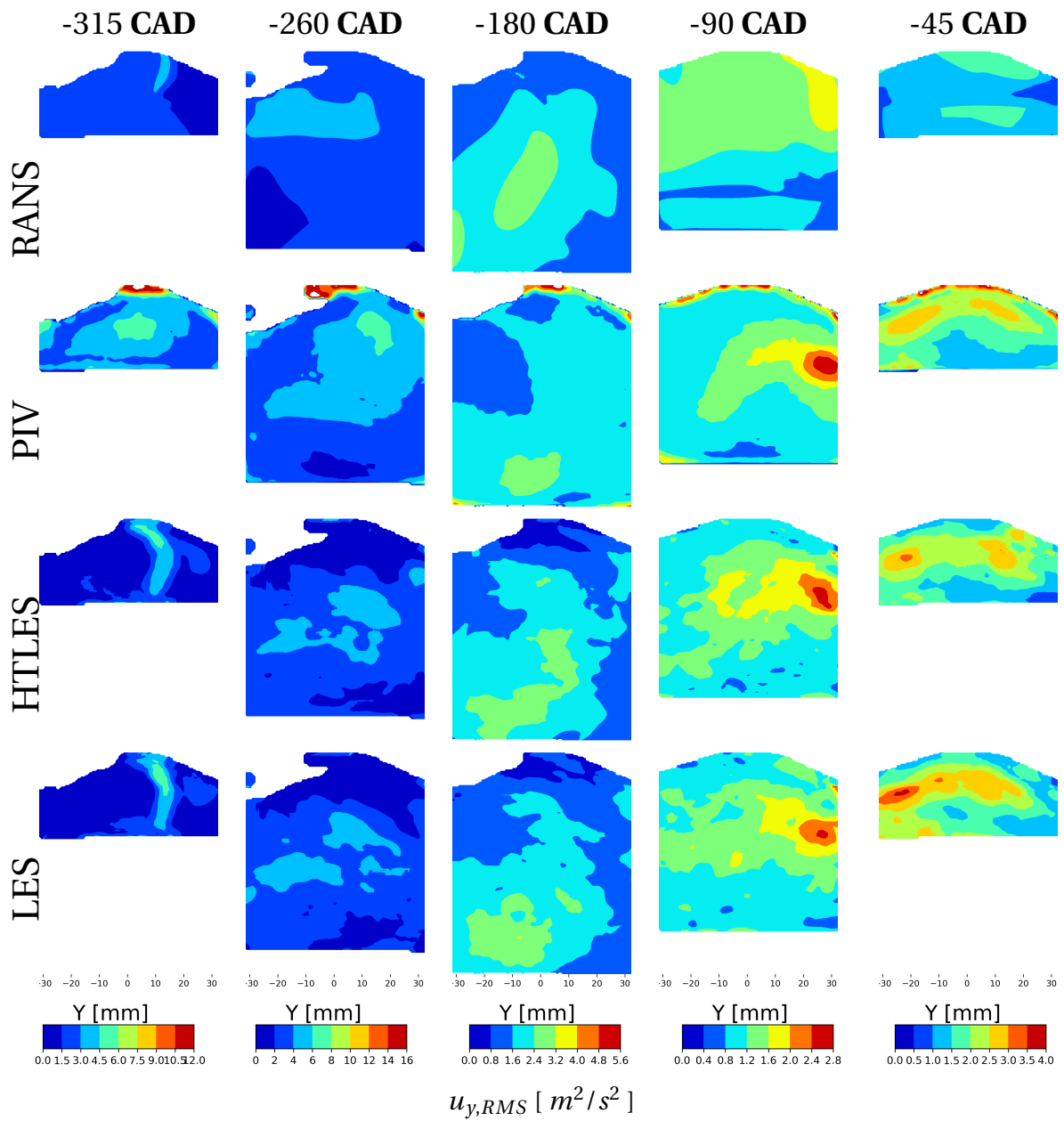


**Fig. 7.22 Darmstadt Engine:** Contours of  $u_{y,RMS}$  in the cylinder symmetry plane during intake and compression.

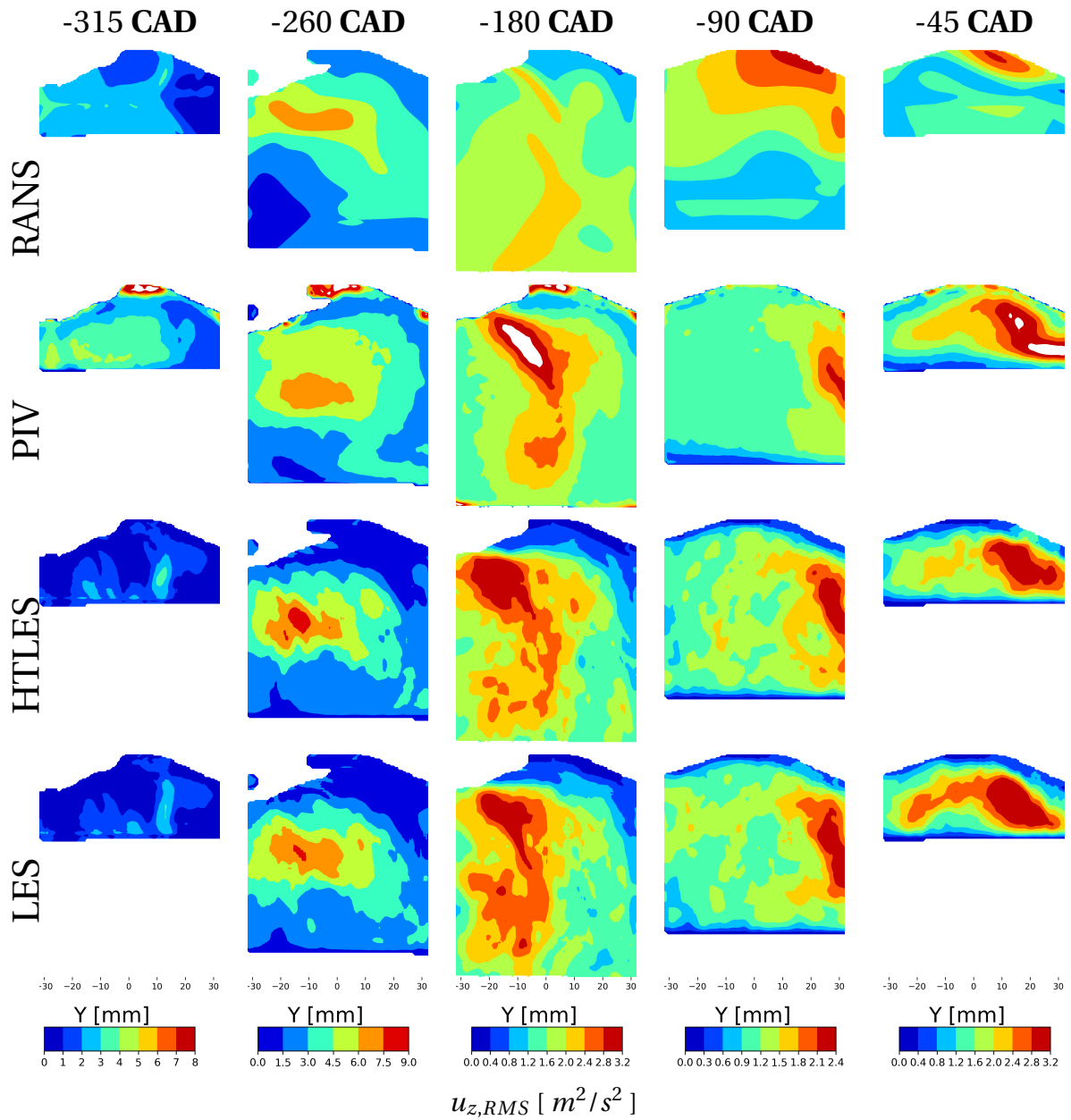


**Fig. 7.23 Darmstadt Engine:** Contours of  $u_{z,RMS}$  in the cylinder symmetry plane during intake and compression.

The contours of the RMS for the  $y$  and  $z$  velocity components are illustrated in Figures 7.22 and 7.23, respectively.

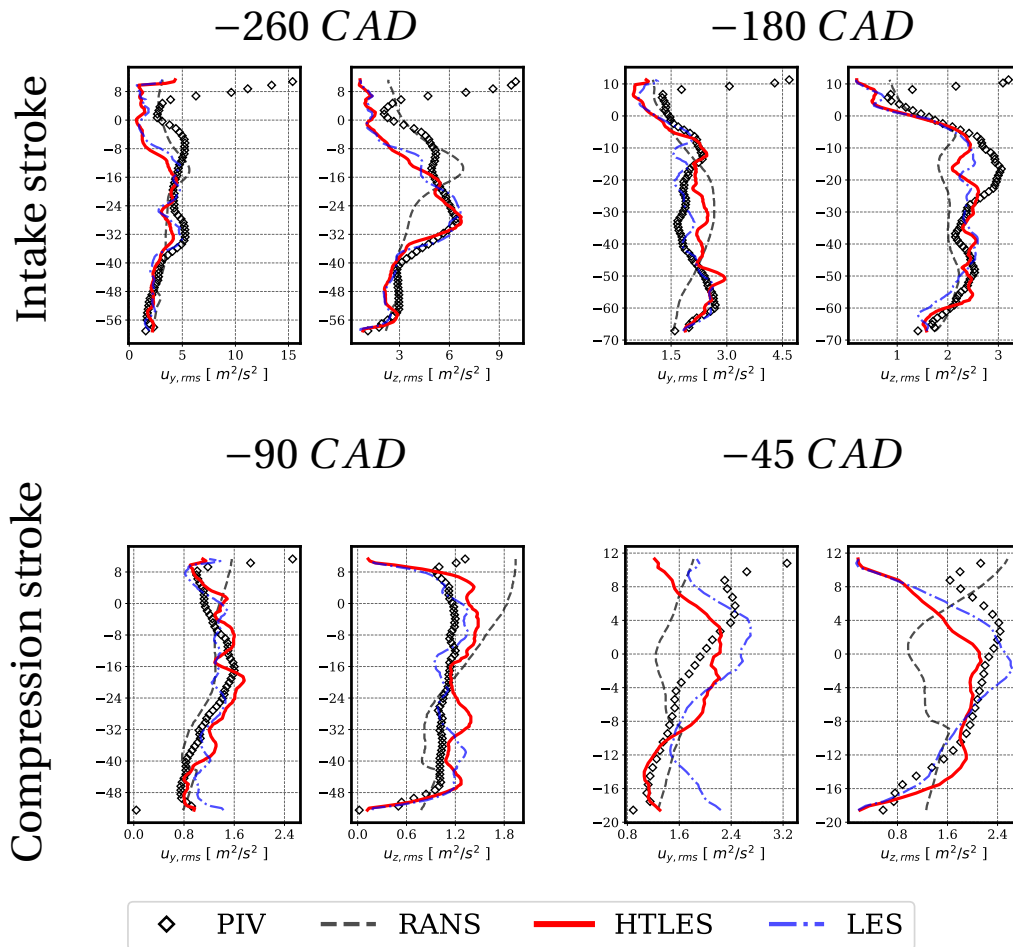


**Fig. 7.24 Darmstadt Engine:** 1D profiles of the RMS velocities over the vertical centerline in the cylinder symmetry plane at four different instants.

At  $-315 \text{ CAD}$ , the PIV findings show that both the in-plane RMS components feature an increase in magnitudes in the core region. HTLES and LES underestimate the RMS magnitudes at this instant, as the flow scales are rather small, and the mesh is not sufficiently fine to resolve turbulent fluctuations. Therefore, HTLES results have to be interpreted with care since the subfilter part (not taken into account in the RMS calculations) may become significant if turbulence is under-resolved. The results are slightly better in RANS.

At the second shown instant, a high extend RMS region appears in the z-component around the tumble rotational core. As shown in the 1D RMS profiles, RANS mislocates the increase in RMS compared to the PIV data, as it failed to accurately predict the location of the tumble rotational core. HTLES and LES well predict this region. Indeed, the local increase observed in the RMS magnitudes is a consequence of substantial variations in the tumble rotational core location from one cycle to another (CCV) [10] that a RANS simula-

tion can hardly predict [117]. At the intake jet region, both HTLES and LES underestimate the RMS magnitudes, as the turbulent intake jet is not well resolved.

At BDC, two distinct high RMS extend regions are identified. The first one appears in the *RMS* *y*-component around the tumble rotational core, and the second one shows up in the *z*-component at the tumble front. RANS significantly underestimates the RMS at this instant, whereas HTLES and LES reproduce fairly well the PIV findings.

The fourth shown instant (-90 *CAD*) is just before the beginning of the tumble breakdown process (see Figure 7.13). The tumble is compressed and becomes unstable, as shown in both *z* and *y* RMS components, which feature a substantial increase around the tumble rotational core. Unlike RANS, This phenomenon is fairly well predicted by HTLES and LES.

The last shown instant lies in the tumble breakdown period when the tumble decomposes into small scales that raise the RMS magnitudes, which is fairly well captured by HTLES and LES.

All the simulations have overall well-predicted results in terms of mean and RMS velocity. RANS provided good results in terms of the tumble generation. Nevertheless, RANS results were progressively less satisfactory as the CCV started raising in the domain. This is particularly true for RMS velocity provoked by the cycle variability of large scales that RANS hardly captures. HTLES and LES provided better results, which were shown to be very similar. The RMS velocities were fairly well predicted compared to the PIV findings. Nevertheless, in some regions such as the inlet jet region, both simulations showed a significant underestimation of RMS magnitudes. This underestimation potentially indicates that the unresolved scales contain a non-negligible part of the turbulent energy, underlining the necessity of considering the subfilter stresses in the calculation of the RMS velocities in HTLES.

### 7.3.5 Grid dependency

This Section focuses on the grid dependency of RANS, HTLES and LES using two meshes: the reference mesh M2, the results of which were already shown in the former Sections, and the coarse mesh M1 (see Section 7.2.1 for a detailed description of each mesh).

The result analysis is organized in two parts. In the first part, the grid dependency of tumble characteristics is examined using the tumble ratio. In the second part, the simulation predictions in terms of mean and RMS velocity are compared with the PIV findings.

### 7.3.5.1 Tumble ratio

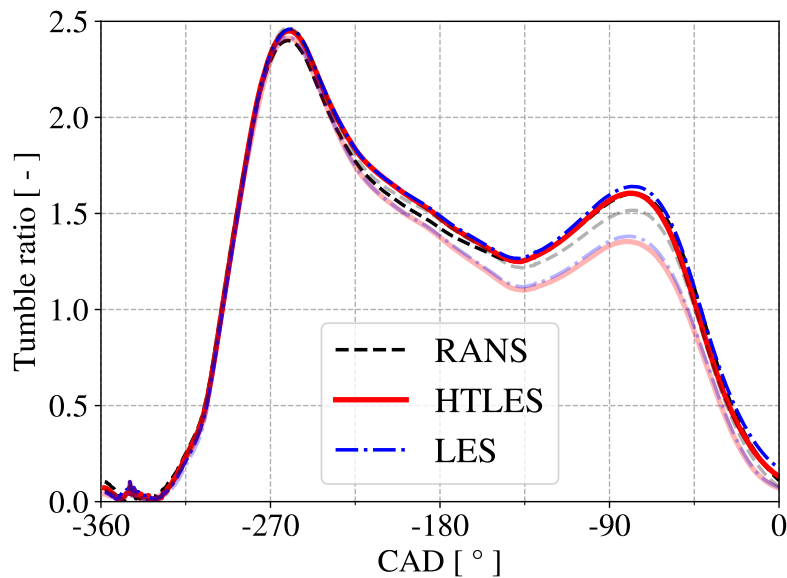


**Fig. 7.25 Darmstadt Engine:** Time evolution of the tumble ratio over the crank angle using M1 (opaque) and M2 (transparent).

The time evolution of the tumble ratio predicted using M1 and M2 with RANS, HTLES and LES are shown in Figure 7.25. While the evolution yielded by RANS slightly depends on the mesh resolution, a stronger impact is visible for HTLES and LES, especially during compression. The predictions with the coarser mesh M1 indeed yield a second peak that is higher by 15 % as compared to the one predicted with the finer mesh M2.

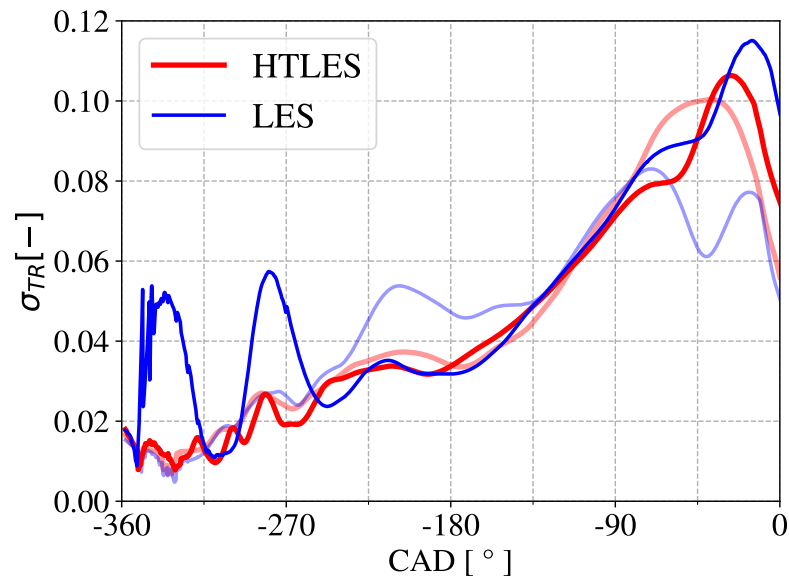


**Fig. 7.26 Darmstadt Engine:** Standard deviation of the tumble ratio predicted by LES and HTLES using M1 (opaque) and M2 (transparent)

The standard deviation of the tumble ratio using M1 and M2 is reproduced in Figure 7.26. The results for HTLES are not too sensitive to the mesh resolution, with a slightly higher level of variability with the coarser mesh at TDC. An important dependency can be observed with LES, right during the intake phase, and to a lesser level at TDC. The reasons for this behavior are yet unclear and would require a detailed analysis.

## 7.3.5.2 Mean and RMS velocities

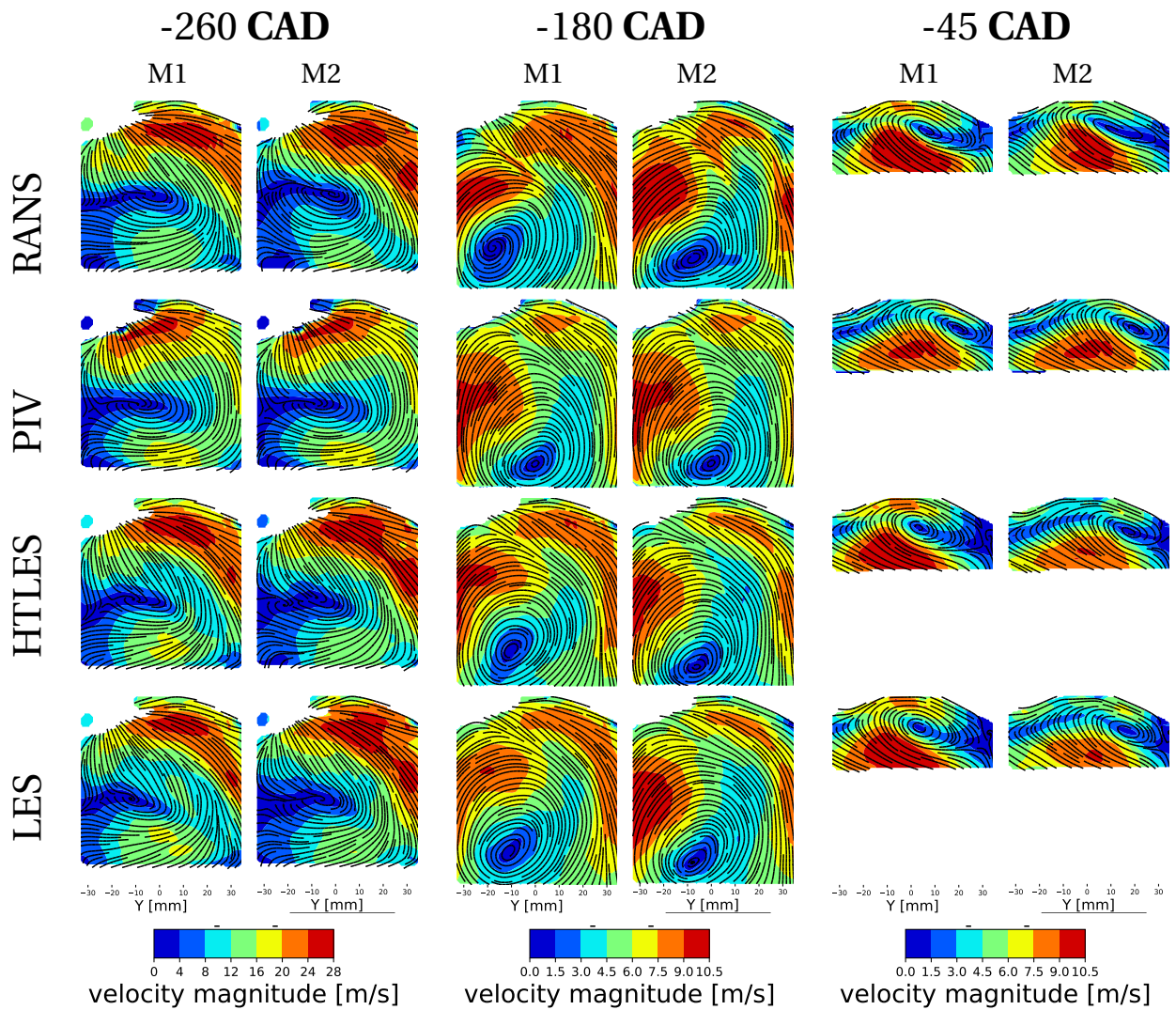


**Fig. 7.27 Darmstadt Engine:** Comparison of the contours and streamlines of the in-plane phase-averaged velocity in the symmetry plane of the cylinder predicted using two meshes: M1 (**coarse**) and M2 (**reference**).

Figure 7.27 compares phase-averaged velocity fields predicted by RANS, HTLES and LES using meshes M1 and M2. Figure 7.28 their corresponding 1D profiles along the vertical centerline in the cylinder symmetry plane.

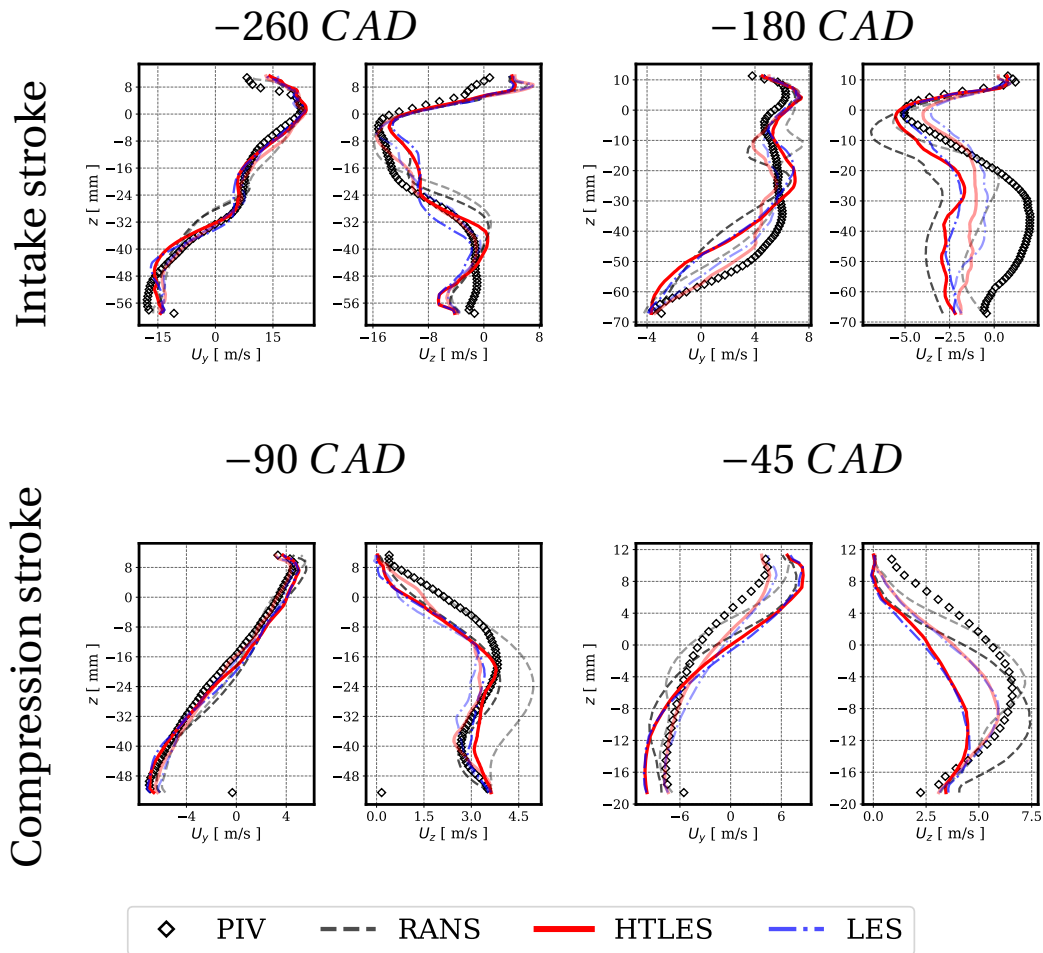


**Fig. 7.28 Darmstadt Engine:** 1D profiles of the phase-averaged velocity along the vertical centerline in cylinder symmetry line using M1 (**opaque**) and M2 (**transparent**) at four different instants.

At  $-260 \text{ CAD}$ , as shown by the tumble ratio, all simulations are relatively less dependent on the mesh. This is confirmed by the velocity fields, which show close predictions of the tumble characteristics in terms of the rotational core and the tumble front in the two meshes. The 1D velocity profiles show that both meshes show good agreement with the PIV findings, except the region beneath the intake ( $-24 \text{ mm} < z < 0 \text{ mm}$ ) that is less well predicted in all the simulations using the coarse mesh (M1) as compared to the results in M2.

Differences become significant at TDC. In RANS, the high velocity extend beneath the intake valve is more overestimated in M1, resulting in a flow that streams more strongly towards the cylinder liner as shown by the streamlines characteristics. The tumble rotational core is shifted close to the cylinder liner, and the tumble front is less well defined

compared to the results in M2. The misestimation of the tumble rotational core results in a significant deterioration of the 1D velocity profiles. Whatever the mesh, HTLES and LES yield fairly similar results. In M1, the tumble is slightly shifted towards the cylinder liner, and the high extend velocity beneath the intake valve is slightly more overestimated. Nonetheless, the results remain acceptable compared to the PIV findings.

During compression at  $-45$  CAD, in the two meshes, RANS results show similar predictions in terms of the tumble core and the high velocity extend, that forms beneath the tumble. For HTLES and LES, even if the results were relatively weakly dependent on the mesh during the intake, during the compression, they were found to deteriorate in M1 significantly. Indeed, unlike the PIV data, the tumble rotational core is shifted far from the cylinder liner, and the high-velocity extend that becomes similar to RANS results.

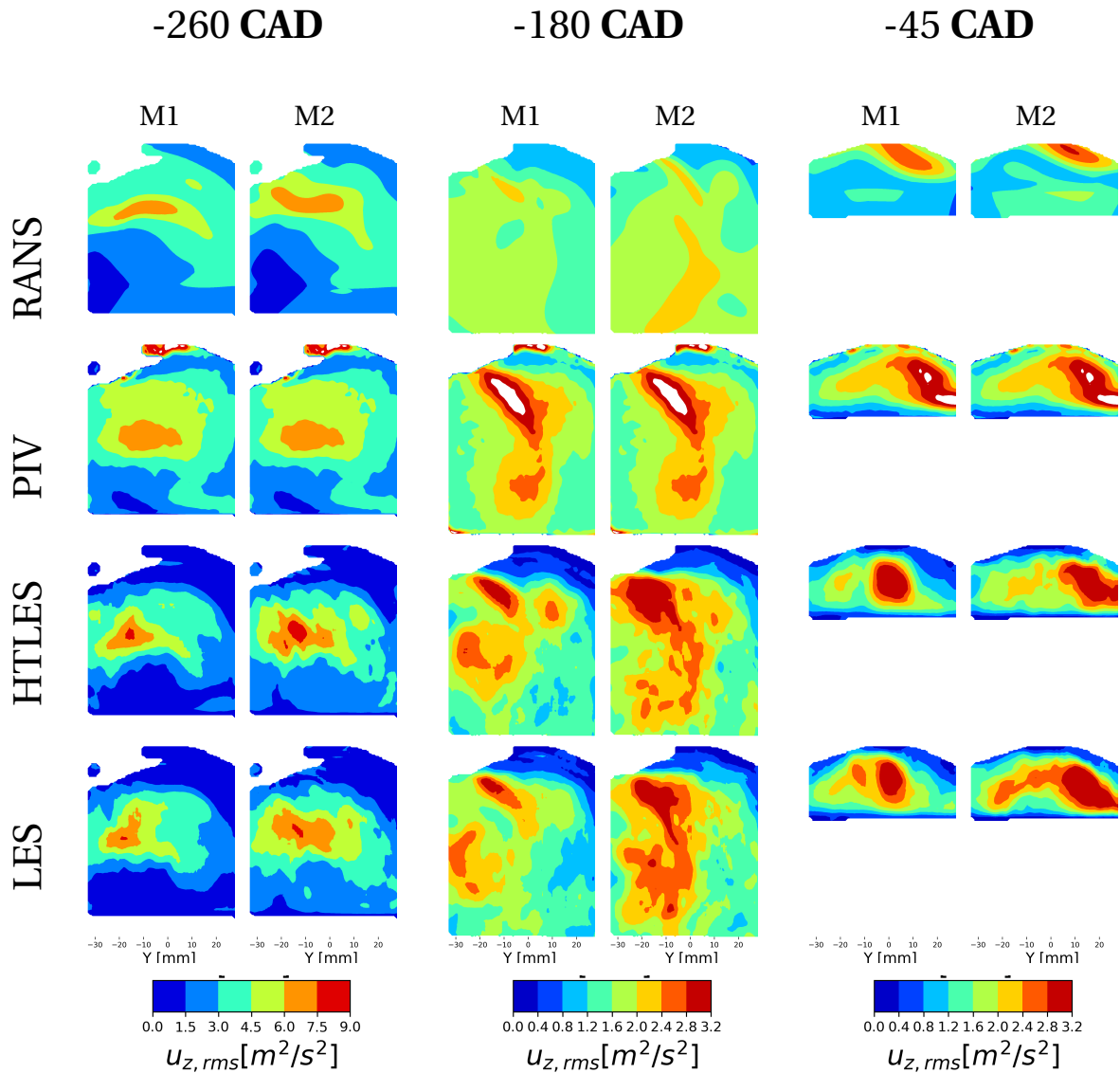


**Fig. 7.29 Darmstadt Engine:** Comparison of  $u_{z,RMS}$  on the tumble plane predicted in: M1 (coarse) and M2 (reference).

Concerning the RMS velocity, the contours of  $u_{z,RMS}$  predicted using M1 and M2 are illustrated in Figure 7.29. RANS results show a weak dependency on the mesh configuration. HTLES and LES results show that when using the coarser M1, the *RMS* magnitudes decrease slightly as less scales are resolved than in M2. This shows that M1 is not sufficiently fine to resolve all the energy-containing scales. Therefore, no conclusion can be drawn for HTLES as the subfilter part, which is not taken into account in the calculation of the RMS may become significant in the coarse mesh. The results deteriorate in M1 at -45 CAD, as the mean velocities were not correctly predicted at this instant.

### 7.3.6 Convergence of the phase average

In order to compare the phase-averaged predictions of LES and HTLES with experimental findings, a certain number of cycles have to be simulated and averaged to yield a meaningful comparison. Thus, a study was performed to evaluate the minimum number of cycles to simulate and include in the averaging to yield statistically converged results. Here the study is conducted using HTLES resolved fields. The convergence of LES was not checked separately, as it was found that LES findings were quite comparable to those of HTLES.

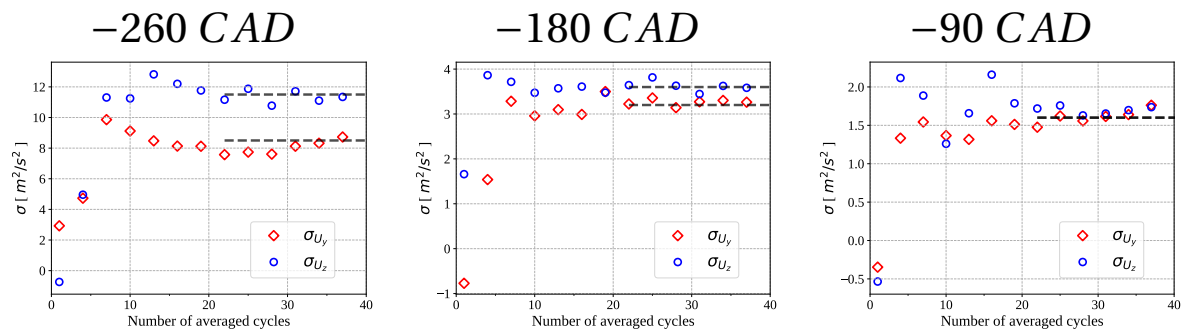


**Fig. 7.30 Darmstadt Engine:** Evolution of the kinetic energy along the number of averaged cycles at: - **Left:**  $-260 \text{ CAD}$ .- **Center:**  $-180 \text{ CAD}$ .- **Right:**  $-90 \text{ CAD}$ .

The kinetic energy of the in-plane resolved velocity components is used as a first indicator for the convergence of the first two statistical moments of the flow. Its spatially weighted value in the cylinder symmetry plane versus the number of included cycles is shown in Figure 7.30 at three instants. For  $-260$  and  $-180 \text{ CAD}$ , the results substantially vary when less than 10 averaged cycles are used. The variations decrease continuously as the averaged cycles is increased until reaching the asymptotic lines once at least 28 cycles are used for averaging. At  $-90 \text{ CAD}$ , the results are more fluctuating and require more averaging cycles to converge potentially due to the increased turbulence during compression. 40 cycles appear to be sufficient to have reasonable converged statistics.

To further investigate the phase-average convergence, 1D profiles of the phase-averaged and RMS velocity over vertical centerline (see Figure 7.9) computed from different numbers of cycles are shown at  $-260$ ,  $-180$  and  $-90 \text{ CAD}$  in Figures 7.31, 7.32 and 7.33, respectively.

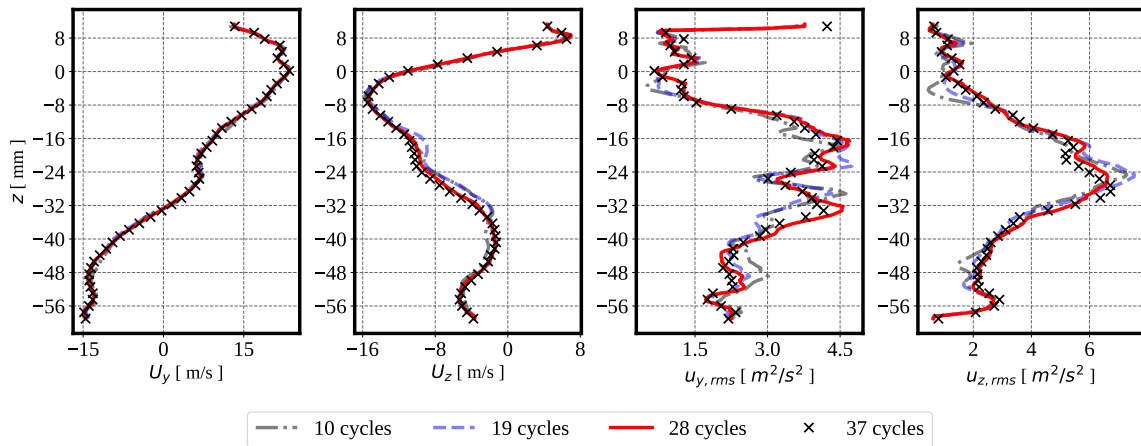


**Fig. 7.31 Darmstadt Engine:** Convergence of the 1D Profiles of the phase averaged velocity and RMS velocity along the vertical centerline at  $-260$  CAD.

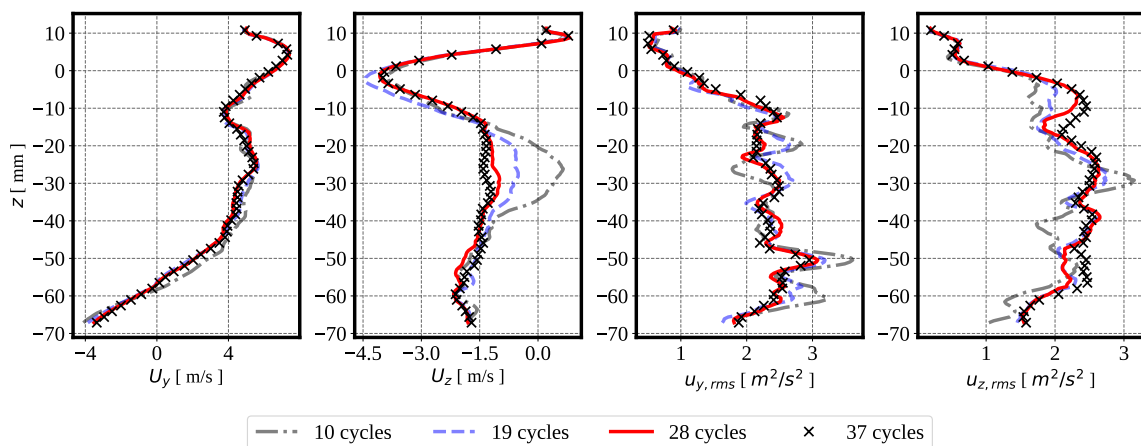


**Fig. 7.32 Darmstadt Engine:** Convergence of the 1D Profiles of the phase averaged velocity and RMS velocity along the vertical centerline at  $-180$  CAD.

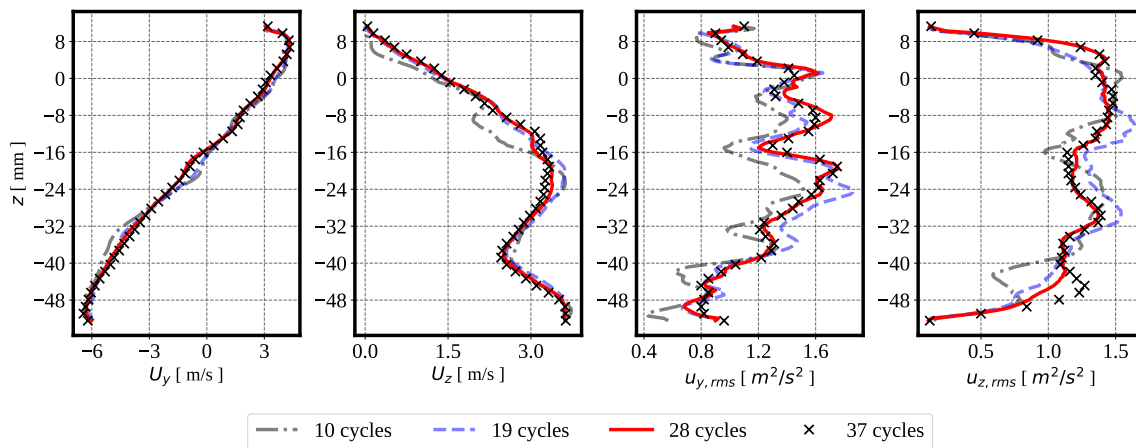


**Fig. 7.33 Darmstadt Engine:** Convergence of the 1D Profiles of the phase averaged velocity and RMS velocity along the vertical centerline at  $-90$  CAD.

For the three instants, one can observe that the phase averages are similar once at least 28 cycles are used for averaging. The RMS profiles show substantial fluctuations if a small number of averaged cycles is used. The difference between the curves significantly decreases if more than 28 cycles are used for averaging, as shown by the curves calculated from 37 cycles.

From these analyses, it is shown that including 40 cycles is sufficient to have reasonable statistics. Therefore, all HTLES and LES simulations will use 40 averaged cycles for phase averaging

## 7.4 Conclusions

A total of 42 consecutive cycles of the Darmstadt engine were simulated using HTLES. The simulation results were compared with RANS, LES and the experiment. Overall, HTLES and LES yield similar predictions in terms of phase-averaged and RMS velocities, and were shown to be more accurate than RANS. Unlike RANS, phenomena that characterize cycle to cycle variability, such as the increase in the RMS magnitudes around the tumble front and tumble rotational core, and cyclic variation of the tumble ratio were captured by HTLES and LES. Nevertheless, the RMS analysis could not be completed since the subfilter stresses were not taken into account. Indeed, in some regions such as the inlet jet region, both HTLES and LES showed a significant underestimation of RMS magnitudes, which

potentially indicates that the flow is under-resolved the subfilter stresses may become non-negligible.

Concerning the grid dependency, all the results deteriorated when using a coarse mesh. RANS results were the less sensitive to the mesh during compression. In HTLES and LES, although the results were not significantly affected by mesh coarsening during intake, they were deteriorated during compression, particularly during the tumble breakdown process.



## **Part IV**

### **Conclusions and perspectives**



# Chapter 8

## Conclusions and perspectives

### 8.1 Conclusions

The objective of the present thesis was to develop and validate a hybrid RANS/LES approach for the simulation of internal aerodynamics in ICE engines, and more specifically SI engines. The main characteristic of ICE flows that had to be accounted for was the fact that they are bounded by solid walls, with some of them moving in time with a prescribed cyclic movement that imposes important geometrical transformations during each engine cycle. In this context, a key ingredient of the model to be developed was the imposition of a RANS mode in the neighborhood of solid walls in order to accurately account for turbulent boundary layer effects without actually resolving them, which would require unrealistic simulation times for ICE flows. Furthermore, the ambition was to develop an approach able to automatically and continuously handle the transition between RANS and LES modes depending on the turbulent scales and the local mesh resolution in certain parts of the computational domain and in the different phases of the engine cycle.

Part I of the manuscript was dedicated to the introduction of key aspects of the modeling of turbulent flows, and to discuss published research on the simulation and turbulence modeling of the internal aerodynamics of SI engines.

Chapter 2 first recalled the fundamental equations of compressible single-phase gas flows, as well as key aspects of turbulence.

Chapter 3 then presented a literature review of modeling approaches for turbulent flows. First, three main CFD approaches to simulate turbulent flows of practical interest – RANS, LES and hybrid RANS/LES - were recalled, along with a presentation of key principles and major modeling approaches. Then, a literature review of published research on CFD modeling and simulation of ICE flows was given. It started with the outline of main characteristics of ICE flows, and in particular of the tumbling flow at the basis of modern SI engine concepts, and of its cyclic variability. After a short overview of published RANS and LES work, a classification and discussion of published applications of hybrid RANS/LES approaches to internal SI aerodynamics was presented.

Part II then detailed the work performed in the present thesis to extend an existing hybrid RANS/LES model so that it can be applicable to ICE flows.

Chapter 4 first exposed the principles of the Hybrid Temporal RANS/LES (HTLES) [80, 81, 129] model that was chosen as the basis of the present thesis, owing to its sound theoretical framework and its compliance with key requirements for the present work. First, the theoretical framework and basic principles of Hybrid RANS/Temporal-LES approaches were recalled. Second, the equations of the HTLES approach based on the  $k - \omega$  SST model were detailed, along with an outline of their implementation into the CONVERGE code. This implementation was the basis for all developments and applications that were presented.

The rest of Chapter 4 then presented work aimed at improving the near-wall behavior of the original HTLES approach. It consisted in implementing in HTLES an elliptic shielding function inspired by work published for PITM [28, 34], based on a Poisson equation derived from the elliptic blending theory [82]. The objective was to enforce the RANS mode in the neighborhood of solid walls. After outlining its combination with HTLES, its validation based on the simulation of a turbulent channel flow was presented. These simulations showed that without such an elliptic shielding, the RANS-LES transition occurred too close to the walls, and resulted in an important over-estimation of the flowrate and a poor reproduction of other flow characteristics. This problem was shown to be efficiently corrected by the use of the elliptic shielding function. Its usage indeed allowed ensuring that the RANS-LES transition took place at an imposed distance based on wall units. This resulted in a much more accurate reproduction of DNS findings for the studied channel flow, and in particular of the resolved velocity fluctuations and flowrate.

Chapter 5 then exposed the development of a version of the HTLES model specifically adapted to the simulation of cyclic ICE flows, as well as first validations on steady flow configurations.

First, the modeling issues resulting from the simulation of a cyclic flow were exposed, which mainly consist in cyclic moving boundaries with important geometrical transformations and time-dependent boundary conditions. The resulting difficulties concern the way HTLES defines the local resolution mode (RANS, LES or intermediate) that is based on phase averaged quantities. After shortly outlining different options envisaged to avoid phase averaging in the model, the development of the EWA-HTLES model was detailed. It consisted in approximating the statistical flow quantities used in HTLES by exponentially weighted averages (EWA). After defining the underlying Eulerian temporal filtering operator, its necessary characteristics to be able to address cyclic flows were exposed: filter out the fast-turbulent fluctuations from the resolved quantities, while keeping the slower time-varying components of the flow variables resulting from the cyclic nature of ICE flows. In order to address these issues, work then consisted in formulating an EWA approach that adjusts its temporal filter width in time and space based on a comparison of a turbulent time scale and of a fraction of the period of the engine cycle. The turbulent time scale was defined based on a synthetic case generated from a HIT spectrum. Then, the fraction of the cycle period was defined based on a sinusoidal time-varying synthetic case in order not to filter the slower time-varying component. This allowed proposing a formulation for the temporal filter width of EWA, that was used in the rest of the presented work.

The developed EWA-HTLES model, including the elliptic shielding and the temporal filter to approximate statistical averages, was then applied to the simulation of two steady flow configurations in order to validate its prediction as compared to the original HTLES model including the elliptic shielding, as well as to RANS and LES.

The first configuration was a turbulent channel, the DNS results of which were available to validate predictions. Preliminary tests allowed quantifying the sensitivity of EWA-HTLES to some key model parameters. It was shown that the details of the calculation of the total turbulent kinetic energy did not have a significant impact on the model predictions. This outlined that even if the EWA approach only provides an estimate of the total turbulent kinetic energy, the model predictions would not be significantly affected. Concerning the EWA filter size it was shown that the provided estimation and calibration allowed correctly to filter out turbulent fluctuations. The EWA-HTLES predictions

were found to be very similar to HTLES, thus validating the basic approximations and performed developments under steady (non-cyclic) flow conditions.

The second configuration was the steady flow bench with a centrally mounted symmetric fixed valve, experimentally investigated by Thobois *et al.* [127]. First, the EWA-HTLES predictions were validated by comparing them to experimental findings, as well as to those by the original HTLES. The two simulations yielded similar results in terms of mean and RMS velocity profiles and predicted fairly well the experimental pressure drop around the valve. This underlined the accurate near-wall modeling in the two HTLES simulations by using the RANS mode. Finally, EWA-HTLES predictions were shown to have advantages over RANS and LES findings. Unlike RANS, its predictions in terms of mean and RMS velocity profiles were as accurate as LES. Furthermore, by switching to RANS near the walls, the experimental pressure drop was more properly predicted than by LES.

Finally, Part III was dedicated to the application of EWA-HTLES to the simulation of two motored engine configurations, to the validation of its predictions against experimental findings, and to comparisons with predictions from RANS and LES approaches.

Chapter 6 presented the results obtained on the compressed tumble engine. A first Section was dedicated to explore the impact of the piston law on the predictions for the uncompressed case. It was shown that the experimental law exhibits small high frequency fluctuations, which induced important oscillations in the simulated velocity and pressure that were not observed in the experiment. A smoothed piston law was accordingly used in all presented simulations to reduce these oscillations. A total number of 43 consecutive cycles of the uncompressed configuration were simulated using EWA-HTLES. The last 40 cycles were used to compute the first two statistical moments. The EWA-HTLES results in terms of mean velocities and mean velocity fluctuations showed predictions comparable to LES and reproduced fairly well the PIV findings during the early stages of the intake. The results were more accurate than RANS, especially in predicting the tumble characteristics, the mean velocity fluctuations, and more specifically the increase in fluctuations in regions characterized by CCV. The predictions of all the simulations were less satisfactory at the end of the intake stroke. However, the exact reason for those discrepancies with PIV could not be explained. Then, a mesh dependency study showed a relatively low sensitivity of EWA-HTLES results when the mesh resolution was coarsened. Nevertheless, increasing the mesh resolution in the intake region improved the predictions of the overall flow. For the compressed configuration, the results were phase averaged using 18 consecutive cycles. All simulations, including EWA-HTLES, showed less satisfactory results during

compression because of the poor prediction of the flow at the end of the intake stroke, the reason of which remained yet unclear.

The final studied configuration was presented in Chapter 7 and concerned the Darmstadt single cylinder motored SI engine. Total of 42 consecutive cycles of the Darmstadt engine were simulated using EWA-HTLES. The results of the last 40 cycles were phase averaged to compare the simulation results with PIV findings, as well as to RANS and LES. EWA-HTLES showed predictions of the tumble characteristics and cyclic variabilities similar to LES. Both simulations predicted the mean and RMS velocities in a fairly similar manner, showing good agreement with the PIV findings. The RANS simulation gave fairly good predictions in terms of mean velocities at the beginning of the intake stroke. EWA-HTLES clearly showed advantages over RANS in the predictions of RMS velocities, which were significantly underestimated by RANS, especially in regions dominated by CCV. Nonetheless, the analysis of the RMS fields predicted with EWA-HTLES remained incomplete, as the subfilter part which represents the contribution of modeled scales could not be analyzed. A mesh dependency study showed that the flow predictions in EWA-HTLES and LES were significantly deteriorated when the mesh resolution was significantly lowered, while RANS showed less dependency to the mesh.

## 8.2 Perspectives

The developments performed in the present thesis open different perspectives for future research in the domain:

- A first step could be to find a way to solve the issue in the CONVERGE code that prevents the elliptic shielding from being activated on moving walls. This would ensure the switching to the RANS mode at the valves and the piston and thus improve the near-wall flow modeling.
- In areas where cyclic variability is small such as the plena and parts of ducts situated far from the combustion chamber, and in areas with attached flows such as straight parts of intake/exhaust ports, the RANS mode can be sufficient to simulate the flow. It was however found in our simulations that the model could not always switch to RANS equations even if the mesh resolution was lowered. For a more efficient way to ensure RANS in these regions, one could manually prescribe RANS through the EWA-HTLES internal parameters, while letting the model automatically

drive the RANS-LES transition in the rest of the domain. This option can lead to a delay in the development of structures resolved in LES at the RANS-LES interface. Therefore, using such an approach would require to further investigate the RANS-HTLES interface to determine how to deal with the lack of resolved flow fluctuations coming from the RANS region .

- In ICE flows, during the generation of the tumble, the intake jet passes through regions where different modeling modes are used: from LES downstream the intake valves to URANS at the cylinder liner and piston, then to LES when it deflects towards the core region. This creates a situation where the jet is subjected to different modeling approaches (LES-URANS-LES). This can affect its characteristics, such as the resolved fluctuations, that can have a major impact on the overall formation of the tumble. A detailed investigation of the boundary-layers and of the impact of the thickness of the RANS region at the walls on the characteristics of the predicted jet could allow a better understanding of such a situation, and of its impacts on the overall flow predictions.
- The EWA-HTLES approach could be combined with the AMR (Automatic Mesh Refinement) capability of CONVERGE. The resolution parameter in HTLES can be used by the AMR to achieve desired levels of resolved turbulent scales. To do so, the user only has to define the target amount of the modeled turbulent kinetic energy among the total turbulent kinetic energy for each region: for example, 1 for RANS and less than 0.2 for LES. The AMR will refine the mesh accordingly so that the HTLES resolution parameter is below this value.
- This work showed the ability of the EWA-HTLES approach to successfully operate in cyclic ICE flows, opening up the possibility to use it in a wide range of non-stationary flow applications. This could be done by adjusting the filter width of the EWA approach by introducing a time scale based on the non-stationary flow properties rather than the period of the cycle.
- Further developments are still needed to use EWA-HTLES under ICE realistic conditions including: spray formation, mixing and combustion. Each of these phenomena uses models that depend on the turbulence modeling approach to define its modeling parameters such as: characteristic turbulent time and length scales of the resolved fields, turbulent kinetic energy, and turbulent viscosity. Preliminary steps to extend EWA-HTLES to these flows would be to study each of the above-mentioned phenomena separately, define how to deal with the substantial variation

---

in the resolved length and time scales induced by the RANS-LES transition, and examine the impact of these variations on the simulated flows.



# Bibliography

- [1] A. H. Afailal, J. Galpin, A. Velghe, and R. Manceau, "Development and validation of a hybrid temporal les model in the perspective of applications to internal combustion engines," *Oil Gas Sci. Technol. - Rev. IFP Energies nouvelles*, vol. 74, p. 56, 2019. DOI: 10.2516/ogst/2019031. [Online]. Available: <https://doi.org/10.2516/ogst/2019031>.
- [2] A. A. Aldama, "Turbulence Modeling," in, 1990, pp. 7–41. DOI: 10.1007/978-3-642-84091-3\_{\\_}2. [Online]. Available: [http://link.springer.com/10.1007/978-3-642-84091-3\\_2](http://link.springer.com/10.1007/978-3-642-84091-3_2).
- [3] A. A. Amsden and M. Findley, "Kiva-3v: A block-structured kiva program for engines with vertical or canted valves,"
- [4] B. Basara, "Pans method as a computational framework from an industrial perspective," in *Progress in Hybrid RANS-LES Modelling*, S. Girimaji, W. Haase, S. Peng, and D. Schwamborn, Eds., Cham: Springer International Publishing, 2015, pp. 3–17, ISBN: 978-3-319-15141-0.
- [5] E. Baum, B. Peterson, B. Böhm, and A. Dreizler, "On the validation of les applied to internal combustion engine flows: Part 1: Comprehensive experimental database," *Flow, Turbulence and Combustion*, vol. 92, no. 1, pp. 269–297, 2014, ISSN: 1573-1987. DOI: 10.1007/s10494-013-9468-6. [Online]. Available: <https://doi.org/10.1007/s10494-013-9468-6>.
- [6] M. Baumann, F. Di Mare, and J. Janicka, "On the validation of large eddy simulation applied to internal combustion engine flows part ii: Numerical analysis," *Flow, Turbulence and Combustion*, vol. 92, no. 1-2, pp. 299–317, 2014, ISSN: 1386-6184. DOI: 10.1007/s10494-013-9472-x.
- [7] M. Baumann, di M. F., and J. J., "On the validation of large eddy simulation applied to internal combustion engine flows part ii: Numerical analysis," *Flow, Turbulence*

- and Combustion*, vol. 92, no. 1, pp. 299–317, 2014. DOI: 10.1007/s10494-013-9472-x. [Online]. Available: <https://doi.org/10.1007/s10494-013-9472-x>.
- [8] J. Bohbot, O. Colin, A. Velghe, J. Michel, M. Wang, P. K. Senecal, and E. Pomraning, “An Innovative Approach Combining Adaptive Mesh Refinement, the ECFM3Z Turbulent Combustion Model, and the TKI Tabulated Auto-Ignition Model for Diesel Engine CFD Simulations,” in *SAE 2016 World Congress and Exhibition*, SAE International, 2016. DOI: <https://doi.org/10.4271/2016-01-0604>.
- [9] J. Borée, D. Marc, R. Bazile, and B. Lecordier, “On the behavior of a large scale tumbling vortex flow submitted to compression,” *ESAIM: Proceedings*, vol. 7, A. Giovannini, G.-H. Cottet, Y. Gagnon, A. F., and E. Meiburg, Eds., pp. 56–65, Aug. 1999, ISSN: 1270-900X. DOI: 10.1051/proc:1999006. [Online]. Available: <http://www.esaim-proc.org/10.1051/proc:1999006>.
- [10] J. Boree, S. Maurel, and J. Bazile, “Disruption of a compressed vortex,” *Physics of Fluids*, vol. 14, no. 7, p. 2543, 2002. DOI: 10.1063/1.1472505. [Online]. Available: <https://doi.org/10.1063/1.1472505>.
- [11] J. Borée and P. C. Miles, “In-Cylinder Flow,” in *Encyclopedia of Automotive Engineering*, Chichester, UK: John Wiley & Sons, Ltd, Apr. 2014, pp. 1–31. DOI: 10.1002/9781118354179.auto119. [Online]. Available: <http://doi.wiley.com/10.1002/9781118354179.auto119>.
- [12] S Buhl, “Scale-resolving simulations of internal combustion engine flows,” Ph.D. dissertation, 2018.
- [13] S. Buhl, F. Dietzsch, C. Buhl, and C. Hasse, “Comparative study of turbulence models for scale-resolving simulations of internal combustion engine flows,” *Computers & Fluids*, vol. 156, pp. 66–80, 2017, ISSN: 00457930. DOI: 10.1016/j.compfluid.2017.06.023.
- [14] S. Buhl, F. Gleiss, M. Köhler, F. Hartmann, D. Messig, C. Brücker, and C. Hasse, “A combined numerical and experimental study of the 3d tumble structure and piston boundary layer development during the intake stroke of a gasoline engine,” *Flow, Turbulence and Combustion*, vol. 98, no. 2, pp. 579–600, 2017, ISSN: 1386-6184. DOI: 10.1007/s10494-016-9754-1.
- [15] S. Buhl, “Scale-resolving simulations of internal combustion engine flows,” Ph.D. dissertation, 2018.

- [16] S. Buhl, D. Hain, F. Hartmann, and C. Hasse, "A comparative study of intake and exhaust port modeling strategies for scale-resolving engine simulations," *International Journal of Engine Research*, vol. 19, no. 3, pp. 282–292, 2018, ISSN: 1468-0874. DOI: 10.1177/1468087417707452.
- [17] S. Buhl, F. Hartmann, and C. Hasse, "Identification of large-scale structure fluctuations in ic engines using pod-based conditional averaging," *Oil & Gas Science and Technology – Revue d'IFP Energies nouvelles*, vol. 71, no. 1, p. 1, 2016, ISSN: 1294-4475. DOI: 10.2516/ogst/2015021.
- [18] W. Cabot and P. Moin, "Approximate wall boundary conditions in the large-eddy simulation of high Reynolds number flow," *Flow, Turbulence and Combustion*, 2000, ISSN: 13866184. DOI: 10.1023/a:1009958917113.
- [19] P. C.D., G. T.B., G. C.E., and T. W.D., "The temporally filtered navier–stokes equations: Properties of the residual stress," *Physics of Fluids*, vol. 15, no. 8, pp. 2127–2140, 2003. DOI: 10.1063/1.1582858.
- [20] C. Chang, B Krumbein, S Jakirlic, C Tropea, B Basara, A Sadiki, J Janicka, B Böhm, A Dreizler, and B Peterson, "Flow dynamics in ic-engine configurations simulated by scale-resolving models," in *International Multidimensional Engine Modeling (IMEM) User's Group Meeting at the SAE Congress, Detroit, MI*, 2016.
- [21] B. Chaouat and R. Schiestel, "A new partially integrated transport model for subgrid-scale stresses and dissipation rate for turbulent developing flows," *Physics of Fluids*, vol. 17, no. 6, p. 065 106, 2005, ISSN: 1070-6631. DOI: 10.1063/1.1928607.
- [22] O. Colin and A. Benkenida, "The 3-Zones Extended Coherent Flame Model (ECFM3Z) for Computing Premixed/Diffusion Combustion," *Oil & Gas Science and Technology*, vol. 59, no. 6, pp. 593–609, 2004, ISSN: 1294-4475. DOI: 10.2516/ogst:2004043.
- [23] Y. M. Dakhoul and K. W. Bedford, "Improved averaging method for turbulent flow simulation. Part I: Theoretical development and application to Burgers' transport equation," *International Journal for Numerical Methods in Fluids*, vol. 6, no. 2, pp. 49–64, Feb. 1986, ISSN: 0271-2091. DOI: 10.1002/fld.1650060202. [Online]. Available: <http://doi.wiley.com/10.1002/fld.1650060202>.
- [24] L. Davidson, *Fluid mechanics, turbulent flow and turbulence modeling*, 2015.
- [25] S. Deck, "Zonal-detached-eddy simulation of the flow around a high-lift configuration," *AIAA Journal*, vol. 43, no. 11, pp. 2372–2384, 2005, ISSN: 0001-1452. DOI: 10.2514/1.16810.

- [26] A. Dejoan and R. Schiestel, "Les of unsteady turbulence via a one-equation subgrid-scale transport model," *International Journal of Heat and Fluid Flow*, vol. 23, no. 4, pp. 398–412, 2002, ISSN: 0142727X. DOI: 10.1016/S0142-727X(02)00144-3.
- [27] "European parliament and council of european union. regulation (ec) no 443/2009 to define the modalities for reaching the 2020 target to reduce co2 emissions from new passenger cars. in: Official journal of the european union," *Official Journal of the European Union*, 2014.
- [28] A. Fadai-Ghotbi, F. Christophe, R. Manceau, T. Gatski, and J. Boree, "Temporal filtering: A consistent formalism for seamless hybrid RANS–LES modeling in inhomogeneous turbulence," *International Journal of Heat and Fluid Flow*, vol. 31, pp. 378–389, Jun. 2010. DOI: 10.1016/j.ijheatfluidflow.2009.12.008.
- [29] A. Fadai-Ghotbi, C. Friess, R. Manceau, and J. Borée, "A seamless hybrid RANS-LES model based on transport equations for the subgrid stresses and elliptic blending," *Physics of Fluids*, vol. 22, no. 5, p. 055 104, 2010. DOI: 10.1063/1.3415254.
- [30] K. D. FERIET and J, "Theoretical and experimental averages of turbulent functions," *Proc. K. Ned. Akad. Wet.*, vol. 53, pp. 389–398, 1951. [Online]. Available: <https://ci.nii.ac.jp/naid/10025388848>.
- [31] J. H. Ferziger, "Simulation of incompressible turbulent flows," *Journal of Computational Physics*, vol. 69, no. 1, pp. 1–48, 1987, ISSN: 0021-9991. DOI: 10.1016/0021-9991(87)90154-9.
- [32] S. Fontanesi, A. d'Adamo, and C. J. Rutland, "Large-eddy simulation analysis of spark configuration effect on cycle-to-cycle variability of combustion and knock," *International Journal of Engine Research*, vol. 16, no. 3, pp. 403–418, 2015, ISSN: 1468-0874. DOI: 10.1177/1468087414566253.
- [33] D. Freudenhammer, E. Baum, B. Peterson, B. Böhm, B. Jung, and S. Grundmann, "Volumetric intake flow measurements of an IC engine using magnetic resonance velocimetry," *Experiments in Fluids*, vol. 55, no. 5, pp. 1–18, May 2014, ISSN: 07234864. DOI: 10.1007/s00348-014-1724-6. [Online]. Available: <https://link.springer.com/article/10.1007/s00348-014-1724-6>.
- [34] C. Friess, R. Manceau, and T. Gatski, "Toward an equivalence criterion for Hybrid RANS/LES methods," *Computers and Fluids*, vol. 122, pp. 233–246, 2015. DOI: 10.1016/j.compfluid.2015.08.010.
- [35] C. Fyhr and O. Dahlberg, "Complete engine modeling using cfd," in. DOI: 10.4271/2004-01-0109.

- [36] *Gasoline direct injection (gdi)*. [Online]. Available: [https://www.aalcar.com/library/what\\_is\\_gasoline\\_direct\\_injection.htm](https://www.aalcar.com/library/what_is_gasoline_direct_injection.htm).
- [37] T. Gatski, C. Rumsey, and R. Manceau, "Current trends in modelling research for turbulent aerodynamic flows," *Philosophical transactions of the royal society of london a: mathematical, physical and engineering sciences*, vol. 365, no. 1859, pp. 2389–2418, 2007.
- [38] T. Gatski, C. Rumsey, and R. Manceau, "Current trends in modelling research for turbulent aerodynamic flows," *Philosophical Transactions of the Royal Society of London Series A*, vol. 365, pp. 2389–2418, 2007. DOI: 10.1098/rsta.2007.2015.
- [39] T. B. Gatski and J.-P. Bonnet, "Kinematics, Thermodynamics and Fluid Transport Properties," in *Compressibility, Turbulence and High Speed Flow*, 2013. DOI: 10.1016/b978-0-12-397027-5.00001-0.
- [40] M. Ghaderi Masouleh, K. Keskinen, O. Kaario, H. Kahila, S. Karimkashi, and V. Vuorinen, "Modeling cycle-to-cycle variations in spark ignited combustion engines by scale-resolving simulations for different engine speeds," *Applied Energy*, vol. 250, pp. 801–820, 2019, ISSN: 03062619. DOI: 10.1016/j.apenergy.2019.03.198. [Online]. Available: <http://www.sciencedirect.com/science/article/pii/S0306261919306142>.
- [41] M. Ghaderi Masouleh, K. Keskinen, O. Kaario, H. Kahila, Y. M. Wright, and V. Vuorinen, "Flow and thermal field effects on cycle-to-cycle variation of combustion: Scale-resolving simulation in a spark ignited simplified engine configuration," *Applied Energy*, vol. 230, pp. 486–505, 2018, ISSN: 03062619. DOI: 10.1016/j.apenergy.2018.08.046.
- [42] S. Ghosal, "An analysis of numerical errors in large-eddy simulations of turbulence," *Journal of Computational Physics*, vol. 125, no. 1, pp. 187–206, Apr. 1996, ISSN: 00219991. DOI: 10.1006/jcph.1996.0088.
- [43] S. Girimaji and B. Basara, "Modelling the cut-off scale supplying variable in bridging methods for turbulence flow simulation," English, in *Proc. of 4th Int. Conference on Jets, Wakes and Separated Flows*, ., 2013.
- [44] S. S. Girimaji, "Partially-averaged navier-stokes model for turbulence: A reynolds-averaged navier-stokes to direct numerical simulation bridging method," in *Journal of Applied Mechanics, Transactions ASME*, vol. 73, American Society of Mechanical Engineers Digital Collection, May 2006, pp. 413–421. DOI: 10.1115/1.2151207.

- [45] M. S. Gritskevich, A. V. Garbaruk, J. Schütze, and F. R. Menter, "Development of ddes and iddes formulations for the k-w shear stress transport model," *Flow, Turbulence and Combustion*, vol. 88, no. 3, pp. 431–449, 2012, ISSN: 1386-6184. DOI: 10.1007/s10494-011-9378-4.
- [46] X. Han and S. Krajnović, "A new very large eddy simulation model for simulation of turbulent flow," in *Progress in Hybrid RANS-LES Modelling*, ser. Notes on Numerical Fluid Mechanics and Multidisciplinary Design, S. Fu, W. Haase, S.-H. Peng, and D. Schwamborn, Eds., vol. 117, Berlin, Heidelberg: Springer Berlin Heidelberg, 2012, pp. 131–140, ISBN: 978-3-642-31817-7. DOI: 10.1007/978-3-642-31818-4\underline{11}.
- [47] Z. Han and R. D. Reitz, "A temperature wall function formulation for variable-density turbulent flows with application to engine convective heat transfer modeling," *International Journal of Heat and Mass Transfer*, vol. 40, no. 3, pp. 613–625, 1997, ISSN: 0017-9310. DOI: [https://doi.org/10.1016/0017-9310\(96\)00117-2](https://doi.org/10.1016/0017-9310(96)00117-2). [Online]. Available: <http://www.sciencedirect.com/science/article/pii/S0017931096001172>.
- [48] C. Hasse, V. Sohm, and B. Durst, "Numerical investigation of cyclic variations in gasoline engines using a hybrid urans/les modeling approach," *Computers & Fluids*, vol. 39, no. 1, pp. 25–48, 2010, ISSN: 00457930. DOI: 10.1016/j.compfluid.2009.07.001.
- [49] C. Hasse, "Scale-resolving simulations in engine combustion process design based on a systematic approach for model development," *International Journal of Engine Research*, vol. 17, no. 1, pp. 44–62, 2016, ISSN: 1468-0874. DOI: 10.1177/1468087415597842.
- [50] C. Hasse, V. Sohm, and B. Durst, "Detached eddy simulation of cyclic large scale fluctuations in a simplified engine setup," *International Journal of Heat and Fluid Flow*, vol. 30, no. 1, pp. 32–43, 2009, ISSN: 0142727X. DOI: 10.1016/j.ijheatfluidflow.2008.10.001. [Online]. Available: <http://www.sciencedirect.com/science/article/pii/S0142727X08001525>.
- [51] J. B. Heywood, "Combustion engine fundamentals," *1ª Edição. Estados Unidos*, 1988.
- [52] A. K. M. F. Hussain and W. C. Reynolds, "The mechanics of an organized wave in turbulent shear flow," *Journal of Fluid Mechanics*, vol. 41, no. 2, pp. 241–258, 1970. DOI: 10.1017/S0022112070000605.

- [53] O. Imberdis, M. Hartmann, H. Bensler, L. Kapitza, and D. Thevenin, "A numerical and experimental investigation of a disi-engine intake port generated turbulent flow," in *SAE Technical Paper Series*, ser. SAE Technical Paper Series, SAE International, 400 Commonwealth Drive, Warrendale, PA, United States, 2007. DOI: 10.4271/2007-01-4047.
- [54] S. Jakirlić, G. Kadavelil, M. Kornhaas, M. Schäfer, D. C. Sternel, and C. Tropea, "Numerical and physical aspects in les and hybrid les/rans of turbulent flow separation in a 3-d diffuser," *International Journal of Heat and Fluid Flow*, vol. 31, no. 5, pp. 820–832, 2010, ISSN: 0142727X. DOI: 10.1016/j.ijheatfluidflow.2010.05.004. [Online]. Available: <http://www.sciencedirect.com/science/article/pii/S0142727X10000937>.
- [55] P. Janas, I. Wlokas, B. Böhm, and A. Kempf, "On the evolution of the flow field in a spark ignition engine," *Flow, Turbulence and Combustion*, vol. 98, no. 1, pp. 237–264, 2017.
- [56] Y. J. Jang, M. A. Leschziner, K. Abe, and L. Temmerman, "Investigation of anisotropy-resolving turbulence models by reference to highly-resolved les data for separated flow," *Flow, Turbulence and Combustion*, vol. 69, no. 2, pp. 161–203, 2002, ISSN: 1573-1987. DOI: 10.1023/A:1024764307706. [Online]. Available: <https://doi.org/10.1023/A:1024764307706>.
- [57] D. Jeandel, J. F. Brison, and J. Mathieu, "Modeling methods in physical and spectral space," *The Physics of Fluids*, vol. 21, no. 2, pp. 169–182, 1978. DOI: 10.1063/1.862211. eprint: <https://aip.scitation.org/doi/pdf/10.1063/1.862211>. [Online]. Available: <https://aip.scitation.org/doi/abs/10.1063/1.862211>.
- [58] J. Jeong and F. Hussain, "On the identification of a vortex," *Journal of Fluid Mechanics*, vol. 285, pp. 69–94, 1995. DOI: 10.1017/S0022112095000462.
- [59] C. Kannepalli and U. Piomelli, "Large-eddy simulation of a three-dimensional shear-driven turbulent boundary layer," *Journal of Fluid Mechanics*, 2000, ISSN: 00221120. DOI: 10.1017/S0022112000001798.
- [60] K. Keskinen, J. Koch, Y. M. Wright, M. Schmitt, M. Nuutinen, O. Kaario, V. Vuorinen, M. Larmi, and K. Boulouchos, "Numerical assessment of wall modelling approaches in scale-resolving in-cylinder simulations," *International Journal of Heat and Fluid Flow*, vol. 74, pp. 154–172, 2018, ISSN: 0142727X. DOI: 10.1016/j.ijheatfluidflow.2018.09.016.

- [61] J. Kim, H. Kim, S. Yoon, and S. Sa, "Effect of intake valve swirl on fuel-gas mixing and subsequent combustion in a cai engine," English, *International Journal of Automotive Technology*, vol. 9, no. 6, pp. 649–657, Dec. 2008, ISSN: 1229-9138. DOI: 10.1007/s12239-008-0077-7.
- [62] S. J. Kline, B. J. Cantwell, and G. M. Lilley, *Stanford conference on complex turbulent flows: Comparison of computation and experiment*. Standford University, 1981.
- [63] Kolmogorov, "Energy dissipation in local isotropic turbulence," in *Dokl. Akad. Nauk SSSR*, vol. 32, 1941, pp. 19–21.
- [64] H. Kosaka, Y. Wakisaka, Y. Nomura, Y. Hotta, M. Koike, K. Nakakita, and A. Kawaguchi, "Concept of "Temperature Swing Heat Insulation" in Combustion Chamber Walls, and Appropriate Thermo-Physical Properties for Heat Insulation Coat," *SAE International Journal of Engines*, vol. 6, no. 1, pp. 2013–01, Apr. 2013, ISSN: 1946-3944. DOI: 10.4271/2013-01-0274. [Online]. Available: <https://www.sae.org/content/2013-01-0274/>.
- [65] R. Kraichnan, "Eulerian and lagrangian renormalization in turbulence theory," *Journal of Fluid Mechanics*, vol. 83, no. 2, 349–374, 1977. DOI: 10.1017/S0022112077001232.
- [66] S. Krajnović and L. Davidson, "A mixed one-equation subgrid model for large-eddy simulation," *International Journal of Heat and Fluid Flow*, vol. 23, no. 4, pp. 413–425, 2002, ISSN: 0142727X. DOI: 10.1016/S0142-727X(01)00153-9.
- [67] V. K. Krastev, G. Di Ilio, G. Falcucci, and G. Bella, "Notes on the hybrid urans/les turbulence modeling for internal combustion engines simulation," *Energy Procedia*, vol. 148, pp. 1098–1104, 2018, ISSN: 1876-6102. DOI: 10.1016/j.egypro.2018.08.047. [Online]. Available: <http://www.sciencedirect.com/science/article/pii/S1876610218303370>.
- [68] V. Krastev, L. Silvestri, and G. Falcucci, "A modified version of the rng k–e turbulence model for the scale-resolving simulation of internal combustion engines," *Energies*, vol. 10, no. 12, p. 2116, 2017. DOI: 10.3390/en10122116.
- [69] V. K. Krastev and G. Bella, "A zonal turbulence modeling approach for ice flow simulation," *SAE International Journal of Engines*, vol. 9, no. 3, pp. 1425–1436, 2016, ISSN: 1946-3944. DOI: 10.4271/2016-01-0584.
- [70] V. K. Krastev, G. Bella, and G. Campitelli, "Some developments in des modeling for engine flow simulation," in *SAE Technical Paper Series*, ser. SAE Technical Paper Series, SAE International400 Commonwealth Drive, Warrendale, PA, United States, 2015. DOI: 10.4271/2015-24-2414.

- [71] V. K. Krastev, L. Silvestri, and G. Bella, "Effects of turbulence modeling and grid quality on the zonal urans/les simulation of static and reciprocating engine-like geometries," *SAE International Journal of Engines*, vol. 11, no. 6, pp. 669–686, 2018, ISSN: 1946-3944. DOI: 10.4271/2018-01-0173.
- [72] V. K. Krastev, L. Silvestri, G. Falcucci, and G. Bella, "A zonal-les study of steady and reciprocating engine-like flows using a modified two-equation des turbulence model," in *SAE Technical Paper Series*, ser. SAE Technical Paper Series, SAE International400 Commonwealth Drive, Warrendale, PA, United States, 2017. DOI: 10.4271/2017-24-0030.
- [73] H. Kuroda, Y. Nakajima, K. Sugihara, Y. Takagi, and S. Muranaka, "The fast burn with heavy EGR, new approach for low NOx and improved fuel economy," in *SAE Technical Papers*, SAE International, Feb. 1978. DOI: 10.4271 / 780006. [Online]. Available: <https://www.sae.org/publications/technical-papers/content/780006/>.
- [74] B. E. Launder and B. I. Sharma, "Application of the energy-dissipation model of turbulence to the calculation of flow near a spinning disc," *Letters in heat and mass transfer*, vol. 1, no. 2, pp. 131–137, 1974.
- [75] G. Lecocq, S. Richard, J.-B. Michel, and L. Vervisch, "A new les model coupling flame surface density and tabulated kinetics approaches to investigate knock and pre-ignition in piston engines," *Proceedings of the Combustion Institute*, vol. 33, no. 2, pp. 3105–3114, 2011, ISSN: 15407489. DOI: 10.1016/j.proci.2010.07.022.
- [76] K. H. Lee and C. S. Lee, "Effects of tumble and swirl flows on turbulence scale near top dead centre in a four-valve spark ignition engine," *Proceedings of the Institution of Mechanical Engineers, Part D: Journal of Automobile Engineering*, 2003, ISSN: 09544070. DOI: 10.1243/095440703322114988.
- [77] M. Lee and R. D. Moser, "Direct numerical simulation of turbulent channel flow up to  $Re_\tau \approx 5,200$ ," *Journal of Fluid Mechanics*, vol. 774, pp. 395–415, 2015. DOI: 10.1017/jfm.2015.268.
- [78] F. S. Lien, W. L. Chen, and M. A. Leschziner, "Low-reynolds-number eddy-viscosity modelling based on non-linear stress-strain/vorticity relations," in *Engineering turbulence modelling and experiments 3. Proceedings*, ser. Elsevier series in thermal and fluid sciences, G. BERGELES and W. Rodi, Eds., vol. 3, Amsterdam: Elsevier, 1996, pp. 91–100, ISBN: 978-0-444-82463-9. DOI: 10.1016 / B978- 0 - 444 - 82463 - 9.50015-0. [Online]. Available: <http://www.sciencedirect.com/science/article/pii/B9780444824639500150>.

- [79] P. C. Ma, T. Ewan, C. Jainski, L. Lu, A. Dreizler, V. Sick, and M. Ihme, "Development and analysis of wall models for internal combustion engine simulations using high-speed micro-piv measurements," *Flow, Turbulence and Combustion*, vol. 98, no. 1, pp. 283–309, 2017, ISSN: 1386-6184. DOI: 10.1007/s10494-016-9734-5.
- [80] R. Manceau, "Progress in Hybrid Temporal LES," in *Progress in hybrid RANS-LES modelling*, ser. Notes on Numerical Fluid Mechanics and Multidisciplinary Design, Y. Hoarau, S. Peng, D. Schwamborn, and A. Revell, Eds., vol. 137, New York NY: Springer Berlin Heidelberg, 2018, pp. 9–25, ISBN: 978-3-319-70030-4. DOI: 10.1007/978-3-319-70031-1{\textunderscore}2.
- [81] R. Manceau, T. Gatski, and C. Friess, "Recent progress in hybrid temporal LES-RANS modeling," *European Conference on Computational Fluid Dynamics*, vol. V, no. 1525–1532, 2010.
- [82] R. Manceau and K. Hanjalić, "Elliptic blending model: A new near-wall reynolds-stress turbulence closure," *Physics of Fluids*, vol. 14, no. 2, pp. 744–754, 2002. DOI: 10.1063/1.1432693. eprint: <https://doi.org/10.1063/1.1432693>. [Online]. Available: <https://doi.org/10.1063/1.1432693>.
- [83] S. Maurel, "Etude par imagerie laser de la génération et de la rupture d'un écoulement tourbillonnaire compressé : Situation modèle pour la validation de simulations aux grandes échelles dans les moteurs," Thèse de doctorat dirigée par Borée, Jacques Dynamique des fluides Toulouse, INPT 2001, Ph.D. dissertation, 2001, 207 p. [Online]. Available: <http://www.theses.fr/2001INPT035H>.
- [84] S Maurel, J Boree, and R Bazile, "Experimental Database on a compressed vortex," *Private communication*, 2001.
- [85] C. Meneveau, T. Lund, and W. Cabot, "A lagrangian dynamic subgrid-scale model of turbulence," *Journal of Fluid Mechanics*, vol. 319, 353–385, 1996. DOI: 10.1017/S0022112096007379.
- [86] F Menter, J. Ferreira, T Esch, and B Konno, "The sst turbulence model with improved wall treatment for heat tranfer predictions in gas turbines," in *Proceedings of the International Gas Turbine Congress, IGTC-2003-TS-059*, 2003.
- [87] F. Menter, J. Ferreira, T. Esch, and B. Konno, "The SST turbulence model with improved wall treatment for heat transfer predictions in gas turbines," *Proceedings of the International Gas Turbine Congress*, pp. 2–7, 2003.

- [88] F. Menter and C. Rumsey, "Assessment of two-equation turbulence models for transonic flows," in *Fluid Dynamics Conference*, ser. Fluid Dynamics and Co-located Conferences, American Institute of Aeronautics and Astronautics, 1994. DOI: 10.2514/6.1994-2343.
- [89] F. R. Menter, "Performance of popular turbulence models for attached and separated adverse pressure gradient flows," *AIAA Journal*, 1992, ISSN: 00011452. DOI: 10.2514/3.11180.
- [90] F. R. Menter and Y. Egorov, "The scale-adaptive simulation method for unsteady turbulent flow predictions. part 1: Theory and model description," *Flow, Turbulence and Combustion*, vol. 85, no. 1, pp. 113–138, 2010, ISSN: 1386-6184. DOI: 10.1007/s10494-010-9264-5.
- [91] C. Mockett, "A comprehensive study of detached-eddy simulation," en, Ph.D. dissertation, Berlin, 2009. DOI: 10.14279 / depositonce - 2305. [Online]. Available: <http://dx.doi.org/10.14279/depositonce-2305>.
- [92] A. S. Monin, A. M. Yaglom, and I. Scripta Technica, "Statistical Fluid Mechanics: Mechanics of Turbulence," *Mechanics of Turbulence MIT Press*, 1971.
- [93] A. Montorfano, F. Piscaglia, and A. Onorati, "A les study on the evolution of turbulent structures in moving engine geometries by an open-source cfd code," in *SAE Technical Paper Series*, ser. SAE Technical Paper Series, SAE International400 Commonwealth Drive, Warrendale, PA, United States, 2014. DOI: 10.4271/2014-01-1147.
- [94] A. Montorfano, F. Piscaglia, M. Schmitt, Y. M. Wright, C. E. Frouzakis, A. G. Tomboulides, K. Boulouchos, and A. Onorati, "Comparison of direct and large eddy simulations of the turbulent flow in a valve/piston assembly," *Flow, Turbulence and Combustion*, vol. 95, no. 2-3, pp. 461–480, 2015, ISSN: 1386-6184. DOI: 10.1007/s10494-015-9620-6.
- [95] A. P. Morse, J. H. Whitelaw, and M. Yianneskis, "Turbulent flow measurements by laser-doppler anemometry in motored piston-cylinder assemblies," *Journal of Fluids Engineering*, vol. 101, no. 2, pp. 208–216, 1979, ISSN: 0098-2202. DOI: 10.1115/1.3448937.
- [96] E. Nicoud, "Quantifying combustion robustness in GDI engines by Large-Eddy Simulation," Ph.D. dissertation, Université Paris-Saclay, 2018.

- [97] F. Nicoud, H. Toda, O. Cabrit, S. Bose, and L. Lee, "Using singular values to build a subgrid-scale model for large eddy simulations," *Physics of Fluids*, vol. 23, no. 8, p. 085 106, 2011. DOI: 10.1063/1.3623274. [Online]. Available: <https://doi.org/10.1063/1.3623274>.
- [98] Y. Orbach and G. E. Fruchter, "Forecasting sales and product evolution: The case of the hybrid/electric car," *Technological Forecasting and Social Change*, vol. 78, no. 7, pp. 1210–1226, Sep. 2011, ISSN: 00401625. DOI: 10.1016/j.techfore.2011.03.018. [Online]. Available: <https://linkinghub.elsevier.com/retrieve/pii/S0040162511000709>.
- [99] G. C. Papageorgakis and D. N. Assanis, "Comparison of linear and nonlinear rng-based k-epsilon models for incompressible turbulent flows," *Numerical Heat Transfer, Part B: Fundamentals*, vol. 35, no. 1, pp. 1–22, 1999, ISSN: 1040-7790. DOI: 10.1080/104077999275983.
- [100] D. J. Patterson, "Cylinder pressure variations, a fundamental combustion problem," in *SAE Technical Papers*, SAE International, Feb. 1966. DOI: 10.4271/660129. [Online]. Available: <https://www.sae.org/publications/technical-papers/content/660129/>.
- [101] U. Piomelli, *Wall-layer models for large-eddy simulations*, 2008. DOI: 10.1016/j.paerosci.2008.06.001.
- [102] F. Piscaglia, A. Montorfano, and A. Onorati, "A scale adaptive filtering technique for turbulence modeling of unsteady flows in ic engines," *SAE International Journal of Engines*, vol. 8, no. 2, pp. 426–436, 2015, ISSN: 1946-3944. DOI: 10.4271/2015-01-0395.
- [103] E. Pomraning and C. J. Rutland, "Dynamic one-equation nonviscosity large-eddy simulation model," *AIAA Journal*, vol. 40, no. 4, pp. 689–701, May 2002, ISSN: 00011452. DOI: 10.2514/2.1701. [Online]. Available: <https://arc.aiaa.org/doi/abs/10.2514/2.1701>.
- [104] S. Pope, *Turbulent Flows*. Cambridge University Press, 2000. DOI: 10.1017/CBO9780511840531.
- [105] L. Prandtl, "7. Bericht über Untersuchungen zur ausgebildeten Turbulenz," *ZAMM - Journal of Applied Mathematics and Mechanics / Zeitschrift für Angewandte Mathematik und Mechanik*, vol. 5, no. 2, pp. 136–139, Jan. 1925. DOI: 10.1002/zamm.19250050212. [Online]. Available: <https://onlinelibrary.wiley.com/doi/full/10.1002/zamm.19250050212><https://onlinelibrary.wiley.com/doi/abs/10.1002/zamm.19250050212><https://onlinelibrary.wiley.com/doi/10.1002/zamm.19250050212>.

- [106] C. Pruet, "Temporal large-eddy simulation: Theory and implementation," *Theoretical and Computational Fluid Dynamics*, vol. 22, no. 3, pp. 275–304, 2008. DOI: 10.1007/s00162-007-0063-0.
- [107] C. D. Pruet, "Eulerian time-domain filtering for spatial large-eddy simulation," *AIAA journal*, vol. 38, no. 9, pp. 1634–1642, May 2000, ISSN: 00011452. DOI: 10.2514/2.1146. [Online]. Available: <https://arc.aiaa.org/doi/abs/10.2514/2.1146>.
- [108] Y. L. Qi, L. C. Dong, H. Liu, P. V. Puzinauskas, and K. C. Midkiff, "Optimization of intake port design for si engine," *International Journal of Automotive Technology*, vol. 13, no. 6, pp. 861–872, 2012, ISSN: 1229-9138. DOI: 10.1007/s12239-012-0087-3.
- [109] O. Redlich and J. Kwong, "On the Thermodynamics of Solutions. V. An Equation of State. Fugacities of Gaseous Solutions," *Chemical Reviews*, vol. 44, no. 1, pp. 233–244, 1949, ISSN: 0009-2665. DOI: 10.1021/cr60137a013.
- [110] O. Reynolds, Reynolds, and Osborne, "IV. On the dynamical theory of incompressible viscous fluids and the determination of the criterion," *Philosophical Transactions of the Royal Society of London. (A.)*, vol. 186, pp. 123–164, Dec. 1895, ISSN: 0264-3820. DOI: 10.1098/rsta.1895.0004. [Online]. Available: <https://ui.adsabs.harvard.edu/abs/1895RSPTA.186..123R/abstract>.
- [111] C. Rhie and W. Chow, "Numerical study of the turbulent flow past an airfoil with trailing edge separation," *AIAA Journal*, vol. 21, no. 11, pp. 1525–1532, 1983, ISSN: 0001-1452. DOI: 10.2514/3.8284.
- [112] K. J. Richards, P. K. Senecal, and E. Pomraning, "Converge v2. 3 documentation," *Convergent Sciences Inc*, 2016.
- [113] L. F. Richardson.
- [114] A. Robert, S. Richard, O. Colin, L. Martinez, and L. De Francqueville, "LES prediction and analysis of knocking combustion in a spark ignition engine," *Proceedings of the Combustion Institute*, vol. 35, no. 3, pp. 2941–2948, 2015, ISSN: 1540-7489. DOI: <https://doi.org/10.1016/j.proci.2014.05.154>.
- [115] C. J. Rutland, "Large-eddy simulations for internal combustion engines – a review," *International Journal of Engine Research*, vol. 12, no. 5, pp. 421–451, 2011, ISSN: 1468-0874. DOI: 10.1177/1468087411407248.
- [116] P. Sagaut, S. Deck, and M. Terracol, *Multiscale and multiresolution approaches in turbulence: LES, DES and hybrid RANS/LES methods / applications and guidelines*, 2nd edition. London: Imperial College Press, 2013, ISBN: 978-1848169869.

- [117] R. Scarcelli, K. Richards, E. Pomraning, P. Senecal, T. Wallner, and J. Sevik, "Cycle-to-Cycle Variations in Multi-Cycle Engine RANS Simulations," in *SAE 2016 World Congress and Exhibition*.
- [118] R. Schiestel and A. Dejoan, "Towards a new partially integrated transport model for coarse grid and unsteady turbulent flow simulations," *Theoretical and Computational Fluid Dynamics*, vol. 18, no. 6, pp. 443–468, 2005. DOI: 10.1007/s00162-004-0155-z.
- [119] Schiestel R., "Multiple-time-scale modeling of turbulent flows in one-point closures," *The Physics of Fluids*, vol. 30, no. 3, pp. 722–731, 1987. DOI: 10.1063/1.866322.
- [120] P. K. Senecal, K. J. Richards, E Pomraning, T. Yang, M. Z. Dai, R. M. McDavid, M. A. Patterson, S. Hou, and T. Shethaji, "A new parallel cut-cell cartesian cfd code for rapid grid generation applied to in-cylinder diesel engine simulations," in *SAE Technical Paper*, SAE International, Apr. 2007. DOI: 10.4271/2007-01-0159. [Online]. Available: <https://doi.org/10.4271/2007-01-0159>.
- [121] J. P. Soltau, "Cylinder Pressure Variations in Petrol Engines," *Proceedings of the Institution of Mechanical Engineers: Automobile Division*, vol. 14, no. 1, pp. 99–117, Jan. 1960, ISSN: 0367-8822. DOI: 10.1243/pime{\\_}auto{\\_}1960{\\_}000{\\_}014{\\_}02. [Online]. Available: [https://journals.sagepub.com/doi/abs/10.1243/PIME\\_AUTO\\_1960\\_000\\_014\\_02](https://journals.sagepub.com/doi/abs/10.1243/PIME_AUTO_1960_000_014_02).
- [122] P. Spalart, W. Jou, M. Strelets, and S. Allmaras, "Comments on the Feasibility of LES for Wings, and on a Hybrid RANS/LES Approach," 1997.
- [123] P. R. Spalart and D. R. Bogue, "The role of CFD in aerodynamics, off-design," *The Aeronautical Journal*, vol. 107, no. 1072, pp. 323–329, 2003, ISSN: 0001-9240. DOI: 10.1017/S0001924000013634. [Online]. Available: /core/journals/aeronautical-journal/article/role-of-cfd-in-aerodynamics-offdesign/266F5861A59DB86B48A36313FA5A68D5.
- [124] C. G. Speziale, "Turbulence modeling for time-dependent rans and vles: A review," *AIAA Journal*, vol. 36, no. 2, pp. 173–184, 1998, ISSN: 0001-1452. DOI: 10.2514/2.7499.
- [125] H. Tennekes, "Eulerian and lagrangian time microscales in isotropic turbulence," *Journal of Fluid Mechanics*, vol. 67, no. 3, 561–567, 1975. DOI: 10.1017/S0022112075000468.
- [126] H Tennekes and J. L. Lumley, *A first course in turbulence MIT Press Cambridge*, 1972.

- [127] L. Thobois, G. Rymer, T. Souleres, and T. Poinso, "Large-Eddy Simulation in IC Engine Geometries," in *2004 SAE Fuels Lubricants Meeting Exhibition*, SAE International, 2004. DOI: <https://doi.org/10.4271/2004-01-1854>.
- [128] M. S. Toledo, L. Le Penven, M. Buffat, A. Cadiou, and J. Padilla, "Large eddy simulation of the generation and breakdown of a tumbling flow," *International Journal of Heat and Fluid Flow*, vol. 28, no. 1, pp. 113–126, 2007, The International Conference on Heat Transfer and Fluid Flow in Microscale (HTFFM-05), ISSN: 0142-727X. DOI: <https://doi.org/10.1016/j.ijheatfluidflow.2006.03.029>. [Online]. Available: <http://www.sciencedirect.com/science/article/pii/S0142727X06000506>.
- [129] T. Tran, R. Manceau, R. Perrin, J. Borée, and A. Nguyen, "A hybrid temporal LES approach. Application to flows around rectangular cylinders: Proc. 9th ERCOFTAC Int. Symp. on Eng. Turb. Modelling and Measurements, Thessaloniki, Greece," 2012.
- [130] A. Travin, M. Shur, M. Strelets, and P. Spalart, "Physical and Numerical Upgrades in the Detached-Eddy Simulation of Complex Turbulent Flows," in *Advances in LES of Complex Flows*, Friedrich R., Rodi, W., Ed., Dordrecht: Springer Netherlands, 2002, pp. 239–254.
- [131] H. Werner and H. Wengle, "Large-Eddy Simulation of Turbulent Flow Over and Around a Cube in a Plate Channel," in *Turbulent Shear Flows 8*, Durst F., Friedrich R., Launder B.E., Schmidt F.W., Schumann U., Whitelaw J.H., Ed., Berlin, Heidelberg: Springer Berlin Heidelberg, 1993, pp. 155–168, ISBN: 978-3-642-77674-8.
- [132] D. C. Wilcox, "Reassessment of the scale-determining equation for advanced turbulence models," *AIAA Journal*, vol. 26, no. 11, pp. 1299–1310, May 1988, ISSN: 00011452. DOI: 10.2514/3.10041. [Online]. Available: <https://arc.aiaa.org/doi/abs/10.2514/3.10041>.
- [133] Y. Wu, A. Montorfano, F. Piscaglia, and A. Onorati, "A study of the organized in-cylinder motion by a dynamic adaptive scale-resolving turbulence model," *Flow, Turbulence and Combustion*, vol. 100, no. 3, pp. 797–827, 2018, ISSN: 1386-6184. DOI: 10.1007/s10494-017-9881-3.





The blending function  $F_1$  should be equal to unity in the near the wall region to have the advantages of the  $k-\omega$  model near-wall and it should be equal to zero in the free stream to operate like the  $k-\varepsilon$  model in order to benefit from the free stream independence of this model. For this purpose,  $F_1$  expresses as:

$$\begin{cases} F_1 & = \tanh(arg^{1/4}) \\ arg_1 & = \min(\max(\frac{\sqrt{k}}{\beta^*\omega y}, \frac{500\nu}{y^2\omega}), \frac{4\rho\sigma_\omega k}{CD_{k\omega}y^2}) \\ CD_{k\omega} & = \max(2\rho\sigma_\omega \frac{1}{\omega} \frac{\partial k}{\partial x_i} \frac{\partial \omega}{\partial x_i}, 10^{-10}) \end{cases} \quad (3)$$

where  $y$  is the shortest distance to the closest surface.

The turbulent viscosity expresses as:

$$v_t = \frac{a_1 k}{\max(a_1\omega, F_2 S)} \quad (4)$$

**Development and validation of a hybrid  
temporal LES model in the perspective of  
applications to internal combustion  
engines**

# Development and validation of a hybrid temporal LES model in the perspective of applications to internal combustion engines

Al Hassan Afaïlal<sup>1,2,3,4,\*</sup>, Jérémy Galpin<sup>1,2</sup>, Anthony Velghe<sup>1,2</sup>, and Rémi Manceau<sup>3,4</sup>

<sup>1</sup>IFP Energies nouvelles, 1-4, avenue de Bois-Préau, 92852 Reuil-Malmaison Cedex, France

<sup>2</sup>Institut Carnot IFPEN Transports, 1-4, avenue de Bois-Préau, 92852 Reuil-Malmaison Cedex, France

<sup>3</sup>CNRS/Univ Pau & Pays Adour/E2S UPPA, Laboratoire de Mathématiques et de leurs Applications de Pau – Fédération IPRA, UMR5142, 64000 Pau, France

<sup>4</sup>Inria Bordeaux Sud-Ouest, 200 avenue de la vieille tour, 33405 Talence Cedex, France

Received: 11 January 2019 / Accepted: 6 May 2019

**Abstract.** CFD simulation tools are increasingly used nowadays to design more fuel-efficient and clean Internal Combustion Engines (ICE). Within this framework, there is a need to benefit from a turbulence model which offers the best compromise between prediction capabilities and computational cost. The Hybrid Temporal LES (HTLES) approach is here retained within the perspective of an application to ICE configurations. HTLES is a hybrid Reynolds-Averaged Navier Stokes/Large Eddy Simulation (RANS/LES) model based on a solid theoretical framework using temporal filtering. The concept is to model the near-wall region in RANS and to solve the turbulent structures in the core region if the temporal and spatial resolutions are fine enough. In this study, a dedicated sub-model called Elliptic Shielding (ES) is added to HTLES in order to ensure RANS in the near-wall region, regardless of the mesh resolution. A modification of the computation of the total kinetic energy and the dissipation rate was introduced as first adaptations of HTLES towards non-stationary ICE configurations. HTLES is a recent approach, which has not been validated in a wide range of applications. The present study intends to further validate HTLES implemented in CONVERGE code by examining three stationary test cases. The first validation consists of the periodic hill case, which is a standard benchmark case to assess hybrid turbulence models. Then, in order to come closer to real ICE simulations, *i.e.*, with larger Reynolds numbers and coarser near-wall resolutions, the method is validated in the case of a channel flow using wall functions and in the steady flow rig case consisting in an open valve at a fixed lift. HTLES results are compared to RANS  $k-\omega$  SST and wall-modeled LES  $\sigma$  simulations performed with the same grid and the same temporal resolution. Unlike RANS, satisfactory reproduction of the flow recirculation has been observed with HTLES in the case of periodic hills. The channel flow configuration has underlined the capability of HTLES to predict the wall friction properly. The steady flow rig shows that HTLES combines advantages of RANS and LES in one simulation. On the one hand, HTLES yields mean and rms velocities as accurate as LES since the scale-resolving simulation is triggered in the core region. On the other hand, hybrid RANS/LES at the wall provides accurate pressure drop in contrast with LES performed on the same mesh. Future work will be dedicated to the extension of HTLES to non-stationary flows with moving walls in order to be able to tackle realistic ICE flow configurations.

## 1 Introduction

The fight against global warming and the reduction of atmospheric pollution are meaningful environmental concerns in industrial societies and involve pursuing the continuous effort of reducing fuel consumption and control of emissions induced by Internal Combustion Engines (ICE). For these reasons, pollutant standards and CO<sub>2</sub> emission

targets are becoming more and more restrictive. In addition to these environmental considerations, the cost and time for the development of new products is a main concern due to the very competitive environment of the automotive industry. In this framework, there is a strong necessity to benefit from simulation tools which offer a good compromise between prediction capabilities and cost. Among all the physical phenomena occurring in internal combustion engines, the motion of the internal flow is one of the key factors as it is known to directly affect the global efficiency of the engine and its emissions.

\* Corresponding author: [al-hassan.afaïlal@ifp.fr](mailto:al-hassan.afaïlal@ifp.fr)

Turbulent flows encountered in ICE are wall-bounded and characterized by high Reynolds numbers of about  $10^5$ . This induces turbulent scales from an order of magnitude of 10 cm related to the bore diameter down to 10  $\mu\text{m}$  for the Kolmogorov turbulent scale. Direct Numerical Simulation (DNS) resolves the entire scale of motion and the computational cost increases as  $\text{Re}_\tau^4$  [1], where  $\text{Re}_\tau$  denotes the Reynolds number based on the friction velocity  $u_\tau$ , and this remains far beyond the capabilities of computers, both at present and in the near future. The reduction of the computational cost by introducing a model for turbulence is thus a necessity, and two main approaches are today commonly employed.

On one hand, Reynolds-Averaged Navier Stokes (RANS), which can also be denoted as URANS for unsteady RANS, in non-stationary flows, is the most used approach and is fully industrialized. Its small CPU requirements, as well as the availability of a large number of models explain its popularity. In the frame of ICE, RANS only provides phase-averaged quantities, which is sufficient for assessing stable and steady operating points. Comparisons between experimental and numerical results exhibit good agreement either for spark ignited engines [2] or for compression ignited engines [3] by using for instance the Extended Coherent Flame Model (ECFM) as combustion model [4]. Nevertheless, due to its averaged nature, RANS can hardly capture fully unsteady phenomena such as Cycle-to-Cycle Variations (CCV), even if recent work suggests that RANS could be relevant for a qualitative assessment [5]. On the other hand, Large Eddy Simulation (LES), based on a spatial filtering of the equations of motion, resolves large scales explicitly and models the small scales. This approach is fully adapted to predict phenomena such as the occurrence of knock or CCV [6]. However, LES requires that the grid size must be sufficient to solve a large amount of the turbulent energy which demands high computational cost, especially near the wall where turbulent structures are rather small [7]. Wall-modeling partially solves this issue by significantly decreasing the computational cost of LES since the grid resolution increases weakly as  $\ln(\text{Re}_\tau)$  instead of  $\text{Re}_\tau^2$  for wall-resolved LES which still remains unfeasible for industrial applications [7]. Setting apart the gain of computational cost, applications of wall-modeled LES in ICE flows have shown limited accuracy for the wall friction assessment [8], potentially due to the inconsistency between resolved LES fields, which relies on the spatial filtering and wall functions that provide statistical averaged quantities rather compatible with the RANS framework.

An alternative to wall-modeled LES consists in achieving the coexistence in the same computation of RANS and LES models. The approach called hybrid RANS/LES modeling has emerged very early since the concept was proposed by Schumann [9], and since then two different families of hybrid methods can be identified according to Sagaut *et al.*'s classification [10]:

- Zonal hybrid methods rely on a discontinuous treatment at the RANS-LES interface. The RANS and LES regions are predefined by the user, and standard

RANS and LES models are used in each region. The main difficulty consists in addressing the management of the interfaces: the resolved content has to be reconstructed explicitly at the inlet of a LES region to take into account the lack of resolved fluctuations in the RANS region.

- Global or seamless methods are based on one set of equations and continuous treatment at the interface between RANS and LES zones. In particular, this approach usually treats the near-wall region with RANS and operates in LES mode where the grid resolution is suitable by reducing the modeled-stresses or the turbulent viscosity of the original RANS model.

Despite the development of a large number of hybrid methods, few of them were applied to ICE flows: Buhl *et al.* [11] performed a comparative study of several hybrid approaches, such as Scale Adaptive Simulation (SAS) and Detached Eddy Simulation (DES), with LES sub-grid models. Moreover, Partially-Averaged Navier-Stokes (PANS) has been recently applied to moving IC engine [12].

Despite their attractiveness, many hybrid models suffer from empirical bases, and do not tackle the issue of mutual combination in the same computational domain of averaged RANS and instantaneous filtered LES quantities. In this framework, the recent seamless model called Hybrid Temporal LES (HTLES) method [13] is preferred because of its solid theoretical formalism. Indeed, the multi-scale approach is used to model the unresolved structures, and the introduction of the temporal filtering [14, 15] solves the inconsistency for stationary flows that appears between the scale-resolving and RANS regions in conventional hybrid methods. The first part of this article is dedicated to recalling the main hypotheses and set of equations of HTLES, and to introducing the Elliptic Shielding (ES) sub-model which intends to enforce RANS near the wall, regardless of the mesh resolution. Further modifications of the computation of the total turbulent kinetic energy and the dissipation rate are added to HTLES implemented in CONVERGE as a first adaptation towards non-stationary flows applications.

Regarding the validation of the HTLES model, Manceau [13] studied the flow around a square-sectioned cylinder and showed that HTLES provides results close to experimental measurements with a substantial computational cost reduction compared to LES. The present paper intends to complete the validation of HTLES and to assess the validity of the proposed modifications of the model. For that purpose, three stationary test cases for which reference data are available are examined. Firstly, the developed HTLES is validated on a flow over periodic hills, which is a common benchmark test case used to assess hybrid turbulence models [16, 17]. Nevertheless, this test case significantly differs from the targeted industrial applications since the separation due to adverse pressure gradient on a smooth wall requires the resolution of the boundary layer down to the wall, which is not a common practice for ICE simulations. In order to evaluate the predictive capabilities of the method in the case of a simulation representing the near-wall region by wall functions, two additional

cases are computed. The channel flow case makes the assessment of the capability to properly predict the wall friction possible. From an automotive engineering standpoint, the correct prediction of friction is of prior importance as it is directly related to the mass of trapped air, which is strongly coupled to the output power of the engine. The third test case is related to a steady flow rig dedicated to studying the flow around an open valve with a fixed lift whose dimensions are very close to actual engines.

## 2 Hybrid temporal large eddy simulation

### 2.1 Solution to the inconsistency issue

Whatever the concept applied for making the model sensitive to the grid resolution, many models define the scale-resolving mode empirically, which can lead to wrong dissipation levels in the LES region as observed with the VLES model [10]. Moreover, few of them address the issue of combining in the same computational domain RANS and LES quantities, which are of different nature [18].

The Temporal Partially Integrated Transport Model (TPITM) [19] addresses the above-mentioned issues. On the one hand, TPITM converts any RANS model into a scale-resolving model [20] in a way similar to the Partially Integrated Transport Model (PITM) to define the sub-filtered scales derived from the consistent multi-scale approach [21–23]. This method uses a spectral cut-off to define the unresolved scales, and makes the simulation of turbulent flows possible on relatively coarse grids when the cut-off wave number can be located in the energy-containing range and as far as the grid-size is suitable to correctly describe the resolved flow. Moreover, TPITM eliminates the inconsistency in the transition zone between LES and RANS in the framework of statistically stationary flows by using a temporal formalism for LES [14], since any temporally filtered quantity tends to the statistically averaged quantity in the limit of an infinite filter width [18].

TPITM transforms any RANS model into a scale-resolving model by reducing the modeled stresses or the turbulent viscosity. In the present work, the sub-filter stress  $\tau_{ij}$  is modeled using the Boussinesq approximation [24]

$$\tau_{ij} - \frac{2}{3} k_{\text{sfs}} \delta_{ij} = 2\nu_{\text{sfs}} S_{ij}, \quad (1)$$

where  $\nu_{\text{sfs}}$  is the sub-filter viscosity and  $S_{ij}$  the resolved strain rate tensor. The sub-filter turbulent kinetic energy,  $k_{\text{sfs}}$ , represents the energy of eddies with higher frequencies than the cut-off frequency imposed by the model.

The TPITM model reduces the sub-filter viscosity of the RANS model by making the dissipation equation sensitive to the temporal filter width via a modified  $C_{\varepsilon 2}$  coefficient. However, applications of this model have shown difficulties in sustaining the correct level of resolved energy, since the energy partition is indirectly controlled through the  $\varepsilon$ -equation and not directly in the  $k$ -equation as it is the case for some hybrid approaches such as DES [25].

As a solution, Tran *et al.* [24] proposed the HTLES model which transfers the dependence of TPITM on the

temporal filter width from the dissipation equation to the sub-filter energy equation to sustain the correct level of resolved energy [26]. To this end, equivalence between TPITM and HTLES is ensured by assuming that both models provide the same level of sub-filter energy for the same filter width and tend to the same RANS model when the filter width approaches infinity. As a consequence, HTLES avoids the main weakness of TPITM of setting the energy partition control on the dissipation equation while keeping all the theoretical advantages of TPITM. The set of equations of HTLES is provided in the following section.

### 2.2 Sub-filter viscosity evaluation

HTLES is based here on the  $k$ - $\omega$  SST model [13, 24], in which the turbulence viscosity expresses as

$$\nu_{\text{sfs}} = \frac{a_1 k_{\text{sfs}}}{\max(a_1 \omega, F_2 S)}, \quad (2)$$

where  $S$  is the strain rate,  $F_2 = \max\left(\frac{\sqrt{k_{\text{sfs}}}}{0.09\omega y}, \frac{500\nu}{y^2\omega}\right)$  and  $a_1 = \sqrt{\beta^*}$ .

In the same way as the two-equation DES, the resolved scales are controlled by an appropriate modification of the dissipation term in the  $k$ -equation, but this modification is based here on a time scale rather than a length scale

$$\frac{D}{dt}(\rho k_{\text{sfs}}) = P_{\text{sfs}} - \rho \frac{k_{\text{sfs}}}{T} + D_{\text{sfs}}, \quad (3)$$

where  $\rho$  is the density,  $P_{\text{sfs}}$  is the sub-filter production,  $D_{\text{sfs}}$  is the sub-filter diffusion and  $T$  is the width of the temporal filter defined as [24, 27]

$$T = \frac{r}{1 + \left(\frac{C_{\varepsilon 2}}{C_{\varepsilon 1}} - 1\right) \left(1 - r^{C_{\varepsilon 2}}\right)} \frac{k_{\text{tot}}}{\varepsilon}, \quad (4)$$

where the energy ratio  $r = \frac{k_{\text{sfs}}}{k_{\text{tot}}}$  is defined as the ratio of the modeled energy  $k_{\text{sfs}}$  to the total turbulent energy  $k_{\text{tot}}$ ,  $\varepsilon = \beta^* k_{\text{sfs}} \omega$  is the dissipation rate, and  $C_{\varepsilon 1} = 1.44$  and  $C_{\varepsilon 2} = 1.92$  are constants. To take into account the cut-off frequency, Tran *et al.* [24] proposed a relation between  $r$  and the cut-off frequency,

$$r = \min\left(1, \frac{1}{\beta} \left(\frac{U_c}{\sqrt{k_{\text{tot}}}}\right)^{\frac{2}{3}} \left(\frac{\omega_c k_{\text{tot}}}{\varepsilon}\right)^{-\frac{2}{3}}\right), \quad (5)$$

where  $U_s = \tilde{U} + \gamma\sqrt{k_{\text{tot}}}$  is the sweeping velocity [13].  $\tilde{U}$  denotes the mean resolved velocity magnitude, and  $\gamma$  is a constant.  $\omega_c = \min\left(\frac{\pi}{dt}, \frac{U_s \pi}{\Delta}\right)$  is the highest cut-off frequency, with  $dt$  and  $\Delta = \max(dx, dy, dz)$  the time and grid steps, respectively, and  $\beta$  is a constant fixed at 0.667, calibrated in order to exhibit the correct amount of dissipation in the case of decaying homogeneous turbulence [24]. HTLES estimates the ratio  $r$  based on the analytical integration of the equilibrium Eulerian spectrum,

$$E_T(\omega) = C_\kappa \varepsilon^{2/3} U_s \omega^{-5/3}, \quad (6)$$

between the cut-off frequency  $\omega_c$  and infinity, with  $C_\kappa \approx 1.5$  is the Kolmogorov constant. The ratio  $r$  is bounded by unity, which corresponds to the RANS mode, and the scale-resolving mode is triggered for values of  $r$  less than one.

The total turbulent kinetic energy introduced above is defined as the sum of the resolved kinetic energy  $k_{\text{res}}$  and the sub-filter kinetic energy  $k_{\text{sfs}}$ ,

$$k_{\text{tot}} = k_{\text{sfs}} + k_{\text{res}}, \quad (7)$$

where  $k_{\text{res}}$  is defined as,

$$k_{\text{res}} = \frac{1}{2} \langle (\tilde{U}_i - \langle \tilde{U}_i \rangle) (\tilde{U}_i - \langle \tilde{U}_i \rangle) \rangle, \quad (8)$$

with  $\tilde{U}_i$  the  $i$ -th component of the resolved velocity, and  $\langle \dots \rangle$  is the statistical average operator.

The parameters used in HTLES are averaged in time. However,  $k_{\text{res}}$  is a statistical quantity that requires a relatively long time-averaging to converge. It was found (not shown here) that the simplified expression,

$$k_{\text{res}} = \frac{1}{2} \langle (\tilde{U}_i - \langle \tilde{U}_i \rangle) (\tilde{U}_i - \langle \tilde{U}_i \rangle) \rangle, \quad (9)$$

does not affect the results significantly, although  $k_{\text{res}}$  is now a fluctuating quantity. Moreover, this simplification is useful for future non-stationary ICE application, in which estimating statistical quantities by time-averaging is not possible. For such cases, using an estimate of  $\langle \tilde{U}_i \rangle$ , based, for instance, on time filtering, will be necessary.

### 2.3 Elliptic shielding

One of the main objectives of hybrid models is to operate in RANS mode in the near-wall region in order to reduce the cost of wall-bounded simulations. However, several hybrid methods do not properly enforce the RANS mode near the wall. For instance, DES is conceptually designed to cover attached boundary layers in RANS mode and to operate in LES mode in detached regions. However, applications to industrial flows show Modeled-Stress Depletion (MSD) and Grid-Induced Separation (GIS) when the model operates in LES mode within the boundary layer with insufficient grid refinement [28]. In the same way as DES, results of the PITM model in a channel flow at  $\text{Re}_\tau = 395$  show similar issues with resolved fluctuations occurring too close to the wall and increasing too rapidly when moving away from wall [19].

First applications of HTLES on wall-bounded flow exhibited similar problems as outlined in PITM simulations [19]. The ratio  $r$  predicted by the model can be less than unity near the wall (Fig. 1), which means that the model may operate in the scale-resolving mode near the wall which is undesirable.

Several solutions were proposed within this context. Shielding functions are added to DES in an enhanced version called Delayed Detached-Eddy Simulation (DDES) [28] in order to enforce the RANS mode in the boundary layer. Similarly, a shielding was proposed in the PITM

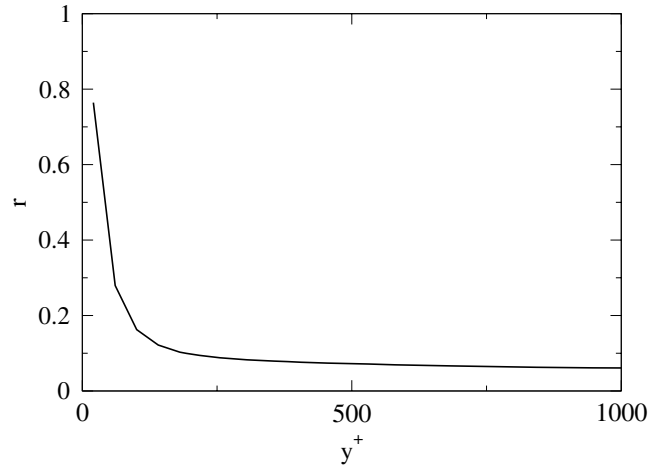


Fig. 1. The statistical average of the ratio  $r$  profile given by the HTLES near the wall in a channel flow at  $\text{Re}_\tau = 1000$ .

framework by adding the wall-distance dependency to the energy ratio [19] using a parameter  $\alpha$  based on the Elliptic Blending (EB) framework, such that the RANS mode is prescribed at walls.

In a similar way, the blending factor  $\alpha$  is added to the expression for  $r$  used in HTLES

$$r = \min \left( 1, (1 - \alpha^2) + \alpha^2 \frac{1}{\beta} \left( \frac{U_c}{\sqrt{k_{\text{tot}}}} \right)^{\frac{2}{3}} \left( \frac{\omega_c k_{\text{tot}}}{\varepsilon} \right)^{-\frac{2}{3}} \right), \quad (10)$$

where  $\alpha$  is the solution of the following equation

$$\alpha - L_{\text{sfs}}^2 \nabla^2 \alpha = 1, \quad (11)$$

with  $\alpha_{\text{wall}} = 0$  and the sub-filter length  $L_{\text{sfs}}$  expresses as

$$L_{\text{sfs}} = C_L \max \left( \frac{k_{\text{sfs}}^{\frac{3}{4}}}{\varepsilon}, r^{\frac{3}{2}} C_\eta \frac{v^{\frac{3}{4}}}{\varepsilon^{\frac{1}{4}}} \right), \quad (12)$$

with  $C_L = 0.161$ ,  $C_\eta = 80$ .

### 2.4 Near wall treatment

The HTLES model reduces the cost of scale-resolving simulations significantly near the wall by using RANS models in the near-wall region. To solve the boundary layer with RANS, the grid resolution must be such that the wall-adjacent cell is as small as  $y^+ = 2$  in the wall-normal direction. This requirement must be verified in the whole domain, which can be challenging in high Reynolds number flows and complex geometries [29]. Further cost reduction for wall-bounded flows mandatory for industrial ICE simulations can be achieved through the use of wall functions, which can be used as an alternative to the explicit resolution of the whole boundary layer.

HTLES is here combined with the automatic wall function [29]. This method offers a versatile formulation which gradually switches from the low-Re formulation to the

log-wall function formulation depending on the grid resolution using a function of  $y^+$ :

- The specific dissipation rate  $\omega$  is computed from a blending formula of the analytical solution of  $\omega$  in the viscous sub-layer  $\omega_{\text{visc}} = \frac{6\nu}{0.075y^2}$  ( $y$  is the distance to nearest wall) and in the logarithmic region  $\omega_{\text{log}} = \frac{1}{3\kappa} \frac{u_\tau}{y}$

$$\omega(y^+) = \sqrt{\omega_{\text{visc}}^2 + \omega_{\text{log}}^2}. \quad (13)$$

- The boundary condition for momentum equations is defined from the formulation of the friction velocity in the viscous sub-layer  $u_{\tau,\text{visc}} = \frac{U_t}{y^+}$  and in the logarithmic region  $u_{\tau,\text{log}} = \frac{U_t}{\kappa \ln(y^+) + C}$ ,

$$u_\tau = \sqrt[4]{u_{\tau,\text{visc}}^4 + u_{\tau,\text{log}}^4}, \quad (14)$$

where  $C = 5.1$  and  $U_t$  is the component of velocity tangential to the wall.

The aforementioned equations require the a priori knowledge of  $y^+$ . An approximation of the friction velocity  $u_\tau$  is used to estimate  $y^+$

$$u_\tau = C_\mu^{0.25} \sqrt{k_{\text{sfs}}}, \quad (15)$$

where  $C_\mu = 0.09$ .

This formulation extends the use of standard wall functions, which are initially valid in the logarithmic region only.

### 3 CONVERGE CFD

HTLES has been implemented in CONVERGE CFD, which is widely used for ICE simulations. CONVERGE is a cell-centered code using the finite-volume method to solve the equations for compressible flows. The mesh is generated automatically using hexahedra far from the walls, while the cells near the walls are cut by the outer surface of the geometry using the cut-cell technique. The pressure-velocity coupling is achieved using a modified Pressure Implicit with Splitting of Operator (PISO) method [30]. The convection and diffusion terms are approximated by second-order central differencing, and they are advanced in time using the Crank-Nicolson second-order scheme. The Redlich-Kwong equation of state [31] is used for gas to couple the density, pressure and temperature. The Rhie-Chow [32] interpolation scheme is used to maintain collocated variable and to prevent pressure velocity decoupling and associated oscillations. A step-flux limiter is used to maintain physical solutions by restricting fluxes and mimicking a switch to a lower-order spatial discretization to avoid spurious oscillations in the solution.

The next section aims to assess the performance of the HTLES method in three statistically stationary flow cases.

## 4 Applications

### 4.1 Methodology

The predictions of HTLES are compared in three different cases (periodic hills, channel flow and steady flow rig) for which experimental or numerical reference data are available. The first part discusses the predictive capabilities of HTLES in periodic hills. This test case is known to be challenging for both RANS and LES. On one hand, RANS can predict the separation accurately, but shows difficulties to locate the reattachment correctly. Moreover, a large sensitivity of the results to the turbulence model used was reported in [33]. On the other hand, LES computational cost is large for solving the flow within the vicinity of the lower wall, which is essential to predict the flow correctly in the whole domain. Then, in order to evaluate the predictive capabilities of the method in the case of a simulation representing the near-wall region by wall functions, the channel flow and the steady flow rig cases are computed.

In order to assess the positioning of HTLES, RANS and LES computations are also performed. RANS simulations are performed using the unsteady two-equation  $k-\omega$  SST (Menter and Rumsey [34]) model combined with the automatic wall functions previously described. For LES, the  $\sigma$ -model [35] combined with Werner and Wengle wall function is used [36].

Regarding RANS simulations, results of the periodic hills and the channel yielded steady solutions. Nevertheless, for the steady flow rig simulations, small-amplitude fluctuations have been observed and no steady solution could be reached and statistical average is thus performed. These fluctuations may be related to the dispersion error of the central differencing scheme, which can produce spatial oscillations acting as perturbations in the detached shear layer [37].

It is worth noting that the same grid is used for all simulations whatever the turbulence modeling approach (HTLES, RANS or LES) in order to focus on the single impact of the models on the results.

### 4.2 Flow over periodic hills

This configuration is part of the ERCOFTAC database and corresponds to a 2-D separating flow over periodic hills. Due to the hill slope, the flow separates downstream the hill, which results in separation and recirculation followed by reattachment on the flat wall upstream the subsequent hill. The Reynolds number based on the hill height  $h = 28$  mm and the bulk velocity is  $Re_h = 10\,595$ .

The dimensions of the computational domain were examined in [38] and are thus chosen as  $L_x = 9.0$  h,  $L_y = 3.035$  h and  $L_z = 4.5$  h. Well-resolved LES with a grid of 12 million elements was performed in [38], which is taken as the reference data. The flow rate is imposed by a stream-wise momentum source term, which is adjusted in order to provide the same mass flow rate as the reference. This configuration has been simulated with the  $k-\omega$  SST model and the HTLES with ES. The same grid, displayed in Figure 2, has been employed for both simulations. The mesh is refined along the bottom wall and in the recirculation

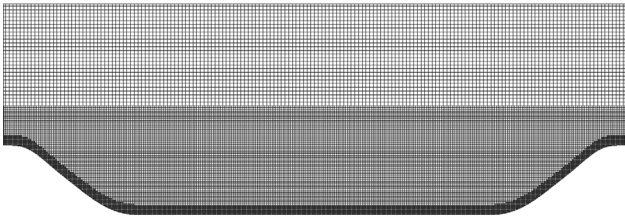


Fig. 2. Cut plane of the hexahedral mesh in the flow over periodic hills.

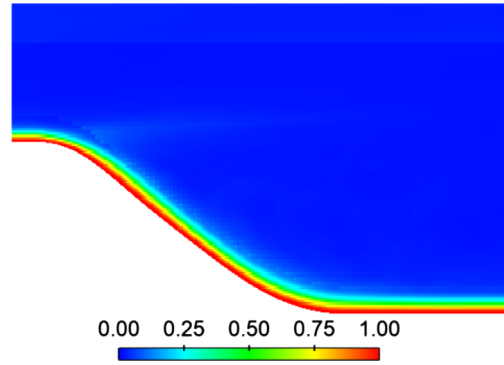


Fig. 4. Center slice of the statistical average of the ratio  $r$  in the lower part of the domain.

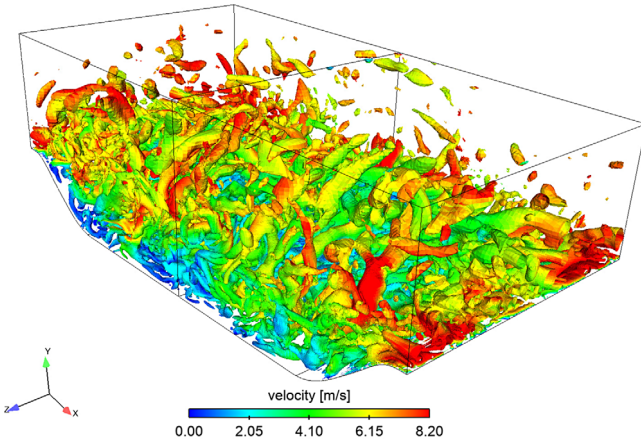


Fig. 3. Iso-surfaces of the non-dimensional  $Q$ -criterion colored by the velocity magnitude given by the HTLES with ES in a flow over periodic hills.

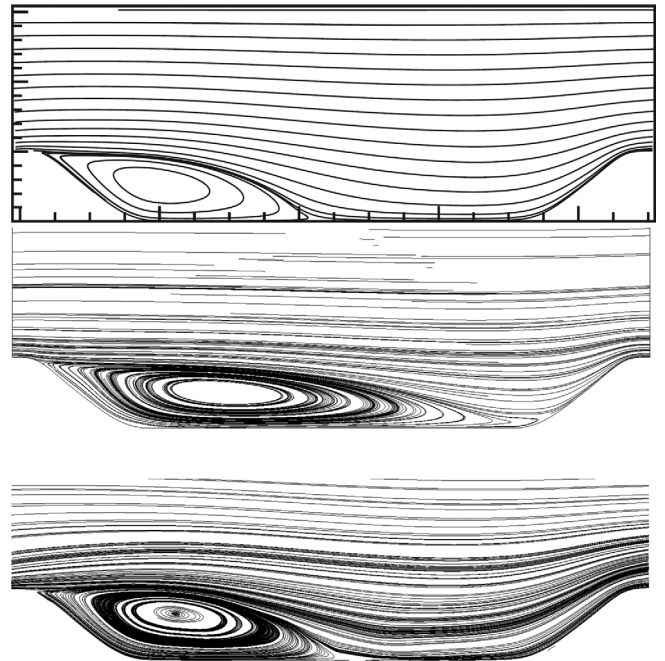


Fig. 5. Statistical average of the streamline patterns in a flow over periodic hills given by: (top) the reference data [17], (middle)  $k-\omega$  SST and (bottom) HTLES.

region. The grid setup consists of 5.8 million cells. At the bottom wall, the grid resolution is refined such that the thickness of the cells adjacent to the wall is around 2 in wall units. Indeed, this typical test-case for hybrid model is commonly performed by solving the wall boundary layer [16, 17] and this best-practice is here also retained.

A total time of 2.5 s was simulated, which approximately corresponds to 67 convective times  $t_x = \frac{L_x}{U_{\text{bulk}}}$ , where  $L_x$  is the length of the channel and  $U_{\text{bulk}}$  the bulk velocity. The flow was first established during 11 convective time and then the statistical average was performed during 56 convective times. The initial field is defined by a prior steady RANS solution performed using the same setup.

In Figure 3, iso-surfaces of the non-dimensional  $Q$ -criterion equal to 0.8 are used to identify the turbulent structures given by the HTLES model. The threshold retained for plotting the  $Q$ -isosurfaces highlights the complex turbulent structures occurring in the bottom part of the geometry while less structures can be seen on the top due to their lower turbulent intensity and the coarse grid resolution. Figure 4 represents the statistical average of the ratio  $r$  around the hill provided by the HTLES. Setting apart the near-wall regions where the ES enforces the RANS mode and thus  $r = 1$ , the domain exhibits very small values of  $r$ , which indicates that the scale-resolving method is active almost everywhere.

The streamlines computed from the results of the statistically-averaged velocities for the simulations performed

and the reference data are compared in Figure 5. One may observe that the  $k-\omega$  SST model overestimates the recirculation length. This issue has already been encountered in previous studies using RANS models [33] since they fail to assess properly flows featured by massively separated structures. Unlike RANS, the streamline pattern shown by HTLES is very similar to the reference data. The center of the recirculation region is properly located, and the flow reattaches at the same location as the reference.

Figure 6 shows the development of the streamwise velocity along the hill channel. As already mentioned, the  $k-\omega$  SST velocity profiles show limited accuracy in this configuration. At the top of the hill, the streamwise velocity is underestimated near the wall because of too late reattachment of the flow upstream the hill. It is observed at  $\frac{x}{h} = 2$

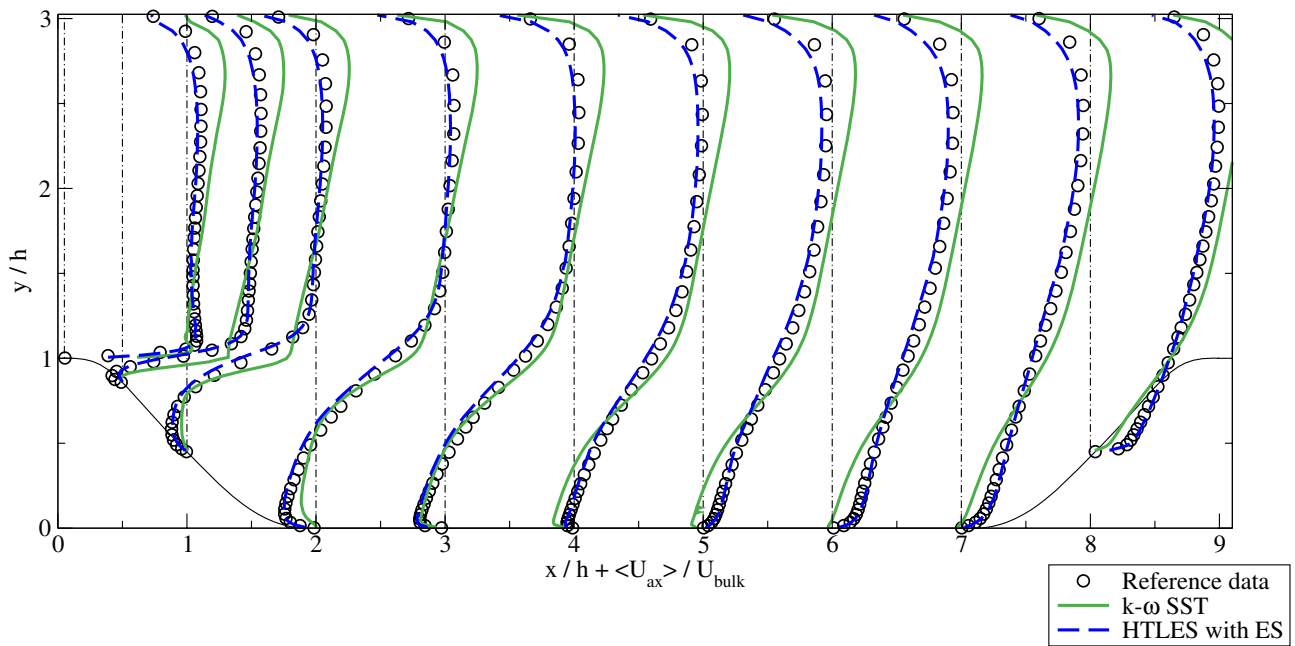


Fig. 6. Statistical average of the streamwise velocity in the periodic hill channel.

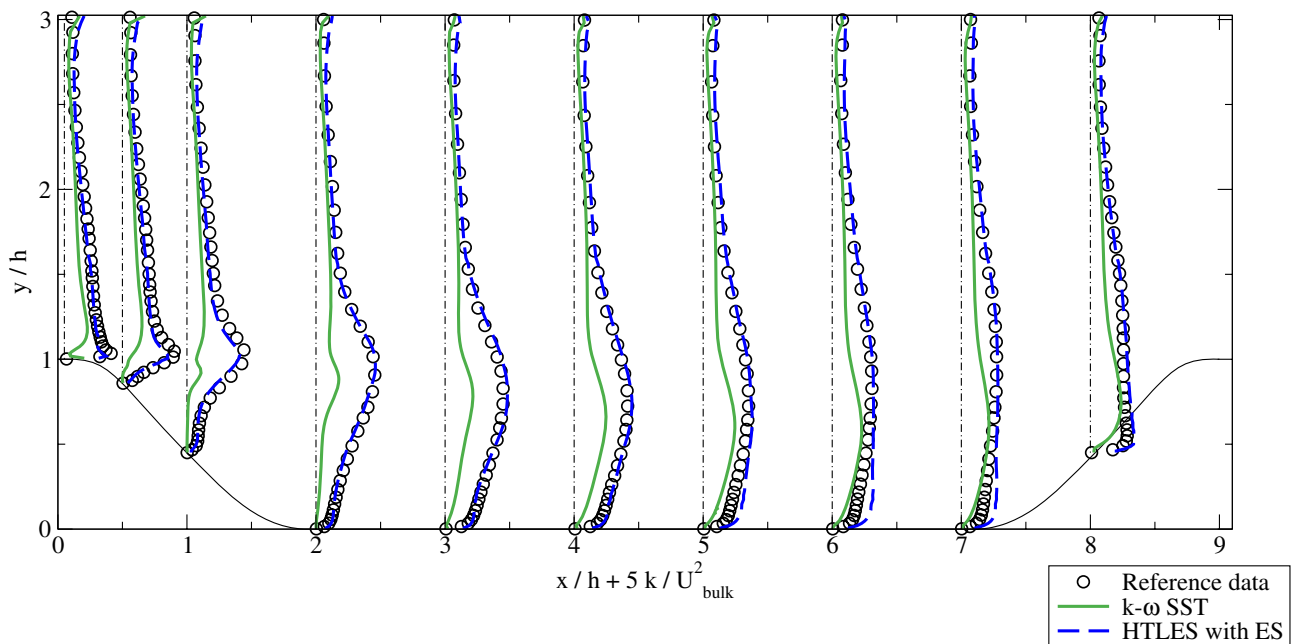


Fig. 7. Statistical average of the kinetic energy in the periodic hill channel.

that the intensity of the backflow is underestimated by the RANS model, and at  $\frac{x}{h} > 5$  that the flow reattaches far too late. Regarding HTLES results, velocity profiles are in a very good agreement with the reference data. The flow separates and reattaches at the proper locations, and the size and intensity of the recirculation region are predicted accurately.

Figure 7 compares total turbulent kinetic energy profiles. The  $k-\omega$  SST model severely underestimates the turbulent kinetic energy, in particular in the separated shear layer, whereas HTLES clearly provides a much better assessment, and especially in the recirculation zones. Downstream the reattachment location, HTLES slightly overestimates the turbulent kinetic energy.

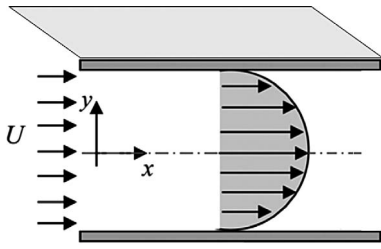


Fig. 8. Sketch of the channel flow.

### 4.3 Channel flow

#### 4.3.1 Flow conditions

The channel flow consists of a flow at constant flow rate between two infinite parallel walls, as shown in Figure 8.

Except for pressure, the flow is periodic in the  $x$ -direction. A streamwise source term equal to 176 Pa/m is added to the momentum equation in the  $x$ -direction in order to sustain the flow. The Reynolds number based on the friction velocity  $u_\tau$  is 1000 and the reference data are extracted from DNS (Lee and Moser [39]).

The flow is initialized using a coarse DNS, performed on the same grid and using a first-order upwind scheme. A physical time of 2 s was simulated, which corresponds to 200 convective times ( $t_x = \frac{L_x}{U_{\text{bulk}}}$ ). Mean quantities are collected over a time period of 180 convective times and are also averaged in the spanwise direction over a distance equal to the channel height. The simulations are performed on a grid which contains  $N_x \times N_y \times N_z = 500 \times 50 \times 100$  hexahedra with a uniform distribution. The height of the cells adjacent to walls has been chosen to target  $y^+ = 30$ . This choice is motivated by the today practice for industrial ICE simulations. Further details of the simulations are summarized in Table 1.

#### 4.3.2 Elliptic shielding in HTLES

Figure 9 represents the dimensionless axial velocity as a function of the wall distance in wall units  $y^+$  along the wall units  $y^+$  of the channel given by HTLES with and without the Elliptic Shielding (ES). One can notice the impact of ES on the flow rate. Table 2 compares flow rates given by the simulations with DNS data. HTLES without ES shows a relative error of +11% compared to DNS data, while HTLES with ES yields accurate flow rate showing an error of -2% only.

Figure 10 represents iso-surfaces of the non-dimensional  $Q$ -criterion equal to 0.2, based on  $U_b$  and  $\delta$ , to identify the turbulent structures given by the HTLES model. Turbulent structures are solved explicitly in the core region whereas unsteady structures can hardly be seen near the walls. This observation shows that HTLES is able to operate in the scale-resolving mode in the near-wall region and sustain the turbulence by means of the direct control of the energy partition directly in the  $k$ -equation unlike some hybrid models that degenerate in RANS mode in this situation [13].

Table 1. Flow conditions for the channel flow case.

Parameter	Value
Fluid	Air
Temperature [K]	320
Pressure [atm]	1
Channel half height $\delta$ [mm]	12.5

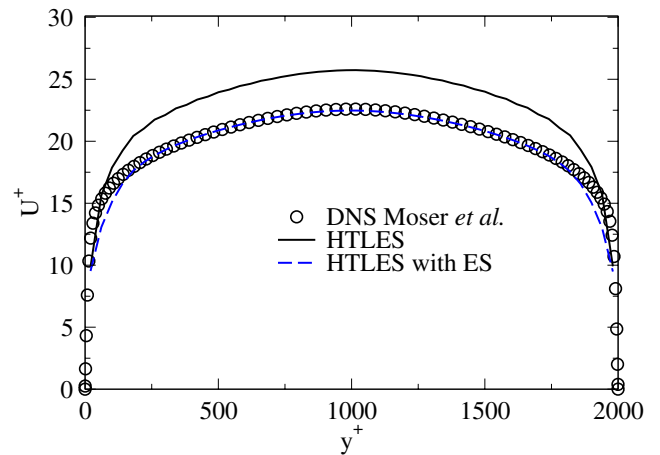


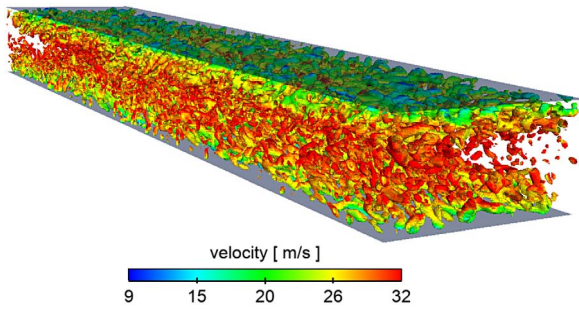
Fig. 9. Impact of the ES on the dimensionless velocity profiles for the channel flow  $Re_\tau = 1000$ .

Table 2. Flow rates given by the HTLES with and without ES.

	DNS	HTLES	HTLES with ES
Flow rate [ $\text{m}^3/\text{s}$ ]	0.71	0.79	0.69
Relative error $\varepsilon_D$ [%]	-	+11.0	-2.3

Figure 11 represents the statistical mean of the ratio  $r$  given by the two simulations. Using ES, the ratio  $r$  reaches unity at wall and decreases at a slope grade, which is less steep than in the simulation without ES. Far from wall, ES does not affect the results since the level of  $r$  is very close to the one without ES.

In-depth analysis is performed by examining the fluctuations given by HTLES with and without the ES as reported in Figure 12, which examines the impact of ES on the streamwise fluctuations. In the near-wall region, the resolved and the sub-filter fluctuations given by HTLES without ES are of the same order of magnitude. The scale-resolving mode is activated too close to the wall due to small values of the ratio  $r$  given by the HTLES model near the wall (Fig. 11). In HTLES with ES, the sub-filter fluctuations are increased near the wall and thus the scale-resolving region is shifted away from the wall. Although the targeted  $r$  plotted in Figure 11, evaluated by equation (10), goes to 1 at the wall, it is observed in Figure 12 that a significant part of the energy of the streamwise fluctuations is resolved. Indeed,  $r$  is only an ingredient of the model



**Fig. 10.** Iso-surfaces of the non-dimensional  $Q$ -criterion colored by the velocity magnitude given by the HTLES with ES in a channel flow.

that enters equation (4), and there is no mechanism in the simulation that imposes that the observed partition of energy among resolved and modeled scale satisfy this target ratio. A favorable side effect of the penetration of the resolved fluctuations in the RANS zone is that the level of resolved energy is high in the region where  $r$  rapidly falls from 1 to about 0.1, such that no modeled stress depletion is observed. It is observed that the near-wall peak of streamwise energy is underestimated in Figure 12 (right). This is due to the fact that, in this region, the simulation mostly rely on the RANS model, which is not able to reproduce this peak.

#### 4.3.3 Comparison to RANS and LES

RANS and LES are also performed in the channel flow case, and velocity profiles are compared to HTLES and to the reference data in Figure 13. The  $k-\omega$  SST shows very accurate velocity profiles in this configuration, and the flow rate is almost the same as DNS with a relative error of  $-0.4\%$ , as listed in Table 3. Unlike RANS, the velocity profile given by LES shows the same overestimation of the flow rate as HTLES without ES. Note that similar conclusions were already outlined in [8] when using wall functions in the channel flow. Indeed, LES combined with wall functions is not adapted for these configurations where the wall vicinity plays an essential role for the dynamics of the entire flow domain.

### 4.4 Steady flow rig

#### 4.4.1 Configuration

The steady flow rig represents a simplified in-cylinder flow around a valve with a fixed lift. The gas is injected in the intake port, which consists of a cylinder and fixed valve placed axisymmetrically inside the jet nozzle. The flow exiting through the valve opening is representative of the intake flow into an IC engine geometry. An overview of the geometry with its dimensions similar to a common passenger car engine are displayed in Figure 14. The Reynolds number based on the diameter of the cylinder and the bulk velocity is 30 000. Laser Doppler Anemometry (LDA) measurements were investigated by Thobois *et al.* [40], which

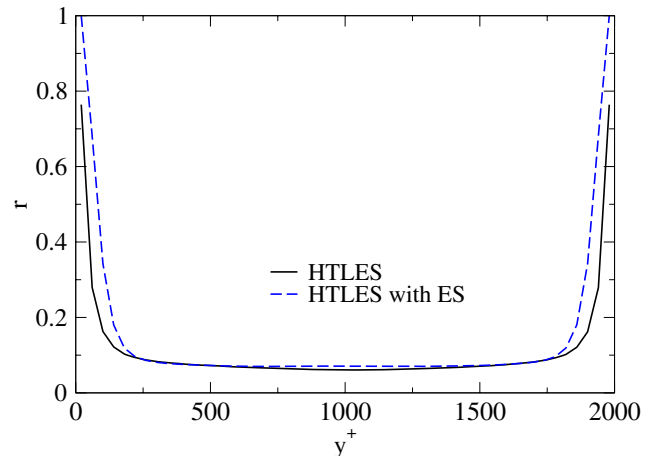


**Fig. 11.** The statistical mean of ratio  $r$  profiles along the wall-normal direction in a channel flow at  $Re_\tau = 1000$ .

provide the mean and rms for axial as well as radial velocity profiles located 20 mm and 70 mm from the abrupt expansion (Fig. 14).

The results shown herein compare three simulations of the flow inside the steady flow rig using the same grid composed of 1 402 628 cells. The side view of the hexahedral grid is shown in Figure 15: the grid step in the core of the domain is 2 mm; a refinement of 1 mm is embedded at the inlet pipe and the head of the valve where the jet develops; at the outlet a coarse grid size of 8 mm is used as a sponge layer to avoid the reflection of acoustic waves inside the chamber. At the walls, the grid resolution is refined insofar as the wall distance is less than 100.

At the inlet of the computational domain, a uniform mean axial velocity profile is imposed without fluctuations with the bulk velocity  $U_{\text{bulk}} = 65 \text{ m s}^{-1}$  at 300 K, such that the experimental mass flow rate is recovered ( $0.06 \text{ kg s}^{-1}$ ). A physical time of 2 s was simulated. The flow is established for a period of  $t = 0.3 \text{ s}$ , equivalent to 8 flow through the intake port; then, the statistics are collected during a period of 44 flow through the intake port which is equivalent to 1.7 s. The static pressure at the outlet is set to 1 bar. The walls are assumed to be hydraulically smooth and adiabatic. The initial field used in the RANS simulation is defined as uniform, equal to the bulk velocity, while HTLES and LES initial fields are defined by the RANS solution.

#### 4.4.2 Qualitative comparison to RANS and LES

Figure 16 shows a section at the center of the computational domain of the mean streamlines for RANS, LES and HTLES. An attached boundary layer develops upstream of the valve. The flow accelerates due to the valve restriction and a cylindrical jet emanates downstream of the valve. The jet creates two axisymmetric, counter rotative recirculation regions: the first one is confined between the head of the chamber and the upper part of the sleeve, the second one appears downstream and is larger. The three

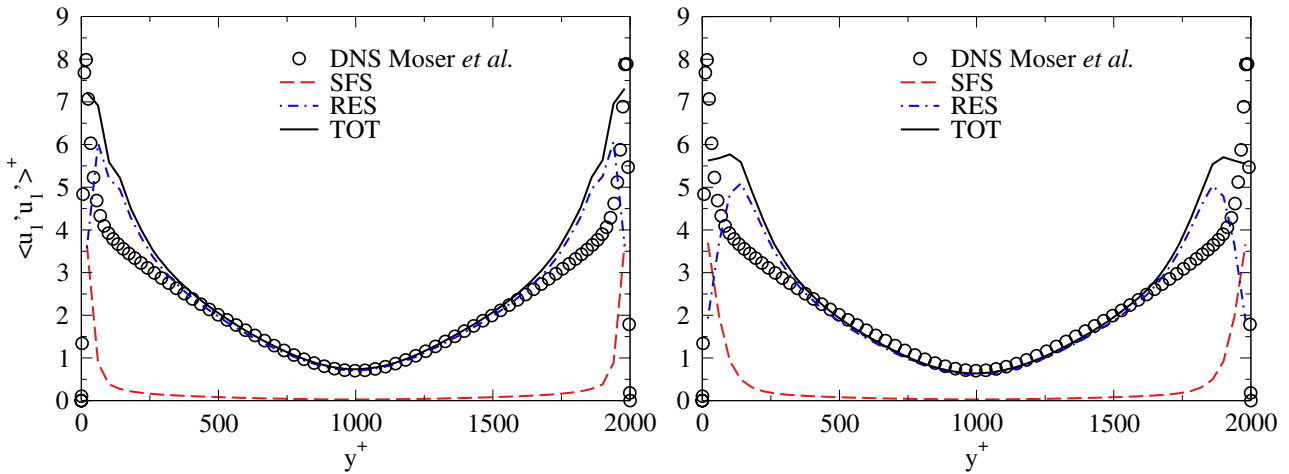


**Fig. 12.** Influence of the ES on the resolved RES =  $\langle u_1' u_1' \rangle^+$ , modeled SFS =  $\langle \tau_{11} \rangle^+$  and total TOT = RES + SFS streamwise component of the fluctuations. Left: HTLES. Right: HTLES with ES.

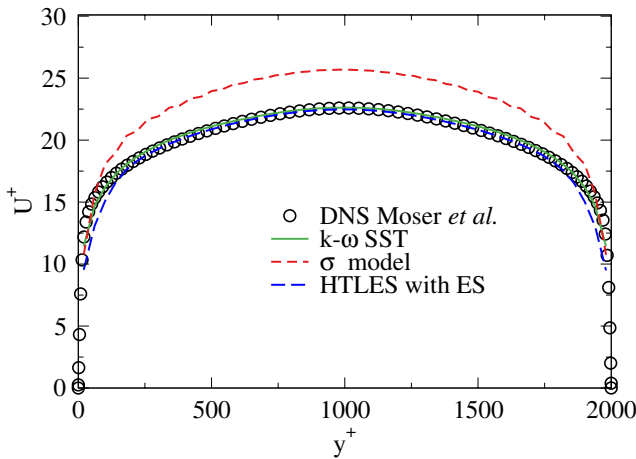


**Fig. 13.** Comparison of the mean axial velocity along the wall-normal direction between RANS, LES and HTLES models.

**Table 3.** Comparison of the flow rates given by different simulation methods to DNS data.

	DNS	RANS	LES	HTLES ES
Flow rate [m <sup>3</sup> /s]	0.71	0.70	0.79	0.69
Relative error $\epsilon_D$ [%]	-	-0.4	10.7	-2.3

simulations accurately reproduce the topology of the first recirculation region, with the same center location identified by a dashed line. Nevertheless, the second recirculation in RANS is longer than for LES and HTLES.

$Q$ -criterion is examined in Figure 17 in order to help visualizing the structures, only one half of the domain is shown. The grid resolution employed here is purposely insufficient for solving the turbulent structures upstream of the valve. Downstream, a part of the turbulent structures

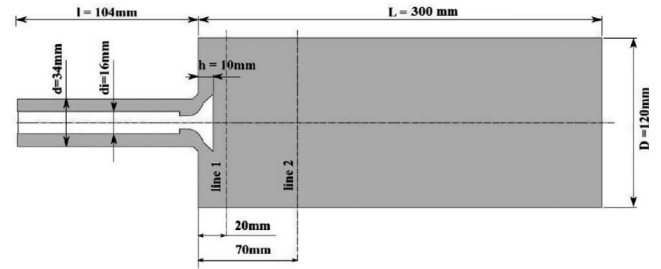


**Fig. 14.** Schematic and geometrical parameters of the steady flow rig.

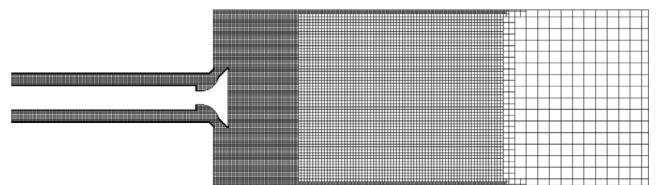


**Fig. 15.** Side view of hexahedral mesh in the steady flow rig.

is solved where the mesh is sufficiently fine, far from the boundaries.

#### 4.4.3 Quantitative comparison to RANS and LES

In order to assess the three approaches quantitatively, mean and rms velocity profiles along line 1 and line 2, respectively at 20 mm and 70 mm from the top of the cylinder (Fig. 14), are compared to the experimental measurements.

The mean axial velocity along line 1, given by the simulations, is compared in Figure 18. All the simulations give similar profiles of the axial velocity at this location. The velocity magnitudes and the shape of the profiles are in a

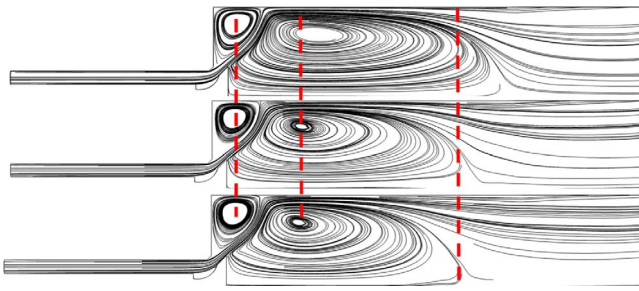


**Fig. 16.** Cut plane of a mean streamlines obtained with (top) RANS (middle) LES (bottom) HTLES.

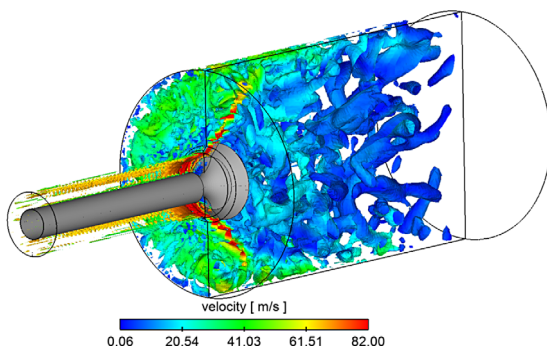


**Fig. 17.** Cut box of iso-surfaces of non-dimensional  $Q$ -criterion at 0.04 colored by the velocity magnitude in HTLES.

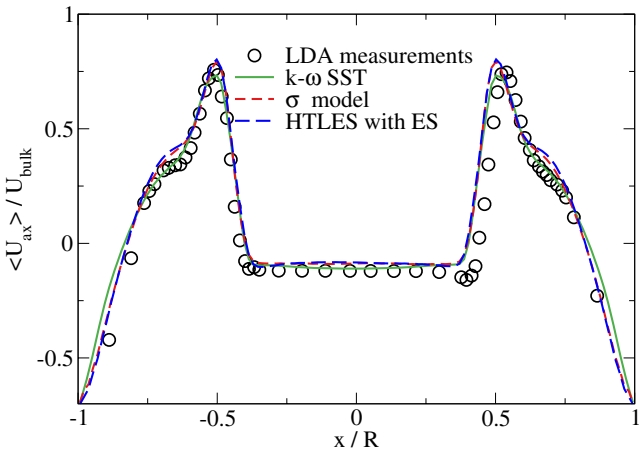


**Fig. 18.** Comparison of dimensionless mean axial velocity along line 1.

good agreement with the experiment. LES and HTLES mean velocity profiles are quasi-identical, and the velocity peaks are slightly better predicted compared to the  $k-\omega$  SST.

Discrepancies between the simulations can be observed for the mean radial velocity profiles as shown in Figure 19. HTLES and LES show similar radial profiles and provide a

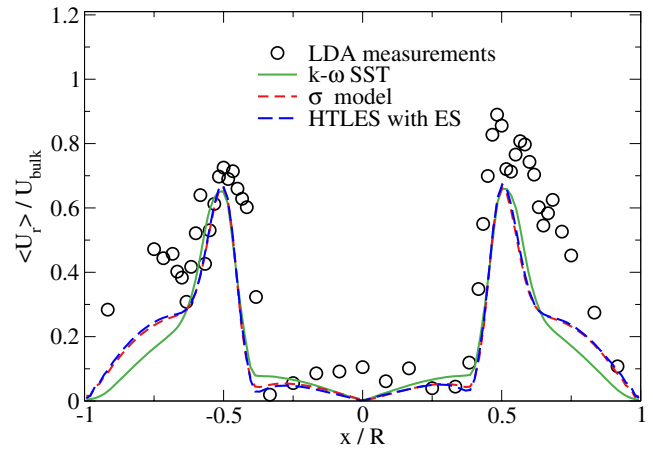


**Fig. 19.** Comparison of dimensionless mean radial velocity along line 1.

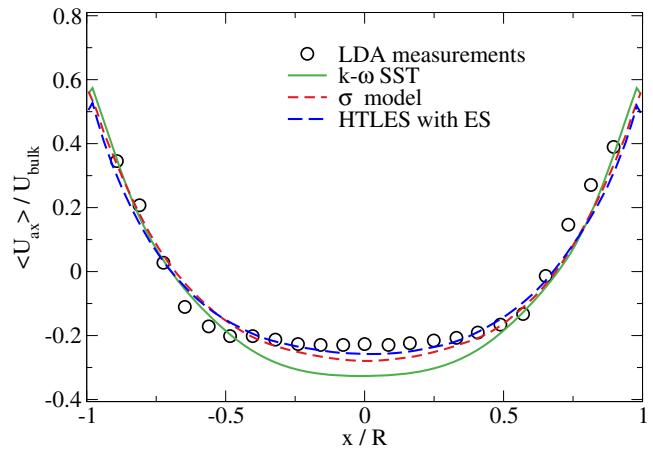


**Fig. 20.** Comparison of dimensionless mean axial velocity along line 2.

good assessment of radial velocity profiles within the recirculation region ( $0.5 < \frac{x}{R} < 1$ ), whereas to the  $k-\omega$  SST underestimates the radial velocity within the recirculation. The experimental data are distributed along a large deviation at this location and hence no clear conclusion can be drawn regarding velocity magnitudes.

The mean axial velocity profiles along line 2 are compared in Figure 20. Similar axial velocity profiles are obtained in HTLES and LES, which are in a good agreement with the experiments. The  $k-\omega$  SST overestimates the axial velocity in the central region where  $-0.5 < \frac{x}{R} < 0.5$ , which confirms that the larger recirculation is overestimated by the RANS simulation.

In Figure 21, the radial velocity along line 2 (Fig. 14) is represented. One can notice the small velocity magnitudes at this location. Despite the axisymmetric configuration, both experimental and simulation data are not fully symmetrical. The asymmetry in experimental data can be related to an intrinsic uncertainty of the measurement device due to the small velocity magnitudes, while the

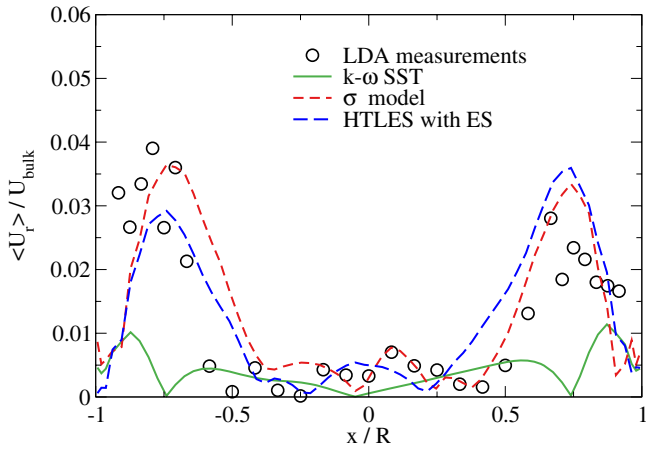


**Fig. 21.** Comparison of dimensionless mean radial velocity along line 2.

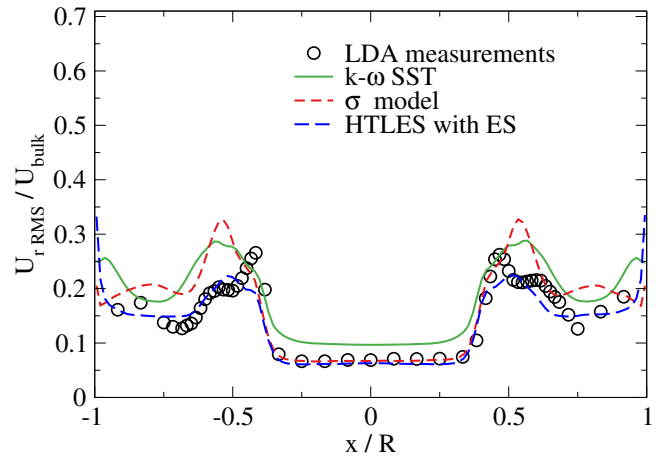


**Fig. 23.** Comparison of dimensionless rms radial velocity along line 1.

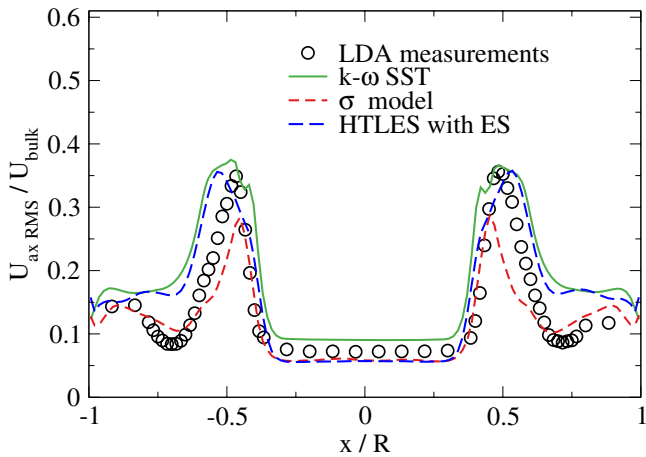


**Fig. 22.** Comparison of dimensionless rms axial velocity along line 1.

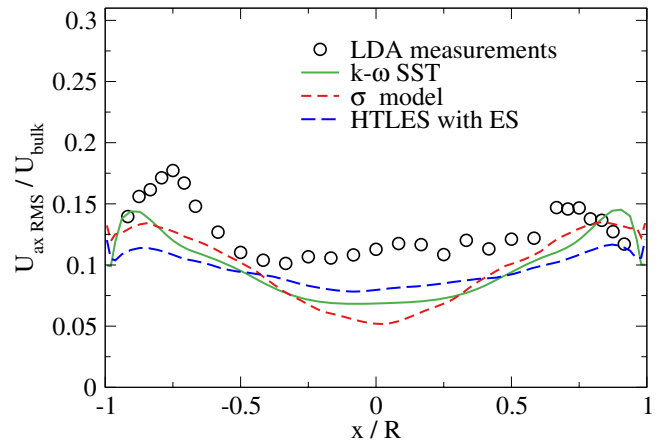


**Fig. 24.** Comparison of dimensionless rms axial velocity along line 2.

asymmetry in the simulations can be related to insufficiently converged statistics. HTLES and LES still provide results close to experimental data, whereas the  $k-\omega$  SST clearly under-estimates the radial velocity at this location.

Profiles are compared hereafter. Both the sub-filter and the resolved parts are taken into account. The axial rms velocity profiles are compared to LDA measurements in Figure 22. All simulations show acceptable results compared to the experimental data. HTLES provides results similar to RANS in the smaller recirculation region and nearly identical to LES in the larger one. These results are consistent with the previous observation since the RANS mode is enforced close to walls and the grid resolution is sufficient to make a transition toward the scale-resolving method. Finally,  $k-\omega$  SST results exhibit higher levels of fluctuations in the core region than HTLES and LES results.

It is observed in Figure 23 that RANS and LES both overestimate the peak of  $U_{r,rms}$  at the location of the

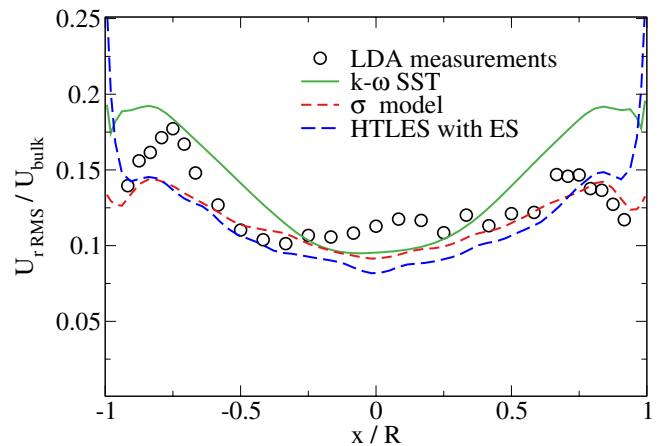


**Fig. 25.** Comparison of dimensionless rms radial velocity along line 2.

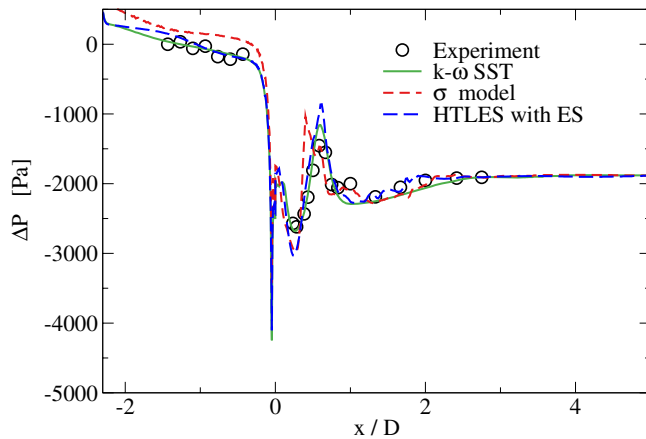


Fig. 26. Comparison of the axial profile of pressure.

Table 4. Comparison of the pressure drop given by the three simulations.

	EXP	RANS	HTLES ES	LES
$\Delta P$ [Pa]	1766	1713	1705	1957
Relative error $\varepsilon_D$ [%]	–	–3	–3	+11

annular jet  $\frac{r}{R} \pm 0.5$  and mispredicts its location. HTLES accurately reproduces the shape of the profile everywhere except for the peak that is completely missed.

Figures 24 and 25 show the profiles along line 2 for the axial and radial velocities, respectively, and the trends are the same as those already noticed for line 1. However, the experimental uncertainties, reflected by the asymmetry of the data, are such that it is difficult to draw any conclusion for rms velocity profiles along this line.

Figure 26 compares the axial profile of the static pressure at the wall in order to assess the pressure drop in the different regions. All the simulations reproduce the stiff pressure decrease at  $x = 0$  due to the sudden expansion, and the recirculation zone featured by a slight pressure increase at  $x/D = 1$ . Despite this good qualitative agreement, the global pressure drop defined as the difference of pressure between the position downstream the valve and outlet of the domain is different between the three simulations. While RANS and HTLES provide a prediction close to the experiment with a relative error of  $-3\%$  (Tab. 4), LES is less accurate with a relative error of  $+11\%$ . As already discussed in the channel flow section, this might be due to the wall modeling employed in the LES.

#### 4.4.4 Analysis of HTLES modeled stress

The ratios  $r$  without and with ES along line 1 and line 2 are compared in Figures 27 and 28, respectively. The ES only affects the values of  $r$  in the near-wall region where it reaches unity, unlike the simulation without ES where  $r$  is much lower than one at the wall along both lines 1 and 2.

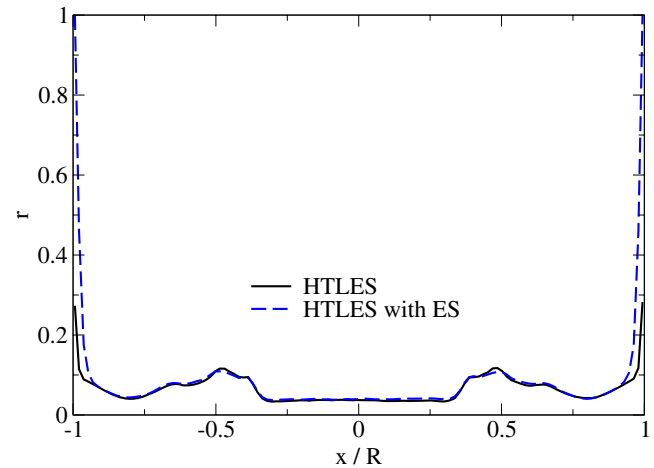


Fig. 27. Profiles along the radius of the cylinder (line 1) of the statistical average of the ratio  $r$ .

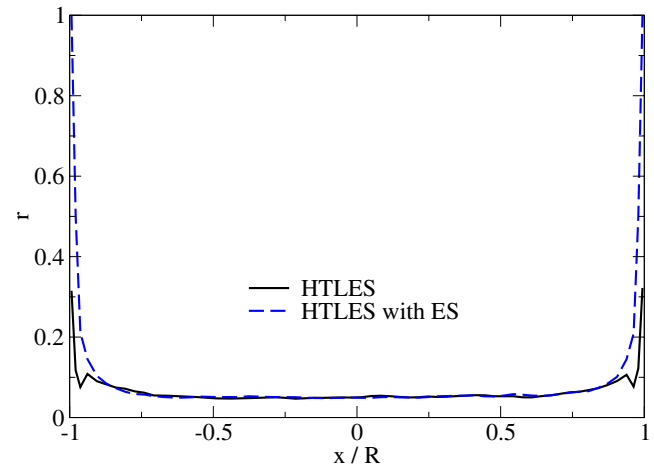
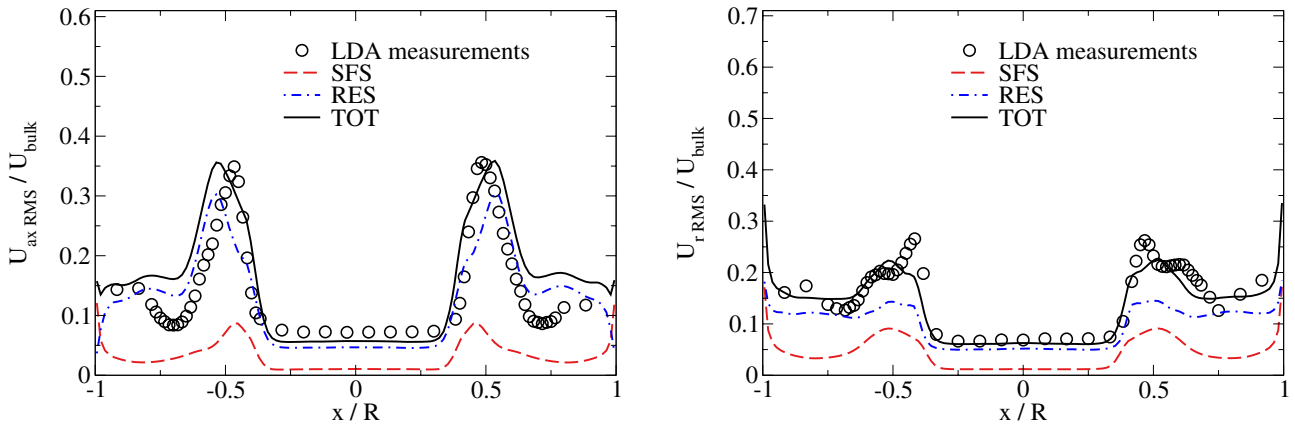


Fig. 28. Profiles along the radius of the cylinder (line 2) of the statistical average of the ratio  $r$ .

This is consistent with the results obtained in the channel flow case (Fig. 11).

In order to perform a deeper analysis of the HTLES modeled stress, rms velocity for both axial and radial components are decomposed into the resolved and sub-filter parts in Figures 29 and 30. Regarding the sub-filter rms velocities, the evolution is consistent, for both components and for both lines, with the evolution of  $r$  displayed in Figures 27 and 28. The sub-filter fluctuations increase at walls and decrease in the core region for both components but are not negligible compared to the resolved ones.

The plots of the resolved rms velocities show that the axial contribution vanishes at the wall along both lines 1 and 2, as expected. However, the radial component surprisingly does not vanish at the wall along both lines. The same issue is observed in RANS and LES simulations in Figures 23 and 25, which points the difficulty of the code to impose tangential velocities to walls.



**Fig. 29.** Decomposition of the dimensionless rms velocity along line 1 into two components, RES the resolved part and SFS the modeled part. Left: axial rms velocity. Right: radial rms velocity.

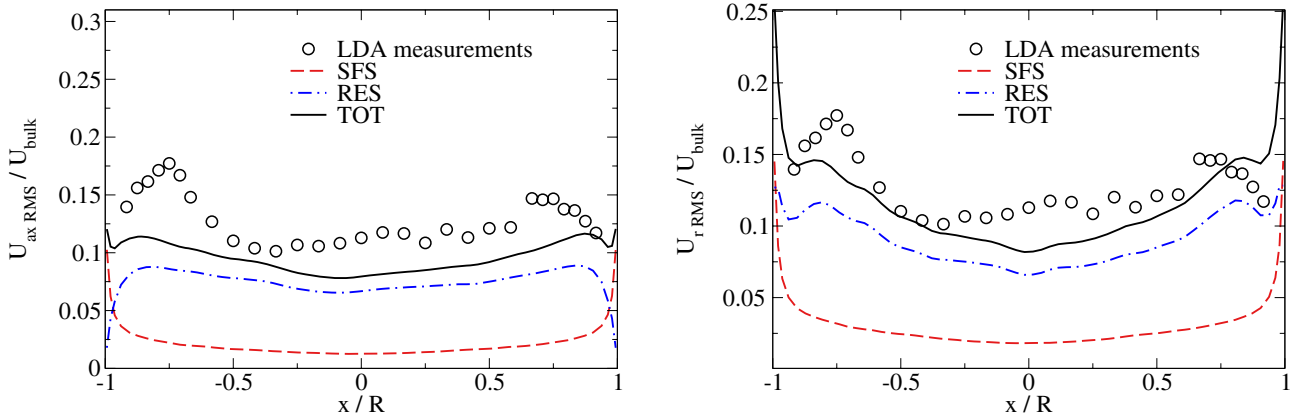


**Fig. 30.** Decomposition of the dimensionless rms velocity along line 2 into two components, RES the resolved part and SFS the modeled part. Left: axial rms velocity. Right: radial rms velocity.

### 5 Conclusion

A first application of a hybrid RANS-LES method, which is intended to be used for simulations of ICE was presented. The proposed HTLES derived from the TPITM model offers a formalism based on the multi-scale approach. The HTLES model relies on the same set of equations as the  $k-\omega$  SST model and introduces a temporal filter width on the dissipation term of the  $k$ -equation, which is made sensitive to the grid and temporal resolutions. ES was adjoined to HTLES to protect the near-wall region from incursions of the scale-resolving method too close to walls. HTLES uses time averaged velocities for assessing the total turbulent kinetic energy which is required for the closing of the dissipation term of the sub-filter energy. A modification from the original HTLES is proposed by applying the averaging process to the resolved kinetic energy instead of the total one, and by removing the averaging process on the dissipation term in the balance equation of the sub-filter kinetic

energy. This constitutes a first step towards the application of HTLES towards unsteady cases and ICE flows.

The HTLES method is applied to three cases and the results are compared with reference data as well as with the URANS  $k-\omega$  SST model and LES  $\sigma$  model. The main conclusions are listed below:

- First validation in the periodic hills has underlined a very good prediction capability of the developed HTLES for this separated flow, whereas the recirculation length obtained with the  $k-\omega$  SST model is severely overestimated.
- Regarding the channel flow case, HTLES with ES solves the wall friction and the unsteadiness of the flow properly. The smooth variation with the wall-distance of the energy ratio induces a smooth transition from the RANS region and the scale-resolving region, and thus no modeled stress depletion is observed. RANS mode at wall yields correct prediction of the flow rate

on the one hand and the scale resolving simulation gives satisfactory assessment of the fluctuations on the rest of the domain.

- HTLES has been employed for the steady flow rig, which is a configuration close to ICE. Very good positioning of HTLES versus RANS and LES was noticed. On the one hand, for the same grid, the results of HTLES in terms of mean and rms velocity profiles are as accurate as LES unlike RANS, which exhibits some discrepancies with the reference data. On the other hand, the experimental pressure drop is properly predicted by HTLES in contrast to LES.

The application of HTLES implemented in the CONVERGE code shows promising results in stationary flows. The only remaining restriction for using HTLES in non-stationary flows is related to the statistical averaging of the velocity required for computing the resolved turbulent kinetic energy, and future work will be dedicated to this issue in order to make HTLES applicable to ICE configuration with moving walls.

## References

- 1 Jiménez J. (2003) Computing high-Reynolds-number turbulence: will simulations ever replace experiments? *J. Turbulence* **4**, N22. doi: [10.1088/1468-5248/4/1/022](https://doi.org/10.1088/1468-5248/4/1/022).
- 2 Chevillard S., Colin O., Bohbot J., Wang M., Pomraning E., Senecal P.K. (2017) Advanced methodology to investigate knock for downsized gasoline direct injection engine using 3D RANS simulations, in: *WCX. 17: SAE World Congress Experience*, SAE International. doi: [10.4271/2017-01-0579](https://doi.org/10.4271/2017-01-0579).
- 3 Bohbot J., Colin O., Velghe A., Michel J.B., Wang M., Senecal P.K., Pomraning E. (2016) An innovative approach combining adaptive mesh refinement, the ECFM3Z turbulent combustion model, and the TKI tabulated auto-ignition model for diesel engine CFD simulations, in: *SAE 2016 World Congress and Exhibition*, SAE International. doi: [10.4271/2016-01-0604](https://doi.org/10.4271/2016-01-0604).
- 4 Colin O., Benkenida A. (2004) The 3-zones extended coherent flame model (ECFM3Z) for computing premixed/diffusion combustion, *Oil Gas Sci. Technol. - Rev. IFP Energies nouvelles* **59**, 6, 593–609. doi: [10.2516/ogst:2004043](https://doi.org/10.2516/ogst:2004043).
- 5 Scarcelli R., Richards K., Pomraning E., Senecal P.K., Wallner T., Sevik J. (2016) Cycle-to-cycle variations in multi-cycle engine RANS simulations, in: *SAE 2016 World Congress and Exhibition*, doi: [10.4271/2016-01-0593](https://doi.org/10.4271/2016-01-0593).
- 6 Robert A., Richard S., Colin O., Martinez L., De Francqueville L. (2015) LES prediction and analysis of knocking combustion in a spark ignition engine, *Proceedings of the Combustion Institute* **35**, 3, 2941–2948. doi: [10.1016/j.proci.2014.05.154](https://doi.org/10.1016/j.proci.2014.05.154).
- 7 Pope S.B. (2000) Turbulent flows, Cambridge University Press, Cambridge, UK, doi: [10.1017/CBO9780511840531](https://doi.org/10.1017/CBO9780511840531).
- 8 Nicoud E. (2018) Quantifying combustion robustness in GDI engines by Large-Eddy simulation, *PhD Thesis*, Université Paris-Saclay, Saint-Aubin, France.
- 9 Schumann U. (1975) Subgrid scale model for finite difference simulations of turbulent flows in plane channels and annuli, *J. Comput. Phys.* **18**, 4, 376–404. doi: [10.1016/0021-9991\(75\)90093-5](https://doi.org/10.1016/0021-9991(75)90093-5).
- 10 Sagaut P., Deck S., Terracol M. (2013) *Multiscale and multiresolution approaches in turbulence: LES, DES and hybrid RANS/LES methods/applications and guidelines*, 2nd edn, Imperial College Press, London.
- 11 Buhl S., Dietzsch F., Buhl C., Hasse C. (2017) Comparative study of turbulence models for scale-resolving simulations of internal combustion engine flows, *Comput. Fluids* **156**, 66–80. doi: [10.1016/j.compfluid.2017.06.023](https://doi.org/10.1016/j.compfluid.2017.06.023).
- 12 Basara B. (2015) PANS method as a computational framework from an industrial perspective, in: Girimaji S., Haase W., Peng S.H., Schwaborn D. (eds), *Progress in hybrid RANS-LES modelling*, volume 137 of Notes on Numerical Fluid Mechanics and Multidisciplinary Design, Springer, Cham, Switzerland, pp. 3–17.
- 13 Manceau R. (2018) Progress in hybrid temporal LES, in: Hoarau Y., Peng S.-H., Schwaborn D., Revell A. (eds), *Progress in hybrid RANS-LES modelling*, Springer, Berlin Heidelberg/New York NY, pp. 9–25.
- 14 Pruet C. (2008) Temporal large-eddy simulation: theory and implementation, *Theor. Comput. Fluid Dyn.* **22**, 3, 275–304. doi: [10.1007/s00162-007-0063-0](https://doi.org/10.1007/s00162-007-0063-0).
- 15 Fadai-Ghotbi A., Christophe F., Manceau R., Gatski T., Boree J. (2010) Temporal filtering: A consistent formalism for seamless hybrid RANS-LES modeling in inhomogeneous turbulence, *Int. J. Heat Fluid Flow* **31**, 378–389. doi: [10.1016/j.ijheatfluidflow.2009.12.008](https://doi.org/10.1016/j.ijheatfluidflow.2009.12.008).
- 16 Saric S., Jakirlic S., Breuer M., Jaffrézic B., Deng G., Chikhaoui O., Fröhlich J., von Terzi D., Manhart M., Peller N. (2007) Evaluation of detached Eddy simulations for predicting the flow over periodic hills, *ESAIM: Proc.* **16**, 133–145. doi: [10.1051/proc:2007016](https://doi.org/10.1051/proc:2007016).
- 17 Fröhlich J., von Terzi D. (2008) Hybrid LES/RANS methods for the simulation of turbulent flows, *Prog. Aerosp. Sci.* **44**, 5, 349–377. doi: [10.1016/j.paerosci.2008.05.001](https://doi.org/10.1016/j.paerosci.2008.05.001).
- 18 Gatski T., Rumsey C., Manceau R. (2007) Current trends in modelling research for turbulent aerodynamic flows, *Philos. Trans. R. Soc. Lond. A* **365**, 1859, 2389–2418.
- 19 Fadai-Ghotbi A., Friess C., Manceau R., Borée J. (2010) A seamless hybrid RANS-LES model based on transport equations for the subgrid stresses and elliptic blending, *Phys. Fluids* **22**, 5, 055104. doi: [10.1063/1.3415254](https://doi.org/10.1063/1.3415254).
- 20 Chaouat B. (2017) The state of the art of hybrid RANS/LES modeling for the simulation of turbulent flows, *Flow Turbul. Combust.* **99**, 2, 279–327. doi: [10.1007/s10494-017-9828-8](https://doi.org/10.1007/s10494-017-9828-8).
- 21 Schiestel R., Dejoan A. (2005) Towards a new partially integrated transport model for coarse grid and unsteady turbulent flow simulations, *Theor. Comput. Fluid Dyn.* **18**, 6, 443–468. doi: [10.1007/s00162-004-0155-z](https://doi.org/10.1007/s00162-004-0155-z).
- 22 Chaouat B., Schiestel R. (2005) A new partially integrated transport model for subgrid-scale stresses and dissipation rate for turbulent developing flows, *Phys. Fluids* **17**, 6, 065106. doi: [10.1063/1.1928607](https://doi.org/10.1063/1.1928607).
- 23 Schiestel R. (1987) Multiple-time-scale modeling of turbulent flows in one-point closures, *Phys. Fluids* **30**, 3, 722–731. doi: [10.1063/1.866322](https://doi.org/10.1063/1.866322).
- 24 Tran T., Manceau R., Perrin R., Borée J., Nguyen A. (2012) A hybrid temporal LES approach. Application to flows around rectangular cylinders, *Proc. 9th ERCOFTAC Int. Symp. on Eng. Turb. Modelling and Measurements*, Thessaloniki, Greece.
- 25 Travin A., Shur M., Strelets M., Spalart P.R. (2002) Physical and numerical upgrades in the detached-Eddy simulation of

- complex turbulent flows, in: Friedrich R., Rodi W. (eds), *Advances in LES of complex flows*, Springer, Dordrecht, The Netherlands, pp. 239–254.
- 26 Manceau R., Gatski T., Friess C. (2010) Recent progress in hybrid temporal LES-RANS modeling, in: Pereira J.C.F., Sequeira A. (eds), *European Conference on Computational Fluid Dynamics, V*, Technical University of Lisbon, Lisbon, pp. 1525–1532.
- 27 Friess C., Manceau R., Gatski T.B. (2015) Toward an equivalence criterion for Hybrid RANS/LES methods, *Comput. Fluids* **122**, 233–246. doi: [10.1016/j.compfluid.2015.08.010](https://doi.org/10.1016/j.compfluid.2015.08.010).
- 28 Spalart P.R. (2009) Detached-eddy simulation, *Annu. Rev. Fluid Mech.* **41**, 1, 181–202. doi: [10.1146/annurev.fluid.010908.165130](https://doi.org/10.1146/annurev.fluid.010908.165130).
- 29 Menter F., Ferreira J.C., Esch T., Konno B. (2003) The SST turbulence model with improved wall treatment for heat transfer predictions in gas turbines, in: *Proceedings of the International Gas Turbine Congress 2003*, Tokyo, IGTC2003-TS-059, pp. 2–7.
- 30 Oliveira P.J., Issa R.I. (2001) An improved PISO algorithm for the computation of buoyancy-driven flows, *Numer. Heat Transf. B Fundam.* **40**, 6, 473–493. doi: [10.1080/104077901753306601](https://doi.org/10.1080/104077901753306601).
- 31 Redlich O., Kwong J.N.S. (1949) On the thermodynamics of solutions. V. An equation of state. Fugacities of gaseous solutions, *Chem. Rev.* **44**, 1, 233–244. doi: [10.1021/cr60137a013](https://doi.org/10.1021/cr60137a013).
- 32 Rhie C.M., Chow W.L. (1983) Numerical study of the turbulent flow past an airfoil with trailing edge separation, *AIAA J.* **21**, 11, 1525–1532. doi: [10.2514/3.8284](https://doi.org/10.2514/3.8284).
- 33 Jakirlic S., Jester-Zurker R., Tropea C. (2001) *9th ERCOFTAC/IAHR/COST Workshop on Refined Turbulence Modelling*, Darmstadt University.
- 34 Menter F., Rumsey C. (1994) Assessment of two-equation turbulence models for transonic flows, in: *Fluid Dynamics Conference, Fluid Dynamics and Co-located Conferences*, American Institute of Aeronautics and Astronautics. doi: [10.2514/6.1994-2343](https://doi.org/10.2514/6.1994-2343).
- 35 Nicoud F., Toda H.B., Cabrit O., Bose S., Lee L. (2011) Using singular values to build a subgrid-scale model for large eddy simulations, *Phys. Fluids* **23**, 8, 085106. doi: [10.1063/1.3623274](https://doi.org/10.1063/1.3623274).
- 36 Werner H., Wengle H. (1993) Large-eddy simulation of turbulent flow over and around a cube in a plate channel, in: Durst F., Friedrich R., Launder B.E., Schmidt F.W., Schumann U., Whitelaw J.H. (eds), *Turbulent shear flows 8*, Springer, Berlin, Heidelberg, pp. 155–168.
- 37 Fadai-Ghotbi A., Manceau R., Borée J. (2009) Revisiting URANS computations of the flow behind a backward-facing step using second moment closures, in: Deconinck H., Dick E. (eds), *Computational fluid dynamics 2006*, Springer, Berlin, Heidelberg, pp. 505–510.
- 38 Frohlich J., Mellen C.P., Rodi W., Temmerman L., Leschziner M.A. (2005) Highly resolved large-eddy simulation of separated flow in a channel with streamwise periodic constrictions, *J. Fluid Mech.* **526**, 19–66. doi: [10.1017/S0022112004002812](https://doi.org/10.1017/S0022112004002812).
- 39 Lee M., Moser R.D. (2015) Direct numerical simulation of turbulent channel flow up to  $Re_t \sim 5200$ , *J. Fluid Mech.* **774**, 395–415. doi: [10.1017/jfm.2015.268](https://doi.org/10.1017/jfm.2015.268).
- 40 Thobois L., Rymer G., Souleres T., Poinot T. (2004) Large-eddy simulation in IC engine geometries, in: *2004 SAE Fuels Lubricants Meeting Exhibition*, SAE International. doi: [10.4271/2004-01-1854](https://doi.org/10.4271/2004-01-1854).

